Design and Development of High-Performance Solid Electrolyte for All-Solid-State Lithium Ion Batteries

A Dissertation
Presented to
The Academic Faculty

by
Zhantao Liu

In Partial Fulfillment
Of the Requirements for the Degree
Doctor of Philosophy in the
School of George W. Woodruff School of Mechanical Engineering

Georgia Institute of Technology
December 2021

Design and Development of High-Performance Solid Electrolyte for All-Solid-State Lithium Ion Batteries

Approved by:

Dr. Hailong Chen, Advisor
School of Mechanical Engineering
Georgia Institute of Technology

Dr. Matthew T. McDowell
School of Mechanical Engineering
Georgia Institute of Technology

Dr. Angus Wilkinson
School of Chemistry and Biochemistry
Georgia Institute of Technology

Dr. Shuman Xia
School of Mechanical Engineering
Georgia Institute of Technology

Dr. Ting Zhu
School of Mechanical Engineering
Georgia Institute of Technology

Date approved: November 29th. 2021

Dedicated to my family.

ACKNOWLEDGEMENTS

Throughout my PhD, many people inspired me and this dissertation would no be possible without their support.

I would like to extend my sincere gratitude to my advisor, Prof. Hailong Chen, for his guidance, encouragement and support. When I came to Georgia Tech, the research in solid-state Li ion conductors was a new direction in our group and there was not much experience. Prof. Chen discussed with me closely and gave me useful advices all the time to overcome challenges. I am very grateful to Prof. Chen for granting me the freedom to pursue my interests. I have been constantly impressed by his great patience, enthusiasm and knowledge. He has greatly improved my critical thinking as well as my overall independence in research.

I would like to thank Prof. Angus Wilkinson, Prof. Matthew T. McDowell, Prof. Shuman Xia and Prof. Ting Zhu for being my PhD defense committee members.

I would like to thank the whole Chen group for support and help. I would like to acknowledge help from Dr. Hai Wang for his tutoring, who was visiting scholar and initiated the work of solid-state electrolyte in our group. I would like to thank Dr. Xuetian Ma, Dr. Shanxiong, Yifan Ma, Aijie Han, Yangyang Li, Zoe Holderness, Jacqueline Baidoo, Changhao Chen, Bo Nan and Shikai Jin for their support and friendship. Especially, I want to thank Dr. Xuetian Ma, Dr. Shanxiong and Yifan Ma, for their support in our tough experiments in national labs.

In addition, I would like to thank my collaborators outside my group. I am grateful for Prof. Yifei Mo, Dr. Xingfeng He and Dr. Shuo Wang at University of Maryland for their outstanding work in theoretical calculation. I would like to thank Dr. Jue Liu, Dr. Po-Hsiu Chien and Dr. Cheng Li at Neutron Scattering Division at Oak Ridge National Laboratory (ORNL) for neutron

diffraction data collection and analysis. I learned a lot from their meticulous attitude towards science. I would also like to extend my gratitude to a number of scientists, Dr. Wenqian Xu, Dr. Andrey Yakovenko and Dr. Kamila Magdalena Wiaderek at Advanced Photon Sources (APS) at Argonne National Laboratory (ANL), Dr. Jianming Bai, Dr. Eric Dooryhee and Dr. Hui Zhong at National Synchrotron Light Source II (NSLS II) at Brookhaven National Laboratory (BNL). Their expertise provides strong technical support, which ensured the success for planned experiments in my beamline trips. I am also grateful for the help of Dr. Biaowan, Pan Liu, Simin Zhao and Prof. Yuanzhi Tang for their help and support in my research projects.

Next, I would also like to acknowledge my funding sources: Georgia Tech startup funding and National Science Foundation for supporting me throughout my graduate studies.

Finally, I will forever be thankful to my friends and family. It is a tough time to finish PhD study during pandemic and their support and encouragement inspire me to keep moving forward all the time. I would like to thank our neighbors Emmett Nash and Daniel Nash, who helped Sangni and me a lot. Especially, I would like to extend my gratitude to my mother-in-law, Nina Li, for flying halfway around the world to take care of our family during the pandemic. I would like to express my deepest gratitude to my wife Sangni Xun for her accompany all the way and appreciated sacrifices. Thank you my newborn baby, Kexin. You are the most precious gift I ever had this year.

Table of Contents

LIST OF FIGURES

LIST OF TABLES

LIST OF SYMBOLS AND ABBREVIATIONS

AIMD	*ab initio* molecular dynamics
ANL	Argonne National Laboratory
APS	Advanced Photon Source
ALSOLIBs	all solid-state lithium-ion batteries
bcc	body-centered cubic
BM	ball mill
BNL	Brookhaven National Laboratory
CE	Coulombic efficiency
BVSE	bond valence site energy
CV	cyclic voltammogram
DEC	diethyl carbonate
DFT	density functional theory
DMC	dimethyl carbonate
EC	ethylene carbonate
EDX	energy dispersive X-ray spectroscopy
EIS	electrochemical impedance spectroscopy
EMC	ethyl methyl carbonate
EXAFS	extended X-ray absorption fine structure
FEC	Fluoroethylene carbonate
fcc	face-centered cubic

FWHM	full width at half maximum
GB	grain boundary
GOF	goodness-of-fit
hcp	hexagonal close-packed
LCO	$LiCoO_2$
LEs	liquid electrolytes
LGPS	$Li_{10}GeP_2S_{12}$
LIBs	Lithium-ion batteries
LISICON	Li superionic conductor
LLZO	$Li_7La_3Zr_2O_{12}$
NASICON	Na super ionic conductor
MAS	magic-angle spinning
NCA	$Li(Ni_{0.8}Co_{.15}Al_{0.05})O_2$
NMC	$Li(Ni_{1/3}Mn_{1/3}Co_{1/3})O_2$
PC	propylene carbonate
NMR	nuclear magnetic resonance
NSLS-II	National Synchrotron Light Source II
PBE	Perdew-Burke-Ernzerhof
PDF	pair distribution function
r.t.	room temperature
SEI	solid electrolyte interphase
SEs	solid electrolytes
VASP	Vienna *Ab initio* Simulation package

VT	variable temperature
XRD	X-ray diffraction
XANES	X-ray absorption near-edge spectroscopy
TEM	Transmission electron microscopy

CHAPTER 1. Introduction

1.1 Background: From Conventional to Solid-State Lithium-Ion Batteries

Rechargeable lithium-ion batteries (LIBs) have gradually become the most widely used rechargeable battery technology for portable electronics since their commercialization by SONY in 1991 [1]. The ever-increasing demands on the green energies call for large-scale energy storage systems with high energy density as well as high powder density[2]. LIBs are considered promising candidates for applications in electric vehicles and grid-scale storage. However, current state-of-the-art LIBs still do not completely meet the requirements of safety, energy density and cost [3] in these applications.

The main components in LIBs include the cathode, anode, separator and electrolyte. In current commercial LIBs, cathode materials are lithium transition metal oxides, such as $LiCoO_2$ (LCO) [4-5], $LiMn_2O_4$ (LMO) [6] and $Li(Ni_{1/3}Mn_{1/3}Co_{1/3})O_2$ (NMC) family materials [7]. One of the major capacity fading mechanisms of these cathode materials is associated with transition metal dissolution in organic electrolytes. In commercial LIBs, most of the electrolytes are non-aqueous solutions with $LiPF_6$ salts dissolved in organic liquid electrolytes (LEs), such as ethylene carbonate (EC), propylene carbonate (PC), dimethyl carbonate (DMC), ethyl methyl carbonate (EMC), diethyl carbonate (DEC) and fluoroethylene carbonate (FEC) [8]. These flammable organic presents great safety risks when the cells are overheated or shorted, which is particularly dangerous for large scale energy storage applications, such as electric cars.

To achieve high energy density, anode materials with high theoretical capacity and low redox potential are highly desired. Li metal is the lightest metal, which has a very negative electrode potential (-3.04 V vs. standard hydrogen electrode) with a high theoretical specific capacity (3860 mAh/g) [9]. In this regard, it is an ideal anode material for rechargeable LIBs. However, the common dendritic growth of Li-metal, which make penetrate the polymer separator and short the cell, presents a huge barrier for applications. Also, low Coulombic efficiency (CE) caused by small pieces of Li falling off from the electrode during repeated Li deposition/stripping processes is a severe problem [10]. In commercial LIBs, graphite is used since it exhibits reversible Li intercalation and deintercalation behavior with a theoretical capacity of 372 mAh/g at an operating potential very close to Li/Li^+ [1, 11]. However, relatively low energy density of graphite is limiting the overall energy density of LIBs [12].

All-solid-state lithium-ion batteries (ALSOLIBs) offer the opportunity to overcome the problems caused by the LEs [2]. Because in ALSOLIBs, the flammable Les are replaced by the non-flammable solid electrolytes and high energy Li-metal can be used as the anode with much improved safety properties. The capacity fading problem caused by transition metal dissolution in LEs can also be resolved by using SEs. SEs also offer new options to enable the use of lithium metal anodes to boost the energy density due to the rigid mechanical properties, as SE is relatively more resistant to the penetration of Li dendrite, although more improvement is still needed [13-14].

In LEs, both (solvated) lithium ions and anions are mobile. With the current flowing through the cell, lithium ions and anions move towards opposite directions due to the influence of electric field. Under high current density, concentration gradients of both cation and anions form due to their slow diffusion rates in the solution, which lead to polarization within the cell and limit the rate performance [15-16]. In contrast, in SEs, the anions form the solid framework which are immobile and only Li ions diffuse within it. I.e. the transference number is unit.

Another advantage of SEs for rate-performance comes from their high charge carrier concentration. In typical LEs, the lithium-ion concentration is about 1-2 mol/dm^3, while those in SEs are much higher (~35 mol/dm^3 in LGPS). At high currents, lithium ions at electrolyte/electrode interface deplete fast and diffusion-limited behavior appears in LIBs with using LEs (Figure 1.1), while the diffusion limitation does not show in ALOSOLIBs with using SEs [17].

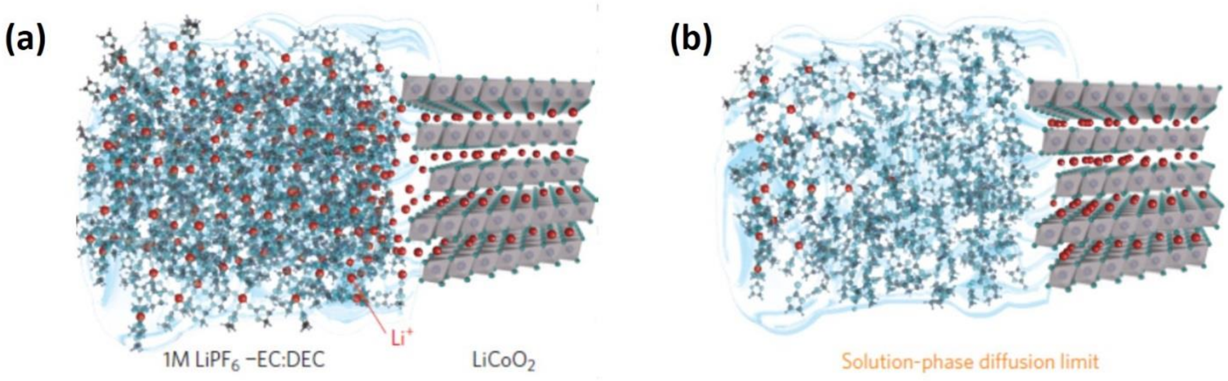

Figure 1.1 Schematic diagrams of cation distributions for the LIBs with using LEs for (a) non-diffusion limitation and (b) diffusion limitation. Reprinted by permission, Nature Publishing Group [17] © 2016.

Another issue of LIBs with LEs is the safety concern. LIBs can rupture, ignite or explode when they are overheated or short-circuiting happens [18]. One of the failure modes in LIBs is thermal runaway, which is caused by the exothermic reactions among the electrolyte, anode and cathode with increased temperature and pressure in the battery. As a result, redundant packing part and battery thermal management systems are necessary, especially when LIBs are used for large-capacity energy storage. Using SEs to replace LEs could solve this problem. Though the detailed thermal and mechanical analysis for ALSOLIBs is still missing, the preliminary thermal analysis results are promising [19]. With using SEs, a simpler bipolar architecture (Figure 1.2) provides decreased “dead space” between single cells, leading to a higher energy density for the cell module and pack [20-21].

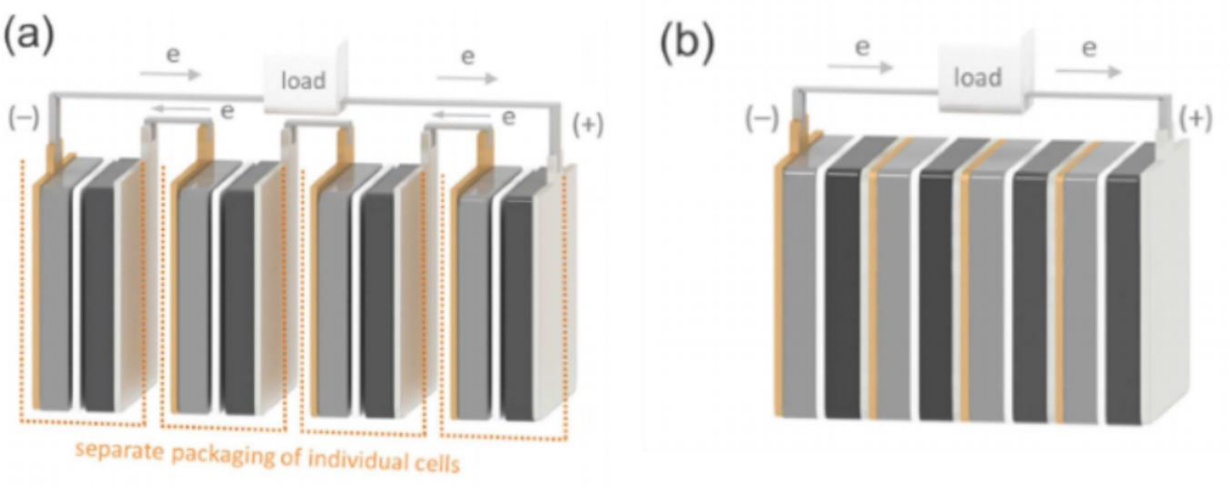

Figure 1.2 Schematic diagrams of (a) monopolar design of current LIBs with Les and (b) bipolar design of ALSOLIBs [21]. Reproduced with permission; © 2019 WILEY-VCH Verlag GmbH & Co. KGaA, Weinheim.

Moreover, current LIBs can only be operated in limited temperature range [22]. At sub-zero temperatures, LIBs suffer severe capacity loss due to the significant rise of internal resistance, which can be ascribed to the effects such as frozen lithium ions diffusion, sluggish kinetics of charge transfer at interfaces and increased solid-electrolyte interphase (SEI) resistance [23-25]. On the other hand, operating LIBs at high temperature usually accelerates the battery aging [26]. At elevated temperature, the lithiated graphite reacts with LEs and the thickness of SEI increases, leading to increased internal resistance [27]. Further increasing the temperature above 100 ^{o}C leads to separator melting and solvent gasification, which further increase the internal resistance and cause rapid capacity fading [26, 28]. While in ALSOLIBs, SEs are not volatile as LEs and the diffusion of lithium ions within SEs is much faster at elevated temperature than that at room temperature. As a result, ALSOLIBs are expected to be capable of operating in wider temperature range. A recent study has shown that ALSOLIBs exhibit superior cycling stability and rate performance at 100 ºC [20], at which LIBs with LEs cannot operate.

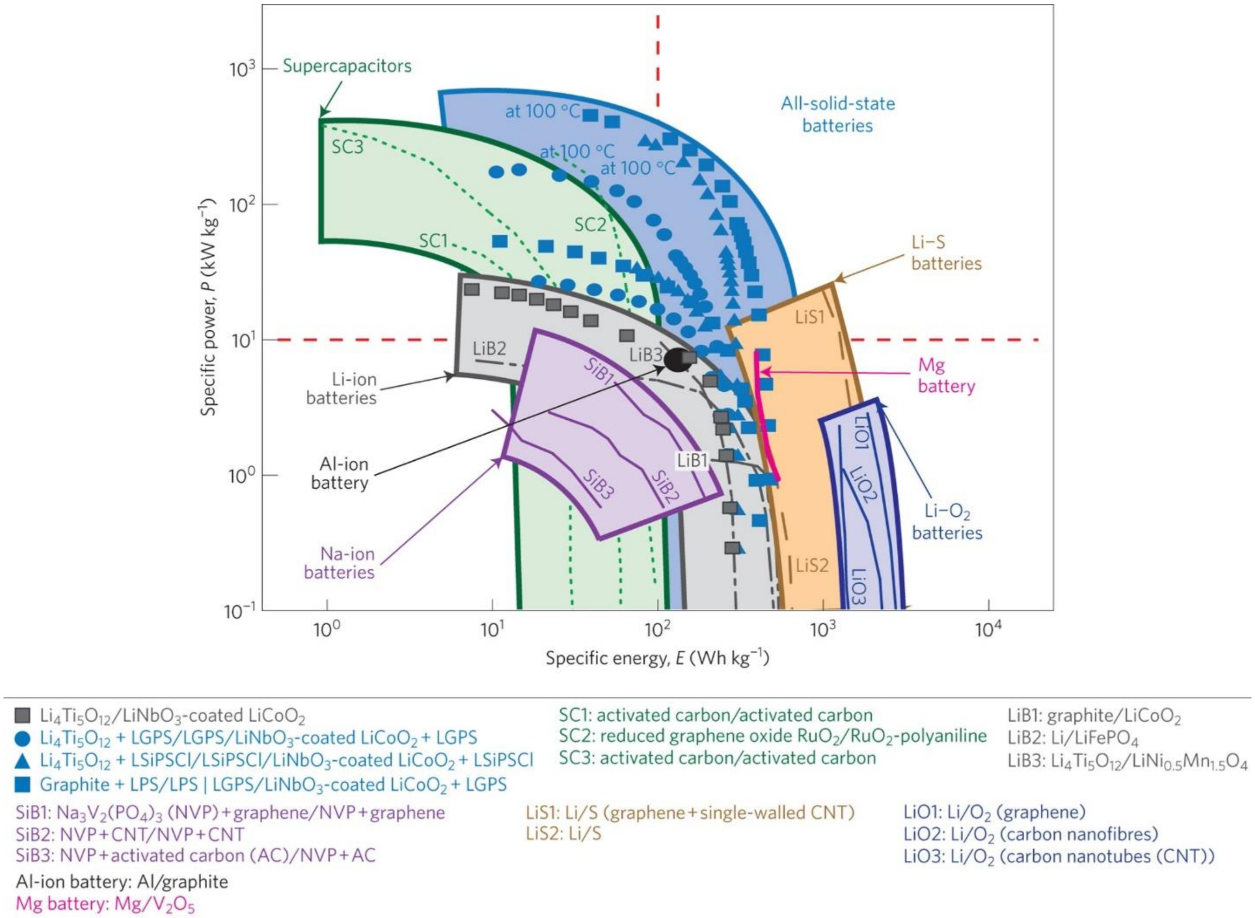

Figure 1.3 Comparison of Ragone plots for different electrochemical device. Reprinted by permission, Nature Publishing Group [17] © 2016.

With above mentioned merits, ALSOLIBs show superior power density than conventional LIBs and higher energy density at the same time. Figure 1.3 compares the Ragone plots of various electrochemical devices [17]. Higher power density and energy density are achieved for ALSOLIBs than LIBs with LEs. At elevated temperature, faster lithium-ion diffusion within SEs, electrode materials and SE/electrode interface can be achieved, leading to a higher power density.

For ALSOLIBs with $LiNbO_3$-coated $LiCoO_2$ operated at 100 ^{o}C, its specific power is even higher than some supercapacitors.

In ALSOLIB, SE is the crucial component, which determines the rate capability and energy density of the battery. To operate ALSOLIBs at ambient temperatures, SEs with high conductivity (10^{-4} S/cm) at room temperature, negligible electronic conductivity and wide electrochemical window are preferred [29-31]. Currently, two major types of SEs have been extensively studied: polymers and inorganic SEs. In polymer SEs, the conducting salt is dissolved in polymer matrix with anion acceptors. Polymer SEs offer the advantages of low-weight, good flexibility and good compatibility with Li metal, but their relatively low r.t ionic conductivity and narrow temperature range of operation limit their applications in ALSOLIBs. Polymer-based SEs are also instable at high potentials. Adding nanoscale inorganic fillers into polymer SEs is an effective strategy to boost the ionic conductivity and enhance the oxidation stability [32-35]. In comparison, inorganic SEs in general exhibit higher conductivity and better thermal stability than polymer SEs. Inorganic SEs can be further classified into three types: crystalline, glasses and glass-ceramics. In line with the main scope of this dissertation, this chapter surveys the current understanding and research progresses of crystalline SEs that relate to their integration in ALSOLIBs.

1.2 Categories of Crystalline SEs

Intensive efforts have been dedicated to the development of ALSOLIBs and a number of crystalline SEs with different compositions and crystal structures were reported. Figure 1.4 summarizes the temperature dependent ionic conductivities of typical SEs. With different chemical compositions and crystal structures, the ionic conductivities of SEs vary from 10^{-6} S/cm to 10^{-2} S/cm at room temperature. SEs can be discussed in five types distinguished by the chemical compositions: nitride, hydride, oxide, sulfide and halide. Different classes of SEs with different chemical compositions exhibit specific advantages and disadvantages, as discussed below.

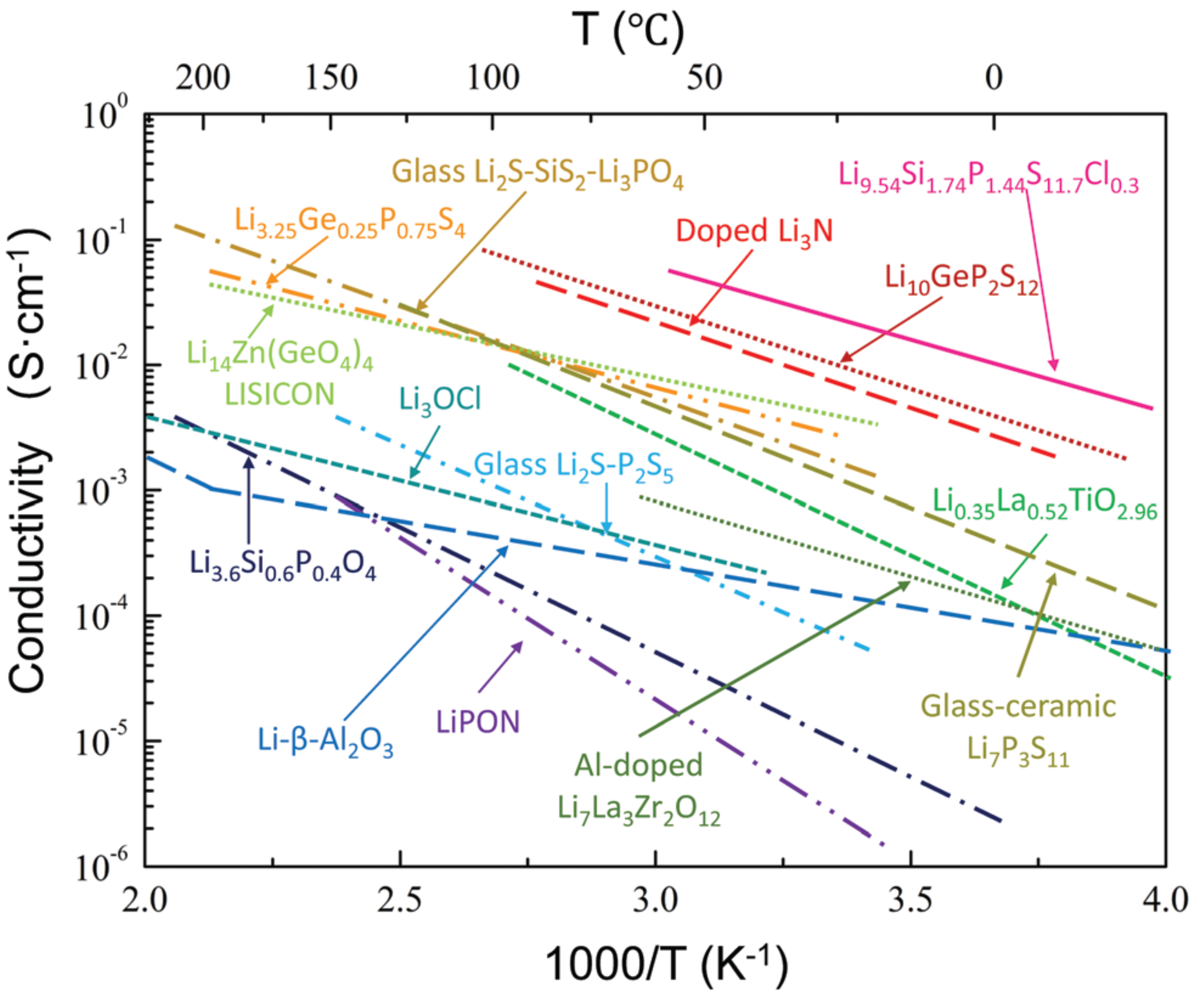

Figure 1.4 Ion conductivity of several well-known solid lithium-ion conductors [29]. Reprinted with permission; © 2018 Royal Society of Chemistry.

1.2.1 Electrochemical stability

Except for high bulk conductivity, the performance of ALSOLIBs is also significantly determined by the compatibility between electrode materials and SEs. To achieve high energy density, anodes with low potential (such as Li) and cathodes with high potential are preferred for ALSOLIBs. However, not all SEs are stable within the full range of the wide voltage window. For example, lithium nitride Li_3N has been known since 1890s and its ionic conductivity measurements were first reported in the 1950s [36]. It consists of alternating hexagonal Li_2N layers and Li layer. The cold pressed pellet exhibit poor conductivity, but single crystal Li_3N exhibits anisotropic high ionic conductivities, where the ionic conductivity along ab-plane was found to be 10^{-3} S/cm at room temperature with a low activation energy of 0.25 eV [37]. As shown in Figure 1.6, it is thermodynamically stable against lithium metal. But its low oxidation voltage of 0.44 V hinders its direct contact with any cathode materials [29, 38]. Recently, it was reported to be used as protective layer for other SEs from direct contact with Li [39-40].

Similar to Li_3N, lithium hydride is also chemically stable against Li metal, but the low oxidation voltage (~2 V vs. Li^+/Li) [41] causes severe side reaction when combined with lithium metal oxide cathodes, leading to a large interfacial resistance, and thus significant capacity loss [42]. Better cycling stability can be achieved when sulfur was used as the cathode materials [43-44], since the redox potential of S is ~2.2 V vs. Li^+/Li, which is much lower than that of lithium metal oxides.

Sulfide SEs have attracted tremendous attentions in the past decade due to their high ionic conductivity which is comparable to LEs and their favorable mechanical properties [20, 45-47]. Though previous research claimed that sulfide SEs showed outstanding stability with electrochemical windows of 0-5 V from cyclic voltammetry (CV) test [45, 48], a high interfacial resistance was observed when sulfide SEs are coupled with high voltage cathodes such as $LiCoO_2$ (LCO), $Li(Ni_{1/3}Mn_{1/3}Co_{1/3})O_2$ (NMC) or $Li(Ni_{0.8}Co_{.15}Al_{0.05})O_2$ (NCA) [49-52]. This is caused by the side reaction between electrode materials and sulfide SEs. With using transmission electron microscopy (TEM) the formation of an interfacial layer between $LiCoO_2$ electrode and Li_2S-P_2S_5 SE is directly observed [53]. As shown in Figure 1.5a and b, the interfacial layer contains Co, S and P elements, indicating the mutual diffusion of elements in both LCO and SEs. Similar phenomenon is also observed between LCO and oxide SE $Li_7La_3Zr_2O_{12}$ (LLZO) (Figure 1.5c and d). Since the formed interface layer is amorphous and the thickness is only a few nanometers, the structure information is not easy to detect. Multiple surface sensitive techniques such as Raman spectroscopy, X-ray photoelectron spectroscopy (XPS), X-ray absorption near-edge spectroscopy (XANES) are employed to investigate the interfacial reaction between high voltage cathode and sulfide SEs [49, 54-55]. The interfacial layer forms mainly at the initial charging process, leading to an irreversible first cycle capacity loss and the partial decomposition of sulfide SEs [49, 54]. To lower the high interfacial resistance between cathode materials and sulfide SEs, materials such as $Li_4Ti_5O_{12}$ [50], $LiNbO_3$ [56], Li_2CO_3 [57], $LiTaO_3$ [58] and Li_2SiO_3 [59] were coated on the surface of cathode materials as buffer layer to suppress the side reaction.

The side reaction does not only occur at the interface of cathode electrodes. Sulfide SEs also decompose at certain voltage range when in contact with the electronic conducting additives. In order to investigate this side reaction, sulfide SEs are mixed with conducting additives to form electronic/ionic mixed conducting composite and act as the cathode electrode, which greatly amplifies this decomposition reaction and facilitates the characterizations [60]. In this battery configuration, β-Li_3PS_4 was found to decompose irreversibly into oxidized sulfur species, which is electronically insulating and passivates further decomposition of SEs. At lower potential, β-Li_3PS_4 undergoes reduction reaction which appears to be reversible. Similar studies were also conducted to Li_6PS_5Cl with argyrodite structure and revealed that Li_6PS_5Cl decomposes into LiCl, P_2S_5 and S upon charging and forms LiCl, Li_2S and Li_3P during discharge process, with combining XPS, X-ray diffraction (XRD) and solid-state magic-angle spinning nuclear magnetic resonance (MAS NMR) techniques [61].

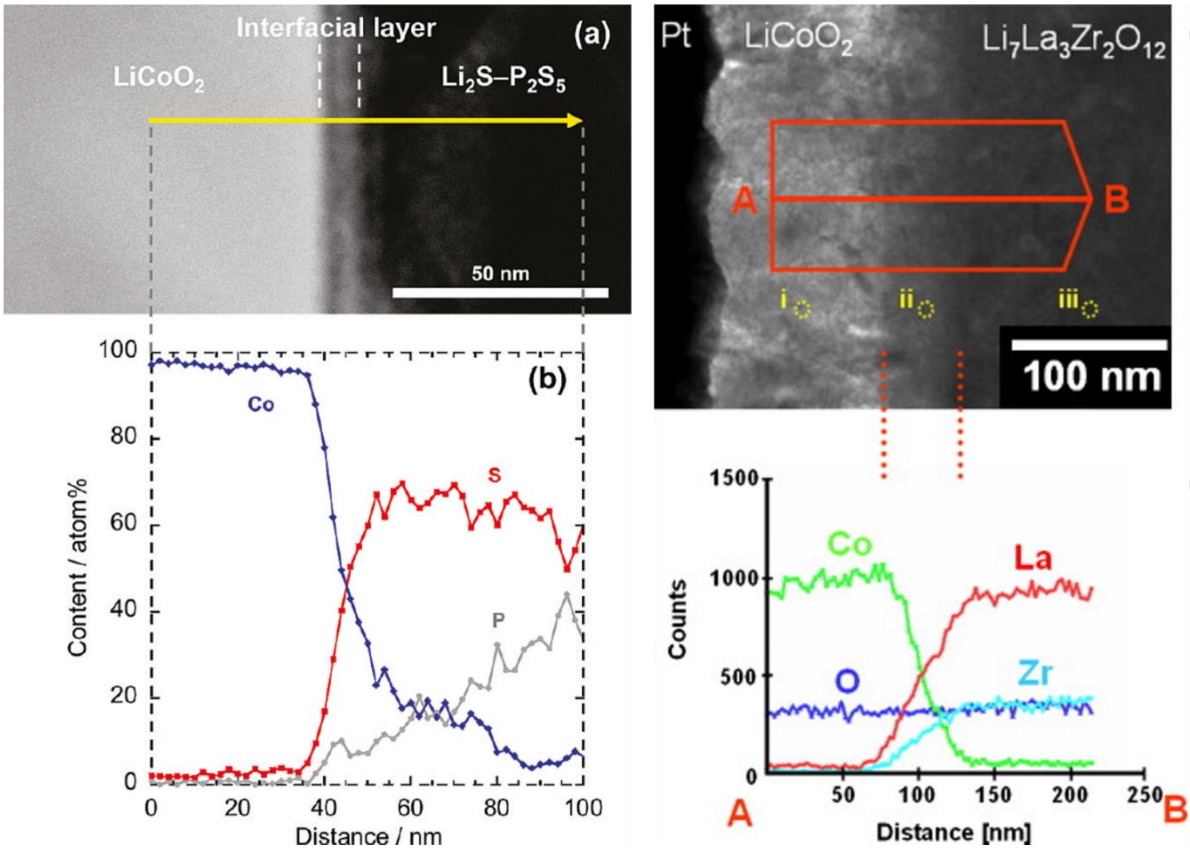

Figure 1.5 (a) Cross-sectional HAADF-STEM image of LCO electrode/ Li2S-P2S5 SE interface after initial charging and (b) cross-sectional EDX line profiles for Co, P and S elements [53]. Reprinted with permission; © 2010 American Chemical Society. (c) Cross-sectional TEM image of LCO/LLZO interface and (d) the EDS line profile for Co, La, Zr and O [62]. Reprinted with permission; © 2011 Elsevier.

To understand the fundamental physical and chemical mechanisms governing the decomposition of SEs and predict decomposition products, theoretical computations were also conducted to evaluate the electrochemical window of different SEs [63-64].

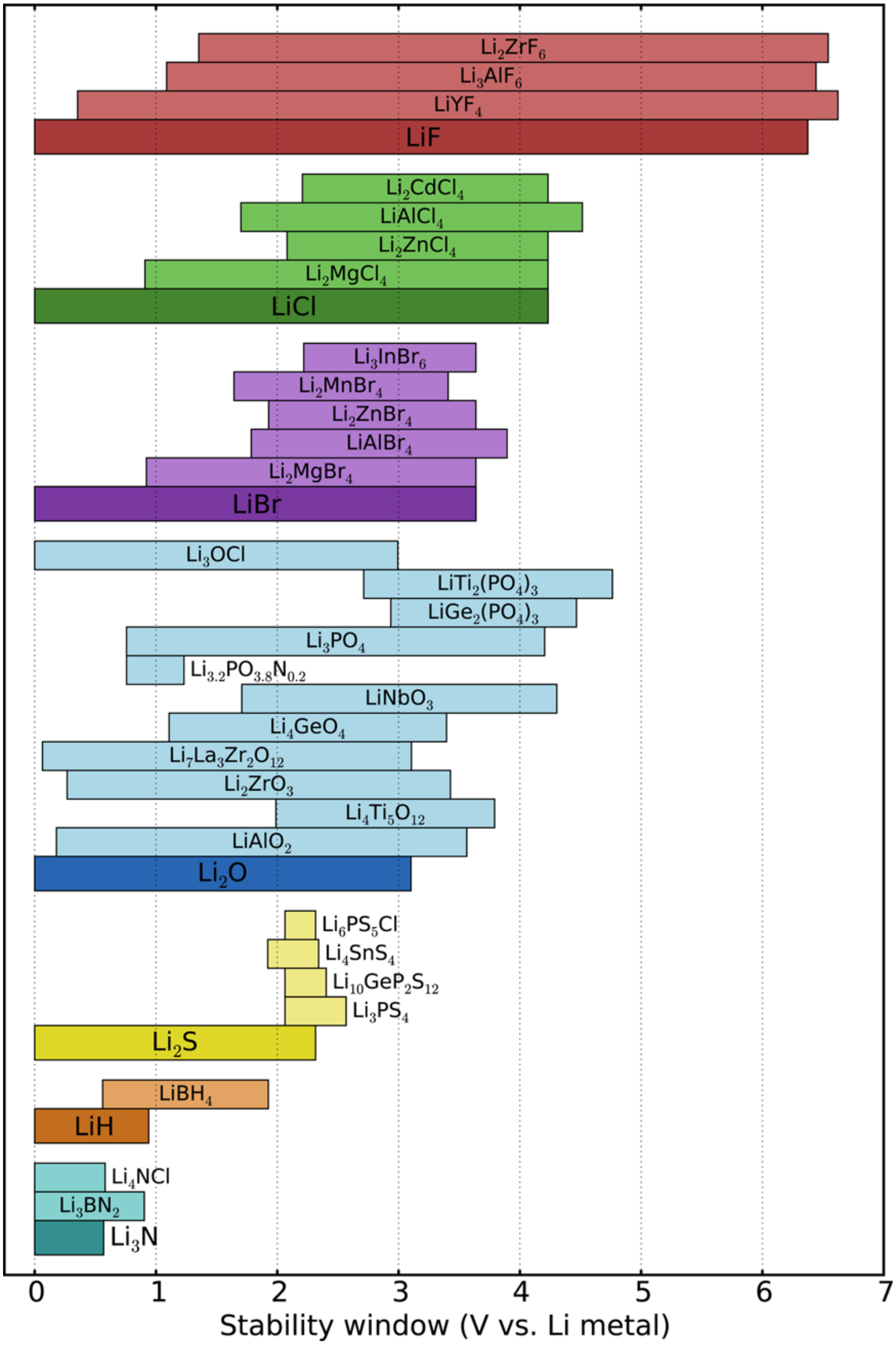

Figure 1.6 Electrochemical stability ranges of various electrolyte materials grouped by anion, with corresponding binary for comparison [63]. Reprinted with permission; © 2016 American Chemical Society.

As shown in Figure 1.6, the electrochemical stabilility windows of sulfide SEs are actually quite narrow. This result is also in consistent with experimental results. While sulfide SEs such as β-Li_3PS_4 and Li_6PS_5Cl are reduced at potential below 2 V versus. Li^+/Li, several experimental studies demonstrated their decomposition products (Li_2S, Li_3P and LiCl for Li_6PS_5Cl; Li_2S and Li_3P for β-Li_3PS_4) serve as stable interfacial layer when operated with lithium metal [48, 65]. Li_2S and LiCl are known as electronic and ionic insulators, but Li_3P ensures lithium ion conduction through the interphase and its electronic conductivity is negligible compared to the ionic conductivity [66]. In comparison, SEs containing elements of Si/Ge/Sn, such as $Li_{9.54}Si_{1.74}P_{1.44}S_{11.7}Cl_{0.3}$ [20], $Li_{10}GeP_2S_{12}$ (LGPS) [45] and $Li_{10}SnP_2S_{12}$ (LSPS) [67], normally form unstable interface with lithium metal since the products of decomposition are Li-Si/Ge/Sn alloy, which are mixed ionic/electronic conductors and promote further decomposition of SEs [68-69].

In comparison with sulfide SEs, oxide SEs have better oxidation stability. $LiTi_2(PO_4)_3$ (LTP), $LiGe_2(PO_4)_3$ (LGP) and Li_3PO_4 show oxidation voltage above 4 V due to the high stability of PO_4^{3-} [63]. Similar to β-Li_3PS_4, although the reduction of Li_3PO_4 starts at ~0.7 V, the decomposition products Li_2O and Li_3P function as passivating layer [70] and enable the stable operation of LCO/Li_3PO_4/Li thin film ALSOLIBs [71]. On the contrary, no stable interphase forms between LTP/LGP and lithium metal and extra protecting layer is necessary to enable the ALSOLIBs with Li anode [72-73].

As mentioned previously, oxide SEs such as $Li_4Ti_5O_{12}$, $LiTaO_3$, $LiNbO_3$ and Li_2SiO_3 are commonly used as coating materials for cathode materials in ALSOLIBs incorporating sulfide SEs. Their electrochemical stable windows are also calculated. The results suggested that the reduction potential for these materials is below 2 V, which is lower than the oxidation potential of sulfide

SEs and secure the interface compatibility. On the other hand, the oxidation potential of these coating materials is 3.7~4.2 V, which is in the operating voltage range of ALSOLIBs during cycling. Due to intrinsic big difference between electronic and ionic conductivities, voltage gradient forms within the coating layer and the voltage on the surface in contact with sulfide SEs thus is within the electrochemical stabilility window of the sulfides [74]. The anode/SEs interface is also stabilized by the same mechanism. As shown in Figure 1.7, in practical ALSOLIBs, the stabilized cathode/SEs and anode/SEs interfacial layers actually extend the stability of SEs.

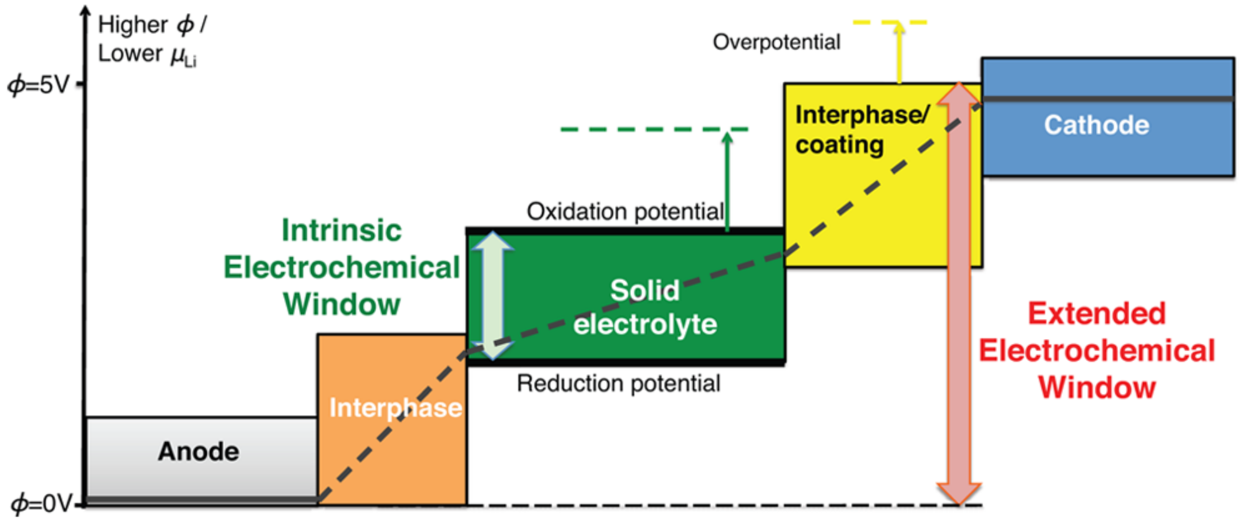

Figure 1.7 Schematic diagram about the electrochemical window in the ALSOLIBs [74]. Reprinted with permission; © 2016 American Chemical Society.

Garnet-type LLZO is another group of oxide SEs which are widely studied. It is considered promising due to its reasonably high ionic conductivity and stable operation with Li metal. However, both theoretical calculation and experimental studies demonstrated that LLZO is not thermodynamically stable in ALSOLIBs, instead, its stability is due to kinetic passivation. First principle calculation gives a reduction potential of 0.05 V which is very close to the Li plating/stripping voltage [74], while experimental studies still revealed the formation of interphase layer with a thickness of ~6 nm between LLZO and Li metal [75], which maintains the Li ion conducting path. Compared with phosphate, the oxidation stability window for LLZO is only 2.91 V and side reactions between high voltage lithium transition metal oxide and LLZO are expected. With using TEM and energy dispersive X-ray spectroscopy (EDX) mutual diffusion between LLZO and LCO were observed at their interphase. Nano-beam electron diffraction results revealed the existence of La_2CoO_4 [62], which blocks lithium diffusion and affects the electrochemical performance [76]. Therefore, additives such as Li_3BO_3 and Li_2CO_3 are introduced in cathode composites to avoid the direct contacts between LCO and LLZO [76-77].

Compared with oxide SEs, halide SEs show similar or even better oxidation stability. With increased electronegativity of the anions, the order of oxidation stability of halide SEs is iodides < bromides < chlorides < fluorides. Fluoride SEs show oxidation potential above 6 V, which makes them thermodynamically stable against high voltage cathode materials. However, their ionic conductivities are too low for applications in ALSOLIBs [78]. Recently, halides with a general formula of Li_3MX_6 (M= In, Y, Sc, Yb or Er, etc., X=Cl or Br) are recognized to be promising candidates because of their high ionic conductivities and good electrochemical stability [79-83]. Especially, ALSOLIBs with chloride SEs and high voltage cathode electrode showed stable long cycling without using any coating as buffer layer [79, 84]. Although the oxidation stability voltage of chloride SEs is calculated to be around 4.2 V [63-64, 85], Nazar et al. cycled NMC with a cutoff voltage of 4.6 V vs. Li^+/Li using $Li_2Sc_{2/3}Cl_4$ as SE and the cell still showed stable cycling performance [86], which suggests the formation of a kinetically stabilized interface. On the other hand, chloride SEs tend to be reduced when in contact with Li metal due to the existence of metal cations. Janek et al. deposited Li metal on Li_3InCl_6 and Li_3YCl_6 SEs with an argon sputter gun and monitored the reaction products with using *in situ* XPS [87]. It was found that the M^{3+} (M = In, Y) cations in Li_3MCl_6 SEs were reduced to metallic state after in contact with Li metal and the formed interface is unstable, leading to a continuously growing interfacial resistance. Therefore, halide SEs are often used as cathode electrolyte coupling with sulfide SEs as anode electrolyte in ALSOLIBs [80, 86, 88-89].

1.2.2 Mechanical properties and grain boundary resistance

In commercial LIBs, the electrode is composed of active materials, conducting additive and binder. LE can easily wet the porous electrode to form a percolating ionic conducting newwork. On the contrary, in ALOLIBs, SEs have no fluidity and long-range ion transport between SE/active materials and SE/SE particles is realized through solid-solid contact. Therefore, in composite electrodes, it is preferred to maximize the contact area between solid particles and lower the porosity. SEs with different chemical compositions exhibit very different mechanical properties and the densification process therefore varies depending on the SEs used. For example, figure 1.8 shows the microstructure of LLZO and $75Li_2S$-$25P_2S_5$ glass pellets obtained both by cold-pressing at 360 MPa [90]. Due to the rigid ceramic nature of oxide, LLZO particles keep irregular morphologies with a lot of voids left after cold pressing. As a result, the cold-pressed LLZO pellet showed a low conductivity which was due to the high grain boundary (GB) resistance. In contrast, sulfide SEs have favorable deformability and densification can be achieved by cold-pressing. With increased pressing pressure, the relative density of sulfide SEs pellet increased gradually along with enhanced ionic conductivity. Similarly, halide and hydride SEs are also soft and ALSOLIBs utilizing them can be obtained by simple cold pressing [43, 79, 88, 91-92].

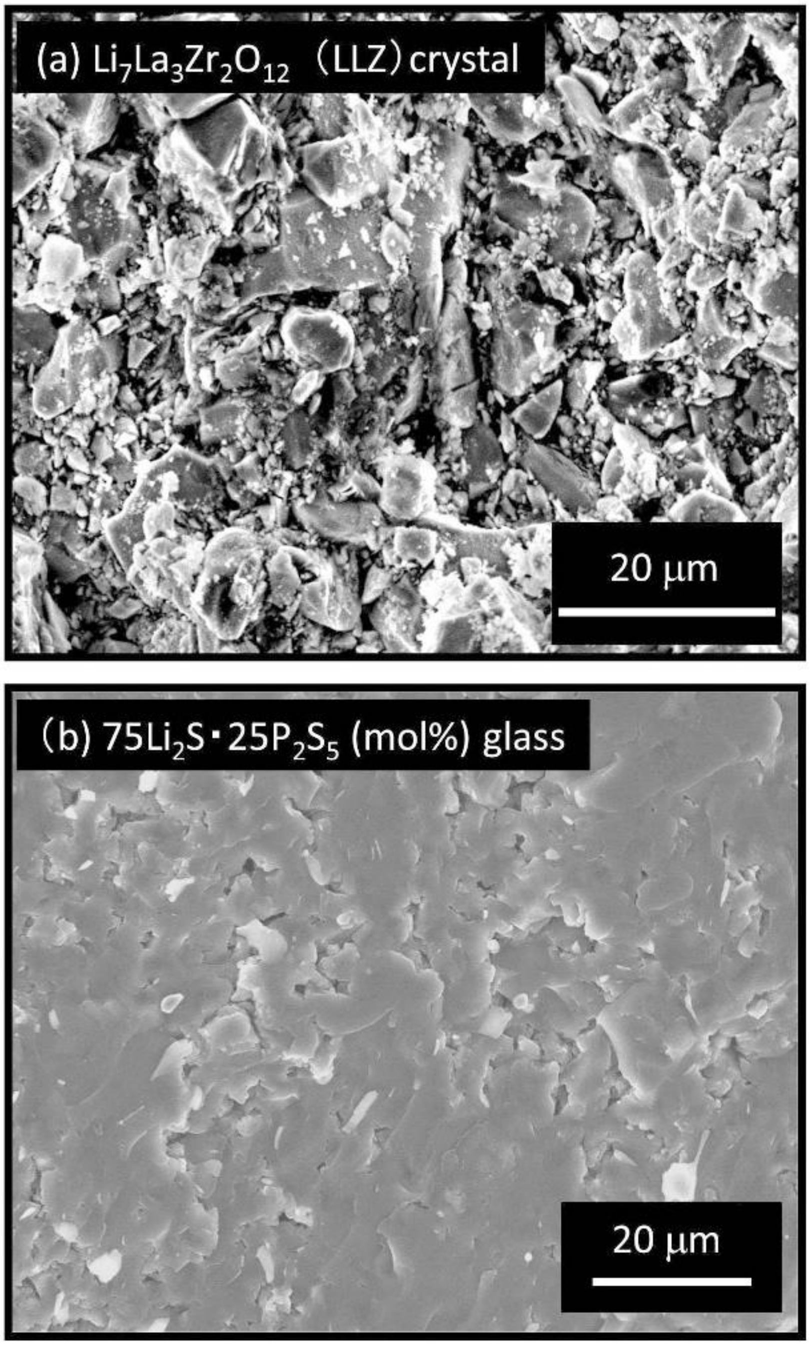

Figure 1.8 SEM images of fracture cross sections of typical solid oxide electrolyte $Li_7La_3Zr_2O_{12}$ and solid sulfide electrolyte particles ($75Li_2S$-$25P_2S_5$ (mol.%)) glass pelletized at room temperature [90]. Reprinted by permission; Nature Publishing Group © 2013.

To mitigate GB resistance in oxide SEs, high temperature sintering is often applied to increase the relative density and fuse the GB [93-94]. The relatively density can be further boosted with the help of high pressure. Sakamoto et al. fabricated LLZO pellet by hot-pressing at 1050 ^{o}C under 62 MPa and compared the ionic conductivities of LLZO with different relative density [95]. It was found that the total ionic conductivity increased from 0.0094 to 0.34 mS/cm by improving the relative density from 85% to 98%.

Another strategy to lower GB resistance of oxide SEs is adding “soft” SEs as binder to realize close contact. Liang et al. mixed β-Li_3PS_4 with LLZO and the obtained composite SE exhibits low GB resistance at room temperature [96].

1.3 Ion Transport within Crystalline SEs

In crystalline SEs, immobile ions form a rigid host framework and the mobile ions, such as Li^+, resides at the sites with lowest energies (typically octahedral or tetrahedral sites for lithium). The hopping of Li ions from a stable site to another requires overcoming periodic high energy sites along the diffusion pathways. To date, two major migration mechanisms of crystalline SEs are raised, as shown in Figure 1.9: (1) single-ion migration and (2) multi-ion concerted migration [97]. In conventional diffusion model, single-ion migration means individual Li ions hopping from one lattice site to another through inter-connected diffusion channels without considering the interaction between Li ions. The highest energy barrier along the pathway is the activation energy for migration [98-99]. The energy landscape of the ion migration is determined by the crystal structural framework [97]. For example, with using density functional theory (DFT) calculation sulfide SEs with S^{2-} anions in body-centered cubic (*fcc*), hexagonal close-packed (*hcp*) and body-centered cubic (*bcc*) sublattices are compared [98]. In sulfide SEs, Li ions commonly prefer to reside at tetrahedral sites as the energy for Li ions sitting at octahedral sites is much higher. In *fcc* and *hcp* S^{2-} anion sublattice, Li ions at tetrahedral sites have to hop to the adjacent tetrahedral sites through octahedral sites, which requires Li ions to overcome a high migration energy barrier. In contrast, tetrahedral sites in *bcc* anion sublattice are connected directly by shared triangle plane. As a result, the interconnected tetrahedral sites with equivalent energies form the pathway for long-range diffusion and the associated activation energy for Li ion diffusion is much lower. Typical superionic conductors such as $Li_7P_3S_{11}$ [100-101] and $Li_{10}GeP_2S_{12}$ [45] with *bcc* anion sublattice exhibit low activation energy and high ionic conductivities over 10 mS/cm at room temperature.

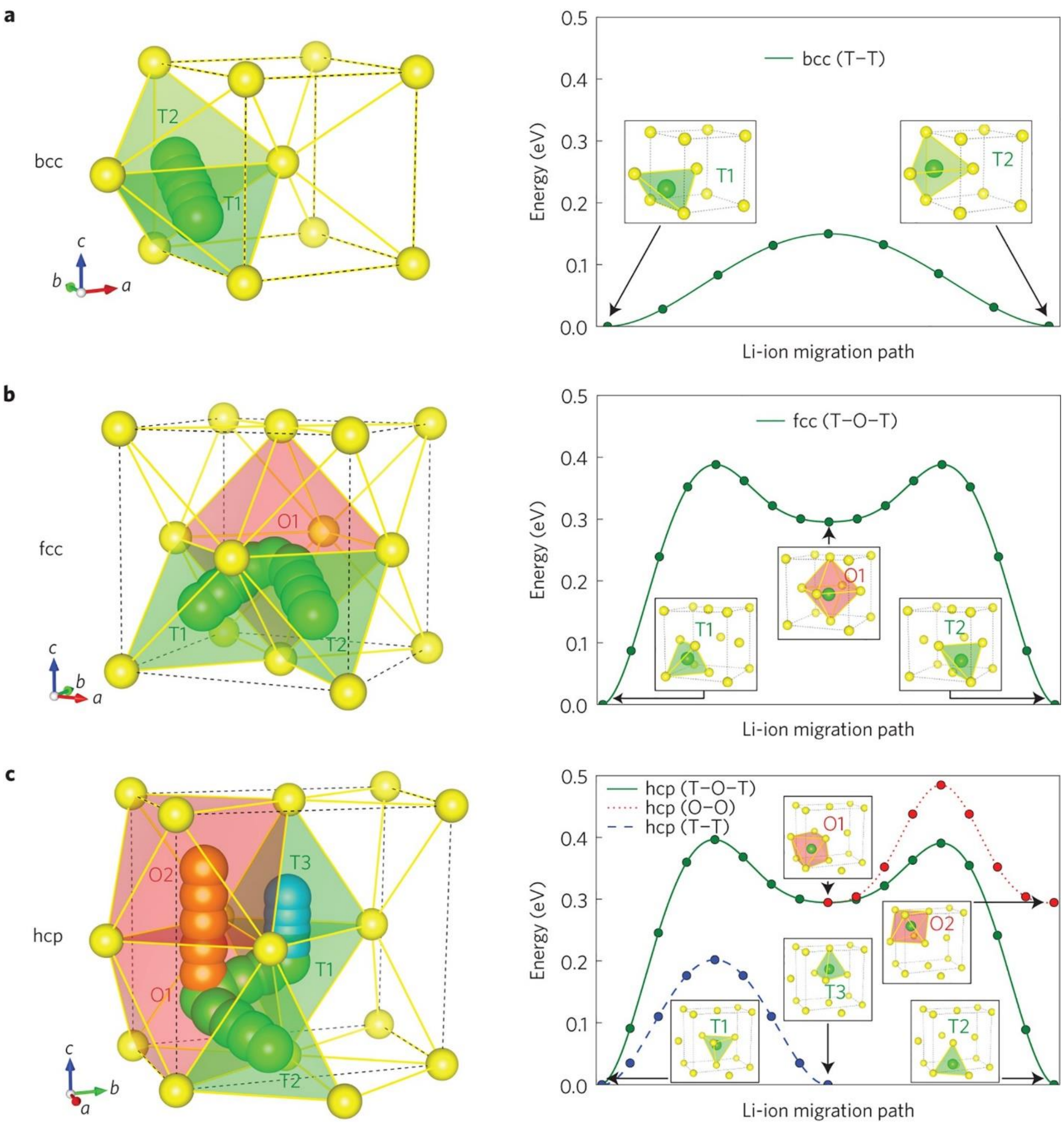

Figure 1.9 Li ion migration pathways in bcc/fcc/hcp-type anion lattices. a-c, Li ion migration path (left panels) and calculated energy path (right panels) in bcc (a), fcc (b) and hcp (c) sulfur lattices [98]. Reprinted by permission; Nature Publishing Group © 2015.

In classical diffusion model, the Li sublattice configurations and the interactions among these ions are neglected. With only considering the anion framework, the DFT calculations give high energy barriers of 0.47, 0.58 and 0.49 eV for $Li_{10}GeP_2S_{12}$ (LGPS), cubic-phase $Li_7La_3Zr_2O_{12}$ (LLZO) and $Li_{1.3}Al_{0.3}Ti_{1.7}(PO_4)_3$ (LATP), respectively [97], while the activation energies extracted from electrochemical impedance spectroscopy (EIS) measurement are only 0.25 [45], 0.32 [93] and 0.31 [102] eV, respectively. The discrepancies between calculated and experimental measured results may be due to the ignored interactions among Li ions. Different from the single-ion hopping process, for the possible concerted migration, multiple adjacent ions can hop simultaneously into their nearest sites (Figure 1.10), which lower the overall energy barrier significantly [97].

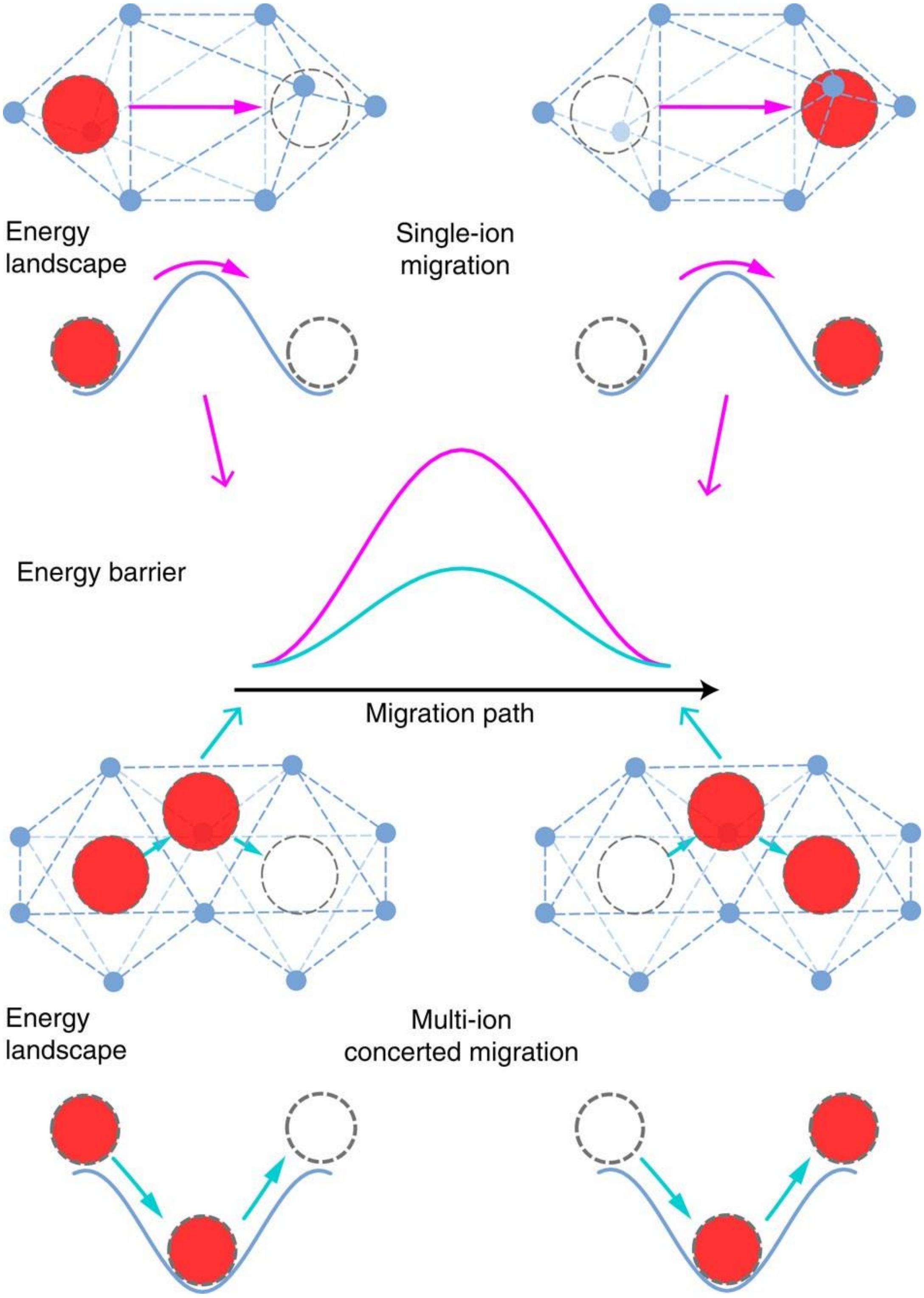

Figure 1.10 Schematic illustration of single-ion versus multi-ion concerted migration [97]. Reprinted by permission; Nature Publishing Group © 2017.

The ionic conductivity, σ, can be defined as the product of charge (q), concentration (n) and mobility (μ) of charge carriers in SEs:

$$\sigma = q\, n\, \mu \tag{1}$$

In SEs with high ionic conductivity, concentration (n) is temperature independent and can be considered constant. Mobility (μ) of charge carriers can be derived from the diffusion coefficient (D) by using Einstein relation [103]:

$$\mu = \frac{Dq}{k_B T} \tag{2}$$

where k_B is the Boltzmann constant and T is the absolute temperature. Supposing Li ions diffuse in random directions and there are no related successive jumps, the theoretical uncorrelated diffusion coefficient D_{uc} is $D_{uc} = \frac{1}{6}\nu a^2$, where ν is the hopping frequency and a is the jump distance. Practically, Li diffusion may be correlated and a correlation factor f is introduced to describe the extent to which successive jumps are related to one another [103]. Therefore, the true self diffusion coefficient D_T can be expressed as below:

$$D_T = \frac{1}{6}\nu a^2 f \tag{3}$$

Assuming that the Li ion hopping is a thermal activation process, the hopping frequency can be written as below:

$$\nu = \nu_0 \exp\left(-\frac{\Delta G}{k_B T}\right) = \nu_0 \exp\left(-\frac{\Delta S}{k_B}\right) \exp(-\frac{E_a}{k_B T}) \tag{4}$$

where ν_0 is the attempt frequency; ΔG, E_a and ΔS denote the Gibbs free energy, the enthalpy (activation energy) for migration and associated entropy, respectively. Substituting (2), (3) and (4) in (1):

$$\sigma T = \frac{1}{6}\frac{nq^2}{k_B} f exp\left(-\frac{\Delta S}{k_B}\right) \mathrm{v}_0 a^2 \exp(-\frac{E_a}{k_B T}) \tag{5}$$

After defining a prefactor $\sigma_0 = \frac{1}{6}\frac{nq^2}{k_B} f exp\left(-\frac{\Delta S}{k_B}\right) \mathrm{v}_0 a^2$, equation (5) can be simplified as below:

$$\sigma T = \sigma_0 \exp(-\frac{E_a}{k_B T}) \tag{6}$$

Therefore, the product of temperature and ionic conductivity in SEs obeys Arrhenius behavior. By measuring the ionic conductivity at varied temperature and plot the graph of the logarithm of the product σT versus reciprocal temperature, the activation energy E_a can be obtained from the slope of the resulting straight line.

If Li diffusion is realized by Li hopping via intrinsic lattice defects, the concentration of defects depends exponentially on reciprocal temperature as well. As a result, the ionic conductivity σ can also be expressed by using the following equation [104]:

$$\sigma = \frac{n\beta a^2 \mathrm{v}\alpha q^2}{kT} \tag{7}$$

where β is the fraction of unoccupied mobile sites which is available for hopping, and α is a geometric factor which is the reciprocal of the number of possible jump directions from a given site (For example, $\alpha = \frac{1}{2}$ for constrained hopping in one dimension and $\alpha = \frac{1}{6}$ for a close packed cubic lattice). In normally defective solids,

$$\beta = \exp\left(-\frac{\Delta G_F}{k_B T}\right) = \exp\left(-\frac{\Delta S_F}{k_B}\right) \exp(-\frac{H_F}{k_B T}) \tag{8}$$

where ΔG_F, ΔS_F and H_F denote the Gibbs free energy, entropy and enthalpy for intrinsic defect pair formation, respectively. This defect model was used to study the ion transporting in Li_2S [105] and it explains the ionic conduction behavior very well.

Based on these equations, certain factors closely govern the ionic conductivity of SEs at ambient temperature: (1) activation energy for Li ions migration; (2) charge carrier concentration; (3) Li ions hopping attempting frequency; (4) Li ions hopping distance and (4) Li ions migration entropy. These factors are usually correlated. For example, the ion hopping frequency is related to the lattice oscillation, which is influenced by the anion polarizability [106-107]. It is suggested that larger polarizability of anions in the same structure causes softer lattice, which lower the attempt frequency of the jump and the migration entropy, leading to a smaller value of prefactor σ_0 [108]. However, a softer lattice also reduces the ion hopping activation barriers, which is beneficial to achieve high ionic conductivity at ambient temperature [99]. Tuning charge carrier concentration also influences the ionic conductivities, which sometimes changes the sublattice of Li ions and triggers multi-ion concerted motion, leading to a much higher ionic conductivity and lower activation energy. Due to the correlation of these diffusion governing factors, there is no straightforward strategy to monotonically increase the conductivity and lower the activation barriers. But with further understanding of the correlation of these factors and carefully tuning the chemical composition and crystal structures, fast ion conduction and overall high-performance of the SEs can be achieved.

1.4 Design Strategies for Solid Electrolytes

In the past decades, the ionic conductivity of a large number of compounds have been measured in the search for new SEs. It was found that compounds with certain crystal structure families, including LISICON (LI SuperIonic CONductor), argyrodite, garnet, NASICON (NA SuperIonic CONductor) and perovskite, can achieve high ionic conductivities above 10^{-4} S/cm at room temperature. As shown in Figure 1.11 [99], with different chemical compositions, SEs show pronounced difference in ionic conductivities even they share the same crystal structure, suggesting that ionic conductivity can be tuned in a wide range through rational selection of crystal and design of chemical compositions.

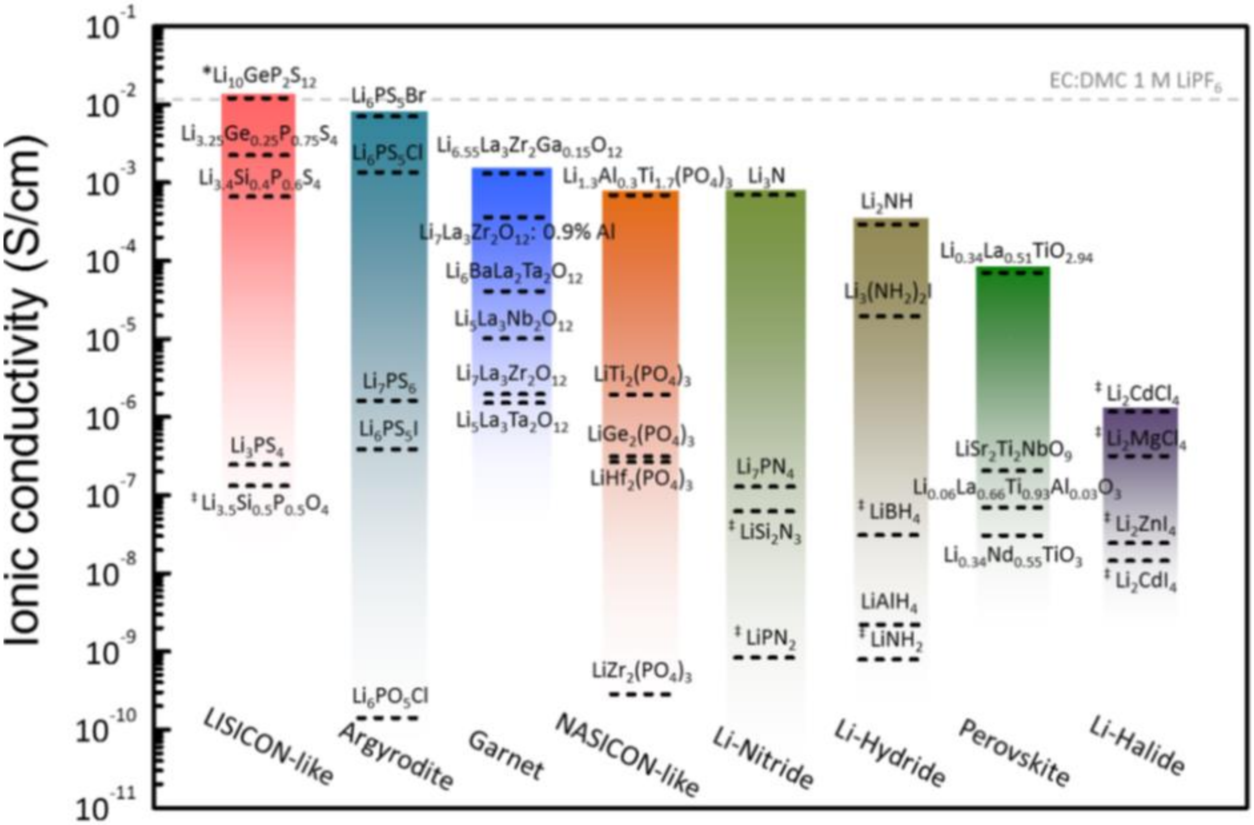

Figure 1.11 Reported total ionic conductivity of solid-state lithium-ion conductors at room temperature [99]. Reprinted with permission; © 2016 American Chemical Society.

In this section, commonly employed strategies to design SEs with high ionic transport properties and chemical stability will be discussed.

1.4.1 Influence of Anion sublattice

1.4.1.1 Anion chemistry and sublattice

As mentioned in Section 1.3, the anion sublattice have a significant influence on the ion transport properties of SEs. It is commonly accepted that anion hosts with bigger radii and higher polarizability are preferred for ionic conduction as they have weaker Li-anion bonds and thus the actication energy (E_a) is lower. For example, lithium argyrodite Li_6PS_5Cl crystallizes in space group $F\bar{4}3m$ and it exhibits a ionic conductivity ~10^{-3} S/cm at room temperature [108-111]. After replacing all S^{2-} by O^{2-}, Li_6PO_5Cl crystallizes in the same space group, but the ionic conductivity drops to ~10^{-9} S/cm at room temperature with a significant higher E_a of 0.66 eV [112].

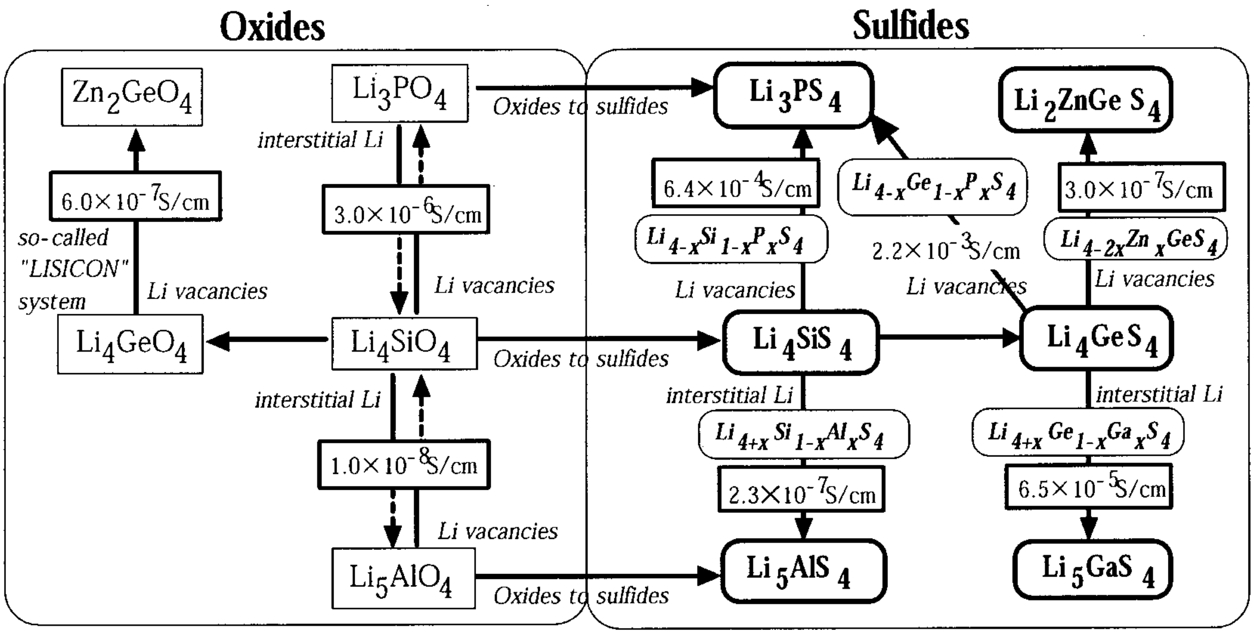

Figure 1.12 The concept of material design for LISICON system Materials belong to the LISICON (oxides) and the thio-LISICON (sulfides) are summarized [113]. Reprinted with permission from IOP Publishing, Ltd © 2001.

Similar phenomenon was also observed in LISICON structure. The best reported ionic conductivity of oxide SEs in LISICON structure is ~10^{-6} S/cm at room temperature [114-115]. In order to boost the ionic conductivity, Kanno et. al synthesized a series of thio-LISICON compounds with a general formula of $Li_{4-x}Ge_{1-x}P_xS_4$ [113], which share similar structure to oxide LISICON. The conductivity value of 2.2 × 10^{-3} S/cm at 25 °C obtained in $Li_{3.25}Ge_{0.25}P_{0.75}S_4$ is much higher than the oxide LISICON such as $Li_{14}Zn(GeO_4)_4$ [116] and $Li_{3.6}Si_{0.6}P_{0.4}O_4$ [115] by three or four orders of magnitude.

Besides the polarizability of anion framework, the valence of anion also plays a critical role in determining the ionic conductivity. Recently, halide SEs such as Li_3YCl_6 [79], Li_3InCl_6 [80, 82] and Li_3ScCl_6 [81] were reported to be promising SE for ALSOLIBs owing to their high ionic conductivity and high oxidation stability [84]. Different from sulfide SEs, which usually need a bcc anion framework to realize fast Li diffusion, in these halide SEs, anions stacking is in *fcc* or *hcp.* DFT calculations suggested an adequately low migration barrier of 0.2 to 0.3 eV [85], which is lower than those in S^{2-} frameworks (~0.4 eV). In comparison with S^{2-}, Cl^- shows higher electronegativity and lower polarizability, which in general do not facilitate Li diffusion. But its low negative charge leads to much weaker coulombic interactions with Li^+, resulting in lower diffusion energy barriers.

For the same reason, halogen-doping is also used to enhance the ion diffusion in sulfide SEs. For example, Nazar et al. partially replaced S anion in argyrodite-type Li_6PS_5Cl by Cl anion and synthesized a series of halide-rich solid solution phases $Li_{6-x}PS_{5-x}Cl_{1+x}$ [46]. $Li_{5.5}PS_{4.5}Cl_{1.5}$ exhibits a conductivity ~10 mS/cm at room temperature, which is four-fold greater than Li_6PS_5Cl and is comparable to metastable superionic $Li_7P_3S_{11}$ [100]. The spectrum of ^7Li MAS NMR shows that the isotropic resonance shifts to much lower frequency with increased halogen substitution, indicating the doped Cl anion has a stronger tendency to draw electron density from Li ions environments than S anions, which is also in accord with the principle that lower valence of halide anions decrease the electrostatic attraction to the mobile Li ions.

1.4.1.2 Anion disordering

In certain types of SEs, the anions can be substituted by other kind of anions, which modifies the ion transport properties via changing the polarizability of anion framework and varying the coupling between the mobile ions and the fixed lattice. To achieve fast long-range transport, Li ions need to go through a variety of inter-connected Li sites/vacancies and the migration barriers along the pathway need to be as low as possible. After introducing the doping anions, which are different from the pristine anions in ionic radius, electronegativity and chemical valence, the local environment and migration barriers of Li^+ can be changed. In some cases, the distribution of doped anions negatively impacts the Li ion transport behaviors by blocking the long-range diffusion path in certain parts. Taking Li argyrodite Li_6PS_5X (X=Cl, Br or I) as examples, if only considering the impact of polarizability of the anion framework, the order of the ionic conductivities is expected to be $Li_6PS_5I > Li_6PS_5Br > Li_6PS_5Cl$, corresponding to the polarizability of the anions. However, in experimental studies it was found that the ionic conductivity of Li_6PS_5I is lower than the other two by about 3 orders of magnitude [108, 111, 117].

The crystal structure of Li argyrodite Li_6PS_5X is shown in Figure 1.13 a. In one formula unit of Li_6PS_5X, 4 S^{2-} bond with P^{5+}, while a "free" S^{2-} and a X^- reside at 4a and 4c sites. In Li_6PS_5Cl and Li_6PS_5Br, X^- and S^{2-} are randomly mixed (i.e. disordered) at 4a and 4c sites. While in Li_6PS_5I, all I^- resides at in 4a sites, leaving all S^{2-} at 4c sites. This ordering is due to the big difference in ionic radii (I^-: 216 pm; S^{2-}: 184 pm) [118]. As shown in Figure 1.13 b, there are two different Li sites and three different jumping processes can occur: doublet jump (48h-24g-48h), intra-cage jump (48h-48h) and inter-cage jump [108, 119]. For long-range Li diffusion, the apparent Li diffusion rate is limited by the slowest jumping process. Wagemaker et al. used ab initio molecular dynamics (AIMD) modeling to explore the diffusion mechanism in Li argyrodite.

Their simulation results at 450 K showed that in Li$_6$PS$_5$Cl all three kinds of jumping processes occur frequently (Figure 1.13 c), while in Li$_6$PS$_5$I, only a few intra-cage jumps take place and no inter-cage jump is observed (Figure 1.13 d) [119].

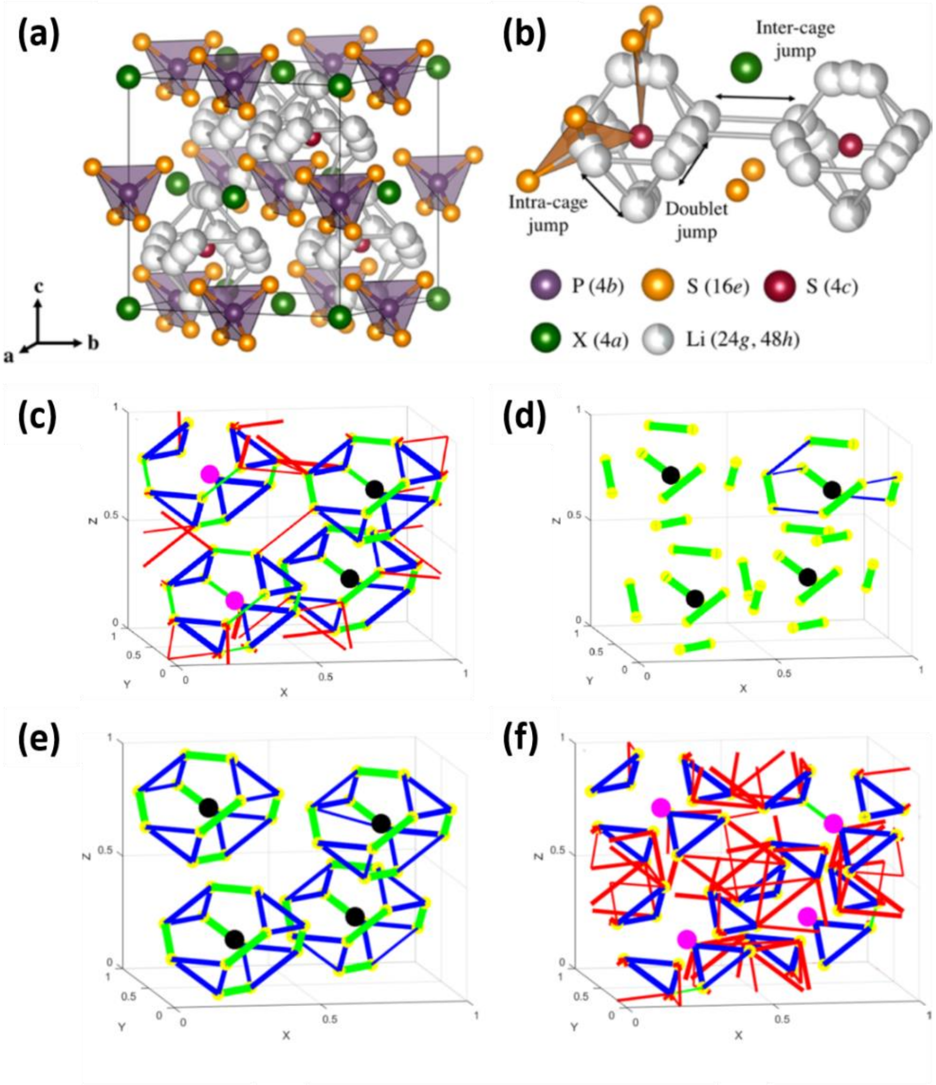

Figure 1.13 (a) Crystal structure of Li$_6$PS$_5$X (X = Cl, Br, I). (b) The two different lithium positions form an octahedral arrangement and three different jump processes can occur [108]. Reprinted with permission; © 2017 American Chemical Society. (c) Jump statistic plots from MD simulations at 450 K of (c) Li$_6$PS$_5$Cl (50 % Cl occupancy of 4a sites), (d) Li$_6$PS$_5$I, (100% I occupancy of 4a sites), (e) Li$_6$PS$_5$Cl (100 % Cl occupancy of 4a sites) and (f) Li$_6$PS$_5$Cl (0 % Cl occupancy of 4a sites). The lines represent the three different types of jumps; green for doublet, blue for intracage, and red for intercage. Thicker lines represent larger jump rates. The colored spheres indicate S^{2-} at site 4c (black), Cl^- at site 4c (pink), and Li-ion sites (48h) (yellow). Reprinted with permission; © 2016 American Chemical Society.

They also took Li_6PS_5Cl as the prototype and simulated the Li diffusion behavior with different anions distributions. With Cl^- fully occupying 4a sites, no inter-cage jump is observed. (Figure 1.13 e). In contrast, if put all Cl^- on the 4c sites, a high inter-cage jump rate is induced, but the doublet jump rate decreases drastically and becomes the rate-limiting process (Figure 1.13 f) [119]. The low ionic conductivity in Li_6PS_5I thus is attributed to the blocked inter-cage jumps due to ordered anions distribution. Therefore, an enhanced ionic conductivity can be expected if the disorder of I^- at 4a and 4c sites can be induced. Wilkening et al. introduced site disorder in Li_6PS_5I by using ball-milling treatment, which boosted ionic conductivity by 2 orders of magnitude [120]. Zeier et al. applied an aliovalent doping strategy in $Li_{6-x}M_xP_{1-x}S_5I$ (M = Si, Ge, Sn) and found that the diffusion pathways for Li^+ expands and disordering of S^{2-} and I^- at 4a and 4c sites appears with increased M^{4+} doping level [121-122]. This disordering results in a steep decrease in the activation energy and a high ionic conductivity of 18.4 mS/cm in sintered $Li_{6.6}M_{0.4}P_{0.6}S_5I$ pellet sample. Nazar et al. designed and synthesized a series of solid solutions $Li_{6+x}M_xSb_{1-x}S_5I$ (M = Si, Ge, Sn) in argyrodite structure with I^-/S^{2-} disorder and newly created interstitial Li sites, from which an ionic conductivity of 14.8 mS/cm at room temperature was achieved with cold-pressed pellets [47].

1.4.2 Li ion concentration and Li sublattice

Besides tuning the anion host framework, optimizing the concentrations of mobile ions and vacancies is another effective strategy to improve the ionic conductivity in given material structures. Change in Li^+ concentration is usually accompanied with Li redistribution at different sites and in some cases this creates new Li sites, changes the energy landscape, and perhaps triggers concerted motion of Li, which favors fast Li transport.

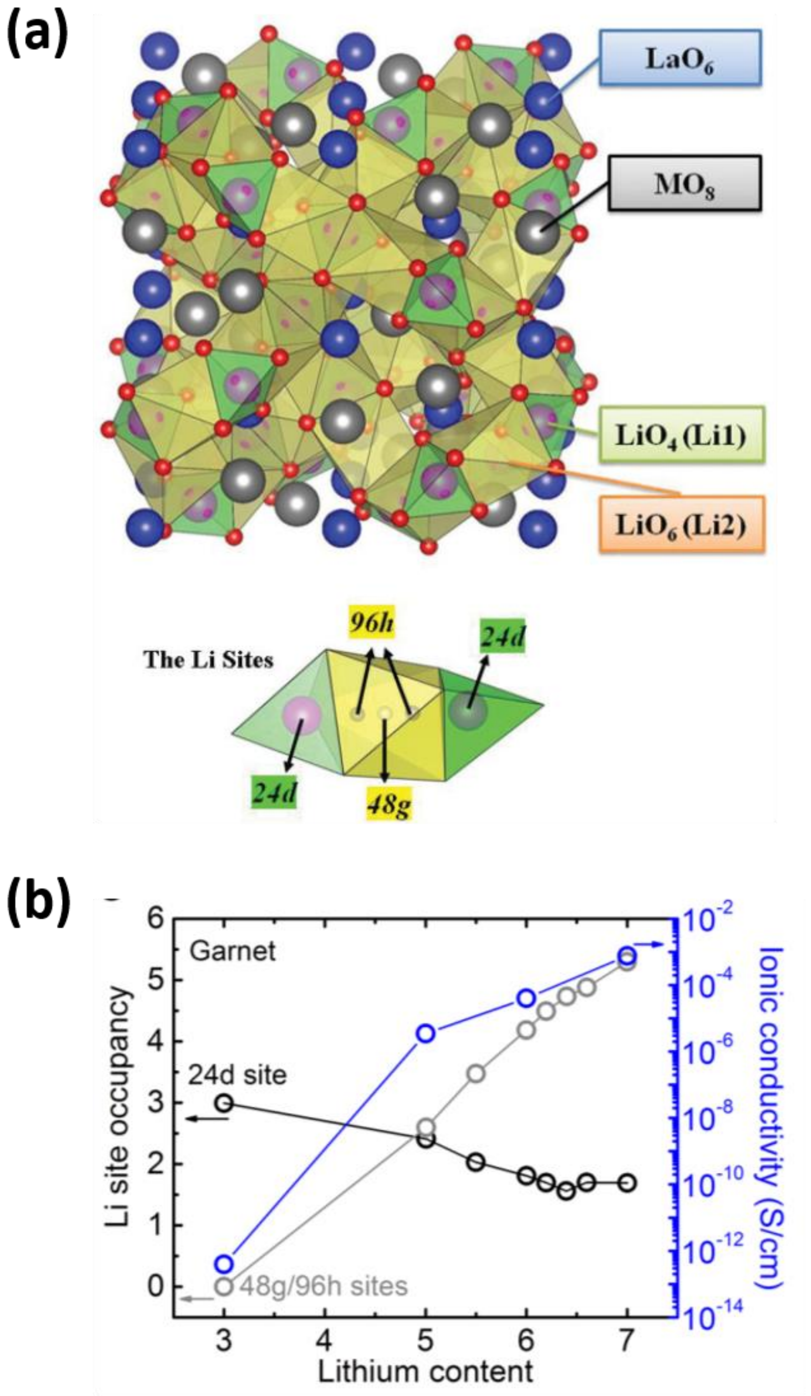

Figure 1.14 (a) The crystal structure of garnet-type LLMO. The green polyhedrons are tetrahedral (24d) Li sites and the yellow ones are octahedral (48g/96h) Li sites [123]. Reprinted with permission; (b) Ionic conductivity for $Li_3Tb_3Te_2O_{12}$ (extrapolated), $Li_5La_3Ta_2O_{12}$, $Li_6BaLa_2Ta_2O_{12}$, and $Li_7La_3Zr_2O_{12}$ and lithium site distribution in the 48g/96h octahedral positions (gray) and 24d tetrahedral positions [99]. Reprinted with permission; © 2016 American Chemical Society.

In one formula unit of garnet-type $Li_{3+x}M_3M'_2O_{12}$ (M and M' denote different metal or metalloid cations) oxide SEs, *x* can be tuned from 0 to 4 with different M and M' cations keeping charge balance. The crystal structure of garnet-type SEs is shown in Figure 1.14 a. There are two kinds of sites to accommodate Li ions (tetrahedral sites: 24d and octahedral sites: 48g/96h sites), which connected to one another by face-sharing, forming 3-D diffusion channels [93, 123-124]. In garnet-type SEs with $x = 0$, Li ions fully occupy low energy tetrahedral sites and the octahedral sites with higher energy are empty, resulting in a low ionic conductivity of $\sim 10^{-7}$ S/cm at 450 ^{o}C [99, 125-126]. With more Li ions incorporated into the crystal structure, the extra Li ions have to take the octahedral sites. However, simultaneous occupation of adjacent octahedral and tetrahedral sites leads short Li-Li distance and strong repulsion, which pushes the Li ion in octahedral site away from the shared faces (48e to 96h) and increases the separation [127-129]. Since Li ion at octahedral sites become closer to the tetrahedral site on the opposite direction, the off-centered Li ion at octahedral site raises the site energy in one of the tetrahedral sites, creating vacancies at the originally fully occupied 24d sites, which facilitates the Li diffusion. Figure 1.14 b shows the influence of Li ions concentration on the Li ion distribution at different sites and ionic conductivity at room temperature [99]. With increased Li ions concentration, the ionic conductivity was boosted by several orders of magnitude, which is not only due to the increased charge carrier, but also due to the triggered correlated motion [97].

The correlated motion triggered by increased Li concentration is also observed in NASICON-type $Li_{1+6x}M^{4+}_{2-x}M'^{3+}_{x}(PO_4)_3$ (M = Ti, Ge, Sn, Hf, or Zr and M' = Cr, Al, Ga, Sc, Y, In or La), where there are two different sites (6-fold coordinated and 8-fold coordinated, respectively) accommodating Li ions and they connect one to another alternatively to form long-range diffusion channels [130-132]. In $LiM_2(PO_4)_3$ with no M'^{3+} substitution, Li ions fully occupy the 6-fold coordinated octahedral sites with a low ionic conductivity of 10^{-6} S/cm with an activation energy of 0.45 eV at room temperature [133]. By substituting M^{4+} with aliovalent M^{3+}, the ionic conductivity can be drastically improved to ~10^{-3} S/cm with reduced activation energy (~0.3 eV) because of the partial occupancies of Li ions on both sites and triggered correlated motion [99, 133].

1.4.3 Stabilizing high ionic conducting phase

SEs usually have several polymorphs and different polymorphs exhibit distinct differences in ionic conductivity and activation energy. In some SEs, the high ionic conducting phases are only stable at elevated temperature, resulting in a low ionic conductivity at room temperature. The phase transition temperature can be tuned with isovalent or Aliovalent doping. For example, $LiBH_4$ was known as a reducing reagent and regarded as potential candidate for hydrogen storage [134]. The Li diffusion behavior in $LiBH_4$ was first studied in 2007 [135] and there is a phase transition from orthorhombic to hexagonal, accompanied with an increase of ionic conductivity to 10^{-3} S/cm at around 390 K. In order to stabilize the high-conducting hexagonal phase at room temperature, lithium halides (LiX: X = Cl, Br, and I) incorporation was applied, which boosted the room temperature conductivity of $LiBH_4$-LiX composites to about 3 orders magnitude higher than that of pure $LiBH_4$ in the orthorhombic structure (Figure 1.15) [136]. $LiNH_2$ doping is another effective strategy to boost the ionic conductivity of $LiBH_4$. The introduction of $LiNH_2$ creates tetrahedral Li sites which coordinated by a combination of BH_4^- and NH_2^-, leading to an enhanced ionic conductivity at low temperature [92, 137-138]. By optimization of the ratio between $LiBH_4$ and $LiNH_2$, an ionic conductivity of 6.4×10^3 S/cm at 313 K can be achieved [139].

Another example of lowering the phase transition temperature involves anion substitution in antiperovskite Li_2OHCl [140]. Li_2OHCl shows an ionic conductivity below 10^{-8} S/cm [141-142] in tetragonal phase at room temperature and transfers into highly ionic conducting cubic phase at 60 °C, which boosts the ionic conductivity by at least two orders of magnitude [141, 143]. Goodenough et al. partial replaced OH^- in Li_2OHCl by F^-, which retains the cubic phase at room temperature with an ionic conductivity of 3.5×10^{-5} S/cm [140].

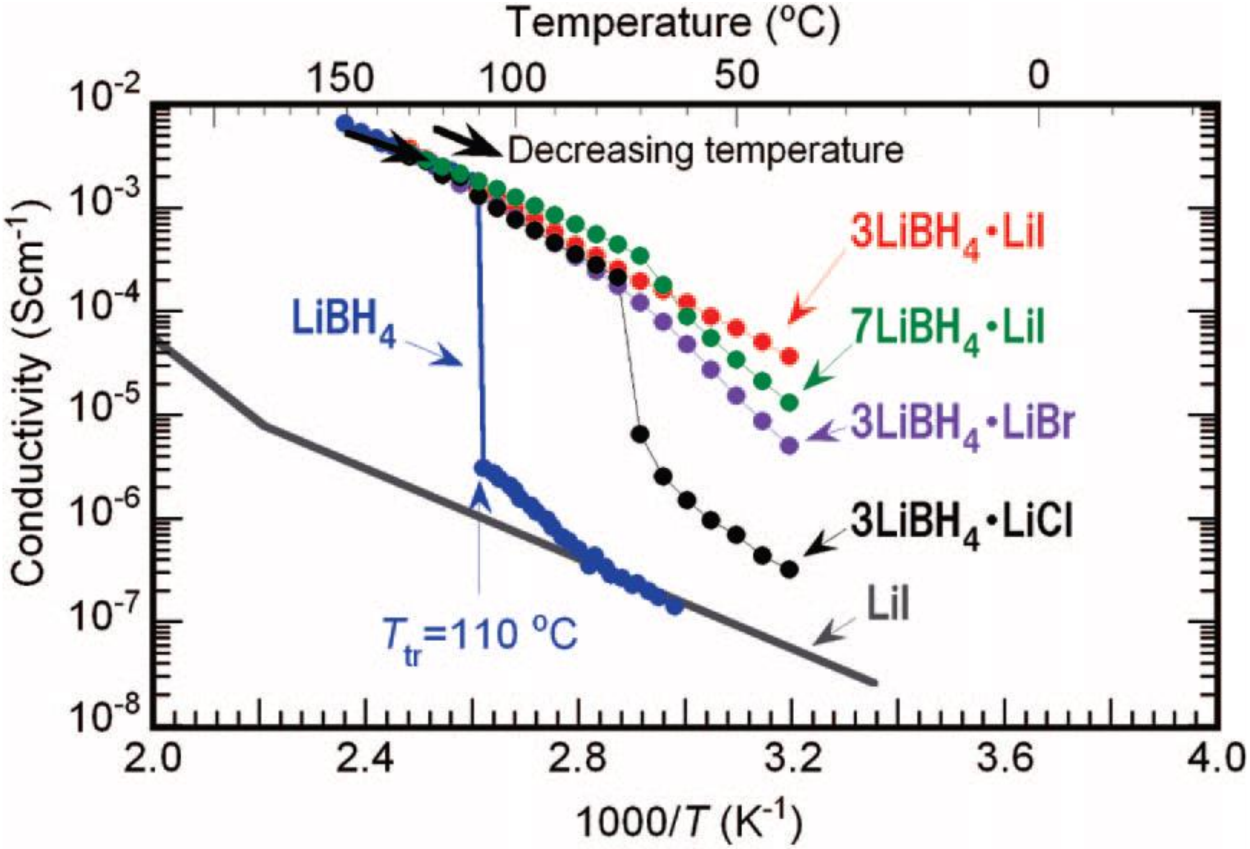

Figure 1.15 Arrhenius plot of $LiBH_4$, LiI and $LiBH_4$-LiI composites (X = Cl, Br and I) [136]. Reprinted with permission; © 2009 American Chemical Society.

1.4.4 Exploring SEs with new crystal structure

In general, there are two strategies to design SEs with fast ionic conduction: one is to modify existing compounds with known crystal structure by composition tuning; the other one is to search for materials with new crystal structure. Inspired by the discovery of LGPS-type SEs which show comparable ionic conductivity to LEs [20, 45, 144-146], tremendous efforts have been devoted into finding new SEs with high ionic conductivity. Although discoveries of fast ionic conductors are often achieved by trial-and-error [99, 147], exploring in phase diagrams where there are known SEs with high ionic conductivity is a good starting point. Kanno et al. explored SEs in thio-LISICON structure in Li_4GeS_4-Li_3PS_4 solid solution system in 2001 [113] and found LGPS in this phase diagram by different heating protocol [45]. Another example is the discovery of $Li_7P_3S_{11}$ [100]. Sulfide glasses in Li_2S-P_2S_5 system have been reported to show high room temperature conductivities around 10^{-4} S/cm in 1980s [148]. Tatsumisago et al. synthesized a series of (100-x) $Li_2S \bullet xP_2S_5$ glass-ceramics by ball-milling and subsequent heat-treatment at moderate temperature (below 250 °C) [149-151] and found that $70Li_2S$-$30P_2S_5$ glass-ceramics shows highest ionic conductivity and its XRD pattern is different from known crystalline phases in the Li_2S-P_2S_5 systems [152], such as Li_3PS_4 [153], $Li_4P_2S_6$ [154] and Li_7PS_6 [155]. The XRD pattern can be indexed to a triclinic cell with P-1 space group and the backbone of crystal structure is built by corner-sharing $P_2S_7^{4-}$ detetrahedra and PS_4^{3-} tetrahedra [101], with Li ions distributed in tetrahedral sites [156].

1.5 Scope of this Work

The objectives of this work include searching for new materials as high-performance SE and gaining better understanding of the influence of crystal structure on Li ion diffusion behavior in solid state ionic conductors. Improvement of the ionic conductivity is key to advance the development of ALSOLIBs. This dissertation mainly focuses on sulfide and halide SEs, considering their advantages in conductivity, cost and manufacturability for future commercialization ALSOLIBs. Different novel strategies were employed to design new compounds with expected boosted ionic conductivities, such as entropy stabilization, anion mixing and Li sublattice tuning, etc. The structure-property relationship in the involved SEs, including the influences of charge concentration, polarizability of anion framework, and anion disordering, etc. on ionic conductivity and activation energy, is systematically investigated with combined experimental and computational approaches. A number of high-performance SEs with record-high room temperature ionic conductivities were successfully designed, synthesized, characterized and electrochemically evaluated.

In Chapter 2, a novel lithium chloro-thiophosphate compound $Li_{15}P_4S_{16}Cl_3$ is discovered in Li_2S-P_2S_5-LiCl phase diagram via a novel in situ XRD for synthesis approach. The crystal structure and electrochemical properties are investigated. $Li_{15}P_4S_{16}Cl_3$ can be synthesized as pure phase via a facile solid-state reaction by heating ball-milled mixture of Li_2S, P_2S_5 and LiCl. The crystal structure of $Li_{15}P_4S_{16}Cl_3$ was refined against neutron and synchrotron X-ray powder diffraction data, revealing that it crystallizes in space group $I\bar{4}3d$. The Li^+ transport in $Li_{15}P_4S_{16}Cl_3$ was also investigated by multiple solid state NMR methods, including variable-temperature NMR line-shape analysis, NMR relaxometry, and pulsed field-gradient NMR. $Li_{15}P_4S_{16}Cl_3$ shows good thermodynamic stability and can be synthesized at relatively low temperature. Though it exhibits a low ionic conductivity at room temperature, it can sever as a new motif crystal structure for the design and development of new solid state electrolytes.

In Chapter 3, aliovalent doping strategy is employed to improve the ionic conductivity of $Li_{15}P_4S_{16}Cl_3$. First principles computation predicts enhanced ionic conduction with increase charge concentration. A series of $Li_{15+x}Ge_xP_{4-x}S_{16}Cl_3$ compounds are designed, synthesized, characterized and tested. Electrochemical measurements show ~ 3 orders of magnitude improvement of ionic conductivity in $Li_{15}P_4S_{16}Cl_3$ upon Ge^{4+} doping. Neutron diffraction proves the creation of new Li sites along with vacancies formation in originally fully occupied Li sites. This study shed light on the diffusion mechanism and provide guideline for design and synthesis new SEs materials.

In Chapter 4, a series of $Li_5PS_4(ClBr)_{1-x/2}(OH)_x$ compounds with unusually high vacancy concentration in argyrodite structure is designed guided by the novel entropy stabilization strategy. Among them, $Li_5PS_4(ClBrOH)_{2/3}$ shows a conductivity of 10.6 mS cm^{-1} in cold-pressed state and a further improved value of 26.9 mS cm^{-1} after hot-pressing at 30 ^oC. Multiple NMR techniques were used to study the Li hopping mechanism. All-solid-state batteries integrating $Li_5PS_4(ClBrOH)_{2/3}$ exhibited outstanding capacities at room temperature and -20 ^oC, demonstrating $Li_5PS_4(ClBrOH)_{2/3}$ has fast Li transporting kinetics and is capable of operating in a wide electrochemical window and a wide temperature range.

In Chapter 5, a halide compound with mixed anions, $Li_3Y(Br_3Cl_3)$, is designed, synthesized, characterized and electrochemically evaluated. A room temperature conductivity of 7.2 mS/cm is achieved in $Li_3Y(Br_3Cl_3)$ via hot-pressing at 200 °C, which exceeds all previously reported r.t. conductivities from halide SEs. Crystal structure characterizations with using synchrotron X-ray and neutron diffraction reveal the existence of Li at new tetrahedral sites and the resulted 3D diffusion pathways. Electrochemical impedance spectroscopy (EIS) results reveal the improved grain boundary contact and lower grain boundary resistance in the hot-pressing process, which also boost the overall conductivity. All-solid-state batteries using $Li_3Y(Br_3Cl_3)$ as the electrolyte demonstrate high capacity and good cycling stability. The new findings open up opportunities for the design of halide ionic conductors and the development of all-solid-state batteries.

1.6 Reference

[1] Yoshino, A., The Birth of the Lithium-Ion Battery. *Angewandte Chemie International Edition* **2012,** *51* (24), 5798-5800.

[2] Janek, J.; Zeier, W. G., A solid future for battery development. *Nature Energy* **2016,** *1*, 16141.

[3] Famprikis, T.; Canepa, P.; Dawson, J. A.; Islam, M. S.; Masquelier, C., Fundamentals of inorganic solid-state electrolytes for batteries. *Nature Materials* **2019,** *18* (12), 1278-1291.

[4] Mizushima, K.; Jones, P. C.; Wiseman, P. J.; Goodenough, J. B., LixCoO2 (0<x<-1): A new cathode material for batteries of high energy density. *Materials Research Bulletin* **1980,** *15* (6), 783-789.

[5] Thackeray, M. M., Structural Considerations of Layered and Spinel Lithiated Oxides for Lithium Ion Batteries. *Journal of The Electrochemical Society* **1995,** *142* (8), 2558-2563.

[6] Tarascon, J. M.; Wang, E.; Shokoohi, F. K.; McKinnon, W. R.; Colson, S., The Spinel Phase of LiMn2 O 4 as a Cathode in Secondary Lithium Cells. *Journal of The Electrochemical Society* **1991,** *138* (10), 2859-2864.

[7] Shaju, K. M.; Subba Rao, G. V.; Chowdari, B. V. R., Performance of layered Li(Ni1/3Co1/3Mn1/3)O2 as cathode for Li-ion batteries. *Electrochimica Acta* **2002,** *48* (2), 145-151.

[8] Xu, K. Nonaqueous Liquid Electrolytes for Lithium-Based Rechargeable Batteries. American Chemical Society, 2004.

[9] Tarascon, J. M.; Armand, M., Issues and challenges facing rechargeable lithium batteries. *Nature* **2001,** *414* (6861), 359-367.

[10] Qian, J.; Henderson, W. A.; Xu, W.; Bhattacharya, P.; Engelhard, M.; Borodin, O.; Zhang, J.-G., High rate and stable cycling of lithium metal anode. *Nature Communications* **2015,** *6* (1), 6362.

[11] Goodenough, J. B.; Park, K.-S., The Li-Ion Rechargeable Battery: A Perspective. *Journal of the American Chemical Society* **2013,** *135* (4), 1167-1176.

[12] Whittingham, M. S., History, Evolution, and Future Status of Energy Storage. *Proceedings of the IEEE* **2012,** *100* (Special Centennial Issue), 1518-1534.

[13] Krauskopf, T.; Hartmann, H.; Zeier, W. G.; Janek, J., Toward a Fundamental Understanding of the Lithium Metal Anode in Solid-State Batteries—An Electrochemo-Mechanical Study on the Garnet-Type Solid Electrolyte Li6.25Al0.25La3Zr2O12. *ACS Applied Materials & Interfaces* **2019,** *11* (15), 14463-14477.

[14] Monroe, C.; Newman, J., The Effect of Interfacial Deformation on Electrodeposition Kinetics. *Journal of The Electrochemical Society* **2004,** *151* (6), A880.

[15] Weiss, M.; Simon, F. J.; Busche, M. R.; Nakamura, T.; Schröder, D.; Richter, F. H.; Janek, J., From Liquid- to Solid-State Batteries: Ion Transfer Kinetics of Heteroionic Interfaces. *Electrochemical Energy Reviews* **2020,** *3* (2), 221-238.

[16] Busche, M. R.; Drossel, T.; Leichtweiss, T.; Weber, D. A.; Falk, M.; Schneider, M.; Reich, M.-L.; Sommer, H.; Adelhelm, P.; Janek, J., Dynamic formation of a solid-liquid electrolyte interphase and its consequences for hybrid-battery concepts. *Nature Chemistry* **2016,** *8* (5), 426-434.

[17] Kato, Y.; Hori, S.; Saito, T.; Suzuki, K.; Hirayama, M.; Mitsui, A.; Yonemura, M.; Iba, H.; Kanno, R., High-power all-solid-state batteries using sulfide superionic conductors. *Nature Energy* **2016,** *1*, 16030.

[18] Wang, Q.; Ping, P.; Zhao, X.; Chu, G.; Sun, J.; Chen, C., Thermal runaway caused fire and explosion of lithium ion battery. *Journal of Power Sources* **2012,** *208*, 210-224.

[19] Inoue, T.; Mukai, K., Are All-Solid-State Lithium-Ion Batteries Really Safe?–Verification by Differential Scanning Calorimetry with an All-Inclusive Microcell. *ACS Applied Materials & Interfaces* **2017,** *9* (2), 1507-1515.

[20] Kato, Y.; Hori, S.; Saito, T.; Suzuki, K.; Hirayama, M.; Mitsui, A.; Yonemura, M.; Iba, H.; Kanno, R., High-power all-solid-state batteries using sulfide superionic conductors. **2016,** *1*, 16030.

[21] Jung, K.-N.; Shin, H.-S.; Park, M.-S.; Lee, J.-W. Solid-State Lithium Batteries: Bipolar Design, Fabrication, and Electrochemistry. 2019.

[22] Ma, S.; Jiang, M.; Tao, P.; Song, C.; Wu, J.; Wang, J.; Deng, T.; Shang, W., Temperature effect and thermal impact in lithium-ion batteries: A review. *Progress in Natural Science: Materials International* **2018,** *28* (6), 653-666.

[23] Senyshyn, A.; Mühlbauer, M. J.; Dolotko, O.; Ehrenberg, H., Low-temperature performance of Li-ion batteries: The behavior of lithiated graphite. *Journal of Power Sources* **2015,** *282*, 235-240.

[24] Huang, C. K.; Sakamoto, J. S.; Wolfenstine, J.; Surampudi, S., The Limits of Low-Temperature Performance of Li-Ion Cells. *Journal of The Electrochemical Society* **2000,** *147* (8), 2893.

[25] Zhang, S. S.; Xu, K.; Jow, T. R., The low temperature performance of Li-ion batteries. *Journal of Power Sources* **2003,** *115* (1), 137-140.

[26] Shim, J.; Kostecki, R.; Richardson, T.; Song, X.; Striebel, K. A., Electrochemical analysis for cycle performance and capacity fading of a lithium-ion battery cycled at elevated temperature. *Journal of Power Sources* **2002,** *112* (1), 222-230.

[27] Feng, X.; Sun, J.; Ouyang, M.; He, X.; Lu, L.; Han, X.; Fang, M.; Peng, H., Characterization of large format lithium ion battery exposed to extremely high temperature. *Journal of Power Sources* **2014,** *272*, 457-467.

[28] Leng, F.; Tan, C. M.; Pecht, M., Effect of Temperature on the Aging rate of Li Ion Battery Operating above Room Temperature. *Scientific Reports* **2015,** *5* (1), 12967.

[29] Zhang, Z.; Shao, Y.; Lotsch, B.; Hu, Y.-S.; Li, H.; Janek, J.; Nazar, L. F.; Nan, C.-W.; Maier, J.; Armand, M.; Chen, L., New horizons for inorganic solid state ion conductors. *Energy & Environmental Science* **2018,** *11* (8), 1945-1976.

[30] Chen, R.; Qu, W.; Guo, X.; Li, L.; Wu, F., The pursuit of solid-state electrolytes for lithium batteries: from comprehensive insight to emerging horizons. *Materials Horizons* **2016,** *3* (6), 487-516.

[31] Manthiram, A.; Yu, X.; Wang, S., Lithium battery chemistries enabled by solid-state electrolytes. *Nature Reviews Materials* **2017,** *2*, 16103.

[32] Zhang, X.; Xie, J.; Shi, F.; Lin, D.; Liu, Y.; Liu, W.; Pei, A.; Gong, Y.; Wang, H.; Liu, K.; Xiang, Y.; Cui, Y., Vertically Aligned and Continuous Nanoscale Ceramic–Polymer Interfaces in Composite Solid Polymer Electrolytes for Enhanced Ionic Conductivity. *Nano Letters* **2018,** *18* (6), 3829-3838.

[33] Li, Z.; Sha, W.-X.; Guo, X., Three-Dimensional Garnet Framework-Reinforced Solid Composite Electrolytes with High Lithium-Ion Conductivity and Excellent Stability. *ACS Applied Materials & Interfaces* **2019,** *11* (30), 26920-26927.

[34] Hu, X.-y.; Jing, M.-x.; Yang, H.; Liu, Q.-y.; Chen, F.; Yuan, W.-y.; Kang, L.; Li, D.-h.; Shen, X.-q., Enhanced ionic conductivity and lithium dendrite suppression of polymer solid electrolytes by alumina nanorods and interfacial graphite modification. *Journal of Colloid and Interface Science* **2021,** *590*, 50-59.

[35] Liu, W.; Liu, N.; Sun, J.; Hsu, P.-C.; Li, Y.; Lee, H.-W.; Cui, Y., Ionic Conductivity Enhancement of Polymer Electrolytes with Ceramic Nanowire Fillers. *Nano Letters* **2015,** *15* (4), 2740-2745.

[36] Alpen, U. v., Li3N: A promising Li ionic conductor. *Journal of Solid State Chemistry* **1979,** *29* (3), 379-392.

[37] Alpen, U. v.; Rabenau, A.; Talat, G. H., Ionic conductivity in Li3N single crystals. *Applied Physics Letters* **1977,** *30* (12), 621-623.

[38] Xia, S.; Wu, X.; Zhang, Z.; Cui, Y.; Liu, W., Practical Challenges and Future Perspectives of All-Solid-State Lithium-Metal Batteries. *Chem* **2019,** *5* (4), 753-785.

[39] Xu, H.; Li, Y.; Zhou, A.; Wu, N.; Xin, S.; Li, Z.; Goodenough, J. B., Li3N-Modified Garnet Electrolyte for All-Solid-State Lithium Metal Batteries Operated at 40 °C. *Nano Letters* **2018,** *18* (11), 7414-7418.

[40] Kızılaslan, A.; Akbulut, H., Assembling All-Solid-State Lithium–Sulfur Batteries with Li3N-Protected Anodes. *ChemPlusChem* **2019,** *84* (2), 183-189.

[41] Gulino, V.; Brighi, M.; Dematteis, E. M.; Murgia, F.; Nervi, C.; Černý, R.; Baricco, M., Phase Stability and Fast Ion Conductivity in the Hexagonal LiBH4–LiBr–LiCl Solid Solution. *Chemistry of Materials* **2019,** *31* (14), 5133-5144.

[42] Takahashi, K.; Hattori, K.; Yamazaki, T.; Takada, K.; Matsuo, M.; Orimo, S.; Maekawa, H.; Takamura, H., All-solid-state lithium battery with LiBH4 solid electrolyte. *Journal of Power Sources* **2013,** *226*, 61-64.

[43] Unemoto, A.; Yasaku, S.; Nogami, G.; Tazawa, M.; Taniguchi, M.; Matsuo, M.; Ikeshoji, T.; Orimo, S.-i., Development of bulk-type all-solid-state lithium-sulfur battery using LiBH4 electrolyte. *Applied Physics Letters* **2014,** *105* (8), 083901.

[44] Kisu, K.; Kim, S.; Oguchi, H.; Toyama, N.; Orimo, S.-i., Interfacial stability between LiBH4-based complex hydride solid electrolytes and Li metal anode for all-solid-state Li batteries. *Journal of Power Sources* **2019,** *436*, 226821.

[45] Kamaya, N.; Homma, K.; Yamakawa, Y.; Hirayama, M.; Kanno, R.; Yonemura, M.; Kamiyama, T.; Kato, Y.; Hama, S.; Kawamoto, K.; Mitsui, A., A lithium superionic conductor. *Nat Mater* **2011,** *10* (9), 682-686.

[46] Adeli, P.; Bazak, J. D.; Park, K. H.; Kochetkov, I.; Huq, A.; Goward, G. R.; Nazar, L. F., Boosting Solid-State Diffusivity and Conductivity in Lithium Superionic Argyrodites by Halide Substitution. *Angewandte Chemie International Edition 0* (0).

[47] Zhou, L.; Assoud, A.; Zhang, Q.; Wu, X.; Nazar, L. F., New Family of Argyrodite Thioantimonate Lithium Superionic Conductors. *Journal of the American Chemical Society* **2019,** *141* (48), 19002-19013.

[48] Liu, Z.; Fu, W.; Payzant, E. A.; Yu, X.; Wu, Z.; Dudney, N. J.; Kiggans, J.; Hong, K.; Rondinone, A. J.; Liang, C., Anomalous High Ionic Conductivity of Nanoporous β-Li3PS4. *Journal of the American Chemical Society* **2013,** *135* (3), 975-978.

[49] Koerver, R.; Aygün, I.; Leichtweiß, T.; Dietrich, C.; Zhang, W.; Binder, J. O.; Hartmann, P.; Zeier, W. G.; Janek, J., Capacity Fade in Solid-State Batteries: Interphase Formation and Chemomechanical Processes in Nickel-Rich Layered Oxide Cathodes and Lithium Thiophosphate Solid Electrolytes. *Chemistry of Materials* **2017,** *29* (13), 5574-5582.

[50] Ohta, N.; Takada, K.; Zhang, L.; Ma, R.; Osada, M.; Sasaki, T., Enhancement of the High-Rate Capability of Solid-State Lithium Batteries by Nanoscale Interfacial Modification. *Advanced Materials* **2006,** *18* (17), 2226-2229.

[51] Sakuda, A.; Nakamoto, N.; Kitaura, H.; Hayashi, A.; Tadanaga, K.; Tatsumisago, M., All-solid-state lithium secondary batteries with metal-sulfide-coated LiCoO2 prepared by thermal decomposition of dithiocarbamato complexes. *Journal of Materials Chemistry* **2012,** *22* (30), 15247-15254.

[52] Seino, Y.; Ota, T.; Takada, K., High rate capabilities of all-solid-state lithium secondary batteries using Li4Ti5O12-coated LiNi0.8Co0.15Al0.05O2 and a sulfide-based solid electrolyte. *Journal of Power Sources* **2011,** *196* (15), 6488-6492.

[53] Sakuda, A.; Hayashi, A.; Tatsumisago, M., Interfacial Observation between LiCoO2 Electrode and Li2S−P2S5 Solid Electrolytes of All-Solid-State Lithium Secondary Batteries Using Transmission Electron Microscopy. *Chemistry of Materials* **2010,** *22* (3), 949-956.

[54] Li, X.; Ren, Z.; Norouzi Banis, M.; Deng, S.; Zhao, Y.; Sun, Q.; Wang, C.; Yang, X.; Li, W.; Liang, J.; Li, X.; Sun, Y.; Adair, K.; Li, R.; Hu, Y.; Sham, T.-K.; Huang, H.; Zhang, L.; Lu, S.; Luo, J.; Sun, X., Unravelling the Chemistry and Microstructure Evolution of a Cathodic Interface in Sulfide-Based All-Solid-State Li-Ion Batteries. *ACS Energy Letters* **2019,** *4* (10), 2480-2488.

[55] Cao, D.; Zhang, Y.; Nolan, A. M.; Sun, X.; Liu, C.; Sheng, J.; Mo, Y.; Wang, Y.; Zhu, H., Stable Thiophosphate-Based All-Solid-State Lithium Batteries through Conformally Interfacial Nanocoating. *Nano Letters* **2020,** *20* (3), 1483-1490.

[56] Ohta, N.; Takada, K.; Sakaguchi, I.; Zhang, L.; Ma, R.; Fukuda, K.; Osada, M.; Sasaki, T., LiNbO3-coated LiCoO2 as cathode material for all solid-state lithium secondary batteries. *Electrochemistry Communications* **2007,** *9* (7), 1486-1490.

[57] Kim, J.; Kim, M.; Noh, S.; Lee, G.; Shin, D., Enhanced electrochemical performance of surface modified LiCoO2 for all-solid-state lithium batteries. *Ceramics International* **2016,** *42* (2, Part A), 2140-2146.

[58] Li, X.; Liu, J.; Banis, M. N.; Lushington, A.; Li, R.; Cai, M.; Sun, X., Atomic layer deposition of solid-state electrolyte coated cathode materials with superior high-voltage cycling behavior for lithium ion battery application. *Energy & Environmental Science* **2014,** *7* (2), 768-778.

[59] Sakuda, A.; Kitaura, H.; Hayashi, A.; Tadanaga, K.; Tatsumisago, M., All-solid-state lithium secondary batteries with oxide-coated LiCoO2 electrode and Li2S–P2S5 electrolyte. *Journal of Power Sources* **2009,** *189* (1), 527-530.

[60] Swamy, T.; Chen, X.; Chiang, Y.-M., Electrochemical Redox Behavior of Li Ion Conducting Sulfide Solid Electrolytes. *Chemistry of Materials* **2019,** *31* (3), 707-713.

[61] Tan, D. H. S.; Wu, E. A.; Nguyen, H.; Chen, Z.; Marple, M. A. T.; Doux, J.-M.; Wang, X.; Yang, H.; Banerjee, A.; Meng, Y. S., Elucidating Reversible Electrochemical Redox of Li6PS5Cl Solid Electrolyte. *ACS Energy Letters* **2019**, 2418-2427.

[62] Kim, K. H.; Iriyama, Y.; Yamamoto, K.; Kumazaki, S.; Asaka, T.; Tanabe, K.; Fisher, C. A. J.; Hirayama, T.; Murugan, R.; Ogumi, Z., Characterization of the interface between LiCoO2 and Li7La3Zr2O12 in an all-solid-state rechargeable lithium battery. *Journal of Power Sources* **2011,** *196* (2), 764-767.

[63] Richards, W. D.; Miara, L. J.; Wang, Y.; Kim, J. C.; Ceder, G., Interface Stability in Solid-State Batteries. *Chemistry of Materials* **2016,** *28* (1), 266-273.

[64] Zhu, Y.; He, X.; Mo, Y., Origin of Outstanding Stability in the Lithium Solid Electrolyte Materials: Insights from Thermodynamic Analyses Based on First-Principles Calculations. *ACS Applied Materials & Interfaces* **2015,** *7* (42), 23685-23693.

[65] Wenzel, S.; Sedlmaier, S. J.; Dietrich, C.; Zeier, W. G.; Janek, J., Interfacial reactivity and interphase growth of argyrodite solid electrolytes at lithium metal electrodes. *Solid State Ionics* **2018,** *318*, 102-112.

[66] Nazri, G., Preparation, structure and ionic conductivity of lithium phosphide. *Solid State Ionics* **1989,** *34* (1), 97-102.

[67] Bron, P.; Johansson, S.; Zick, K.; Schmedt auf der Günne, J.; Dehnen, S.; Roling, B., Li10SnP2S12: An Affordable Lithium Superionic Conductor. *Journal of the American Chemical Society* **2013,** *135* (42), 15694-15697.

[68] Bron, P.; Roling, B.; Dehnen, S., Impedance characterization reveals mixed conducting interphases between sulfidic superionic conductors and lithium metal electrodes. *Journal of Power Sources* **2017,** *352*, 127-134.

[69] Wu, B.; Wang, S.; Evans Iv, W. J.; Deng, D. Z.; Yang, J.; Xiao, J., Interfacial behaviours between lithium ion conductors and electrode materials in various battery systems. *Journal of Materials Chemistry A* **2016,** *4* (40), 15266-15280.

[70] Xu, B.; Li, W.; Duan, H.; Wang, H.; Guo, Y.; Li, H.; Liu, H., Li3PO4-added garnet-type Li6.5La3Zr1.5Ta0.5O12 for Li-dendrite suppression. *Journal of Power Sources* **2017,** *354*, 68-73.

[71] Kuwata, N.; Iwagami, N.; Matsuda, Y.; Tanji, Y.; Kawamura, J., Thin Film Batteries with Li3PO4 Solid Electrolyte Fabricated by Pulsed Laser Deposition. *ECS Transactions* **2019,** *16* (26), 53-60.

[72] Yang, Z.; Yuan, H.; Zhou, C.; Wu, Y.; Tang, W.; Sang, S.; Liu, H., Facile interfacial adhesion enabled LATP-based solid-state lithium metal battery. *Chemical Engineering Journal* **2020,** *392*, 123650.

[73] Hao, X.; Zhao, Q.; Su, S.; Zhang, S.; Ma, J.; Shen, L.; Yu, Q.; Zhao, L.; Liu, Y.; Kang, F.; He, Y.-B., Constructing Multifunctional Interphase between Li1.4Al0.4Ti1.6(PO4)3 and Li Metal by Magnetron Sputtering for Highly Stable Solid-State Lithium Metal Batteries. *Advanced Energy Materials* **2019,** *9* (34), 1901604.

[74] Zhu, Y.; He, X.; Mo, Y., First principles study on electrochemical and chemical stability of solid electrolyte–electrode interfaces in all-solid-state Li-ion batteries. *Journal of Materials Chemistry A* **2016,** *4* (9), 3253-3266.

[75] Ma, C.; Cheng, Y.; Yin, K.; Luo, J.; Sharafi, A.; Sakamoto, J.; Li, J.; More, K. L.; Dudney, N. J.; Chi, M., Interfacial Stability of Li Metal–Solid Electrolyte Elucidated via in Situ Electron Microscopy. *Nano Letters* **2016,** *16* (11), 7030-7036.

[76] Park, K.; Yu, B.-C.; Jung, J.-W.; Li, Y.; Zhou, W.; Gao, H.; Son, S.; Goodenough, J. B., Electrochemical Nature of the Cathode Interface for a Solid-State Lithium-Ion Battery: Interface between LiCoO2 and Garnet-Li7La3Zr2O12. *Chemistry of Materials* **2016,** *28* (21), 8051-8059.

[77] Han, F.; Yue, J.; Chen, C.; Zhao, N.; Fan, X.; Ma, Z.; Gao, T.; Wang, F.; Guo, X.; Wang, C., Interphase Engineering Enabled All-Ceramic Lithium Battery. *Joule* **2018,** *2* (3), 497-508.

[78] Esaka, T.; Okuyama, R.; Iwahara, H., Ionic conduction in sintered fluorocomplexes LimMF6, M□Al, Ti. *Solid State Ionics* **1989,** *34* (3), 201-205.

[79] Asano, T.; Sakai, A.; Ouchi, S.; Sakaida, M.; Miyazaki, A.; Hasegawa, S., Solid Halide Electrolytes with High Lithium-Ion Conductivity for Application in 4 V Class Bulk-Type All-Solid-State Batteries. *Advanced Materials* **2018,** *30* (44), 1803075.

[80] Li, X.; Liang, J.; Chen, N.; Luo, J.; Adair, K. R.; Wang, C.; Banis, M. N.; Sham, T.-K.; Zhang, L.; Zhao, S.; Lu, S.; Huang, H.; Li, R.; Sun, X., Water-Mediated Synthesis of a Superionic Halide Solid Electrolyte. *Angewandte Chemie International Edition* **2019,** *58* (46), 16427-16432.

[81] Liang, J.; Li, X.; Wang, S.; Adair, K. R.; Li, W.; Zhao, Y.; Wang, C.; Hu, Y.; Zhang, L.; Zhao, S.; Lu, S.; Huang, H.; Li, R.; Mo, Y.; Sun, X., Site-Occupation-Tuned Superionic LixScCl3+xHalide Solid Electrolytes for All-Solid-State Batteries. *Journal of the American Chemical Society* **2020,** *142* (15), 7012-7022.

[82] Li, X.; Liang, J.; Luo, J.; Norouzi Banis, M.; Wang, C.; Li, W.; Deng, S.; Yu, C.; Zhao, F.; Hu, Y.; Sham, T.-K.; Zhang, L.; Zhao, S.; Lu, S.; Huang, H.; Li, R.; Adair, K. R.; Sun, X., Air-stable Li3InCl6 electrolyte with high voltage compatibility for all-solid-state batteries. *Energy & Environmental Science* **2019,** *12* (9), 2665-2671.

[83] Schlem, R.; Muy, S.; Prinz, N.; Banik, A.; Shao-Horn, Y.; Zobel, M.; Zeier, W. G., Mechanochemical Synthesis: A Tool to Tune Cation Site Disorder and Ionic Transport Properties of Li3MCl6 (M = Y, Er) Superionic Conductors. *Advanced Energy Materials n/a* (n/a), 1903719.

[84] Li, X.; Liang, J.; Yang, X.; Adair, K. R.; Wang, C.; Zhao, F.; Sun, X., Progress and perspectives on halide lithium conductors for all-solid-state lithium batteries. *Energy & Environmental Science* **2020,** *13* (5), 1429-1461.

[85] Wang, S.; Bai, Q.; Nolan, A. M.; Liu, Y.; Gong, S.; Sun, Q.; Mo, Y., Lithium Chlorides and Bromides as Promising Solid-State Chemistries for Fast Ion Conductors with Good Electrochemical Stability. *Angewandte Chemie International Edition* **2019,** *58* (24), 8039-8043.

[86] Zhou, L.; Kwok, C. Y.; Shyamsunder, A.; Zhang, Q.; Wu, X.; Nazar, L. F., A new halospinel superionic conductor for high-voltage all solid state lithium batteries. *Energy & Environmental Science* **2020,** *13* (7), 2056-2063.

[87] Riegger, L. M.; Schlem, R.; Sann, J.; Zeier, W. G.; Janek, J., Lithium-Metal Anode Instability of the Superionic Halide Solid Electrolytes and the Implications for Solid-State Batteries. *Angewandte Chemie International Edition* **2021,** *60* (12), 6718-6723.

[88] Park, K.-H.; Kaup, K.; Assoud, A.; Zhang, Q.; Wu, X.; Nazar, L. F., High-Voltage Superionic Halide Solid Electrolytes for All-Solid-State Li-Ion Batteries. *ACS Energy Letters* **2020**, 533-539.

[89] Kwak, H.; Han, D.; Lyoo, J.; Park, J.; Jung, S. H.; Han, Y.; Kwon, G.; Kim, H.; Hong, S.-T.; Nam, K.-W.; Jung, Y. S., New Cost-Effective Halide Solid Electrolytes for All-Solid-State Batteries: Mechanochemically Prepared Fe3+-Substituted Li2ZrCl6. *Advanced Energy Materials* **2021,** *11* (12), 2003190.

[90] Sakuda, A.; Hayashi, A.; Tatsumisago, M., Sulfide Solid Electrolyte with Favorable Mechanical Property for All-Solid-State Lithium Battery. *Scientific Reports* **2013,** *3*, 2261.

[91] Mohtadi, R.; Orimo, S.-i., The renaissance of hydrides as energy materials. *Nature Reviews Materials* **2016,** *2* (3), 16091.

[92] Cuan, J.; Zhou, Y.; Zhou, T.; Ling, S.; Rui, K.; Guo, Z.; Liu, H.; Yu, X., Borohydride-Scaffolded Li/Na/Mg Fast Ionic Conductors for Promising Solid-State Electrolytes. *Advanced Materials* **2019,** *31* (1), 1803533.

[93] Murugan, R.; Thangadurai, V.; Weppner, W., Fast Lithium Ion Conduction in Garnet-Type Li7La3Zr2O12. *Angewandte Chemie International Edition* **2007,** *46* (41), 7778-7781.

[94] Li, Y.; Wang, Z.; Li, C.; Cao, Y.; Guo, X., Densification and ionic-conduction improvement of lithium garnet solid electrolytes by flowing oxygen sintering. *Journal of Power Sources* **2014,** *248*, 642-646.

[95] Kim, Y.; Jo, H.; Allen, J. L.; Choe, H.; Wolfenstine, J.; Sakamoto, J., The Effect of Relative Density on the Mechanical Properties of Hot-Pressed Cubic Li7La3Zr2O12. *Journal of the American Ceramic Society* **2016,** *99* (4), 1367-1374.

[96] Rangasamy, E.; Sahu, G.; Keum, J. K.; Rondinone, A. J.; Dudney, N. J.; Liang, C., A high conductivity oxide–sulfide composite lithium superionic conductor. *Journal of Materials Chemistry A* **2014,** *2* (12), 4111-4116.

[97] He, X.; Zhu, Y.; Mo, Y., Origin of fast ion diffusion in super-ionic conductors. *Nature Communications* **2017,** *8* (1), 15893.

[98] Wang, Y.; Richards, W. D.; Ong, S. P.; Miara, L. J.; Kim, J. C.; Mo, Y.; Ceder, G., Design principles for solid-state lithium superionic conductors. *Nature Materials* **2015,** *14* (10), 1026-1031.

[99] Bachman, J. C.; Muy, S.; Grimaud, A.; Chang, H.-H.; Pour, N.; Lux, S. F.; Paschos, O.; Maglia, F.; Lupart, S.; Lamp, P.; Giordano, L.; Shao-Horn, Y., Inorganic Solid-State Electrolytes for Lithium Batteries: Mechanisms and Properties Governing Ion Conduction. *Chemical Reviews* **2016,** *116* (1), 140-162.

[100] Seino, Y.; Ota, T.; Takada, K.; Hayashi, A.; Tatsumisago, M., A sulphide lithium super ion conductor is superior to liquid ion conductors for use in rechargeable batteries. *Energy & Environmental Science* **2014,** *7* (2), 627-631.

[101] Yamane, H.; Shibata, M.; Shimane, Y.; Junke, T.; Seino, Y.; Adams, S.; Minami, K.; Hayashi, A.; Tatsumisago, M., Crystal structure of a superionic conductor, Li7P3S11. *Solid State Ionics* **2007,** *178* (15), 1163-1167.

[102] Zhao, E.; Ma, F.; Jin, Y.; Kanamura, K., Pechini synthesis of high ionic conductivity Li1.3Al0.3Ti1.7 (PO4)3 solid electrolytes: The effect of dispersant. *Journal of Alloys and Compounds* **2016,** *680*, 646-653.

[103] McGeehin, P.; Hooper, A., Fast ion conduction materials. *Journal of Materials Science* **1977,** *12* (1), 1-27.

[104] Huggins, R. A., 9 - Very Rapid Ionic Transport in Solids. In *Diffusion in Solids*, Nowick, A. S.; Burton, J. J., Eds. Academic Press: 1975; pp 445-486.

[105] Lorger, S.; Usiskin, R. E.; Maier, J., Transport and Charge Carrier Chemistry in Lithium Sulfide. *Advanced Functional Materials* **2019,** *29* (6), 1807688.

[106] Zeller, H. R.; Brüesch, P.; Pietronero, L.; Strässler, S., Lattice Dynamics and Ionic Motion in Superionic Conductors. In *Superionic Conductors*, Mahan, G. D.; Roth, W. L., Eds. Springer US: Boston, MA, 1976; pp 201-215.

[107] Brüesch, P.; Pietronero, L.; Strässler, S.; Zeller, H. R., Brownian motion in a polarizable lattice: Application to superionic conductors. *Physical Review B* **1977,** *15* (10), 4631-4637.

[108] Kraft, M. A.; Culver, S. P.; Calderon, M.; Böcher, F.; Krauskopf, T.; Senyshyn, A.; Dietrich, C.; Zevalkink, A.; Janek, J.; Zeier, W. G., Influence of Lattice Polarizability on the Ionic Conductivity in the Lithium Superionic Argyrodites Li6PS5X (X = Cl, Br, I). *Journal of the American Chemical Society* **2017,** *139* (31), 10909-10918.

[109] Zhou, L.; Park, K.-H.; Sun, X.; Lalère, F.; Adermann, T.; Hartmann, P.; Nazar, L. F., Solvent-Engineered Design of Argyrodite Li6PS5X (X = Cl, Br, I) Solid Electrolytes with High Ionic Conductivity. *ACS Energy Letters* **2019,** *4* (1), 265-270.

[110] Yu, C.; van Eijck, L.; Ganapathy, S.; Wagemaker, M., Synthesis, structure and electrochemical performance of the argyrodite Li6PS5Cl solid electrolyte for Li-ion solid state batteries. *Electrochimica Acta* **2016,** *215*, 93-99.

[111] Deiseroth, H.-J.; Maier, J.; Weichert, K.; Nickel, V.; Kong, S.-T.; Reiner, C., Li7PS6 and Li6PS5X (X: Cl, Br, I): Possible Three-dimensional Diffusion Pathways for Lithium Ions and Temperature Dependence of the Ionic Conductivity by Impedance Measurements. *Zeitschrift für anorganische und allgemeine Chemie* **2011,** *637* (10), 1287-1294.

[112] Kong, S.-T.; Deiseroth, H.-J.; Maier, J.; Nickel, V.; Weichert, K.; Reiner, C., Li6PO5Br and Li6PO5Cl: The first Lithium-Oxide-Argyrodites *Zeitschrift für anorganische und allgemeine Chemie* **2010,** *636* (11), 1920-1924.

[113] Kanno, R.; Murayama , M., Lithium Ionic Conductor Thio-LISICON: The Li2 S - GeS2 - P 2 S 5 System. *Journal of The Electrochemical Society* **2001,** *148* (7), A742-A746.

[114] Shannon, R. D.; Taylor, B. E.; English, A. D.; Berzins, T., New Li solid electrolytes. *Electrochimica Acta* **1977,** *22* (7), 783-796.

[115] Hu, Y. W.; Raistrick, I. D.; Huggins, R. A., Ionic Conductivity of Lithium Orthosilicate—Lithium Phosphate Solid Solutions. *Journal of The Electrochemical Society* **1977,** *124* (8), 1240-1242.

[116] Hong, H. Y. P., Crystal structure and ionic conductivity of Li14Zn(GeO4)4 and other new Li+ superionic conductors. *Materials Research Bulletin* **1978,** *13* (2), 117-124.

[117] Rayavarapu, P. R.; Sharma, N.; Peterson, V. K.; Adams, S., Variation in structure and Li+-ion migration in argyrodite-type Li6PS5X (X = Cl, Br, I) solid electrolytes. *Journal of Solid State Electrochemistry* **2012,** *16* (5), 1807-1813.

[118] Hanghofer, I.; Brinek, M.; Eisbacher, S. L.; Bitschnau, B.; Volck, M.; Hennige, V.; Hanzu, I.; Rettenwander, D.; Wilkening, H. M. R., Substitutional disorder: structure and ion dynamics of the argyrodites Li6PS5Cl, Li6PS5Br and Li6PS5I. *Physical Chemistry Chemical Physics* **2019,** *21* (16), 8489-8507.

[119] de Klerk, N. J. J.; Rosłoń, I.; Wagemaker, M., Diffusion Mechanism of Li Argyrodite Solid Electrolytes for Li-Ion Batteries and Prediction of Optimized Halogen Doping: The Effect of Li Vacancies, Halogens, and Halogen Disorder. *Chemistry of Materials* **2016,** *28* (21), 7955-7963.

[120] Brinek, M.; Hiebl, C.; Wilkening, H. M. R., Understanding the Origin of Enhanced Li-Ion Transport in Nanocrystalline Argyrodite-Type Li6PS5I. *Chemistry of Materials* **2020,** *32* (11), 4754-4766.

[121] Kraft, M. A.; Ohno, S.; Zinkevich, T.; Koerver, R.; Culver, S. P.; Fuchs, T.; Senyshyn, A.; Indris, S.; Morgan, B. J.; Zeier, W. G., Inducing High Ionic Conductivity in the Lithium Superionic Argyrodites Li6+xP1–xGexS5I for All-Solid-State Batteries. *Journal of the American Chemical Society* **2018,** *140* (47), 16330-16339.

[122] Ohno, S.; Helm, B.; Fuchs, T.; Dewald, G.; Kraft, M. A.; Culver, S. P.; Senyshyn, A.; Zeier, W. G., Further Evidence for Energy Landscape Flattening in the Superionic Argyrodites Li6+xP1–xMxS5I (M = Si, Ge, Sn). *Chemistry of Materials* **2019,** *31* (13), 4936-4944.

[123] Xu, M.; Park, M. S.; Lee, J. M.; Kim, T. Y.; Park, Y. S.; Ma, E., Mechanisms of Li+ transport in garnet-type cubic Li3+xLa3M2O12 (M = Te, Nb, Zr). *Physical Review B* **2012,** *85* (5), 052301.

[124] Rettenwander, D.; Redhammer, G.; Preishuber-Pflügl, F.; Cheng, L.; Miara, L.; Wagner, R.; Welzl, A.; Suard, E.; Doeff, M. M.; Wilkening, M.; Fleig, J.; Amthauer, G., Structural and Electrochemical Consequences of Al and Ga Cosubstitution in Li7La3Zr2O12 Solid Electrolytes. *Chemistry of Materials* **2016,** *28* (7), 2384-2392.

[125] O'Callaghan, M. P.; Lynham, D. R.; Cussen, E. J.; Chen, G. Z., Structure and Ionic-Transport Properties of Lithium-Containing Garnets Li3Ln3Te2O12 (Ln = Y, Pr, Nd, Sm−Lu). *Chemistry of Materials* **2006,** *18* (19), 4681-4689.

[126] Cussen, E. J.; Yip, T. W. S.; O'Neill, G.; O'Callaghan, M. P., A comparison of the transport properties of lithium-stuffed garnets and the conventional phases Li3Ln3Te2O12. *Journal of Solid State Chemistry* **2011,** *184* (2), 470-475.

[127] O'Callaghan, M. P.; Cussen, E. J., Lithium dimer formation in the Li-conducting garnets Li5+xBaxLa3−xTa2O12 (0 < x ≤ 1.6). *Chemical Communications* **2007,** (20), 2048-2050.

[128] Cussen, E. J., The structure of lithium garnets: cation disorder and clustering in a new family of fast Li+ conductors. *Chemical Communications* **2006,** (4), 412-413.

[129] Miara, L. J.; Ong, S. P.; Mo, Y.; Richards, W. D.; Park, Y.; Lee, J.-M.; Lee, H. S.; Ceder, G., Effect of Rb and Ta Doping on the Ionic Conductivity and Stability of the Garnet Li7+2x–y(La3–xRbx)(Zr2–yTay)O12 ($0 \leq x \leq 0.375$, $0 \leq y \leq 1$) Superionic Conductor: A First Principles Investigation. *Chemistry of Materials* **2013,** *25* (15), 3048-3055.

[130] AONO, H.; SUGIMOTO, E.; SADAOKA, Y.; IMANAKA, N.; ADACHI, G., ChemInform Abstract: The Electrical Properties of Ceramic Electrolytes for LiMxTi2-x(PO4)3 + yLi2O, M: Ge, Sn, Hf, and Zr Systems. *ChemInform* **1993,** *24* (45).

[131] Ortiz, G. F.; López, M. C.; Lavela, P.; Vidal-Abarca, C.; Tirado, J. L., Improved lithium-ion transport in NASICON-type lithium titanium phosphate by calcium and iron doping. *Solid State Ionics* **2014,** *262*, 573-577.

[132] Subramanian, M. A.; Subramanian, R.; Clearfield, A., Lithium ion conductors in the system AB(IV)2(PO4)3 (B = Ti, Zr and Hf). *Solid State Ionics* **1986,** *18-19*, 562-569.

[133] Aono, H.; Sugimoto, E.; Sadaoka, Y.; Imanaka, N.; Adachi, G.-y., Ionic conductivity and sinterability of lithium titanium phosphate system. *Solid State Ionics* **1990,** *40-41*, 38-42.

[134] Orimo, S.-i.; Nakamori, Y.; Eliseo, J. R.; Züttel, A.; Jensen, C. M., Complex Hydrides for Hydrogen Storage. *Chemical Reviews* **2007,** *107* (10), 4111-4132.

[135] Matsuo, M.; Nakamori, Y.; Orimo, S.-i.; Maekawa, H.; Takamura, H., Lithium superionic conduction in lithium borohydride accompanied by structural transition. *Applied Physics Letters* **2007,** *91* (22), 224103.

[136] Maekawa, H.; Matsuo, M.; Takamura, H.; Ando, M.; Noda, Y.; Karahashi, T.; Orimo, S.-i., Halide-Stabilized LiBH4, a Room-Temperature Lithium Fast-Ion Conductor. *Journal of the American Chemical Society* **2009,** *131* (3), 894-895.

[137] Noritake, T.; Aoki, M.; Towata, S.; Ninomiya, A.; Nakamori, Y.; Orimo, S., Crystal structure analysis of novel complex hydrides formed by the combination of LiBH4 and LiNH2. *Applied Physics A* **2006,** *83* (2), 277-279.

[138] Matsuo, M.; Remhof, A.; Martelli, P.; Caputo, R.; Ernst, M.; Miura, Y.; Sato, T.; Oguchi, H.; Maekawa, H.; Takamura, H.; Borgschulte, A.; Züttel, A.; Orimo, S.-i., Complex Hydrides with (BH4)− and (NH2)− Anions as New Lithium Fast-Ion Conductors. *Journal of the American Chemical Society* **2009,** *131* (45), 16389-16391.

[139] Yan, Y.; Kühnel, R.-S.; Remhof, A.; Duchêne, L.; Reyes, E. C.; Rentsch, D.; Łodziana, Z.; Battaglia, C., A Lithium Amide-Borohydride Solid-State Electrolyte with Lithium-Ion Conductivities Comparable to Liquid Electrolytes. *Advanced Energy Materials* **2017,** *7* (19), 1700294.

[140] Li, Y.; Zhou, W.; Xin, S.; Li, S.; Zhu, J.; Lü, X.; Cui, Z.; Jia, Q.; Zhou, J.; Zhao, Y.; Goodenough, J. B., Fluorine-Doped Antiperovskite Electrolyte for All-Solid-State Lithium-Ion Batteries. *Angewandte Chemie International Edition* **2016,** *55* (34), 9965-9968.

[141] Hood, Z. D.; Wang, H.; Samuthira Pandian, A.; Keum, J. K.; Liang, C., Li2OHCl Crystalline Electrolyte for Stable Metallic Lithium Anodes. *Journal of the American Chemical Society* **2016,** *138* (6), 1768-1771.

[142] Koedtruad, A.; Patino, M. A.; Ichikawa, N.; Kan, D.; Shimakawa, Y., Crystal structures and ionic conductivity in Li2OHX (X = Cl, Br) antiperovskites. *Journal of Solid State Chemistry* **2020,** *286*, 121263.

[143] Song, A.-Y.; Xiao, Y.; Turcheniuk, K.; Upadhya, P.; Ramanujapuram, A.; Benson, J.; Magasinski, A.; Olguin, M.; Meda, L.; Borodin, O.; Yushin, G., Protons Enhance Conductivities in Lithium Halide Hydroxide/Lithium Oxyhalide Solid Electrolytes by Forming Rotating Hydroxy Groups. *Advanced Energy Materials* **2018,** *8* (3), 1700971.

[144] Sun, Y.; Suzuki, K.; Hori, S.; Hirayama, M.; Kanno, R., Superionic Conductors: Li10+δ[SnySi1–y]1+δP2−δS12 with a Li10GeP2S12-type Structure in the Li3PS4–Li4SnS4–Li4SiS4 Quasi-ternary System. *Chemistry of Materials* **2017,** *29* (14), 5858-5864.

[145] Hori, S.; Kato, M.; Suzuki, K.; Hirayama, M.; Kato, Y.; Kanno, R., Phase Diagram of the Li4GeS4–Li3PS4 Quasi-Binary System Containing the Superionic Conductor Li10GeP2S12. *Journal of the American Ceramic Society* **2015,** *98* (10), 3352-3360.

[146] Hori, S.; Suzuki, K.; Hirayama, M.; Kato, Y.; Saito, T.; Yonemura, M.; Kanno, R., Synthesis, structure, and ionic conductivity of solid solution, Li10+δM1+δP2−δS12 (M = Si, Sn). *Faraday Discussions* **2014,** *176* (0), 83-94.

[147] Park, K. H.; Bai, Q.; Kim, D. H.; Oh, D. Y.; Zhu, Y.; Mo, Y.; Jung, Y. S., Design Strategies, Practical Considerations, and New Solution Processes of Sulfide Solid Electrolytes for All-Solid-State Batteries. *Advanced Energy Materials* **2018,** *8* (18), 1800035.

[148] Mercier, R.; Malugani, J.-P.; Fahys, B.; Robert, G., Superionic conduction in Li2S - P2S5 - LiI - glasses. *Solid State Ionics* **1981,** *5*, 663-666.

[149] Akitoshi, H.; Shigenori, H.; Hideyuki, M.; Masahiro, T.; Tsutomu, M., High Lithium Ion Conductivity of Glass–Ceramics Derived from Mechanically Milled Glassy Powders. *Chemistry Letters* **2001,** *30* (9), 872-873.

[150] Hayashi, A.; Hama, S.; Minami, T.; Tatsumisago, M., Formation of superionic crystals from mechanically milled Li2S–P2S5 glasses. *Electrochemistry Communications* **2003,** *5* (2), 111-114.

[151] Mizuno, F.; Hayashi, A.; Tadanaga, K.; Tatsumisago, M., New Lithium-Ion Conducting Crystal Obtained by Crystallization of the Li2S – P2S5 Glasses. *Electrochemical and Solid-State Letters* **2005,** *8* (11), A603-A606.

[152] Mizuno, F.; Hayashi, A.; Tadanaga, K.; Tatsumisago, M., New, Highly Ion-Conductive Crystals Precipitated from Li2S–P2S5 Glasses. *Advanced Materials* **2005,** *17* (7), 918-921.

[153] Homma, K.; Yonemura, M.; Kobayashi, T.; Nagao, M.; Hirayama, M.; Kanno, R., Crystal structure and phase transitions of the lithium ionic conductor Li3PS4. *Solid State Ionics* **2011,** *182* (1), 53-58.

[154] Local structural investigations, defect formation and ionic conductivity of the lithium ionic conductor Li4P2S6. *Chemistry of Materials* **2016**.

[155] Kong, S. T.; Reiner, C.; Deiseroth, H. J., Synthesis and Characterization of Lithium Argyrodite, Li7PS6. *Zeitschrift für anorganische und allgemeine Chemie* **2006,** *632* (12-13), 2100-2100.

[156] Onodera, Y.; Mori, K.; Otomo, T.; Arai, H.; Uchimoto, Y.; Ogumi, Z.; Fukunaga, T., Structural origin of ionic conductivity for Li7P3S11 metastable crystal by neutron and X-ray diffraction. *Journal of Physics: Conference Series* **2014,** *502*, 012021.

CHAPTER 2. $Li_{15}P_4S_{16}Cl_3$, a New Lithium Chloro-thiophosphate as a Solid-State Ionic Conductor

2.1 Introduction

All-**so**lid-state **Li**-ion **b**atteries (ALSOLIBs) are considered an emerging battery technology for next generation electrochemical energy storage. Currently used commercial Li-ion batteries (LIBs) contain flammable organic electrolytes, which may cause fire or explosion in harsh or abusive environments. Compared with commercial LIBs, ALSOLIBs with non-flammable solid electrolyte (SEs) not only have much better safety properties, but also potentially have higher energy density, if Li-metal anode can be enabled [1-4].

As the key component of ALSOLIB, the SE must meet the requirements in multiple categories of properties, including high ionic conductivity at ambient temperature, good chemical and electrochemical stability and good mechanical durability, etc. Commonly, SEs with room temperature (r.t.) ionic conductivity higher than10^{-4} S cm^{-1} are preferred [5-6]. To date, predominantly two groups of SEs have attracted much attentions: sulfide-based and oxide-based electrolytes. Oxide electrolytes, such as compounds with perovskite, NASICON or garnet structures, exhibit r.t. ionic conductivity from 10^{-5} to 10^{-3} S cm^{-1} [7-9]. However, large grain boundary (GB) resistance was often observed because of the poor electrical contact among the particles. High temperature sintering may help to mitigate the GB resistance, which significantly increases the complexity and cost of the manufacturing process [10-12] and may result in unwanted side reactions with the cathode materials [13-14]. In contrast, sulfide SEs are soft and ductile. Good electrical contact among the particles and thus low GB resistance can be relatively easily achieved by facile cold-pressing [15]. A number of lithium sulfides with high r.t. ionic conductivities reaching or even exceeding 10^{-3} S cm^{-1} have been reported [16-18], including Li_3PS_4-Li_4GeS_4 solid solutions with LISICON structure [19], Li_6PS_5X (X=Cl, Br, I) with argyrodite structure [20-23], $Li_7P_3S_{11}$ glass ceramics [24], and $Li_{10}GeP_2S_{12}$ (LGPS) [25], etc. Some of these SEs, such as LGPS, exhibit very high r. t. ionic conductivity of 10^{-2} S cm^{-1}, which exceeds that of liquid electrolytes [26], demonstrating the great potential of sulfide SEs. However, most of these known sulfide SEs require sophisticated processing (such as long time, high speed ball-milling and precise control of starting materials) and high temperature (>500°C) synthesis to achieve the expected high conductivities [17]. SEs with not only high r.t. conductivity, but also facile and low cost synthesis, are still very much desired. From crystal structure point of view, all these known sulfide SEs only present a few limited types of crystal structures. Most of current designs and developments of SEs are focused on the elementary modifications based on these known structure types, which can be limited sometimes. Addition of new crystal structure motifs is also desired. Compared with the relatively extensively explored Li-P-S ternary phase diagram, the quaternary phase diagrams of Li-P-S-X (X=halogen elements) are much less explored, which provides high potential to find new prototypes of Li-ion conducting crystal structures. For example, Li_4PS_4I was recently reported and its ionic conductivity is 1.2×10^{-4} S/cm [6]. One group of Li-P-S-X compounds, the argyrodites Li_6PS_5X (X=Cl, Br, I), recently attracted a lot of attentions owing to their high conductivities [5, 21, 27-28], demonstrating high potential of these quaternary compounds. Besides the argyrodites, no other Li-P-S-X quaternary compounds have been reported and a large area in the phase diagram remains unexplored. Recent computational works predicted that $Li_{15}P_4S_{16}Cl_3$ [29-30], can be thermodynamically stable. But no synthesis condition and crystal structure information was disclosed to date. Here we successfully synthesized a new compound

$Li_{15}P_4S_{16}Cl_3$ with a new crystal structure distinguished from all known sulfide SEs. The structural characterizations and ionic conduction behaviors of the compound are elaborated below.

2.2 Results and Discussion

2.2.1 Synthesis and Crystal Structure Characterizations

The quaternary Li-P-S-Cl phase diagram can be plotted in an equivalent Li_2S-P_2S_5-LiCl ternary phase diagram with better clarity, as shown in Figure 2.1. The argyrodite Li_6PS_5Cl is the only known phase in the middle of the phase diagram but it is very unlikely that it is the only phase. In this phase diagram, Li_2S, LiCl, P_2S_5 and Li_3PS_4 are considered thermodynamically stable, while $Li_7P_3S_{11}$ [31], Li_7PS_6 [32] and Li_6PS_5Cl [33] were predicted to be metastable in static DFT calculations at 0K. Previous studies showed that the formation energy of $Li_{15}P_4S_{16}Cl_3$ is 8 meV/atom, indicating $Li_{15}P_4S_{16}Cl_3$ is just slightly metastable in the relevant Li-P-S-Cl phase diagram [29] similar to $Li_7P_3S_{11}$ [31], Li_7PS_6 [32] and Li_6PS_5Cl [33]. The formation energy of $Li_{15}P_4S_{16}Cl_3$ from the precursor phases, Li_2S, P_2S_5 and LiCl is -3.203 eV/atom, indicating it is energetically favorable formation during synthesis. Therefore, we conducted a systematical exploration on selected regions of the phase diagram with the help of in situ XRD for synthesis. The lithium-rich region on the top right area of the phase diagram was first explored and one new phase was quickly identified. In situ XRD on the solid state synthesis of starting materials with various materials ratios were performed.

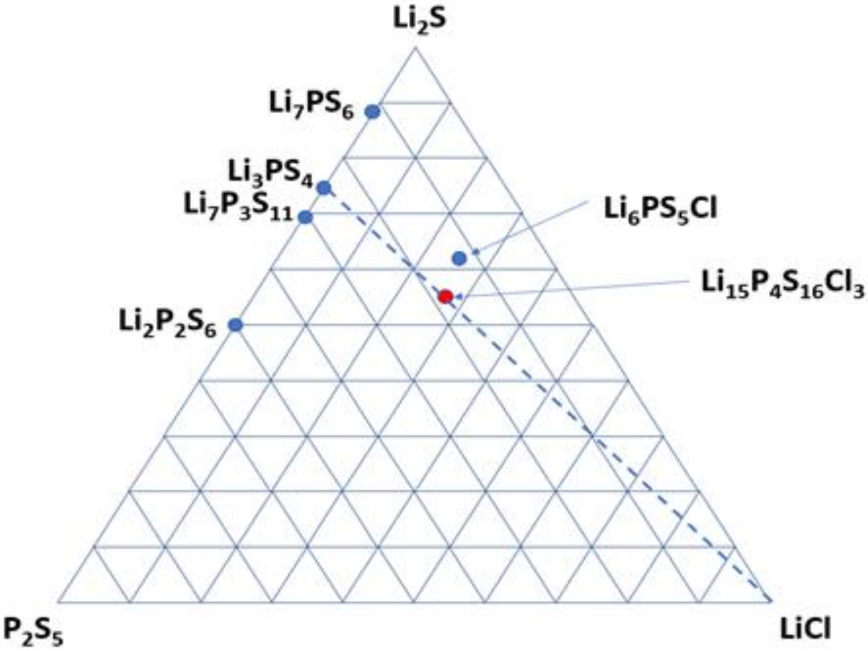

Figure 2.1 Li-P-S-Cl quaternary phase diagram plotted in Li_2S-P_2S_5-LiCl ternary manner.

In situ XRD on the solid state syntheses of starting materials with various materials ratios were performed. Figure. 2.2 shows the in situ XRD patterns collected from the starting materials with ratio of Li_2S: P_2S_5: LiCl = 3:1:1.5. The sample was heated from r.t. to 450 °C. The diffraction pattern at 50 °C shows the amorphous characteristics of the ball-milled mixture and low intensity peaks, which can be indexed as Li_2S and LiCl. As the temperature increases, the intensity of these peaks becomes higher, indicating the crystallization of Li_2S and LiCl. Starting from 150 °C, the reflections from Li_2S start to decrease, accompanied by the appearance of the reflections belonging to β-Li_3PS_4 phase. At 300 °C, a new set of peaks appear, which could not be indexed to any known phases. Meanwhile, the intensity of the β-Li_3PS_4 and LiCl peaks starts to decrease, implying that a new phase is formed from the reaction between β-Li_3PS_4 and LiCl. The mixture fully converted into the new phase at 340 °C, where no more reflections from β-Li_3PS_4 and LiCl can be seen. The new phase is stable up to 400 °C and decomposes to β-Li_3PS_4 and LiCl at 420 °C. At 440 °C, β-Li_3PS_4 turns into α-Li_3PS_4.

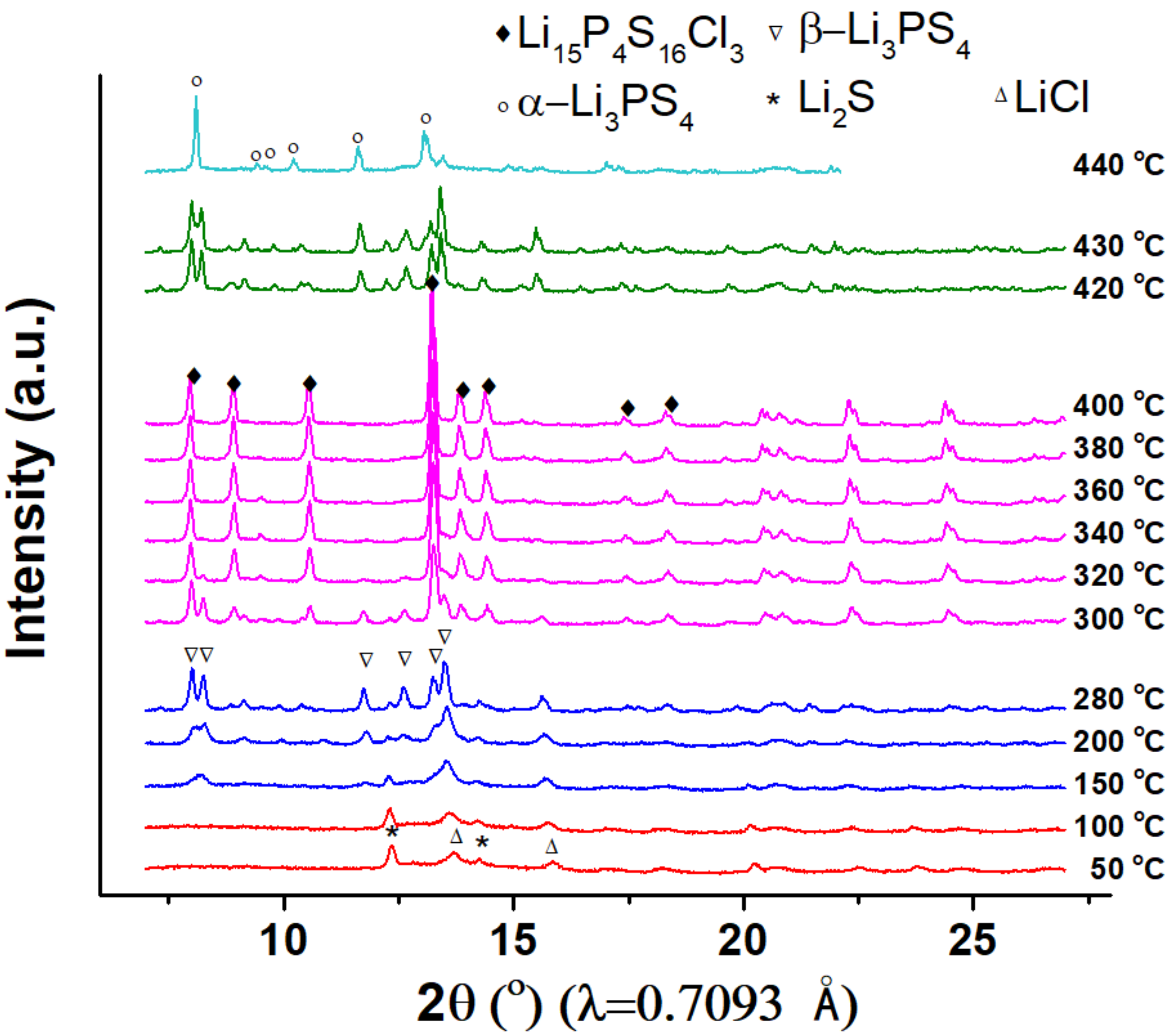

Figure 2.2 In situ XRD patterns of ball-milled starting materials Li_2S, P_2S_5, and LiCl with molar ratio of 3:1:1.5, heated from 50 to 440 °C.

Since no other phases were seen at 360 °C, it can be assumed that all starting materials were converted into this new phase. Therefore, the ratio of the elements in this new phase is Li :P: S: Cl = 15: 4: 16 :3, and the formation reaction can be written as follows:

$$4Li_3PS_4 + 3LiCl \rightarrow Li_{15}P_4S_{16}Cl_3 \tag{i}$$

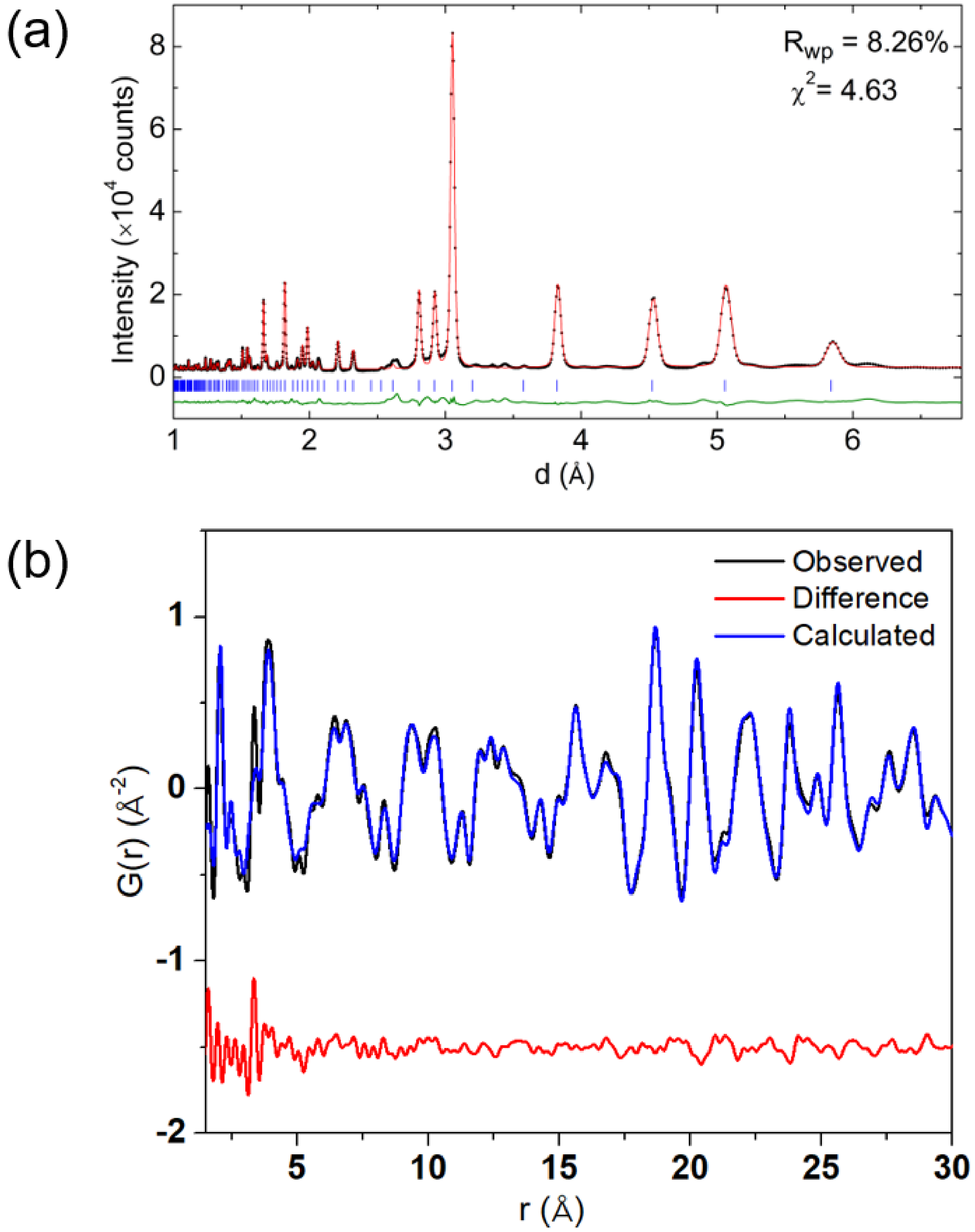

Figure 2.3 (a) Rietveld refinement of the long range structure of $Li_{15}P_4S_{16}Cl_3$ against synchrotron X-ray diffraction data (λ=0.24116 Å). (b) Least square refinement of the intermediate range structure of $Li_{15}P_4S_{16}Cl_3$ with using synchrotron X-ray PDF data.

$Li_{15}P_4S_{16}Cl_3$ is a new composition that has not been reported on its detailed crystal structure. However, its silver analogue $Ag_{15}P_4S_{16}Cl_3$ does exist and its XRD pattern very much resembles the pattern observed in Figure 2.2. Given the similarity in charge and ionic radius of Ag^+ and Li^+, the similar XRD patterns strongly imply that the actual elementary composition of the new phase is likely $Li_{15}P_4S_{16}Cl_3$. To verify this assumption, high resolution powder synchrotron XRD data was collected and Rietveld refinement was performed with using the crystal structure of $Ag_{15}P_4S_{16}Cl_3$ as the starting model, with keeping the space group and replacing all Ag atoms by Li atoms. Figure 2.3a shows the synchrotron XRD pattern and the results of refinement with using $I\bar{4}3d$ space group. A good fitting with a wR_p value of 8.26% was achieved, confirming that this new compound is indeed $Li_{15}P_4S_{16}Cl_3$ with the same structure as $Ag_{15}P_4S_{16}Cl_3$. The good PDF fit (R_w=18.6%) corroborates the crystal structure description (Figure 2.3b). The minor discrepancy in the low r-range may result from a small amount of amorphous phase, as seen in $Li_2P_2S_6$ and $Li_4P_2S_6$ [34-35].

The Li positions were further confirmed with using Fourier difference map analysis of both neutron and synchrotron X-ray powder diffraction data with the framework obtained from synchrotron X-ray diffraction patterns, as shown in Figure 2.4. It clearly indicates the two plausible Li sites, which matches well those Li positions obtained from Rietveld refinements.

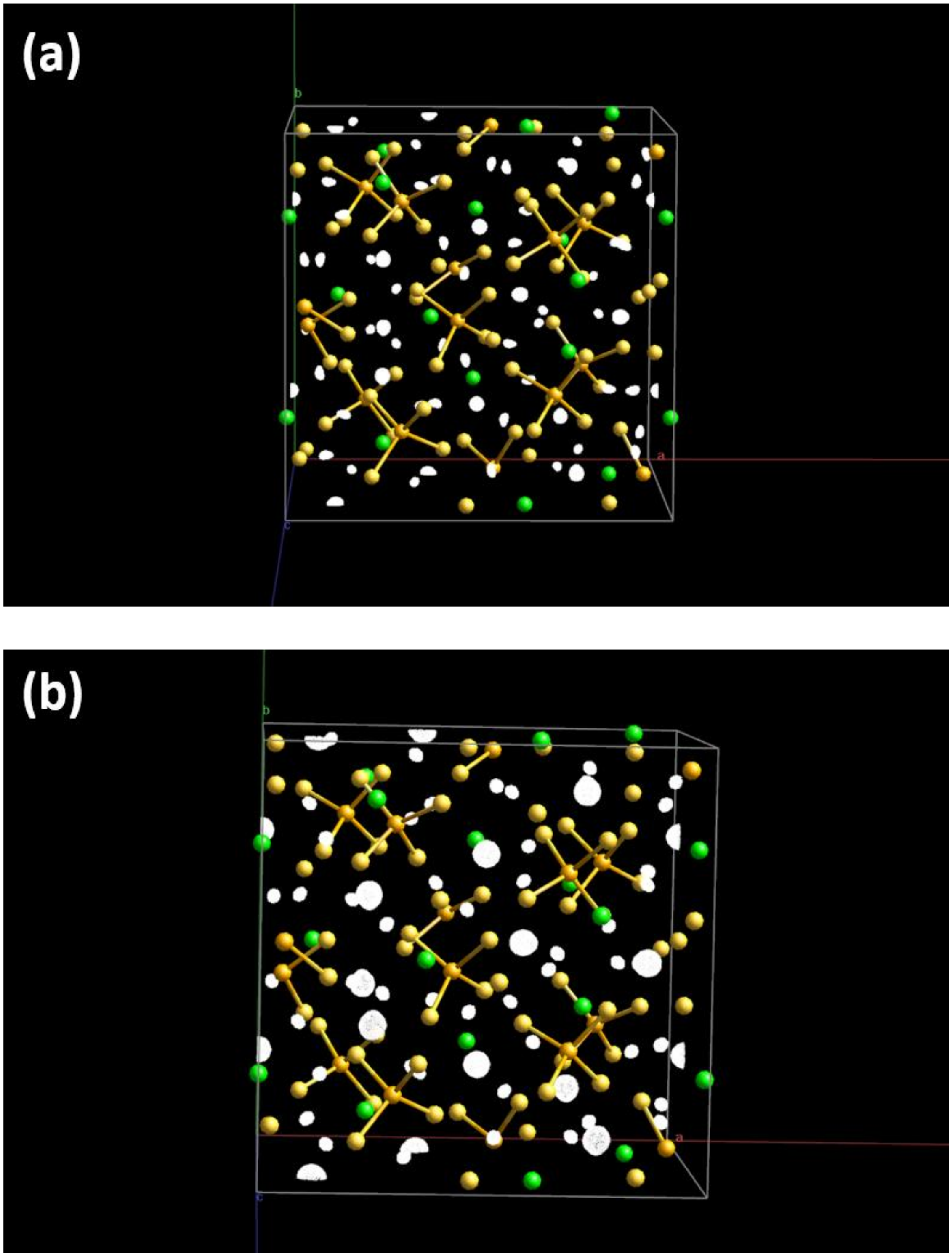

Figure 2.4 Difference Fourier maps used to identify Li sites generated from (a) synchrotron X-ray diffraction data and (b) time-of-flight neutron diffraction

The final Rietveld refinement of the crystal structure of $Li_{15}P_4S_{16}Cl_3$ against neutron diffraction data is shown in Figure 2.5. The refined cell parameter *a* of 14.3052(3) Å is smaller than that of $Ag_{15}P_4S_{16}Cl_3$ (*a*=14.838 Å) [36], in accordance with that Li^+ has smaller ionic radii (0.59 Å , four coordinated) relative to Ag^+ (1.00 Å , four coordinated) [37]. The crystallographic information extracted from neutron diffraction data is listed in Table 1.1. The crystal structure drawn based on the refinement result is shown in Figure 2.6. The structure is built by three kinds of tetrahedra: PS_4, LiS_4 and $Li(S_3Cl)$. All tetrahedra are connected via common corners. Every S or Cl atom is corner shared by 4 tetrahedra. Li atoms occupy two different tetrahedral sites: Li(1) occupies the 12*a* site and is bonded to four S^{2-} ions; while Li(2) occupies the 48*e* site and is bonded to three S^{2-} and one Cl^-.

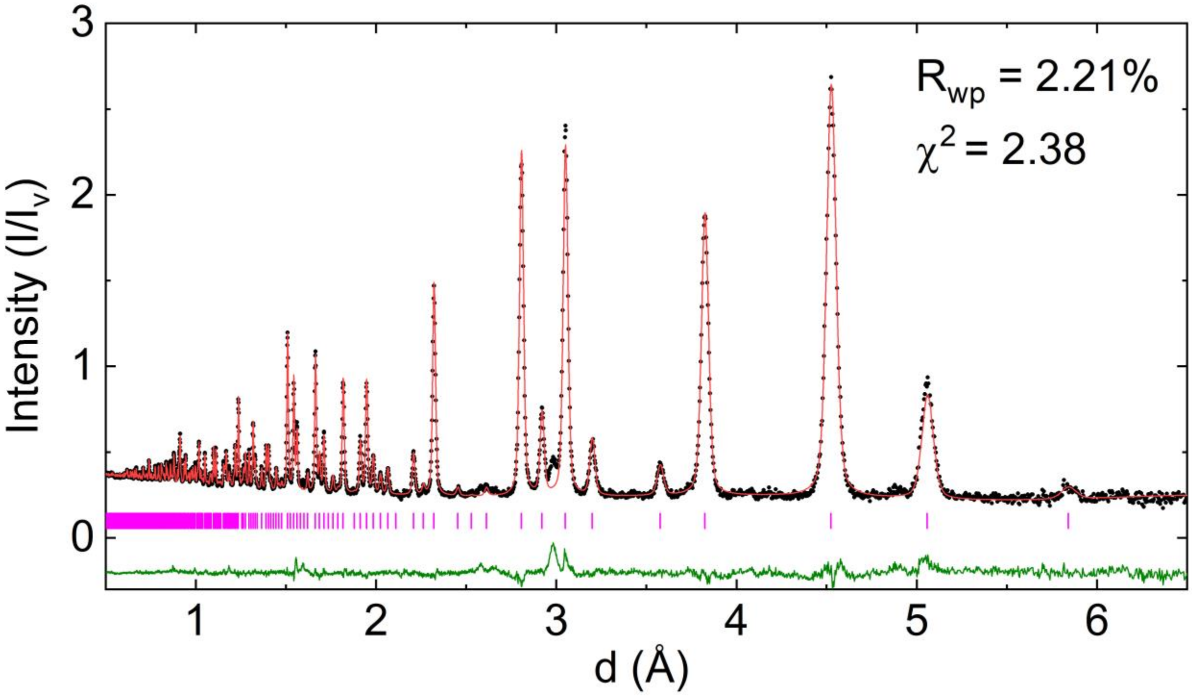

Figure 2.5 Rietveld refinement of $Li_{15}P_4S_{16}Cl_3$ against time-of-flight neutron diffraction data (POWGEN). The experiment data are shown in black dots, calculated data in red curve and difference curve in olive. The Bragg reflections are shown in blue markers. There is one unidentified peak around 3 Å, indicating the co-existence of impurity phase(s).

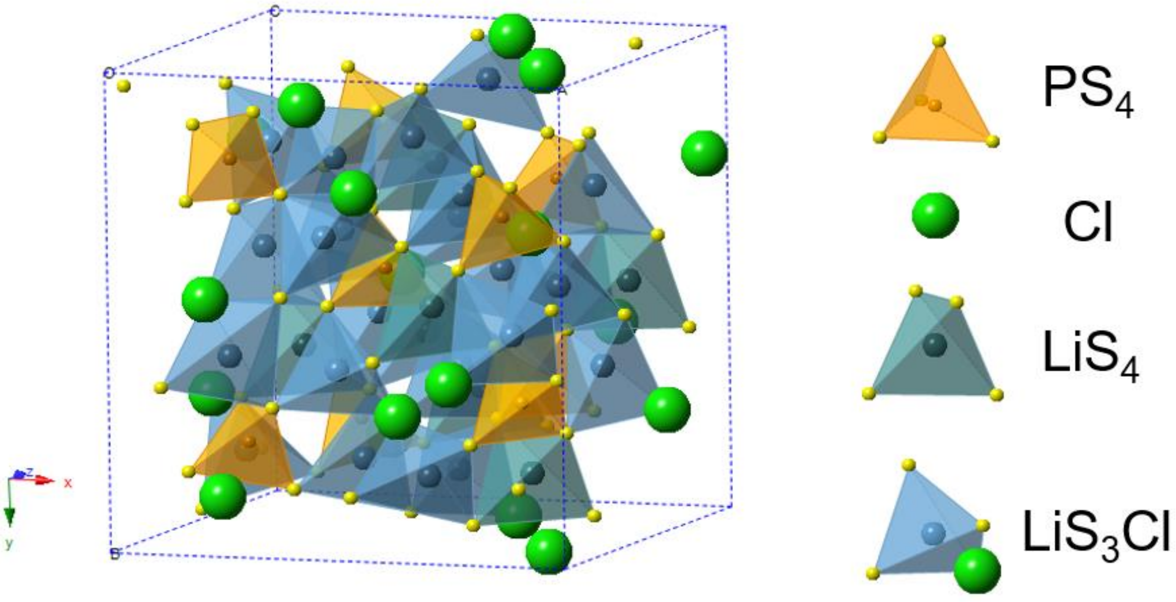

Figure 2.6 Refined crystal structure of $Li_{15}P_4S_{16}Cl_3$ using neutron powder diffraction data.

Table 2.1 Refined structure of $Li_{15}P_4S_{16}Cl_3$ using neutron diffraction data.

S.G. *I*-43d a = 14.3052(3) Å

Site	Wyck.	x	y	z	Occ.	B_{iso} (Å^2)
Li(1)	12a	0.00000	0.25000	0.37500	1	1.85(7)
Li(2)	48e	0.1420(3)	0.2145(3)	0.5825(4)	1	1.85(7)
S(1)	16c	0.0320(2)	0.0320(2)	0.0320(2)	1	1.09(4)
S(2)	48e	0.1080(2)	0.3433(2)	0.4713(2)	1	1.09(4)
Cl(1)	12b	0.00000	0.25000	0.87500	1	1.71(4)
P(1)	16c	0.1997(1)	0.1997(1)	0.1997(1)	1	0.90(4)

SEM images of as synthesized $Li_{15}P_4S_{16}Cl_3$ are shown in Figure 2.7. The primary particles with a dimension ranging from 1 to 5 μm are of cubic/cuboid shapes, in accordance with its space group symmetry. The primary particles are agglomerated to form secondary particles of a few tens micrometers, which is likely due to the fact that the sample was cooled down from a molten phase.

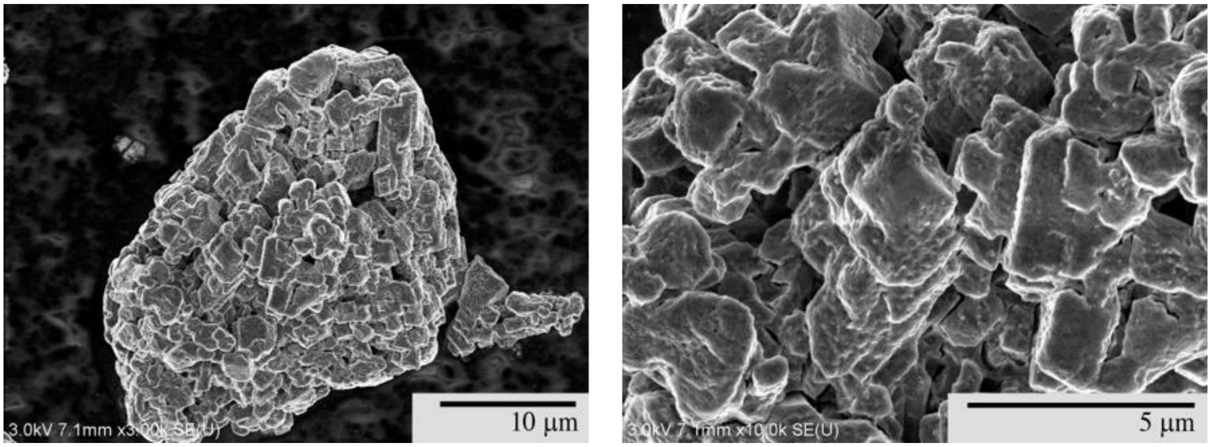

Figure 2.7 SEM images of $Li_{15}P_4S_{16}Cl_3$.

The local structure around the Li and the P ions was investigated by ^6Li and ^{31}P MAS NMR spectroscopy, respectively. The spectra are shown in Figure 2.8. The ^6Li NMR spectrum (Figure 2.8a) reveals two well-resolved narrow peaks. The stronger one at 1.0 ppm can be assigned to the Li(2) site at 48*e* position, and the weaker peak is assigned to the Li(1) site at 12*a* position. The ^{31}P spectrum (Figure 2.8b) shows two well-resolved peaks at 88.8 ppm and 85.7 ppm. Both can be assigned to isolated $[PS_4]^{3-}$ tetrahedra in the crystal structure[34], in agreement with the crystal structure derived from X-ray/neutron diffraction. The fact that two very similar environments are visible in the ^{31}P NMR spectrum although only one site was determined by X-ray/neutron diffraction could hint at small amount of amorphous phase existing. We ascribe the peak at 88.8 ppm to $[PS_4]^{3-}$ from crystalline $Li_{15}P_4S_{16}Cl_3$ and peak at 85.7 ppm to amorphous phase, based on the observation that the intensity of peak at 85.7 ppm decreases as heating time is extended and the crystallinity increases.

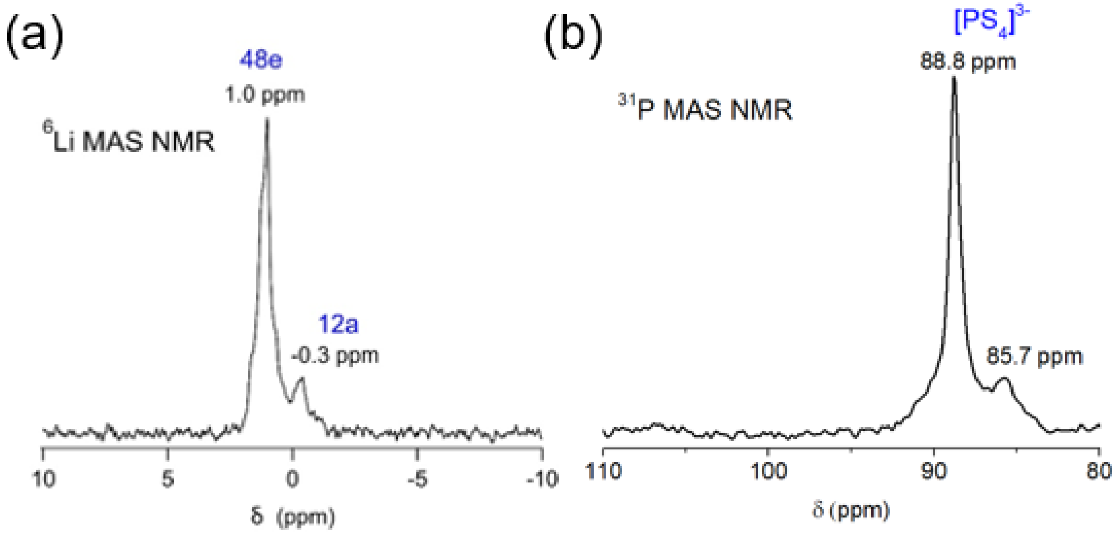

Figure 2.8 ^{6}Li and ^{31}P MAS NMR spectra of $Li_{15}P_4S_{16}Cl_3$.

2.2.2 Li ion diffusion behavior

The conductivity of $Li_{15}P_4S_{16}Cl_3$ was measured by electrochemical impedance spectroscopy (EIS). The relative density of the pellet is about 80%, under a uniaxial pressure of 10 MPa. Bulk and grain boundary contributions to the total resistance cannot be deconvoluted (Figure 2.9a). Figure 2.9b shows the temperature dependence of the conductivity of $Li_{15}P_4S_{16}Cl_3$. $Li_{15}P_4S_{16}Cl_3$ exhibited a low ionic conductivity of 1.0×10^{-7} S/cm at 30 °C, which is similar to β-Li_3PS_4 (9×10^{-7} S/cm) and γ- Li_3PS_4 (3×10^{-7} S/cm) [3]. When increasing the temperature to 90 °C, the ionic conductivity reached 3.4×10^{-6} S/cm. The calculated activation energy is 0.57 eV, which is different from β-Li_3PS_4 (0.16 eV) and γ- Li_3PS_4 (0.22 eV). This value is also much higher than those of typical lithium ion conductors such as $Li_7P_3S_{11}$, Li_6PS_5Cl and $Li_{10}GeP_2S_{12}$ [21, 25, 38].

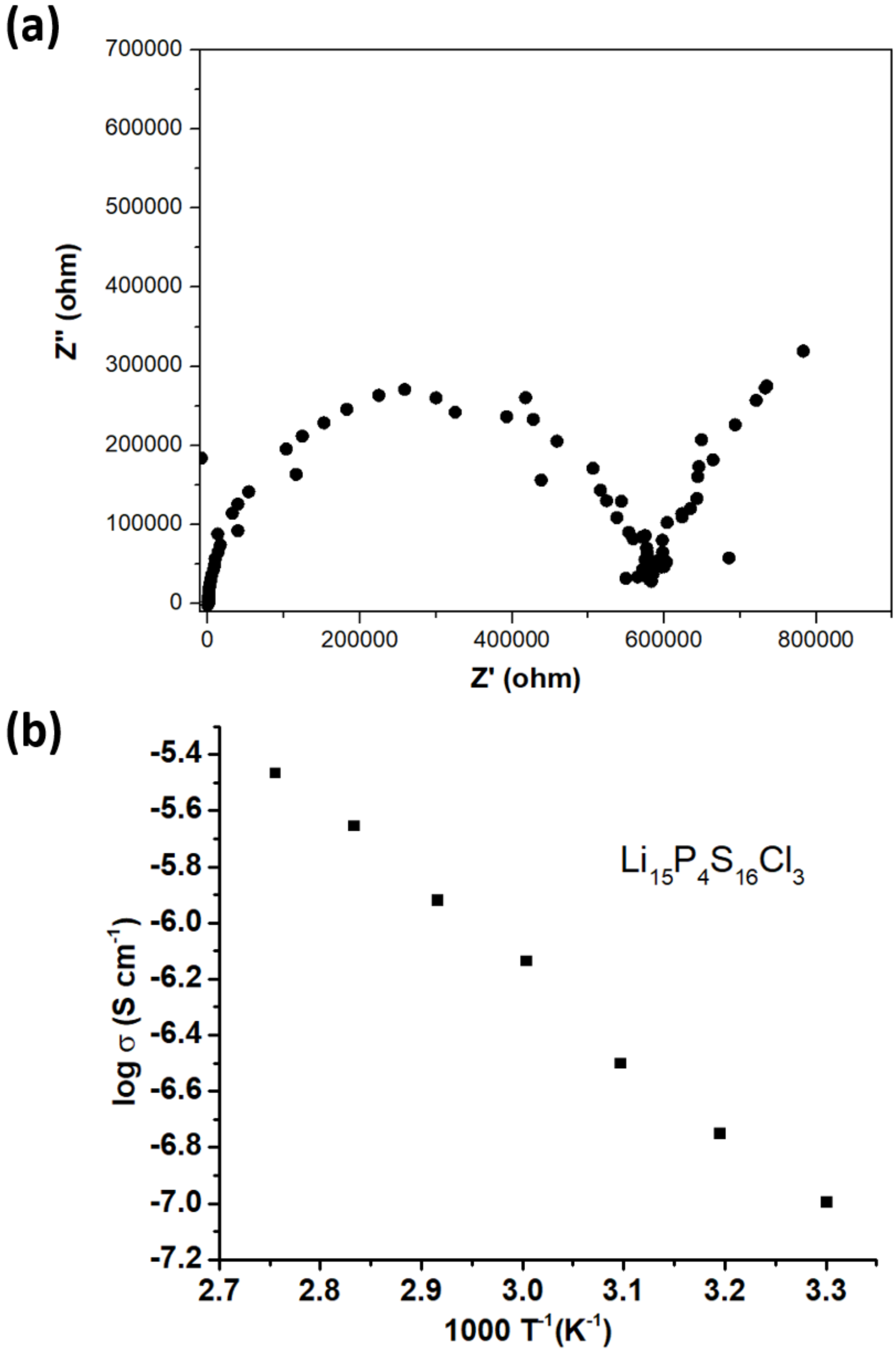

Figure 2.9 (a) Nyquist plot of $Li_{15}P_4S_{16}Cl_3$ at 30 °C. (b) Arrhenius plot of $Li_{15}P_4S_{16}Cl_3$. The activation energy is 0.57 eV.

Ab initio molecular dynamics (AIMD) was also used to calculate the theoretical ionic conductivity of this compound. The calculated ionic conductivity is around 10^{-14} S/cm, which is much lower than the experimental results. The conductivity of the sample being much higher than the calculated theoretical value may be caused by the existence of small amount of amorphous impurity phase and defects in the $Li_{15}P_4S_{16}Cl_3$ material. The amorphous impurity phase may be more conductive than $Li_{15}P_4S_{16}Cl_3$, which increase the overall measured conductivity. The other reason is that the formation of the impurity could results in slight off-stoichiometry in $Li_{15}P_4S_{16}Cl_3$, and mobile defects, such as Li vacancies or interstitial Li ions, may exist in $Li_{15}P_4S_{16}Cl_3$ material, which increases the conductivity. In the AIMD computation, a perfect bulk-phase crystal $Li_{15}P_4S_{16}Cl_3$ with no pre-existing defects were used, which may result in a limited carrier concentration for ion conduction. These differences in experiments and computation may have resulted in the differences in conductivity values. The results of the theoretical calculation suggest that lithium ions at both Li(1) and Li(2) sites are involved in the diffusion pathway. The Mean-squared Displacement-time (MSD-t) relationship (Figure. 2.10a) and Li trajectories within 2ps at 1150 K (Figure 2.10b) indicated that the lithium diffusion path in $Li_{15}P_4S_{16}Cl_3$ is three-dimensional.

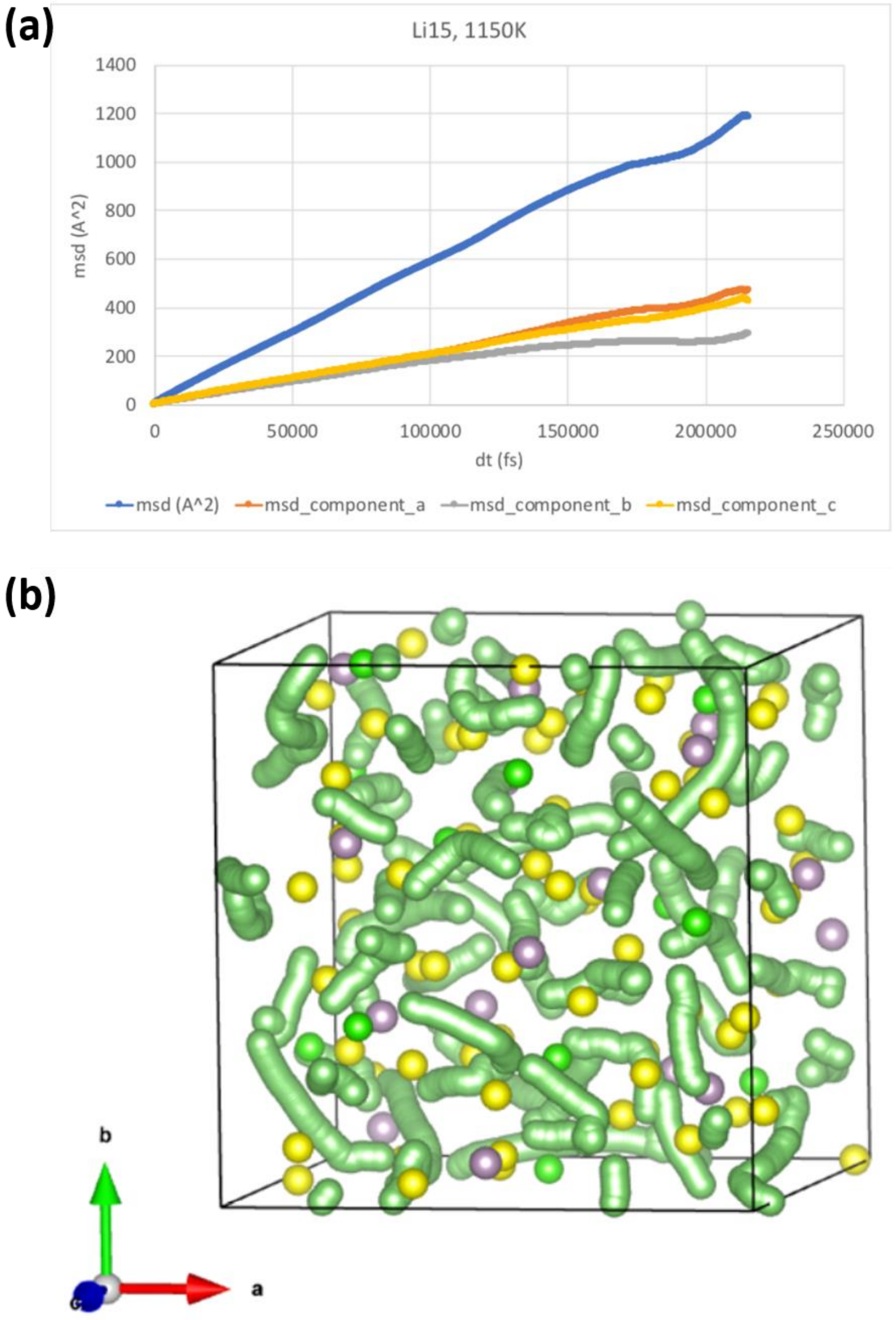

Figure 2.10 (a) The Mean-squared Displacement-time (MSD-t) relationship and (b) Li trajectories within 2 ps at 1150 K, as obtained from AIMD simulation.

In addition to its ability to investigate local structures element-specifically, solid state NMR is also a powerful tool to probe the dynamics of mobile ions in solids on different time and length scales [39]. Figure 2.11a shows the temperature dependence of static ^{7}Li NMR spectra of $Li_{15}P_4S_{16}Cl_3$.

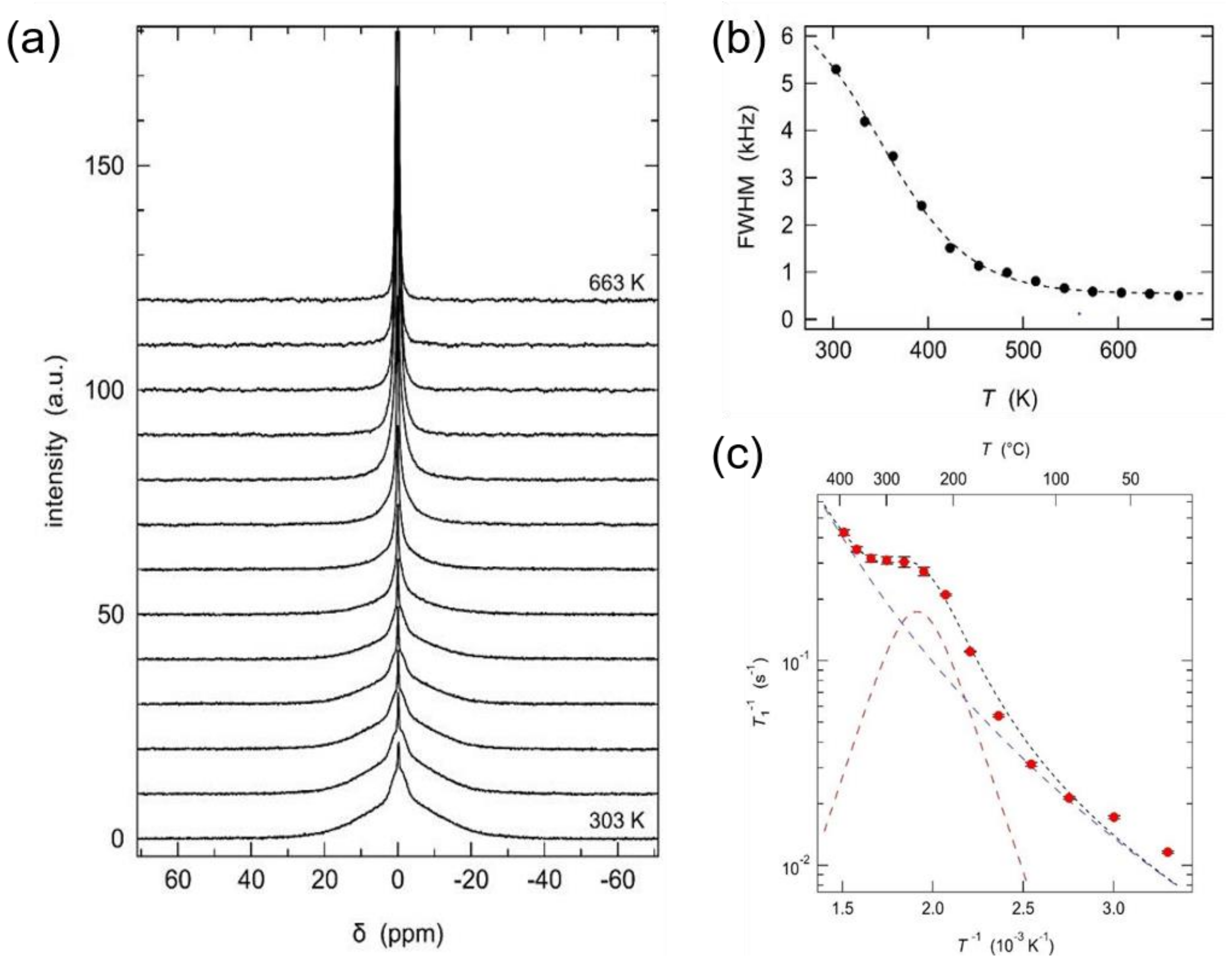

Figure 2.11 (a) static ^{7}Li NMR spectra at temperatures between 303 K and 663 K. b) FWHM vs temperature for the broad component in the static ^{7}Li NMR spectra. c) ^{7}Li NMR spin-lattice relaxation rates T1-1 vs inverse temperature.

At low temperatures, the spectra consist of three different contributions, all centered around 0 ppm: (i) a broad contribution in the range from +25 ppm to -25 ppm represents the satellite transitions of the ^{7}Li nuclei (nuclear spin $I = 3/2$), (ii) a narrower signal between +3 ppm and -3 ppm represents the central transition, and (iii) a very narrow component with a width of about 0.5 ppm represents Li ions that are already mobile at these low temperatures. When the temperature is increased, the broader contributions show a clear so-called motional narrowing. This reflects the temporal averaging of the local environments around the Li ions due the increasingly fast motions of these ions. At 663 K, only a single contribution is visible in the static ^{7}Li NMR spectrum. The full width at half maximum (FWHM) of the broader component is plotted in Figure 2.11b vs temperature. The curve shows no clear plateau at low temperatures and thus reveals that the motional averaging already started well below room temperature. The motion of the Li ions was additionally probed on very short time scales (few nanoseconds) by measuring ^{7}Li NMR relaxation rates T_1^{-1} as a function of (inverse) temperature (Fig. 2.11c). A clear maximum, as it was observed for Li_3PS_4 or $Li_{10}SnP_2S_{12}$, could not be observed for $Li_{15}P_4S_{16}Cl_3$. The relaxation rate rather shows a monotonic increase with increasing temperature and a shoulder at 523 K. The data can be described by a superposition of a diffusion-induced maximum [39-40] and a power law contribution (dashed lines in Figure 2.11c), which is a commonly used approach to describe such data [41]. The latter one might represent another jump process with a maximum at temperatures too high to be reached in these experiments. The fact that a clear maximum in the overall data is not visible can be ascribed to the quite slow diffusion and thus to a smaller diffusion-induced contribution.

This behavior reveals a quite complex diffusion mechanism involving different jump processes between different Li sites. The diffusion-induced maximum reveals an average hopping rate of the Li ions of about 5×10^8 s^{-1} at 523 K and an activation barrier for these jumps of (0.53 ± 0.06) eV. From the jump rate, a Li ion conductivity of about 10^{-6} S/cm can be extrapolated for 298 K. These values are in good agreement with the EIS results.

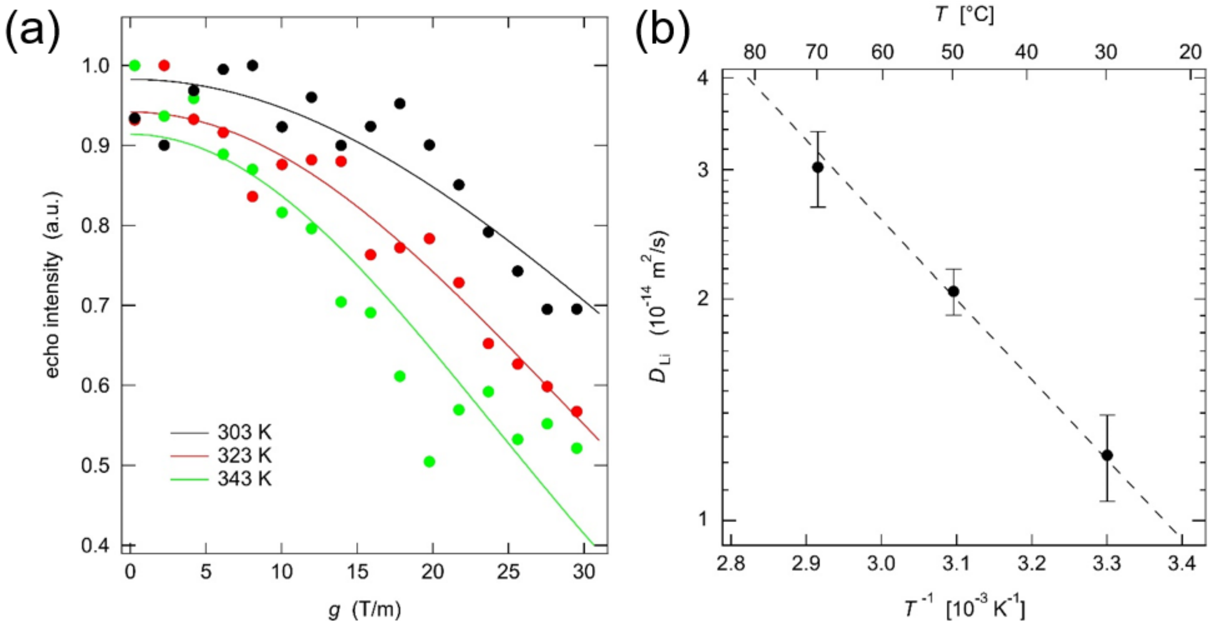

Figure 2.12 ^{7}Li PFG NMR results on $Li_{15}P_4S_{16}Cl_3$. (a) the echo intensity vs gradient field strength for three different temperatures (gradient duration δ = 3 ms, diffusion time Δ = 300 ms). (b) the derived diffusion coefficients vs inverse temperature.

Pulsed field gradient (PFG) NMR experiments were performed to study the long-range transport of Li ions, on the time scale of about one second. The echo damping is shown in Figure 2.12a for three different temperatures. As expected, a stronger echo damping is observed with increasing temperature due to faster Li diffusion. The echo damping as a function of gradient field strength *g* can be well described with a Gaussian function according to the Sejskal-Tanner equation [42] (solid lines in Figure 2.12a). The derived diffusion coefficients are displayed in Figure 2.12b vs inverse temperature. They show an Arrhenius-type behavior with an activation energy of (0.22 ± 0.04) eV. At 298 K, a diffusion coefficient of 10^{-14} m^2/s can be estimated. Assuming an uncorrelated, three-dimensional motion of all Li ions and using the number density of all Li ions (2×10^{28} m^{-3}), this would correspond to a Li ion conductivity of 1.3×10^{-5} S/cm, as derived from the Nernst-Einstein equation. This value is higher than the total conductivity measured with impedance spectroscopy, and also the activation energy derived from PFG NMR is much lower than the 0.57 eV measured with EIS. This might hint at a stronger influence of grain boundaries on the impedance data than on the PFG results that are probing the transport on a time scale of 0.3 s, and thus on a length scale of 0.1 μm. Overall, the NMR results reveal a complex motion of the Li ions involving different types of jump processes, as expected from the crystal structure. The relatively slow dynamics of the Li ions is probably caused by the fully occupied Li(1) and Li(2) sites and the quite dense crystal structure. This provides multiple possibilities for future materials optimization, e.g. via cation and anion doping.

2.3 Summary

$Li_{15}P_4S_{16}Cl_3$, a new crystalline thiophosphate was successfully synthesized for the first time. It is a novel quaternary compound in the Li-P-S-Cl system, in addition to argyrodite Li_6PS_5Cl. The crystal structure of $Li_{15}P_4S_{16}Cl_3$ was identified and confirmed by synchrotron XRD and neutron diffraction. Although the room temperature conductivity of this material is low, which may not have practical use in devices that requires high ionic conductivities such as solid state batteries, evidences in both computational predictions and our ongoing follow-up experiments have shown that the conductivity can be drastically improved by cation or anion doping/replacement in this crystal structure, which shows the value of identification of new compound as the motif structure for solid state ionic conductors. The very low formation temperature (<350 °C) and good thermodynamic stability also imply that it can be a good basic structure for design. In fact, we have tried the synthesis of $Li_{15}P_4S_{16}Br_3$ and $Li_{15}P_4S_{16}I_3$. $Li_{15}P_4S_{16}Br_3$ can also be successfully obtained at a lower temperature, implying abundant possibilities of future materials design, similar to what has been done with argyrodites, which may lead to new ionic conductors with higher conductivity or better stability.

2.4 Method

$Li_{15}P_4S_{16}Cl_3$ was synthesized via a ball-milling and subsequent calcination process. The starting materials Li_2S (99.98%, Sigma-Aldrich), P_2S_5 (99%, Sigma-Aldrich) and LiCl (>99%, Sigma-Aldrich) were weighed in desired molar ratio and mixed in a high energy planetary ball mill (PM 200, Retsch) with using a zirconia jar. 10 zirconia balls of 10 mm diameter were put in each jar. The starting materials are ball-milled for 20 h at a rotation speed of 370 rpm. The ball-milled mixture was then pressed into pellets of ½ inch in diameter and sealed in a quartz tube. The pellets were heated at 360 °C for 20 h and cooled down inside the furnace. The pellets were ground into powder in an agate mortar and kept in an Ar gas filled glove box for the following characterizations. All materials were handled under Argon atmosphere during the synthesis, characterization and electrochemical testing processes.

The X-ray diffraction (XRD) data of the powder samples was first collected by using a D8 Advance X-ray Diffractometer (Bruker AXS) with molybdenum radiation ($\lambda_{K\alpha1}$ = 0.7093 Å). *In situ* XRD data of the synthesis process was also collected with using a heat chamber (HTK1200N, Anton Paar) mounted on the diffractometer as follows. The powder of ball-milled mixture of starting materials was filled in quartz capillary in the glove box and sealed. The tube was used for in situ XRD data collection and heated from room temperature to 440 ^{o}C.. XRD data were collected in a step size of 20 ^{o}C while the temperature was kept constant during each XRD scan.

Synchrotron XRD and pair distribution function (PDF) data were collected at beam line 17-BM-B at the Advanced Photon Source (APS) at Argonne National Laboratory (ANL), with a wavelength of 0.24116 Å. High quality powder neutron diffraction (ND) data were collected on beam line POWGEN at the Spallation Neutron Source (SNS) at Oak Ridge National Laboratory (ORNL) using the frame with a center wavelength of 0.8 Å. Rietveld refinement against the XRD and ND data was performed with using GSAS II and TOPAS (version 6) software [43-44]. The conversion from time-of-flight to d-spacing was done using a 2nd order polynomial function (TOF = d0 + dfc*d + dfa*d^2) calibrated from a NIST Si 640e standard sample. During the refinement, d0 and dfc were fixed to the values refined from Si standard while dfa was allowed to vary to account for the sample displacement. The crystal structure model obtained from the Rietveld refinement was used as the starting model for the analysis of PDF data. The X-ray PDF data was processed with using PDFgetX3 [45]. The total scattering structure factor S(Q) data were Fourier transformed to the PDF with a maximum Q-range (Q_{max}) of 19 $Å^{-1}$. The collected data were corrected for background and sample absorption. PDFgui and TOPAS (version 6) were used for the PDF data analysis [44, 46].

Scanning Electron Microscopy (SEM) images were taken by using a Hitachi SU8010 scanning electron microscope. The sample was transferred from the glove box in well-sealed container to minimize the air exposure.

^{6}Li and ^{31}P magic-angle spinning (MAS) NMR spectroscopy was performed with a Bruker Avance 500 MHz spectrometer. The magnetic field of 11.7 T corresponds to Larmor frequencies of 73.6 for ^{6}Li and 202.5 MHz for ^{31}P. The samples were rotated in 2.5 mm zirconia rotors at a spinning speed of 20 kHz. All spectra were acquired with a Hahn-echo pulse sequence [47]. The chemical shifts were referenced to an aqueous 1M ^{6}LiCl solution for ^{6}Li and to H_3PO_4 (85%) for ^{31}P.

Temperature-dependent measurements of static ^{7}Li NMR line shapes and ^{7}Li spin−lattice relaxation times were performed with a Bruker 200 MHz spectrometer at a magnetic field of 4.7 T, on samples sealed in 10 mm glass vials. These spectra were acquired with a quadrupolar-echo sequence, a π/2 pulse length of about 3 μs, and a recycle delay of 20 s. ^{7}Li T_1 measurements were performed with a saturation-recovery pulse sequence[39, 48]. ^{7}Li pulsed field-gradient (PFG)

NMR measurements were acquired with a stimulated-echo sequence including bipolar gradients, on a Bruker Avance 300 MHz spectrometer operated with a Diff50 probe that provides pulsed field gradients up to 30 T/m [49].

Density functional theory (DFT) calculations were conducted with using the Vienna *Ab initio* Simulation package (VASP)[50] within the projector augmented-wave approach with Perdew-Burke-Ernzerhof (PBE)[51] generalized-gradient approximation (GGA). A*b initio* molecular dynamic (AIMD) simulations were performed to investigate Li diffusion. A Γ-centered *k*-point in the non-spin-polarized DFT calculations were used. The time step was 2 fs. NVT ensemble using Nosé-Hoover thermostat[52] was used. The total time of AIMD simulations were in the range of 100 ps to 600 ps. The ionic conductivity and the error bars were calculated and estimated following previously established methods[53].

Ionic conductivity was determined by electrochemical impedance spectroscopy (EIS) method by an electrochemical impedance analyzer (VMP3, Bio-Logic) and a custom-built electrochemical cell. Typically, ~130 mg $Li_{15}P_4S_{16}Cl_3$ powder was pressed into a pellet with a diameter of ½ inch at a pressure of 100 bars. Two stainless steel rods were used as the current collectors. EIS data were collected in the temperature range of 30 °C to 90 °C at frequencies between 1MHz and 1Hz and with AC amplitude of 500 mV.

2.5 Notes to Chapter 2

This Chapter is based on the paper entitled "$Li_{15}P_4S_{16}Cl_3$, a new lithium chloro-thiophosphate as a solid-state ionic conductor" published in Inorganic Chemistry [54].

2.6 References

[1] Auvergniot, J.; Cassel, A.; Ledeuil, J.-B.; Viallet, V.; Seznec, V.; Dedryvère, R., Interface Stability of Argyrodite Li6PS5Cl toward LiCoO2, LiNi1/3Co1/3Mn1/3O2, and LiMn2O4 in Bulk All-Solid-State Batteries. *Chemistry of Materials* **2017,** *29* (9), 3883-3890.

[2] Auvergniot, J.; Cassel, A.; Foix, D.; Viallet, V.; Seznec, V.; Dedryvère, R., Redox activity of argyrodite Li6PS5Cl electrolyte in all-solid-state Li-ion battery: An XPS study. *Solid State Ionics* **2017,** *300* (Supplement C), 78-85.

[3] Homma, K.; Yonemura, M.; Kobayashi, T.; Nagao, M.; Hirayama, M.; Kanno, R., Crystal structure and phase transitions of the lithium ionic conductor Li3PS4. *Solid State Ionics* **2011,** *182* (1), 53-58.

[4] Murayama, M.; Sonoyama, N.; Yamada, A.; Kanno, R., Material design of new lithium ionic conductor, thio-LISICON, in the Li2S–P2S5 system. *Solid State Ionics* **2004,** *170* (3), 173-180.

[5] de Klerk, N. J. J.; Rosłoń, I.; Wagemaker, M., Diffusion Mechanism of Li Argyrodite Solid Electrolytes for Li-Ion Batteries and Prediction of Optimized Halogen Doping: The Effect of Li Vacancies, Halogens, and Halogen Disorder. *Chemistry of Materials* **2016,** *28* (21), 7955-7963.

[6] Sedlmaier, S. J.; Indris, S.; Dietrich, C.; Yavuz, M.; Dräger, C.; von Seggern, F.; Sommer, H.; Janek, J., Li4PS4I: A Li+ Superionic Conductor Synthesized by a Solvent-Based Soft Chemistry Approach. *Chemistry of Materials* **2017,** *29* (4), 1830-1835.

[7] Liu, X.; Chen, Y.; Hood, Z. D.; Ma, C.; Yu, S.; Sharafi, A.; Wang, H.; An, K.; Sakamoto, J.; Siegel, D. J.; Cheng, Y.; Jalarvo, N. H.; Chi, M., Elucidating the mobility of H+ and Li+ ions in (Li6.25−xHxAl0.25)La3Zr2O12 via correlative neutron and electron spectroscopy. *Energy & Environmental Science* **2019**.

[8] Hood, Z. D.; Wang, H.; Samuthira Pandian, A.; Keum, J. K.; Liang, C., Li2OHCl Crystalline Electrolyte for Stable Metallic Lithium Anodes. *Journal of the American Chemical Society* **2016,** *138* (6), 1768-1771.

[9] Deng, Y.; Eames, C.; Nguyen, L. H. B.; Pecher, O.; Griffith, K. J.; Courty, M.; Fleutot, B.; Chotard, J.-N.; Grey, C. P.; Islam, M. S.; Masquelier, C., Crystal Structures, Local Atomic Environments, and Ion Diffusion Mechanisms of Scandium-Substituted Sodium Superionic Conductor (NASICON) Solid Electrolytes. *Chemistry of Materials* **2018,** *30* (8), 2618-2630.

[10] Suzuki, N.; Richards, W. D.; Wang, Y.; Miara, L. J.; Kim, J. C.; Jung, I.-S.; Tsujimura, T.; Ceder, G., Synthesis and Electrochemical Properties of I$\bar{4}$-Type Li1+2xZn1–xPS4 Solid Electrolyte. *Chemistry of Materials* **2018,** *30* (7), 2236-2244.

[11] Kaup, K.; Lalère, F.; Huq, A.; Shyamsunder, A.; Adermann, T.; Hartmann, P.; Nazar, L. F., Correlation of Structure and Fast Ion Conductivity in the Solid Solution Series Li1+2xZn1–xPS4. *Chemistry of Materials* **2018,** *30* (3), 592-596.

[12] Aihara, Y.; Ito, S.; Omoda, R.; Yamada, T.; Fujiki, S.; Watanabe, T.; Park, Y.; Doo, S., The Electrochemical Characteristics and Applicability of an Amorphous Sulfide-Based Solid Ion Conductor for the Next-Generation Solid-State Lithium Secondary Batteries. *Frontiers in Energy Research* **2016,** *4* (18).

[13] Miara, L.; Windmüller, A.; Tsai, C.-L.; Richards, W. D.; Ma, Q.; Uhlenbruck, S.; Guillon, O.; Ceder, G., About the Compatibility between High Voltage Spinel Cathode Materials and Solid Oxide Electrolytes as a Function of Temperature. *ACS Applied Materials & Interfaces* **2016,** *8* (40), 26842-26850.

[14] Uhlenbruck, S.; Dornseiffer, J.; Lobe, S.; Dellen, C.; Tsai, C.-L.; Gotzen, B.; Sebold, D.; Finsterbusch, M.; Guillon, O., Cathode-electrolyte material interactions during manufacturing of inorganic solid-state lithium batteries. *Journal of Electroceramics* **2017,** *38* (2), 197-206.

[15] Hayashi, A.; Sakuda, A.; Tatsumisago, M., Development of Sulfide Solid Electrolytes and Interface Formation Processes for Bulk-Type All-Solid-State Li and Na Batteries. *Frontiers in Energy Research* **2016,** *4* (25).

[16] Knauth, P., Inorganic solid Li ion conductors: An overview. *Solid State Ionics* **2009,** *180* (14), 911-916.

[17] Park, K. H.; Bai, Q.; Kim, D. H.; Oh, D. Y.; Zhu, Y.; Mo, Y.; Jung, Y. S., Design Strategies, Practical Considerations, and New Solution Processes of Sulfide Solid Electrolytes for All-Solid-State Batteries. *Advanced Energy Materials* **2018,** *8* (18), 1800035.

[18] Xiong, S.; Liu, Z.; Rong, H.; Wang, H.; McDaniel, M.; Chen, H., Na3SbSe4−xSxas Sodium Superionic Conductors. *Scientific Reports* **2018,** *8* (1), 9146.

[19] Kanno, R.; Murayama , M., Lithium Ionic Conductor Thio-LISICON: The Li2 S - GeS2 - P 2 S 5 System. *Journal of The Electrochemical Society* **2001,** *148* (7), A742-A746.

[20] Yu, C.; Ganapathy, S.; van Eck, E. R. H.; van Eijck, L.; Basak, S.; Liu, Y.; Zhang, L.; Zandbergen, H.; Wagemaker, M., Revealing the relation between the structure, Li-ion conductivity and solid-state battery performance of the argyrodite Li6PS5Br solid electrolyte. *Journal of Materials Chemistry A* **2017**.

[21] Deiseroth, H.-J.; Maier, J.; Weichert, K.; Nickel, V.; Kong, S.-T.; Reiner, C., Li7PS6 and Li6PS5X (X: Cl, Br, I): Possible Three-dimensional Diffusion Pathways for Lithium Ions and Temperature Dependence of the Ionic Conductivity by Impedance Measurements. *Zeitschrift für anorganische und allgemeine Chemie* **2011,** *637* (10), 1287-1294.

[22] Rao, R. P.; Adams, S., Studies of lithium argyrodite solid electrolytes for all-solid-state batteries. *physica status solidi (a)* **2011,** *208* (8), 1804-1807.

[23] Ziolkowska, D. A.; Arnold, W.; Druffel, T.; Sunkara, M.; Wang, H., Rapid and Economic Synthesis of a Li7PS6 Solid Electrolyte from a Liquid Approach. *ACS Applied Materials & Interfaces* **2019,** *11* (6), 6015-6021.

[24] Yamane, H.; Shibata, M.; Shimane, Y.; Junke, T.; Seino, Y.; Adams, S.; Minami, K.; Hayashi, A.; Tatsumisago, M., Crystal structure of a superionic conductor, Li7P3S11. *Solid State Ionics* **2007,** *178* (15), 1163-1167.

[25] Kamaya, N.; Homma, K.; Yamakawa, Y.; Hirayama, M.; Kanno, R.; Yonemura, M.; Kamiyama, T.; Kato, Y.; Hama, S.; Kawamoto, K.; Mitsui, A., A lithium superionic conductor. *Nat Mater* **2011,** *10* (9), 682-686.

[26] Brant, J. A.; Massi, D. M.; Holzwarth, N. A. W.; MacNeil, J. H.; Douvalis, A. P.; Bakas, T.; Martin, S. W.; Gross, M. D.; Aitken, J. A., Fast Lithium Ion Conduction in Li2SnS3: Synthesis, Physicochemical Characterization, and Electronic Structure. *Chemistry of Materials* **2015,** *27* (1), 189-196.

[27] Kraft, M. A.; Culver, S. P.; Calderon, M.; Böcher, F.; Krauskopf, T.; Senyshyn, A.; Dietrich, C.; Zevalkink, A.; Janek, J.; Zeier, W. G., Influence of Lattice Polarizability on the Ionic Conductivity in the Lithium Superionic Argyrodites Li6PS5X (X = Cl, Br, I). *Journal of the American Chemical Society* **2017,** *139* (31), 10909-10918.

[28] Kraft, M. A.; Ohno, S.; Zinkevich, T.; Koerver, R.; Culver, S. P.; Fuchs, T.; Senyshyn, A.; Indris, S.; Morgan, B. J.; Zeier, W. G., Inducing High Ionic Conductivity in the Lithium Superionic Argyrodites Li6+xP1–xGexS5I for All-Solid-State Batteries. *Journal of the American Chemical Society* **2018,** *140* (47), 16330-16339.

[29] Zhu, Z.; Chu, I.-H.; Ong, S. P., Li3Y(PS4)2 and Li5PS4Cl2: New Lithium Superionic Conductors Predicted from Silver Thiophosphates using Efficiently Tiered Ab Initio Molecular Dynamics Simulations. *Chemistry of Materials* **2017,** *29* (6), 2474-2484.

[30] Haomin, C. Computational design of inorganic ionic conductors. Thesis, National University of Singapore, ScholarBank@NUS Repository, 2017.

[31] Wang, Y.; Lu, D.; Bowden, M.; El Khoury, P. Z.; Han, K. S.; Deng, Z. D.; Xiao, J.; Zhang, J.-G.; Liu, J., Mechanism of Formation of Li7P3S11 Solid Electrolytes through Liquid Phase Synthesis. *Chemistry of Materials* **2018,** *30* (3), 990-997.

[32] Holzwarth, N. A. W.; Lepley, N. D.; Du, Y. A., Computer modeling of lithium phosphate and thiophosphate electrolyte materials. *Journal of Power Sources* **2011,** *196* (16), 6870-6876.

[33] Deng, Z.; Zhu, Z.; Chu, I.-H.; Ong, S. P., Data-Driven First-Principles Methods for the Study and Design of Alkali Superionic Conductors. *Chemistry of Materials* **2017,** *29* (1), 281-288.

[34] Dietrich, C.; Weber, D. A.; Culver, S.; Senyshyn, A.; Sedlmaier, S. J.; Indris, S.; Janek, J.; Zeier, W. G., Synthesis, Structural Characterization, and Lithium Ion Conductivity of the Lithium Thiophosphate Li2P2S6. *Inorganic Chemistry* **2017,** *56* (11), 6681-6687.

[35] Dietrich, C.; Sadowski, M.; Sicolo, S.; Weber, D. A.; Sedlmaier, S. J.; Weldert, K. S.; Indris, S.; Albe, K.; Janek, J.; Zeier, W. G., Local Structural Investigations, Defect Formation, and Ionic Conductivity of the Lithium Ionic Conductor Li4P2S6. *Chemistry of Materials* **2016,** *28* (23), 8764-8773.

[36] Jörgens, S.; Mewis, A., Ag5PS4Cl2 and Ag15(PS4)4Cl3 – Crystal structures and their relation to Ag3PS4. *Solid State Sciences* **2007,** *9* (2), 213-217.

[37] Shannon, R., Revised effective ionic radii and systematic studies of interatomic distances in halides and chalcogenides. *Acta Crystallographica Section A* **1976,** *32* (5), 751-767.

[38] Seino, Y.; Ota, T.; Takada, K.; Hayashi, A.; Tatsumisago, M., A sulphide lithium super ion conductor is superior to liquid ion conductors for use in rechargeable batteries. *Energy & Environmental Science* **2014,** *7* (2), 627-631.

[39] Paul Heitjans; Sylvio Indris; Wilkening, M., Solid-State Diffusion and NMR. *Diffusion Fundamentals* **2005,** *2* (45), 1-20.

[40] Vinod Chandran, C.; Pristat, S.; Witt, E.; Tietz, F.; Heitjans, P., Solid-State NMR Investigations on the Structure and Dynamics of the Ionic Conductor Li1+xAlxTi2–x(PO4)3 (0.0 ≤ x ≤ 1.0). *The Journal of Physical Chemistry C* **2016,** *120* (16), 8436-8442.

[41] Wilkening, M.; Heitjans, P., Li jump process in h-Li0.7TiS2 studied by two-time 7Li spin-alignment echo NMR and comparison with results on two-dimensional diffusion from nuclear magnetic relaxation. *Physical Review B* **2008,** *77* (2), 024311.

[42] Stejskal, E. O.; Tanner, J. E., Spin Diffusion Measurements: Spin Echoes in the Presence of a Time-Dependent Field Gradient. *The Journal of Chemical Physics* **1965,** *42* (1), 288-292.

[43] Toby, B. H.; Von Dreele, R. B., GSAS-II: the genesis of a modern open-source all purpose crystallography software package. *Journal of Applied Crystallography* **2013,** *46* (2), 544-549.

[44] Perl, J.; Shin, J.; Schümann, J.; Faddegon, B.; Paganetti, H., TOPAS: An innovative proton Monte Carlo platform for research and clinical applications. *Medical Physics* **2012,** *39* (11), 6818-6837.

[45] Juhas, P.; Davis, T.; Farrow, C. L.; Billinge, S. J. L., PDFgetX3: a rapid and highly automatable program for processing powder diffraction data into total scattering pair distribution functions. *Journal of Applied Crystallography* **2013,** *46* (2), 560-566.

[46] Farrow, C. L.; Juhas, P.; Liu, J. W.; Bryndin, D.; Božin, E. S.; Bloch, J.; Th, P.; Billinge, S. J. L., PDFfit2 and PDFgui: computer programs for studying nanostructure in crystals. *Journal of Physics: Condensed Matter* **2007,** *19* (33), 335219.

[47] Duer, M. J., *Introduction to Solid-State NMR Spectroscopy*. Blackwell Publishing: Oxford: 2004.

[48] Fukushima, E.; Roeder, S. B. W., *Experimental Pulse NMR – A Nuts and Bolts Approach*. Addison-Wesley: Reading: 1981.

[49] Price, W. S., Pulsed-field gradient nuclear magnetic resonance as a tool for studying translational diffusion: Part 1. Basic theory. *Concepts in Magnetic Resonance* **1997,** *9* (5), 299-336.

[50] Kresse, G.; Furthmüller, J., Efficient iterative schemes for ab initio total-energy calculations using a plane-wave basis set. *Physical Review B* **1996,** *54* (16), 11169-11186.

[51] Perdew, J. P.; Ernzerhof, M.; Burke, K., Rationale for mixing exact exchange with density functional approximations. *J. Chem. Phys.* **1996,** *105* (22), 9982–9985.

[52] Nose, S., Constant temperature molecular dynamics methods. *Prog. Theor. Phys. Suppl.* **1991,** *103*, 1–46.

[53] He, X.; Zhu, Y.; Epstein, A.; Mo, Y., Statistical variances of diffusional properties from ab initio molecular dynamics simulations. *npj Computational Materials* **2018,** *4* (1), 18.

[54] Liu, Z.; Zinkevich, T.; Indris, S.; He, X.; Liu, J.; Xu, W.; Bai, J.; Xiong, S.; Mo, Y.; Chen, H., Li15P4S16Cl3, a Lithium Chlorothiophosphate as a Solid-State Ionic Conductor. *Inorganic Chemistry* **2020,** *59* (1), 226-234.

CHAPTER 3. Exploring Aliovalent Substitutions in Lthium Chloro-Thiophosphate $Li_{15}P_4S_{16}Cl_3$

3.1 Introduction

All-solid-state lithium ion batteries (ALSOLIBs) are emerging next generation energy storage technology [1] and their performance of ASOLIBs is majorly limited by the ionic conductivity and related properties of solid electrolytes (SEs). Currently, three kinds of inorganic SEs are widely studied: oxide, halide and sulfide SEs. Among them, sulfides SEs show advantages in terms of ionic conductivity and favorable mechanical properties, such as formability, processability and elastic modulus [2-3]. Oxide SEs with perovskite, NASICON and garnet structures exhibit ionic conductivity in the range 10^{-4}~10^{-3} S/cm [4-6], but they generally show large grain boundary resistance and high temperature sintering process is needed. Halide and sulfide SEs are ductile and the grain boundary resistance can be easily reduced by simple room-temperature pressing [7-9], while the ionic conductivity of halide SEs is not as high as that of best reported sulfide SEs [10-12].

Since the report of thio-lithium super ionic conductor (LISICON) in 2001 [13], crystalline sulfide SEs are extensively studied in the Li_2S-P_2S_5 system. $Li_2P_2S_6$ (1Li_2S-1P_2S_5), $Li_7P_3S_{11}$ (7Li_2S-3P_2S_5), Li_3PS_4 (3Li_2S-1P_2S_5) and Li_7PS_6 (7Li_2S-1P_2S_5) are typical crystalline compound in Li_2S-P_2S_5 system [14-17]. From $Li_2P_2S_6$ to Li_7PS_6, the lithium ions content increased gradually. However, the ionic conductivity is not simply positive or negative correlated, which revealed that crystal structures have a significant influence on the lithium diffusion process. In order to boost the ionic conductivity of compound with known crystal structure, aliovalent atoms doping is a commonly used method to tune the Li^+ ions or vacancy density. For example, Kanno et al. used substitution $Ge^{4+} + Li^+ \rightarrow P^{5+}$ in Li_3PS_4 and obtained the $Li_{4-x}Ge_{1-x}P_xS_4$ solid solution [13] with similar structure to γ-Li_3PO_4 [13] and the ionic conductivity was boosted to 2.2×10^{-3} S/cm at 25 ^{o}C, while the pure ionic conductivity of γ-Li_3PS_4 is only 3×10^{-7} S/cm at room temperature [15]. Inspired by this phenomenon, Kanno group expands their search for new crystalline lithium ion conductors in Li_2S-GeS_2-P_2S_5 system and reported compounds with high ionic conductivity such as $Li_{10}GeP_2S_{12}$ ($\sigma=1.2\times10^{-2}$ S/cm) and $Li_7Ge_3PS_{12}$ ($\sigma=1.1\times10^{-4}$ S/cm) [18-19].

Another promising family of sulfide lithium ion conductor is lithium argyrodites Li_6PS_5X (X=Cl, Br) [20]. Li_6PS_5Cl ($5Li_2S$-$1P_2S_5$-2LiCl) is a crystalline compound with high ionic conductivity over 10^{-3} S/cm in Li_2S-P_2S_5-LiCl system. However, there is still large area unexplored in this ternary system, which provides high potential to find new prototypes of Li-ion conducting crystal structure. Recently, our group successfully synthesized and identified a new lithium chloro-thiophosphate in Li_2S-P_2S_5-LiCl system: $Li_{15}P_4S_{16}Cl_3$ [21]. However, it exhibits low ionic conductivity at room temperature with high activation energy. In order to trigger high ionic conductivity in this crystal structure, here we designed and successfully synthesized a series of solid solution $Li_{15+x}Ge_xP_{4-x}S_{16}Cl_3$ and the influence of Ge doping on the crystal structure is examined by synchrotron and neutron diffraction. The ionic conductivity is increased with more Ge doping content and we attribute such increase in ionic conductivity is owing to the created interstitial Li^+ sites and vacancies in originally fully occupied Li sites. The Li^+ diffusion behavior of $Li_{15+x}Ge_xP_{4-x}S_{16}Cl_3$ is examined experimentally by using electrochemical impedance spectroscopy (EIS) and further studied by A*b initio* molecular dynamic (AIMD) simulations.

3.2 Results and Discussion

The crystal structure of $Li_{15}P_4S_{16}Cl_3$ is shown in Figure 3.1a, representing the cubic unit cell in the $I\bar{4}3d$ space group [21]. The backbone is built up by PS_4 groups centered at 16c sites, with Cl occupying 12b site. There are two types of Li sites existing in $Li_{15}P_4S_{16}Cl_3$: Li1 site is tetrahedrally coordinated by 3 S and 1 Cl and Li2 site is surrounded by 4 S. In one formula $Li_{15}P_4S_{16}Cl_3$, there are 12 Li1 sites and 3 Li2 sites and both sites are fully occupied, leading to a poor ionic conductivity. Besides Li1 and Li2 sites, there are another two types of interstitial sites which can accommodate Li ions. In $Li_{15}P_4S_{16}Cl_3$, Li2 sites are tetrahedrally coordinated by 4 octahedral interstices, which are coordinated by 5 S and 1 Cl (Figure 3.1b). Here, we name the octahedral interstices Li3 sites and it is close to Li2 site by 2.2 Å. There are 12 Li3 sites in a formula of $Li_{15}P_4S_{16}Cl_3$. The other sites which can accommodate Li ions are tetrahedrally coordinated by 4 S. Here, we call them Li4 sites and each Li4 site is connected with two Li1 sites through shared face. The distance between Li1 and Li4 site is 2.0 Å and there are 6 Li4 sites in a formula of $Li_{15}P_4S_{16}Cl_3$.

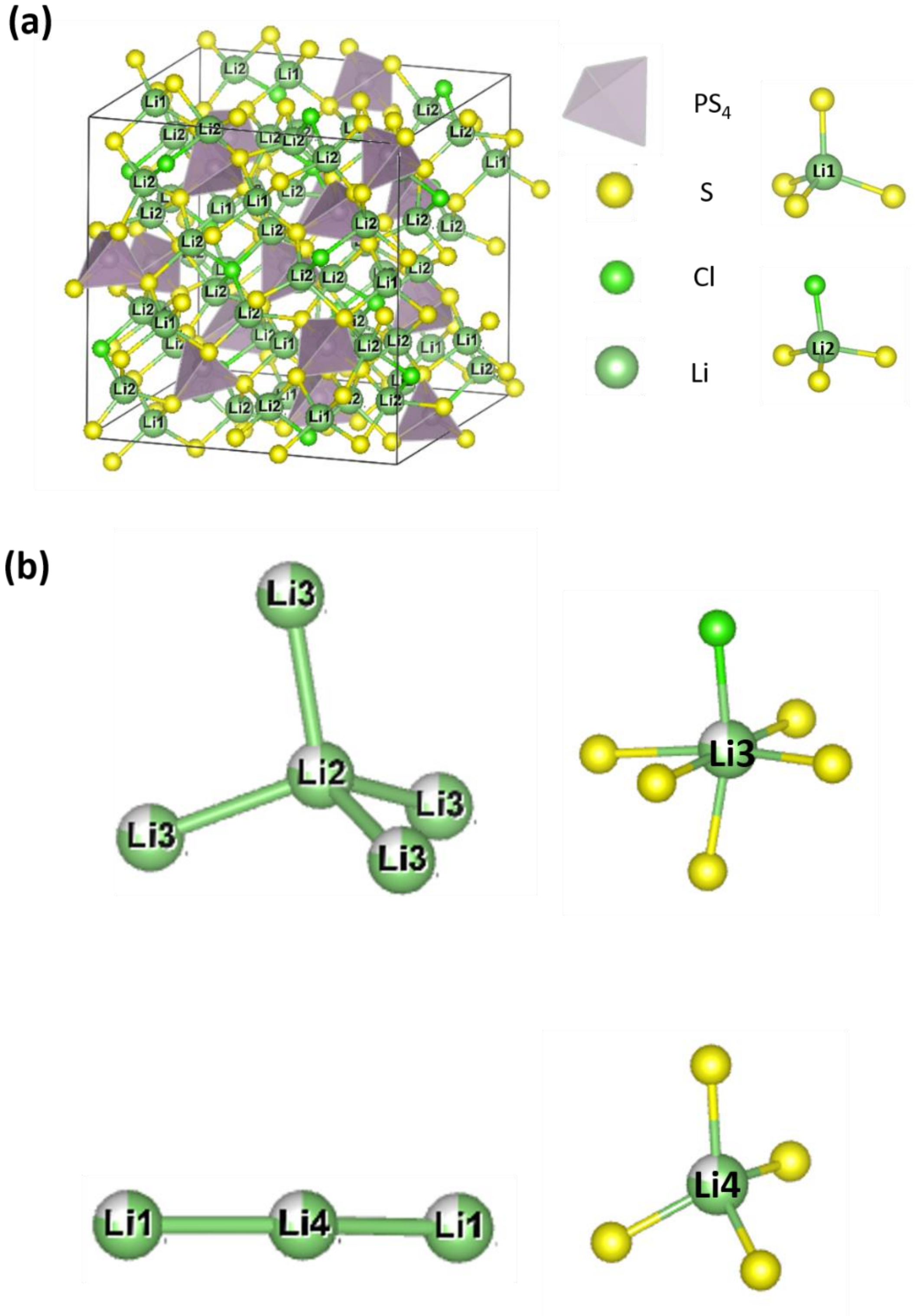

Figure 3.1 (a) Crystal structure of $Li_{15}P_4S_{16}Cl_3$. (b) There are two new Li sites: Li3 is octahedral site and Li4 is tetrahedral site.

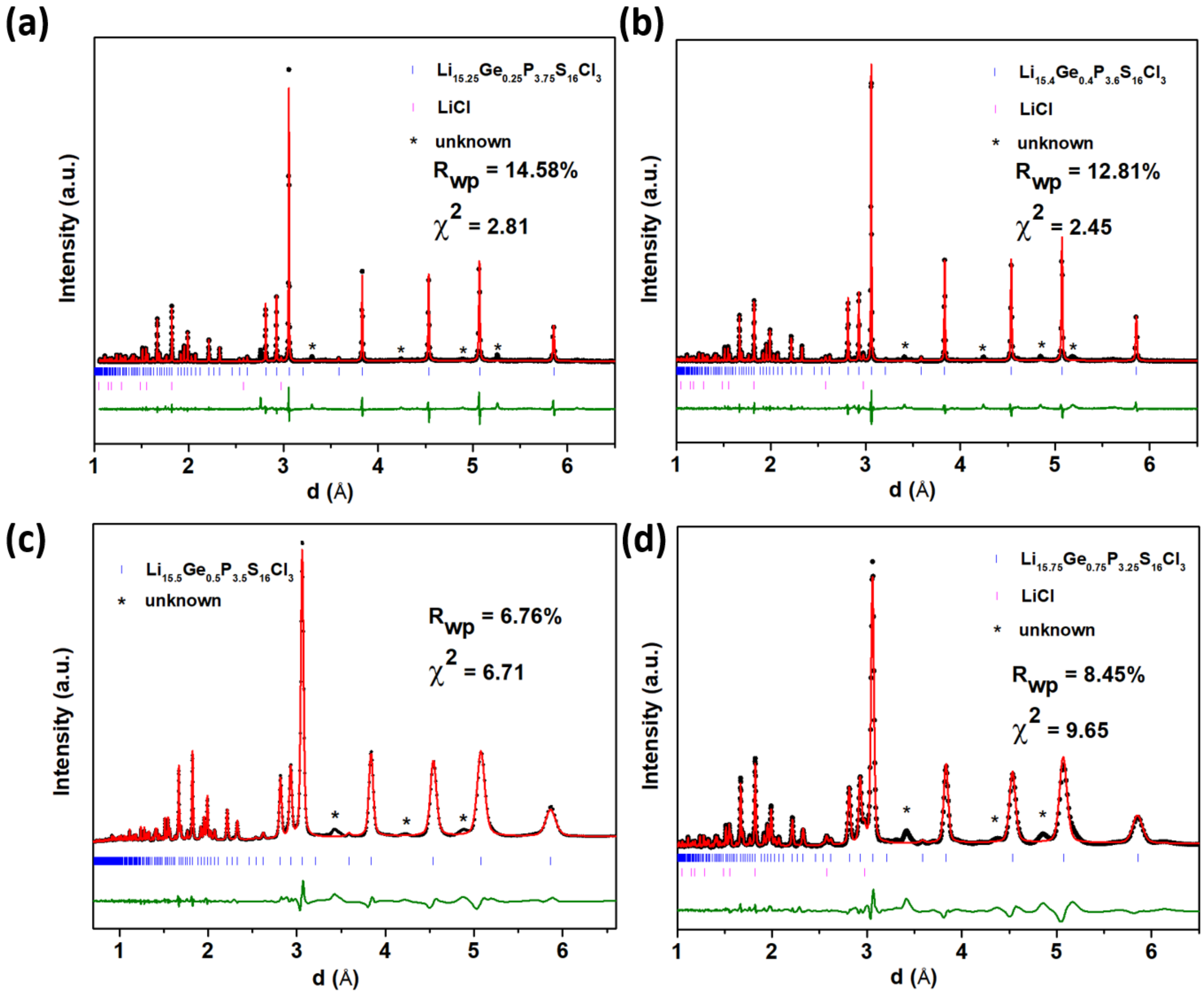

Figure 3.2 Rietveld refinement results of (a) Li $_{15.25}Ge_{0.25}P_{3.75}S_{16}Cl_3$, (b) $Li_{15.4}Ge_{0.4}P_{3.6}S_{16}Cl_3$, (c) $Li_{15.5}Ge_{0.5}P_{3.5}S_{16}Cl_3$ and (d) $Li_{15.75}Ge_{0.75}P_{3.25}S_{16}Cl_3$ against synchrotron diffraction data.

Although in original $Li_{15}P_4S_{16}Cl_3$ structure Li1 and Li2 are fully occupied, the two empty interstitial sites offer the possibility to insert extra Li ions into the crystal structure to improve the ionic conductivity. This can be realized by using aliovalent doping strategy and tetravalent Ge^{4+} is chosen to replace pentavalent P^{5+} for higher Li ions density. The targeted composition $Li_{15+x}Ge_xP_{4-x}S_{16}Cl_3$ (x = 0.25, 0.4, 0.5, 0.75) were synthesized and their crystal structures are characterized by using synchrotron diffraction. The Rietveld refinement against synchrotron diffraction data of $Li_{15+x}Ge_xP_{4-x}S_{16}Cl_3$ are shown in Figure 3.2. The diffraction patterns of $Li_{15+x}Ge_xP_{4-x}S_{16}Cl_3$

samples can all be indexed to the $I\bar{4}3d$ space group. Ge^{4+} are all assigned to share the same sites with P^{5+} during refinement. The lattice parameters show a linear increasing trend along with increasing Ge^{4+} content up to x = 0.5, indicating successful formation of solid solution (Figure 3.3). The expanded lattice parameters are due to the larger ionic radius of Ge^{4+} (0.39 Å) relative to P^{5+} (0.17 Å) [22-23] and extra inserted Li ions. In addition, the volume of $(Ge/P)S_4$ tetrahedra in $Li_{15.5}Ge_{0.5}P_{3.5}S_{16}Cl_3$ is slightly larger than that in $Li_{15}P_4S_{16}Cl_3$ (4.5230 Å^3 vs. 4.4864 Å^3), which is also in consistency with the difference in radius between Ge^{4+} and P^{5+}. The $Li_{15}P_4S_{16}Cl_3$ structure is still hold when x is further increased to 0.75, but no further expansion in lattice parameter can be observed, along with increase in peaks intensity for unknown impurity, which indicates the solid solution limit is already reached at x = 0.5.

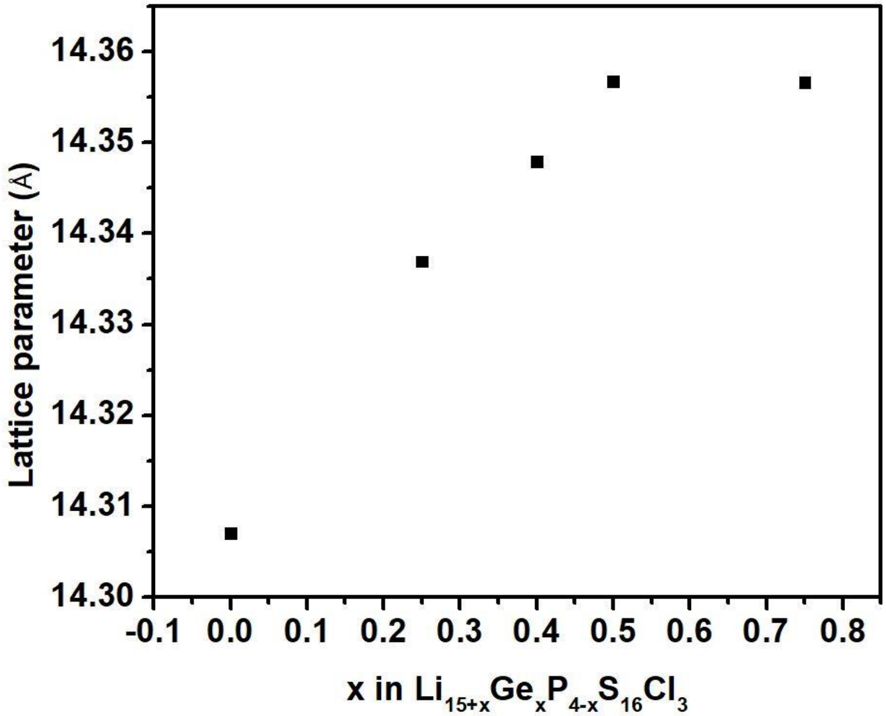

Figure 3.3 Lattice parameters obtained from $Li_{15+x}Ge_xP_{4-x}S_{16}Cl_3$ (x=0, 0.25, 0.4, 0.5, 0.75) Rietveld refinement against synchrotron diffraction data.

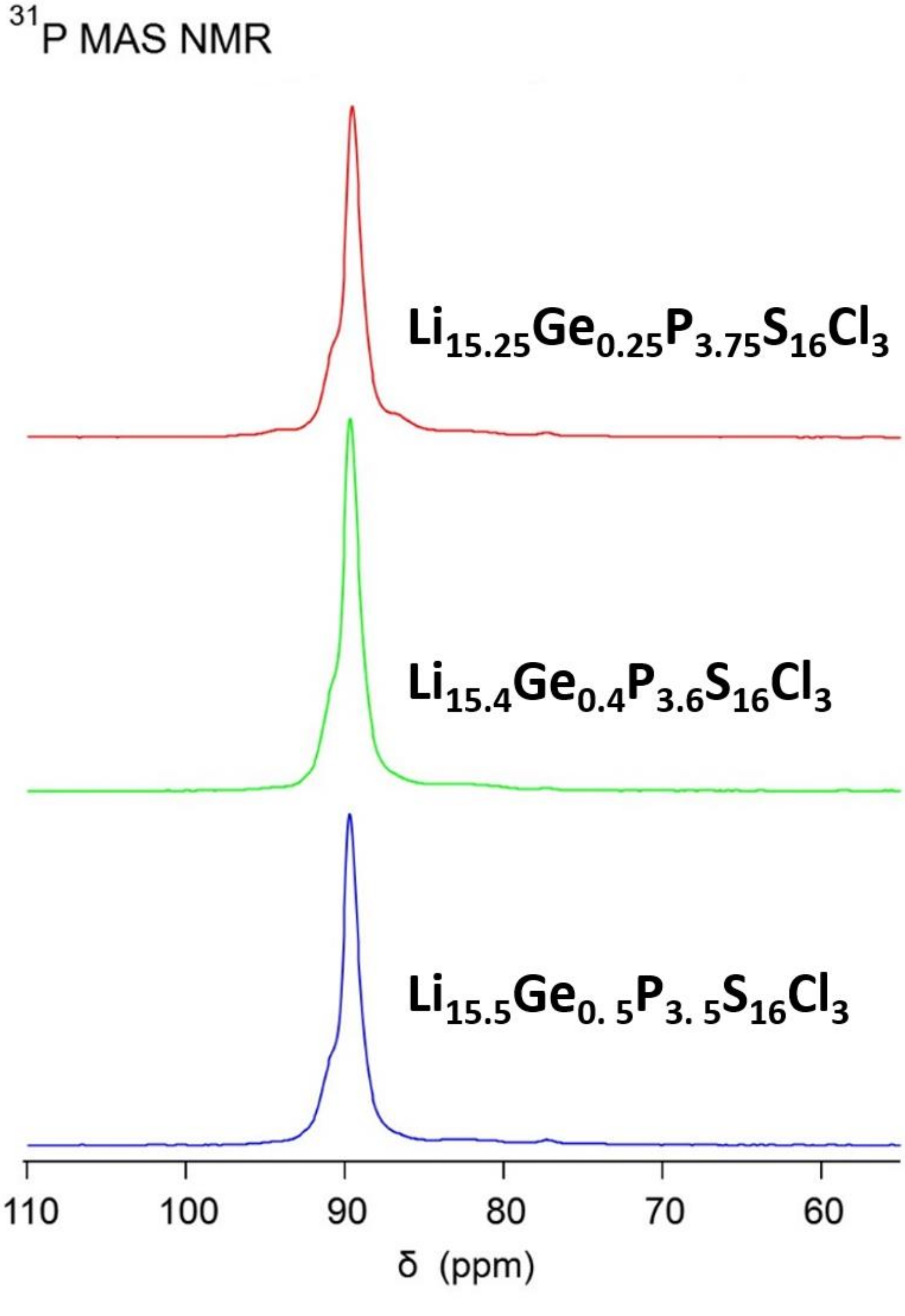

Figure 3.4 ^{31}P MAS NMR of $Li_{15+x}Ge_xP_{4-x}S_{16}Cl_3$ (x = 0.25, 0.4, 0.5)

^{31}P magic-angle spinning (MAS) nuclear magnetic resonance (NMR) shows that $Li_{15+x}Ge_xP_{4-x}S_{16}Cl_3$ exhibits a strong resonance peak at 88.8 ppm, similar to pure $Li_{15}P_4S_{16}Cl_3$ [21]. In addition, the peak from amorphous phase at 85.7 ppm in $Li_{15}P_4S_{16}Cl_3$ ^{31}P MAS NMR does not appear in $Li_{15+x}Ge_xP_{4-x}S_{16}Cl_3$ samples. Instead, a small shoulder at ~91 ppm emerges, which may come from the unidentified impurity phase or amorphous $Li_{15+x}Ge_xP_{4-x}S_{16}Cl_3$.

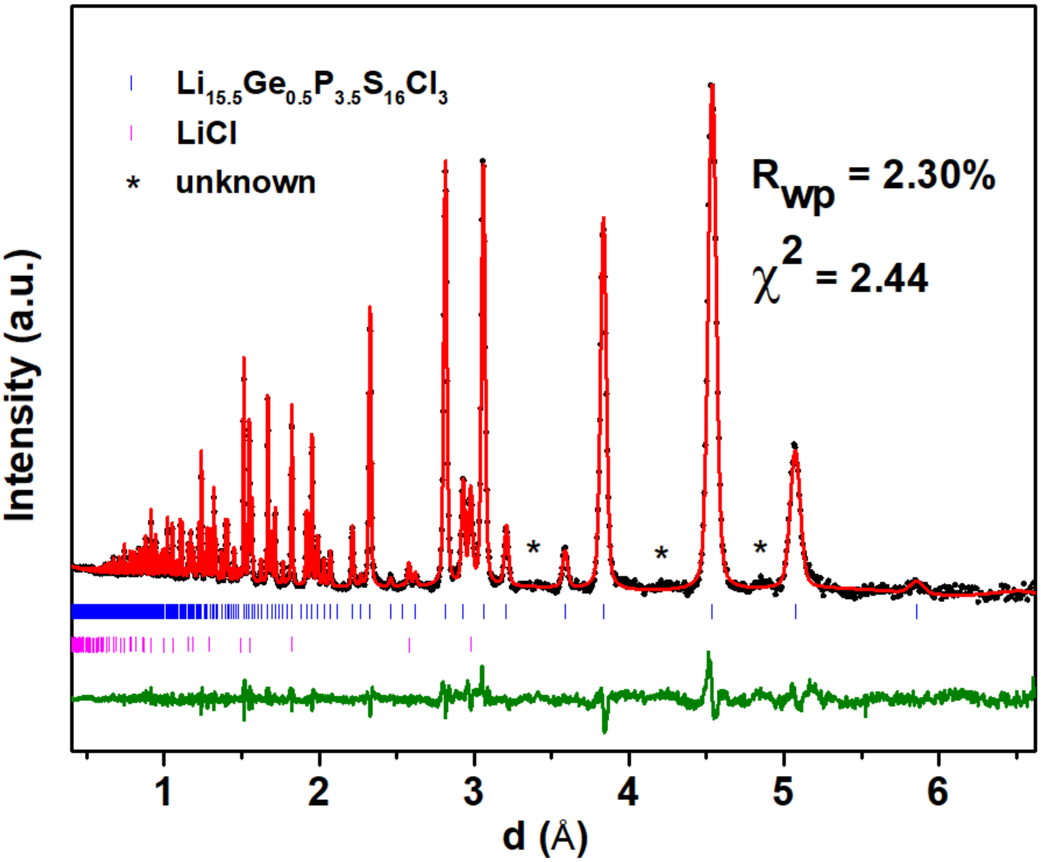

Figure 3.5 Rieveld refinement results of $Li_{15.5}Ge_{0.5}P_{3.5}S_{16}Cl_3$ against neutron diffraction patterns.

To identify the extra inserted Li ions positions, a room temperature neutron diffraction patterns of $Li_{15.5}Ge_{0.5}P_{3.5}S_{16}Cl_3$ was collected (Figure. 3.5). The extra Li occupied sites cannot be identified from the difference Fourier map generated from neutron diffraction of

$Li_{15.5}Ge_{0.5}P_{3.5}S_{16}Cl_3$ since the population of extra inserted Li ion is low. Both Li3 and Li4 sites were attempted in $Li_{15}P_4S_{16}Cl_3$ model and Rietveld refinement results suggested that the inserted Li ions are all located in the Li4 tetrahedral sites rather than the Li3 octahedral sites. In addition, due to the close distance between Li1 and Li4 sites (2.0 Å), the big electrostatic repulsion between Li ions leads to vacancies formation at Li1 sites, which is beneficial for better Li diffusion. The crystallographic information extracted from neutron diffraction is listed in Table 3.1.

Table 3.1 Refined structure of $Li_{15.5}Ge_{0.5}P_{3.5}S_{16}Cl_3$ using neutron diffraction data.

S.G. *I*-43d a = 14.3499(0) Å

Site	Wyck.	X	y	z	Occ.	U_{iso} (Å^2)
Li(2)	12a	0.00000	0.25000	0.37500	1	0.028(2)
Li(1)	48e	0.1424(7)	0.2146(5)	0.5839(7)	0.98(3)	0.036(0)
Li(4)	24d	0.00000	0.25000	0.17671	0.11(7)	0.030(5)
S(1)	16c	0.0315(5)	0.0315(5)	0.0315(5)	1	0.014(7)
S(2)	48e	0.1076(5)	0.3432(6)	0.4724(5)	1	0.018(0)
Cl(1)	12b	0.00000	0.25000	0.87500	1	0.030(1)
P(1)	16c	0.1997(1)	0.1997(1)	0.1997(1)	0.875	0.017(4)
Ge(1)	16c	0.1997(1)	0.1997(1)	0.1997(1)	0.125	0.031(0)

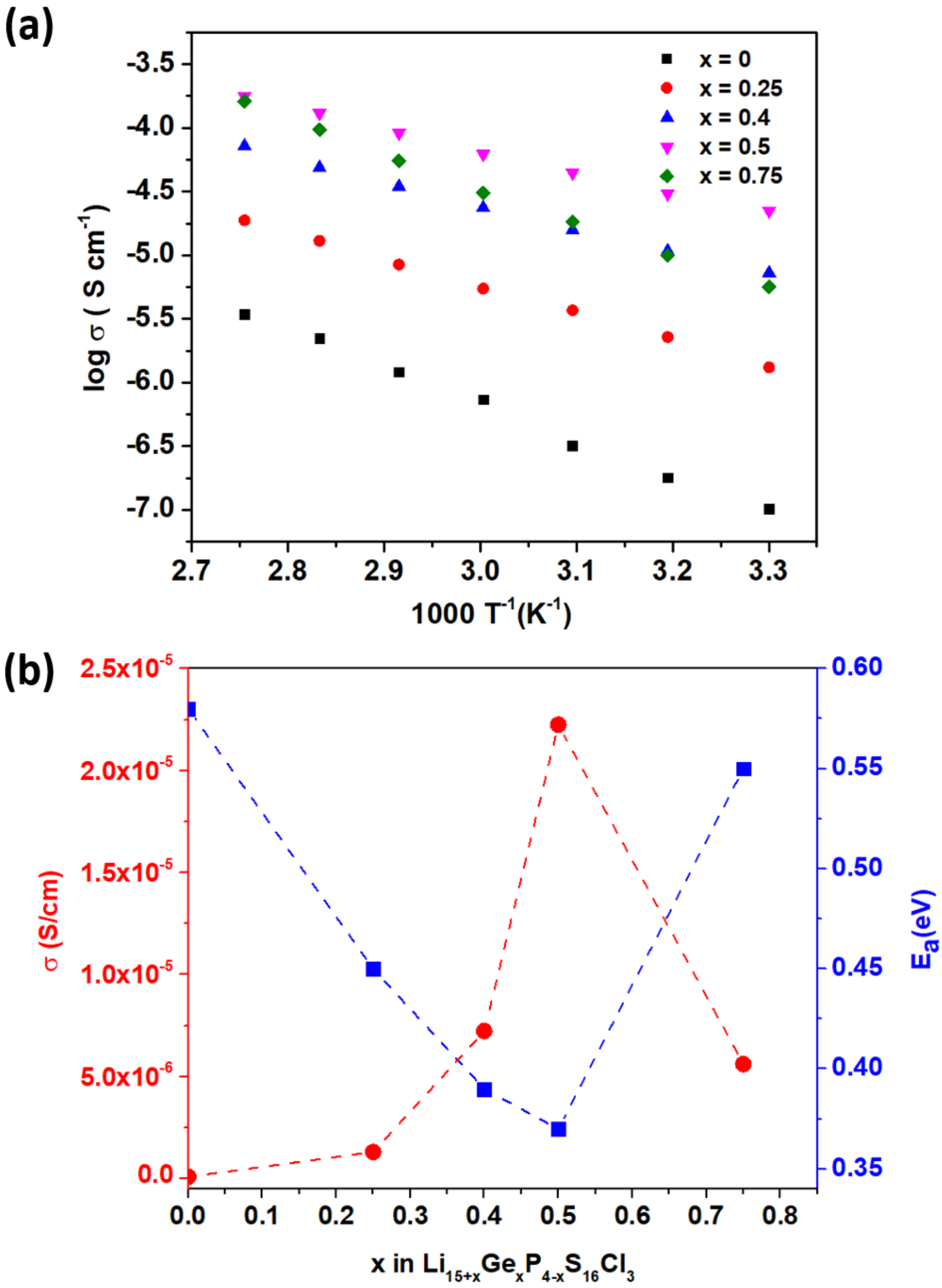

Figure 3.6 (a) Arrhenius plot of $Li_{15+x}Ge_xP_{4-x}S_{16}Cl_3$; (b) conductivity and activation energy for $Li_{15+x}Ge_xP_{4-x}S_{16}Cl_3$ obtained from fitting.

Temperature-dependent electrochemical impedance spectroscopy was performed to assess the influence of Ge doping on ionic conductivity. Figure 3.6a shows the Arrhenius plots of $Li_{15+x}Ge_xP_{4-x}S_{16}Cl_3$. With increased Li^+ and Ge^{4+} contents, the conductivities of $Li_{15+x}Ge_xP_{4-x}S_{16}Cl_3$ are enhanced along with decreased activation energy when x is smaller than 0.5 (Figure 3.6b). At x = 0.5, the ionic conductivity reached the highest value of 2.2×10^{-5} S cm^{-1} at 30 ^oC and lowest activation energy of 0.37 eV. Further increasing the x to 0.75 lowers the ionic conductivity and the activation energy of $Li_{15.75}Ge_{0.75}P_{3.25}S_{16}Cl_3$ is much higher than $Li_{15.5}Ge_{0.5}P_{3.5}S_{16}Cl_3$ (0.55 eV vs. 0.37 eV), which may be caused by the impurity phase.

Moreover, first-principles calculation was performed to further reveal the diffusion mechanism and evaluate the influence of Ge^{4+} doping on ionic conductivity. In original $Li_{15}P_4S_{16}Cl_3$ structure without Ge^{4+} doping, Li1 and Li2 sites are fully occupied (a fully ordered status). Ab initio molecular dynamics (AIMD) simulation results suggested that there is an order-disorder transition near 900 K (Figure 3.7). Below 900 K, the lithium diffusion coefficients D exhibit a high activation energy of 1.32 eV and the extrapolated conductivity at 300 K is as low as 10^{-11} mS/cm. The big difference between theoretical calculation and experimental measured results of pure $Li_{15}P_4S_{16}Cl_3$ may come from the existence of amorphous phase or defects within crystal [21]. However, AIMD simulation shows Ge doping is an effective strategy to boost the ionic conductivity. Along with Ge^{4+} doping, extra Li ions are inserted into the interstitial sites and vacancies are created at originally fully-occupied Li sites, which decreases the order-disorder transition temperature and enhances the Li diffusivity significantly. As shown in Figure 3.7, the order-disorder transition disappeared within simulation temperature range when $x \geq 0.5$ in $Li_{15+x}Ge_xP_{4-x}S_{16}Cl_3$, leading to an extrapolated ionic conductivity of 10^{-2} mS/cm at 300 K, which is 9 orders of magnitude higher than $Li_{15}P_4S_{16}Cl_3$ without Ge^{4+} doping. Further increasing Ge doping contents leads to higher ionic conductivity at room temperature and an ionic conductivity of 4.1 mS/cm is expected at composition $Li_{18}Ge_3PS_{16}Cl_3$.

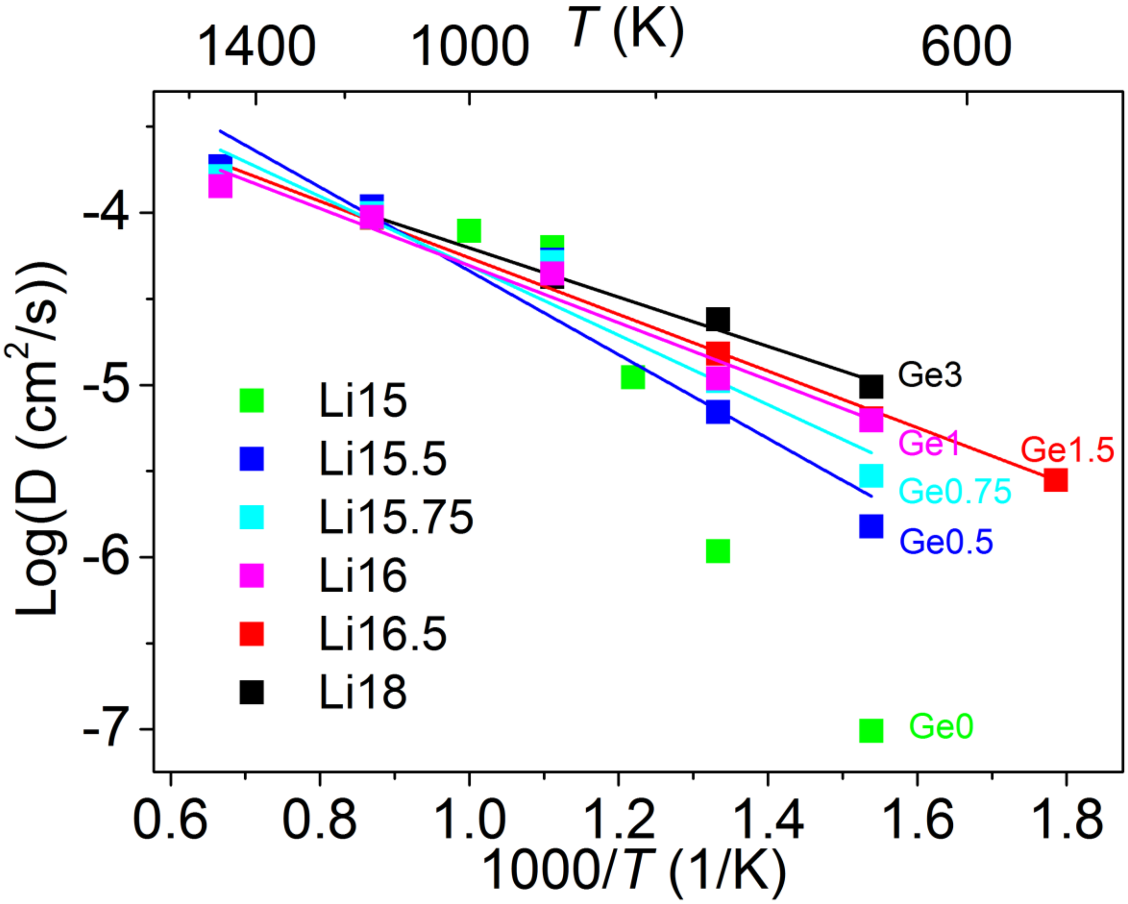

Figure 3.7 Arrhenius plot of Li^+ diffusivity in $Li_{15+x}Ge_xP_{4-x}S_{16}Cl_3$ from AIMD simulations.

Although higher Ge^{4+} doping content is expected to enhance the ionic conductivity to higher level, it also destabilizes crystal structure of $Li_{15}P_4S_{16}Cl_3$. The stability of $Li_{15+x}Ge_xP_{4-x}S_{16}Cl_3$ is evaluated by the energy above hull (E_{hull}). The higher E_{hull} value indicates a higher tendency of this material to decompose. As shown in Table 2.2, E_{hull} increases gradually when more Ge^{4+} are introduced. Considering both the stability and conductivity, $Li_{16.5}Ge_{1.5}P_{2.5}S_{16}Cl_3$ is quite promising, showing an extrapolated ionic conductivity of 1.1 mS/cm with relatively low E_{hull} (21 meV/atom). However, doping more Ge into the crystal structure is not successful and the solid solution limit is already achieved at $Li_{15.5}Ge_{0.5}P_{3.5}S_{16}Cl_3$. Compared with AIMD simulation results, the ionic conductivity at room temperature is higher than the simulated results but within the error bound. The activation energy of $Li_{15.5}Ge_{0.5}P_{3.5}S_{16}Cl_3$ extracted from electrochemical impedance spectroscopy is lower than AIMD results and the unknown phase or possible presence of amorphous phase may be responsible for that.

Table 3.2 Calculated Li^+ conductivities and activation energies for $Li_{15+x}Ge_xP_{4-x}S_{16}Cl_3$ from AIMD simulations.

Composition	E above hull (meV/atom)	E_a (eV)	σ at 300 K ($mS \cdot cm^{-1}$)	Error bound $[\sigma_{min}, \sigma_{max}]$ ($mS \cdot cm^{-1}$)
Ge 0	0	1.32 (fit lower 4 points)	1E-11	
Ge 0.5	4	0.48 ± 0.07	0.01	[7E-3, 0.2]
Ge 0.75	6	0.40 ± 0.05	0.1	[0.01, 1.1]
Ge 1	12	0.33 ± 0.03	0.9	[0.2, 3.4]
Ge 1.5	21	0.36 ± 0.01	1.1	[0.6, 1.9]
Ge 3	49	0.28 ± 0.02	4.1	[1.7, 9.6]

3.3 Summary

In this work, I design and synthesis a solid solution series $Li_{15+x}Ge_xP_{4-x}S_{16}Cl_3$ and the influence of Ge^{4+} doping on crystal structure and Li ions diffusion behavior were investigated by employing synchrotron and neutron diffraction, variable temperature EIS and first-principles calculations. With increasing Ge^{4+} content, a significantly change in the activation energy and ionic conductivity can be observed. The limit of the solid solution range, $Li_{15.5}Ge_{0.5}P_{3.5}S_{16}Cl_3$, exhibits an ionic conductivity of 2.2×10^{-5} S cm^{-1} at 30 ^{o}C, which is 3 orders of magnitude higher than the undoped $Li_{15}P_4S_{16}Cl_3$. AIMD simulation results predict promising ionic conductivity if more Li ions can be inserted into the crystal structure. This work serves as a good demonstration of structural-properties relationship. Owing to the extra Li ions insertion to the tetrahedral interstitial sites and created vacancies at originally fully-occupied Li sites, concerted migration was triggered in $Li_{15}P_4S_{16}Cl_3$, which significantly lower the activation barrier for Li ions.

3.4 Method

The starting materials Li_2S (99.98%, Sigma-Aldrich), P_2S_5 (99%, Sigma-Aldrich) and GeS_2 (American Elements) were first weighed in desired molar ratio and mechanical milled by planetary ball mill in zirconia pot with 10 zirconia balls (diameter: 10 mm) in Ar-filled glovebox. The rotation speed is fixed to 300 rpm and the milling time is 16h. After that the ball-milled mixture were pressed into pellet and sealed in quartz glass tube. The pellets were heated at 350 °C for 10h and cooled down within the furnace to obtain the $Li_{3+x}Ge_xP_{1-x}S_4$ solid solution. The obtained solid solution was then mixed with LiCl and ball-milling process was applied for another 16h at 300 rpm. The obtained mixtures were pressed into pellets and sealed in quartz glass tubes. The samples were heated at different temperature for 20h in a furnace.

The X-ray diffraction data of the samples were collected by a D8 Advance X-ray Diffractometer (Bruker AXS, Germany) with a Molybdenum radiation [λ Kα1 = 0.7093 Å]). Synchrotron data was collected at the beam line 17-BM at the Advanced Photon Source (APS) at Argonne National Laboratory. The wavelength is 0.24116 Å. High-quality powder neutron diffraction (ND) data were collected at r.t. at POWGEN at the Spallation Neutron Source (SNS) at Oak Ridge National Laboratory (ORNL) with a center wavelength 0.8 Å. For the structure analysis of $Li_{15}P_4S_{16}Cl_3$, Rietveld refinement was performed by using GSAS II software [24].

Ionic conductivity was determined using an alternating current (AC) impedance spectroscopy with custom build electrochemical cell set up. Typically, ~130 mg $Li_{15}P_4S_{16}Cl_3$ powder was pressed into pellet under 100 bars with a diameter of ½ inch. Stainless steel rods were used as current collector. Electrochemical impedance analysis (EIS) was conducted in the temperature range of 30 °C to 90 °C using a VMP3 impedance analyzer (Biologic) 1MHz-1Hz with an amplitude of 500 mV.

Density functional theory (DFT) calculations were conducted with using the Vienna *Ab initio* Simulation package (VASP) [25] within the projector augmented-wave approach with Perdew-Burke-Ernzerhof (PBE) [26] generalized-gradient approximation (GGA). A*b initio* molecular dynamic (AIMD) simulations were performed to investigate Li diffusion. A Γ-centered *k*-point in the non-spin-polarized DFT calculations were used. The time step was 2 fs. NVT ensemble using Nosé-Hoover thermostat [27] was used. The total time of AIMD simulations were in the range of 100 ps to 600 ps. The ionic conductivity and the error bars were calculated and estimated following previously established methods [28].

3.5 References

[1] Janek, J.; Zeier, W. G., A solid future for battery development. *Nature Energy* **2016,** *1*, 16141.

[2] Kaup, K.; Lalère, F.; Huq, A.; Shyamsunder, A.; Adermann, T.; Hartmann, P.; Nazar, L. F., Correlation of Structure and Fast Ion Conductivity in the Solid Solution Series Li1+2xZn1−xPS4. *Chemistry of Materials* **2018,** *30* (3), 592-596.

[3] Hayashi, A.; Sakuda, A.; Tatsumisago, M., Development of Sulfide Solid Electrolytes and Interface Formation Processes for Bulk-Type All-Solid-State Li and Na Batteries. *Frontiers in Energy Research* **2016,** *4* (25).

[4] Murugan, R.; Thangadurai, V.; Weppner, W., Fast Lithium Ion Conduction in Garnet-Type Li7La3Zr2O12. *Angewandte Chemie International Edition* **2007,** *46* (41), 7778-7781.

[5] Huang, B.; Xu, B.; Li, Y.; Zhou, W.; You, Y.; Zhong, S.; Wang, C.-A.; Goodenough, J. B., Li-Ion Conduction and Stability of Perovskite Li3/8Sr7/16Hf1/4Ta3/4O3. *ACS Applied Materials & Interfaces* **2016,** *8* (23), 14552-14557.

[6] Aono, H.; Sugimoto, E.; Sadaoka, Y.; Imanaka, N.; Adachi, G. y., Ionic Conductivity of the Lithium Titanium Phosphate (Li1 + X M X Ti2 − X (PO 4) 3 , M = Al , Sc , Y , and La) Systems. *Journal of The Electrochemical Society* **1989,** *136* (2), 590-591.

[7] Hayashi, A.; Noi, K.; Sakuda, A.; Tatsumisago, M., Superionic glass-ceramic electrolytes for room-temperature rechargeable sodium batteries. *Nature Communications* **2012,** *3,* 856.

[8] Tatsumisago, M.; Nagao, M.; Hayashi, A., Recent development of sulfide solid electrolytes and interfacial modification for all-solid-state rechargeable lithium batteries. *Journal of Asian Ceramic Societies* **2013,** *1* (1), 17-25.

[9] Asano, T.; Sakai, A.; Ouchi, S.; Sakaida, M.; Miyazaki, A.; Hasegawa, S., Solid Halide Electrolytes with High Lithium-Ion Conductivity for Application in 4 V Class Bulk-Type All-Solid-State Batteries. *Advanced Materials* **2018,** *30* (44), 1803075.

[10] Park, K.-H.; Kaup, K.; Assoud, A.; Zhang, Q.; Wu, X.; Nazar, L. F., High-Voltage Superionic Halide Solid Electrolytes for All-Solid-State Li-Ion Batteries. *ACS Energy Letters* **2020**, 533-539.

[11] Liang, J.; Li, X.; Wang, S.; Adair, K. R.; Li, W.; Zhao, Y.; Wang, C.; Hu, Y.; Zhang, L.; Zhao, S.; Lu, S.; Huang, H.; Li, R.; Mo, Y.; Sun, X., Site-Occupation-Tuned Superionic LixScCl3+xHalide Solid Electrolytes for All-Solid-State Batteries. *Journal of the American Chemical Society* **2020,** *142* (15), 7012-7022.

[12] Kamaya, N.; Homma, K.; Yamakawa, Y.; Hirayama, M.; Kanno, R.; Yonemura, M.; Kamiyama, T.; Kato, Y.; Hama, S.; Kawamoto, K.; Mitsui, A., A lithium superionic conductor. *Nat Mater* **2011,** *10* (9), 682-686.

[13] Kanno, R.; Murayama, M., Lithium Ionic Conductor Thio-LISICON: The Li2 S - GeS2 - P 2 S 5 System. *Journal of The Electrochemical Society* **2001,** *148* (7), A742-A746.

[14] Dietrich, C.; Weber, D. A.; Culver, S.; Senyshyn, A.; Sedlmaier, S. J.; Indris, S.; Janek, J.; Zeier, W. G., Synthesis, Structural Characterization, and Lithium Ion Conductivity of the Lithium Thiophosphate Li2P2S6. *Inorganic Chemistry* **2017,** *56* (11), 6681-6687.

[15] Homma, K.; Yonemura, M.; Kobayashi, T.; Nagao, M.; Hirayama, M.; Kanno, R., Crystal structure and phase transitions of the lithium ionic conductor Li3PS4. *Solid State Ionics* **2011,** *182* (1), 53-58.

[16] Seino, Y.; Ota, T.; Takada, K.; Hayashi, A.; Tatsumisago, M., A sulphide lithium super ion conductor is superior to liquid ion conductors for use in rechargeable batteries. *Energy & Environmental Science* **2014,** *7* (2), 627-631.

[17] Kong, S. T.; Reiner, C.; Deiseroth, H. J., Synthesis and Characterization of Lithium Argyrodite, Li7PS6. *Zeitschrift für anorganische und allgemeine Chemie* **2006,** *632* (12-13), 2100-2100.

[18] Kamaya, N.; Homma, K.; Yamakawa, Y.; Hirayama, M.; Kanno, R.; Yonemura, M.; Kamiyama, T.; Kato, Y.; Hama, S.; Kawamoto, K.; Mitsui, A., A lithium superionic conductor. *Nature Materials* **2011,** *10*, 682.

[19] Inoue, Y.; Suzuki, K.; Matsui, N.; Hirayama, M.; Kanno, R., Synthesis and structure of novel lithium-ion conductor Li7Ge3PS12. *Journal of Solid State Chemistry* **2017,** *246*, 334-340.

[20] Deiseroth, H.-J.; Kong, S.-T.; Eckert, H.; Vannahme, J.; Reiner, C.; Zaiß, T.; Schlosser, M., Li6PS5X: A Class of Crystalline Li-Rich Solids With an Unusually High Li+ Mobility. *Angewandte Chemie International Edition* **2008,** *47* (4), 755-758.

[21] Liu, Z.; Zinkevich, T.; Indris, S.; He, X.; Liu, J.; Xu, W.; Bai, J.; Xiong, S.; Mo, Y.; Chen, H., Li15P4S16Cl3, a Lithium Chlorothiophosphate as a Solid-State Ionic Conductor. *Inorganic Chemistry* **2020,** *59* (1), 226-234.

[22] Shannon, R., Revised effective ionic radii and systematic studies of interatomic distances in halides and chalcogenides. *Acta Crystallographica Section A* **1976,** *32* (5), 751-767.

[23] Hori, S.; Kato, M.; Suzuki, K.; Hirayama, M.; Kato, Y.; Kanno, R., Phase Diagram of the Li4GeS4–Li3PS4 Quasi-Binary System Containing the Superionic Conductor Li10GeP2S12. *Journal of the American Ceramic Society* **2015,** *98* (10), 3352-3360.

[24] Toby, B. H.; Von Dreele, R. B., GSAS-II: the genesis of a modern open-source all purpose crystallography software package. *Journal of Applied Crystallography* **2013,** *46* (2), 544-549.

[25] Kresse, G.; Furthmüller, J., Efficient iterative schemes for ab initio total-energy calculations using a plane-wave basis set. *Physical Review B* **1996,** *54* (16), 11169-11186.

[26] Perdew, J. P.; Ernzerhof, M.; Burke, K., Rationale for mixing exact exchange with density functional approximations. *J. Chem. Phys.* **1996,** *105* (22), 9982–9985.

[27] Nose, S., Constant temperature molecular dynamics methods. *Prog. Theor. Phys. Suppl.* **1991,** *103*, 1–46.

[28] He, X.; Zhu, Y.; Epstein, A.; Mo, Y., Statistical variances of diffusional properties from ab initio molecular dynamics simulations. *npj Computational Materials* **2018,** *4* (1), 18.

CHAPTER 4. Entropy Stabilized Lithium Argydodite Structure with High Concentration of Li Vacancies Realized by OH$^-$ Doping with High Ionic Conductivity

4.1 Introduction

Solid electrolytes (SEs) are crucial for the overall performance of all-solid-state lithium ion batteries (ALSOLIBs). To enable ALSOSLIBs that can be operated in ambient temperature, SSEs with high ionic conductivity (>10^{-4} S cm^{-1} at room temperature) and wide electrochemical window are desirable [1-3]. Among various inorganic SSEs, sulfide-based SEs have attracted intensive interests because of their intrinsic high ionic conductivity and favorable deformability [4-5]. Several sulfide SEs with ionic conductivity exceeding 10^{-3} S/cm have been reported, including Li_3PS_4-Li_4GeS_4 solid solutions with LISICON structure [6], Li_6PS_5X (X=Cl, Br) with argyrodite structure [7-9], $Li_7P_3S_{11}$ glass ceramics [10], and $Li_{10}GeP_2S_{12}$ (LGPS) [11], etc. Among them, $Li_{10}GeP_2S_{12}$ (LGPS) with an ultra-high ionic conductivity of 1.2×10^{-2} S/cm at room temperature was reported in 2011, which already surpass the typical value of organic electrolyte [11]. However, it contains expensive Ge element, which limits its practical applications. In order to lower the cost, Si- and Sn-based analogues in LGPS structure were identified, exhibiting excellent ionic conductivity [12-14]. Especially, a nominal composition $Li_{9.54}Si_{1.74}P_{1.44}S_{11.7}Cl_{0.3}$ shows an exceptionally high conductivity of 2.5×10^{-2} S/cm [15]. Although these compounds exhibit high ionic conductivity, incorporation of IV A group elements makes them cannot form stable passivation layer with Li metal because of formation of electronically and ionic conducting Li-M (M=Si, Ge, Sn) alloys [16-18]. In order to obtain materials in LGPS structure with good stability, $Li_{9.6}P_3S_{12}$ was successfully synthesized, which exhibits better compatibility with Li metal but lower ionic conductivity [15].

Lithium argyrodites represent another promising family of solid electrolytes with ionic conductivity exceeding 10^{-3} S/cm and good compatibility with Li metal [19]. The framework of cubic argyrodites is built by isolated PS_4 units centered at 4b sites and the free sulfur or halogen atoms occupy 4a and 4c sites. Li atoms are randomly distributed in 48h sites. change in anion site-disorder and lattice softness have a big influence on these three kinds hopping frequencies and the ionic conductivities. In Li_6PS_5Cl and Li_6PS_5Br, the halogen and sulfur atoms site exhibited obvious anion site-disorder, which is thought responsible for the high ionic conductivity [20-21]. On the contrary, due to the large difference in atom size between I^- and S^{2-}, I^- tends to occupy all the 4a sites and no disorder can be observed, which leads to a low ionic conductivity in Li_6PS_5I [21-22]. Based on these phenomenon, mixed halide argyrodite were proposed and Li_6PS_5X ($X=Cl_{0.75}Br_{0.25}$, $Cl_{0.5}Br_{0.5}$ and $Cl_{0.25}Br_{0.75}$) show higher ionic conductivities compared to the single-halide phases [23-24].

Another strategy to increase the ionic conductivity in SSEs is cation doping, which tunes the lattice parameter and create more vacancies or increase Li density within the crystal structure. For example, $Li_{6+x}Si_xP_{1-x}S_5Br$ was synthesized by aliovalent doping with increasing in the ionic conductivity [25]; Ge is successfully doped into Li_6PS_5I, which not only expands the lattice parameter but also induces the disorder of I^- and S^{2-}, thus boosting the ionic conductivity to around 5.4×10^{-3} S/cm in cold-press state [26].

Except for the cation doping to increase the Li concentration, replacing the S^{2-} at 4a and 4c site by halide atoms is also explored theoretically and experimentally. DFT MD calculation shows that the position of halide ions can have significantly influence on the Li ion jump rates, and thus on conductivities and $Li_5PS_4X_2$(X=Cl, Br) are suggested to be promising solid electrolyte with high ionic conductivity[20]. Nazar group reported halide-rich solid solution phases in the argyrodite Li_6PS_5Cl family, $Li_{6-x}PS_{5-x}Cl_{1+x}$. At the limit of the solid solution regime, the composition $Li_{5.5}PS_{4.5}Cl_{1.5}$ exhibits a cold-pressed conductivity of 9.4 ± 0.1 mS/cm at room temperature and 12.0 ± 0.2 mS/cm on sintering [27]. By substituting divalent S^{2-} with monovalent Cl^-, increased site disorder and higher lithium vacancy population were obtained, which enhanced lithium ion conductivity. Currently, there is no report on the successful synthesis of $Li_5PS_4Cl_2$, $Li_5PS_4Br_2$ or $Li_5PS_4I_2$ where the free S^{2-} can be totally replaced, though $Li_5PS_4X_2$ is predicted to have similar stability with Li_6PS_5X based on formation enthalpy [28]. Usually, the formation enthalpy is obtained by density functional theory calculation conducted at 0 K, while entropy predominates the free-energy landscape at elevated temperature. It has been shown that the entropic contribution to the Gibbs free energy can stabilize alloys, oxide and sulfide phases at finite temperature [29-31]. In these high entropy stabilized compounds, several different metal elements or cations are introduced into the structure, which increased the entropy and stabilize the single-phase. However, there are seldom report on the anion stabilized high entropy compound.

Here we propose and realize a new “anion doping triggered high entropy” strategy to stabilize Argyrodite structure with high Li vacancies: the free S^{2-} can be totally replaced and the argyrodite structure can be stabilized by increased entropy with introducing OH^-. The created Li vacancies and high anion site-disorder boost the ionic conductivity to 2.69×10^{-2} S/cm at 30 ^oC. The fabricated all solid-state batteries show excellent rate performance and long cycle life at room temperature.

4.2 Results and Discussion

Firstly, *in situ* XRD technique was used to explore the possibility to synthesize $Li_5PS_4Cl_2$ and $Li_5PS_4Br_2$ in argyrodite structure and the *in situ* XRD patterns are shown in Figure 4.1 (a) and (b). The XRD pattern of nominal $Li_5PS_4Cl_2$ mixture at 100 ^oC shows typical amorphous characteristics with weak peaks which can be indexed to Li_2S and LiCl. As temperature increases, β-Li_3PS_4 [32] appears at 250 ^oC and more LiCl crystallizes from amorphous phase. Further increasing temperature to 350 ^oC triggers the reaction between β-Li_3PS_4 and LiCl to form $Li_{15}P_4S_{16}Cl_3$ [33] with excess LiCl existing. The mixture melts at 450 ^oC and only minor LiCl phases is observed. During the whole heating process, no argyrodite structure forms, despite the very similar ion radius of Cl^- (1.81 pm) and S^{2-} (1.84 pm) [22]. In the heating process of nominal $Li_5PS_4Br_2$ mixture, only β-Li_3PS_4 and LiBr appear during the whole process and there were also no signs of argyrodite structure forming.

In thermodynamics consideration, the stability of compounds is determined by the Gibbs free energy ($G = H - TS$, G: Gibbs free energy; H: enthalpy; T: temperature; S: entropy) and the entropic contribution can be used to stabilize phase at certain temperature. Theoretical calculation predicted $Li_5PS_4X_2$ and Li_6PS_5X have similar formation enthalpy [28]. However, in Li_6PS_5X with argyrodite structure, free S^{2-} and halogen atoms randomly distribute at 4a and 4c sites. If the free S^{2-} are substituted by the same kinds of halogen atoms completely, anion site configurational entropy becomes lower, which potentially destabilized the argyrodite structure. If disorder configuration at 4a and 4c sites can be induced by introducing different kinds of monovalent anions, the increased entropy may promote the formation of argyrodite structure with the same Li site deficiencies as $Li_5PS_4Cl_2$ or $Li_5PS_4Br_2$.

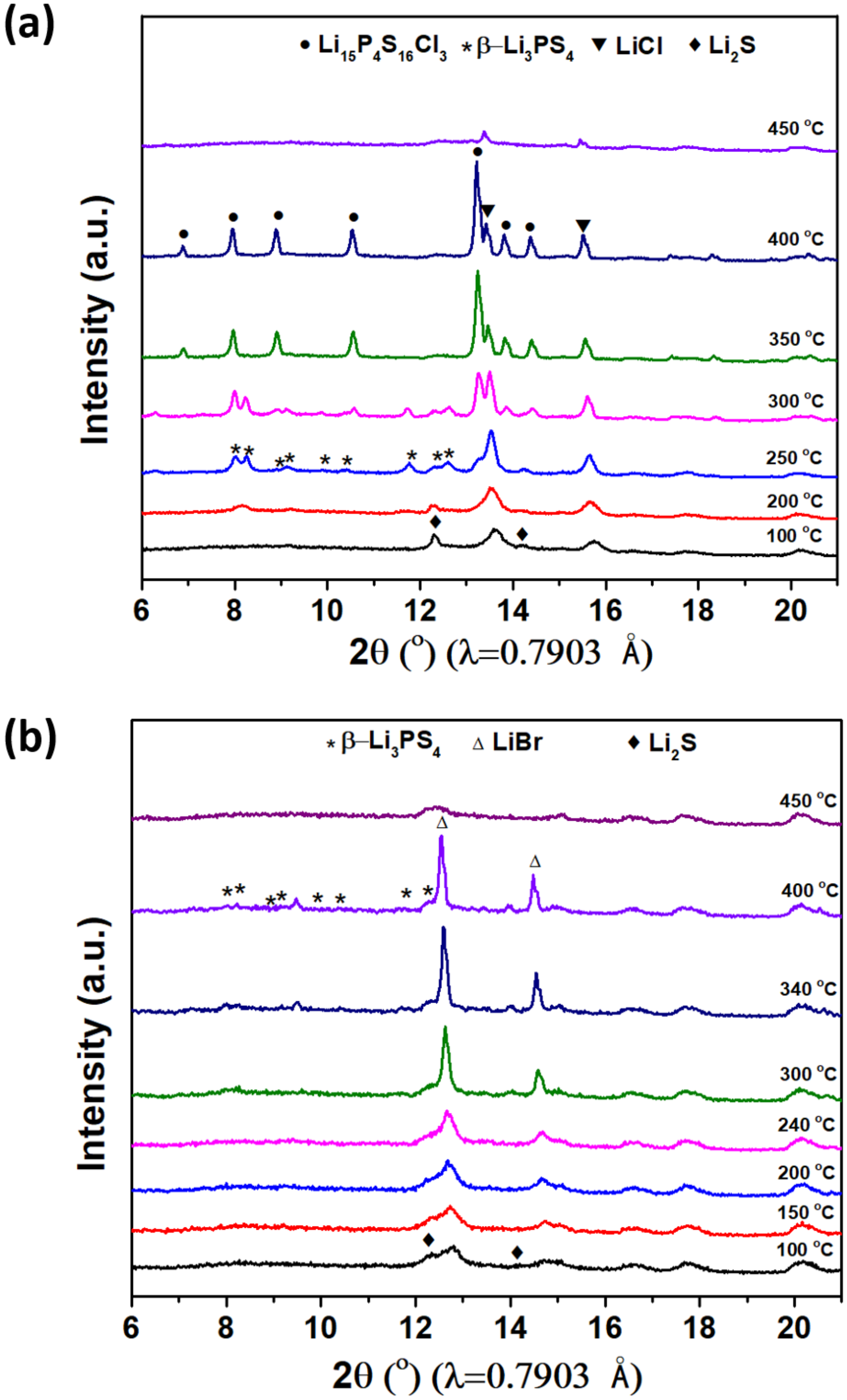

Figure 4.1 *In situ* XRD patterns of (a) $Li_5PS_4Cl_2$ and (b) $Li_5PS_4Br_2$, heated up to 450 °C.

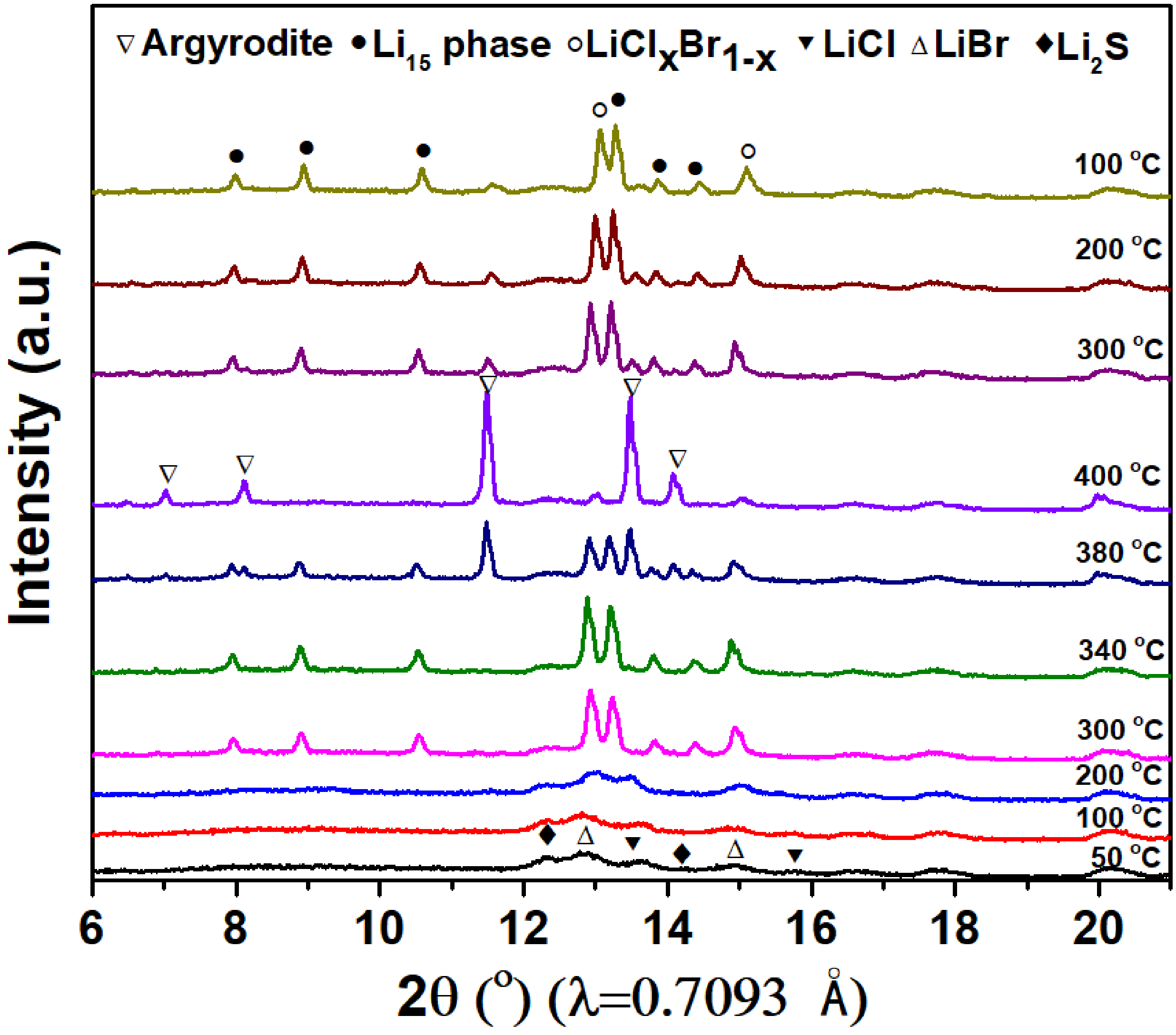

Figure 4. 2 *In situ* XRD patterns of Li_5PS_4ClBr in heating and cooling process.

To verify this hypothesis, a nominal composition of Li_5PS_4ClBr was designed and *in situ* XRD was applied to monitor the phase evolution during heating and cooling process. As shown in Figure 4.2, at 300 °C, the mixture turnes into $Li_{15}P_4S_{16}Cl_{3-y}Br_y$ and $LiCl_xBr_{1-x}$. As the temperature increases, $Li_{15}P_4S_{16}Cl_{3-y}Br_y$ starts to reacted with $LiCl_xBr_{1-x}$ to form argyrodite structure at 380 °C and a pure argyrodite phase is achieved successfully at 400 °C. The argyrodite structure Li_5PS_4ClBr, however, is only stable in high temperature range. It decomposed into $Li_{15}P_4S_{16}Cl_{3-y}Br_y$ and $LiCl_xBr_{1-x}$ again in cooling process, which evidently demonstrates that this compound is entropy stabilized at high temperature. At lower temperature, contribution from enthalpy predominates, which drives the decomposition of Li_5PS_4ClBr. Compared with $Li_5PS_4X_2$ (X=Cl, Br), the increased entropy in Li_5PS_4ClBr triggers the appearance of argyrodite structure at 450 ^oC, but it is not high enough to stabilize the argyrodite structure at room temperature. The anion configuration entropy needs to be further increased and it can be achieved by introducing more kinds of anions at 4a and 4c sites. Here we chose OH^- as the third kind of monovalent anions doped at 4a and 4c sites. To maximize the anions configuration entropy, $Li_5PS_4(ClBrOH)_{2/3}$ is designed.

Figure 4.3 shows the *in situ* XRD of nominal composition $Li_5PS_4(ClBrOH)_{2/3}$ during heating and cooling process. The argyrodite structure starts to form at 200 ^oC and keeps stable up to 550 ^oC. Compared with argyrodite Li_5PS_4ClBr, the formation temperature for argyrodite $Li_5PS_4(ClBrOH)_{2/3}$ is much lower, owing to the increased anion configuration entropy. Furthermore, the formed $Li_5PS_4(ClBrOH)_{2/3}$ in argyrodite structure does not decompose as the temperature decreases and remains stable at room temperature. This is the first time that OH^- is successfully doped into the sulfide argyrodite structure, which provide a new choice for materials design. With the help of OH^- doping, multiple kinds of monovalent anions are able to substitute the free S^{2-} at 4a and 4c sites completely, which creates high Li^+ vacancy concentration in argyrodite structure. In fact, by adjusting the ratio between S^{2-} and monovalent anions at 4a and 4c sites, the Li^+ vacancy concentration can be tuned in a wide range (from $Li_5PS_4X_2$, X=monovalent anions, to Li_7PS_6). In the following experiments, we design a series of solid solution in formula of $Li_5PS_4(ClBr)_{1-x/2}(OH)_x$, which fixes the ratio between Cl^- and Br^- to 1 and compounds with nominal components $Li_5PS_4(ClBr)_{0.75}(OH)_{0.5}$, $Li_5PS_4(ClBrOH)_{2/3}$, $Li_5PS_4(ClBr)_{0.5}OH$ and $Li_5PS_4(ClBr)_{0.25}(OH)_{1.5}$ were synthesized.

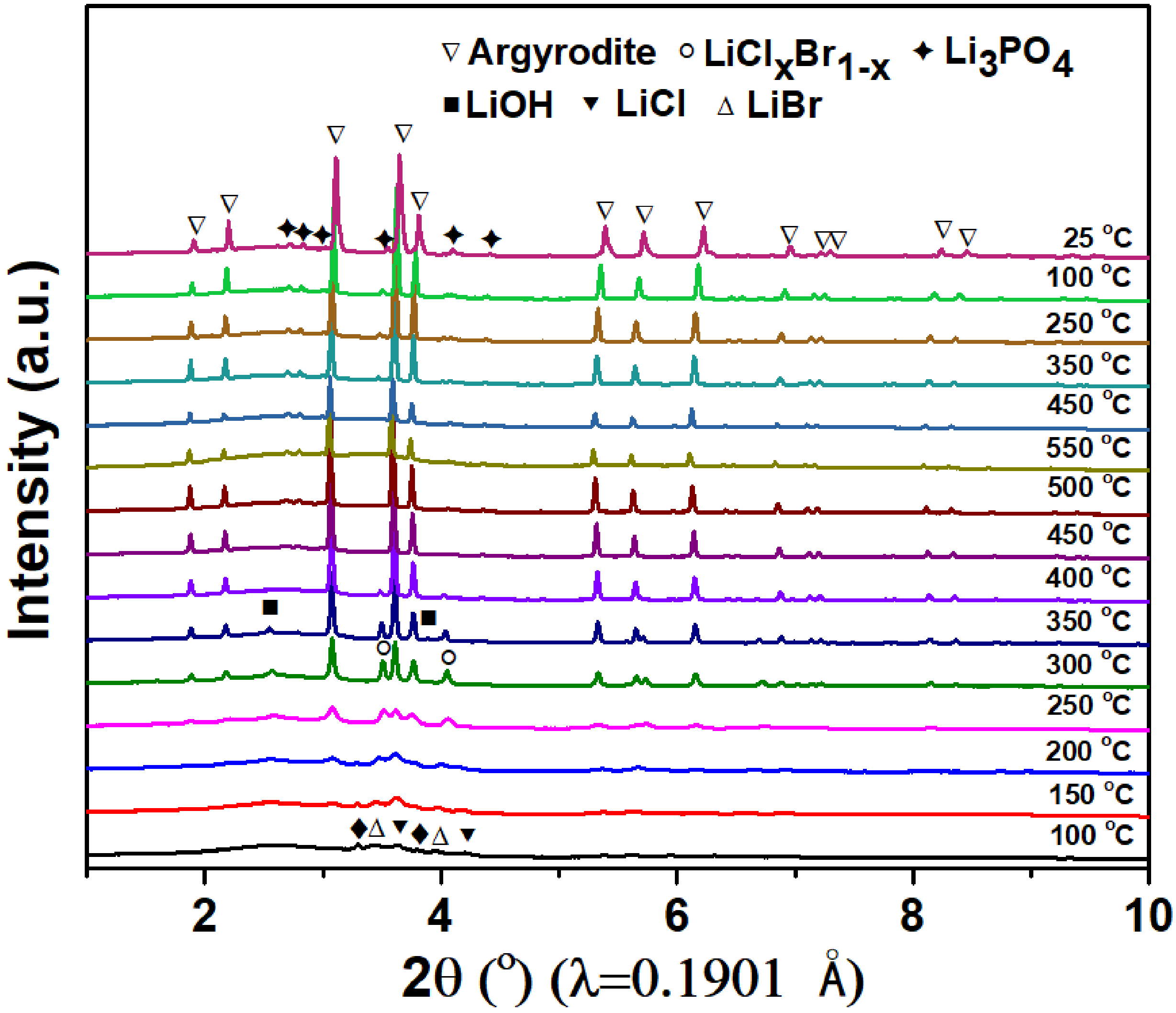

Figure 4.3 *In situ* XRD patterns of $Li_5PS_4(ClBrOH)_{2/3}$ in heating and cooling process.

The XRD patterns are shown in Figure 4.4a. Argyrodite structure forms in all the compositions, with minor Li_3PO_4 impurities. The extracted cubic lattice parameters of $Li_5PS_4(ClBr)_{1-x/2}(OH)_x$ from Rietveld refinement agaisnt synchrotron diffration data is shown in Figure 4.4b. The lattice parameter expands linearly with increased OH^- doping content when $x \leq 1$.

Further increasing OH$^-$ doping content leads to a deviation of Vegard's law of the lattice parameter, along with appearance of Li_2S.

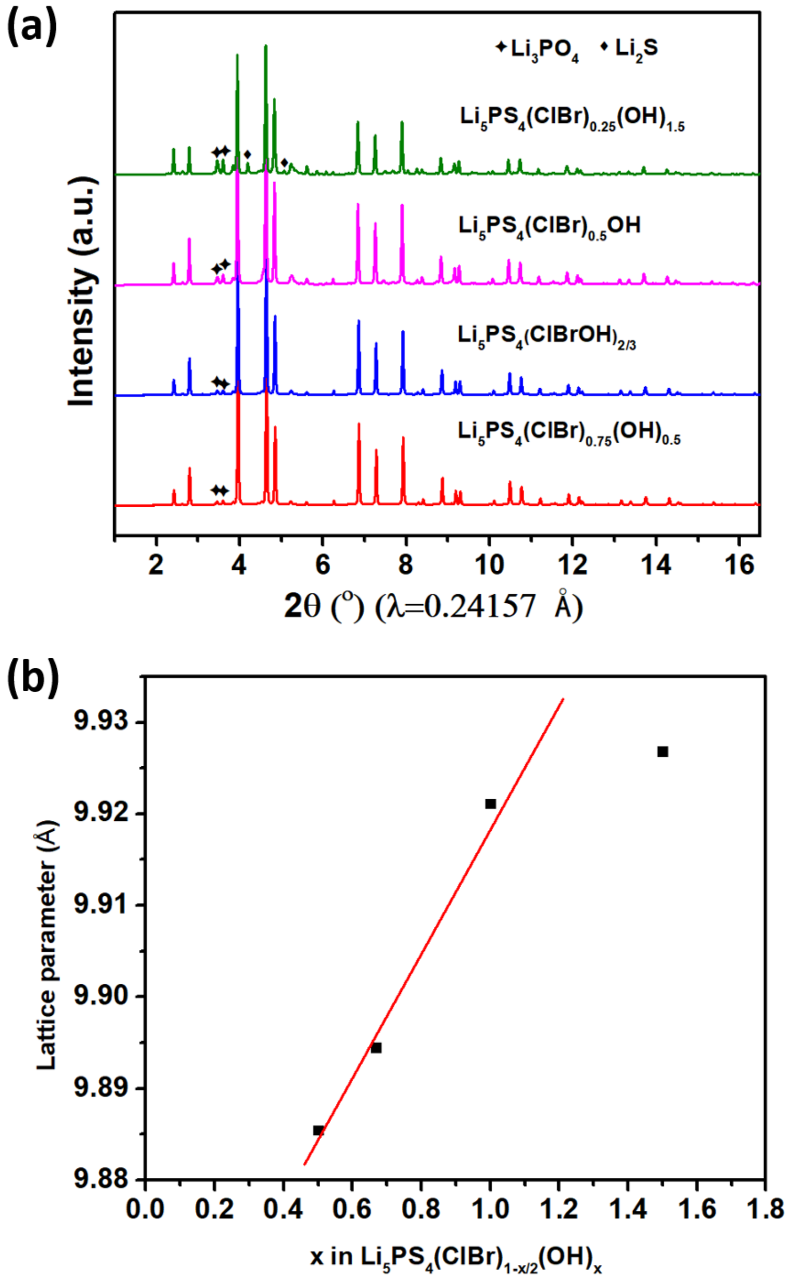

Figure 4.4 (a) XRD pattern of $Li_5PS_4(ClBr)_{0.75}(OH)_{0.5}$, $Li_5PS_4(ClBrOH)_{2/3}$, $Li_5PS_4(ClBr)_{0.5}OH$ and $Li_5PS_4(ClBr)_{0.25}(OH)_{1.5}$. (b) Lattice parameter of $Li_5PS_4(ClBr)_{1-x/2}(OH)_x$ vs. x.

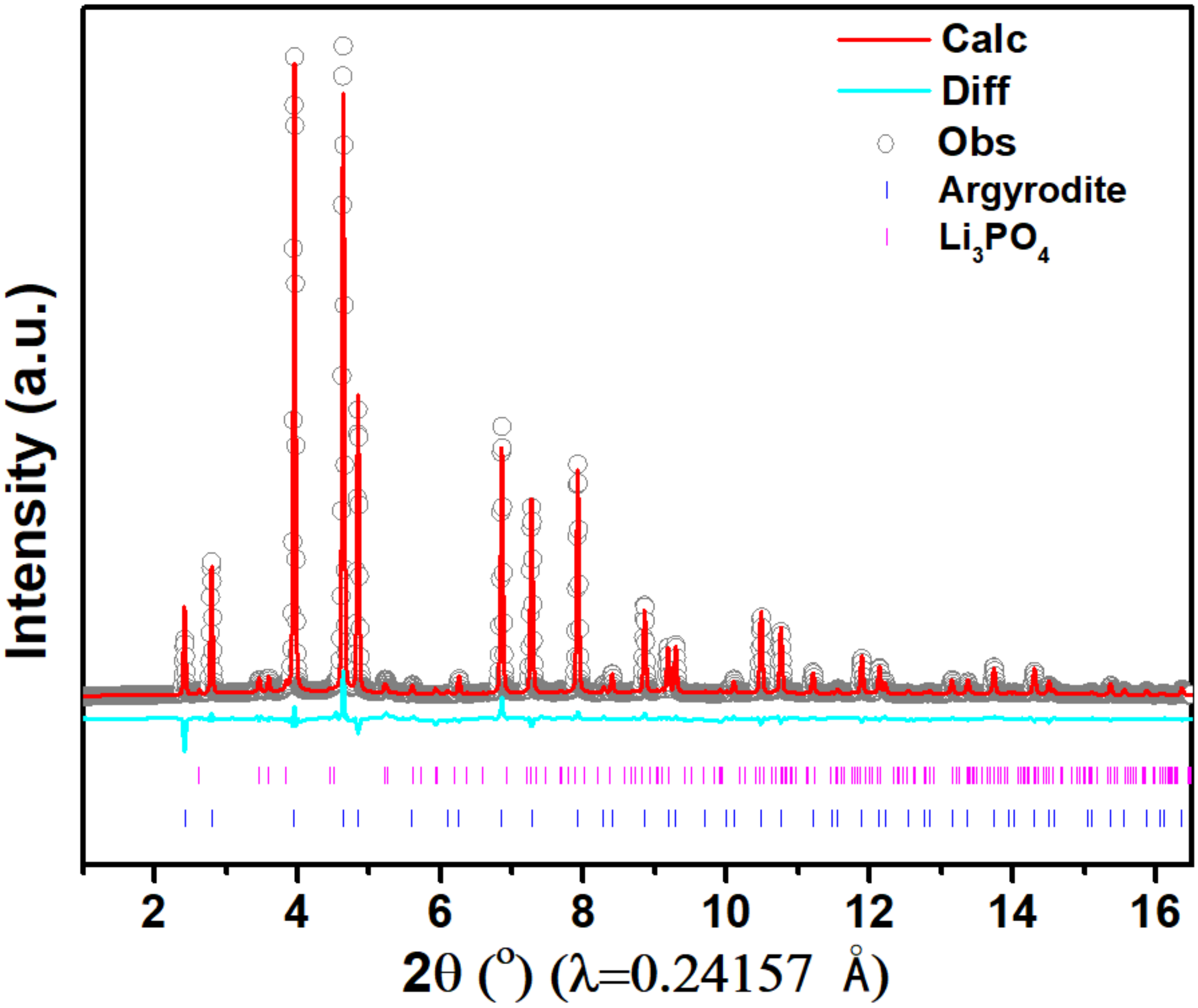

Figure 4.5 The Rietveld refinements against synchrotron X-ray.

Figure 4.5 shows the representative Rietveld refinement of the most highly ionically conductive material, $Li_5PS_4(ClBrOH)_{2/3}$ and the refined crystal structure is listed in table 4.1. Cl^-, Br^- and OH^- share the 4a and 4c sites.

Table 4.1 Refined structure of $Li_5PS_4(ClBrOH)_{2/3}$ using synchrotron diffraction data

Atom	x	y	z	occupancy	site	U_{iso}
Li(1)	0.320(3)	0.018(2)	0.679(8)	0.417	48h	0.100(6)
Br(1)	0	0	1	0.394(3)	4a	0.021(1)
Br(2)	0.25	0.25	0.75	0.272(4)	4c	0.023(8)
P(1)	0	0	0.5	1	4b	0.047(7)
Cl(1)	0	0	1	0.406(8)	4a	0.017(9)
Cl(2)	0.25	0.25	0.75	0.259(8)	4c	0.029(8)
S(1)	0.12	-0.12	0.62	1	16e	0.063(0)
O(1)	0	0	1	0.1988	4a	0.010(0)
O(2)	0.25	0.25	0.75	0.4679	4c	0.010(0)

Figure 4.6 shows the Arrhenius plots of the as synthesized $Li_5PS_4(ClBr)_{0.75}(OH)_{0.5}$, $Li_5PS_4(ClBrOH)_{2/3}$ and $Li_5PS_4(ClBr)_{0.5}OH$ in cold-pressing state measured by electrochemical impedance spectroscopy (EIS) test. All the samples show much higher ionic conductivity than the value reported for classic argyrodite structure (1~3 mS cm^{-1} for Li_6PS_5Cl and for Li_6PS_5Br) [23-24, 34-35]. Despite $Li_5PS_4(ClBr)_{0.5}OH$ has the largest lattice parameter, it shows the modest ionic conductivity of 9.5 mS cm^{-1} at 30 ^oC. while $Li_5PS_4(ClBrOH)_{2/3}$ exhibited the highest ionic conductivity of 10.6 mS cm^{-1}. To better eliminate the influence of grain boundary, $Li_5PS_4(ClBrOH)_{2/3}$ was hot-pressed at 450 ^oC for 2 minutes and the ionic conductivity was further boosted to 26.9 mS cm^{-1}, which is comparable with $Li_{9.54}Si_{1.74}P_{1.44}S_{11.7}Cl_{0.3}$ (25 mS cm^{-1}) [15].

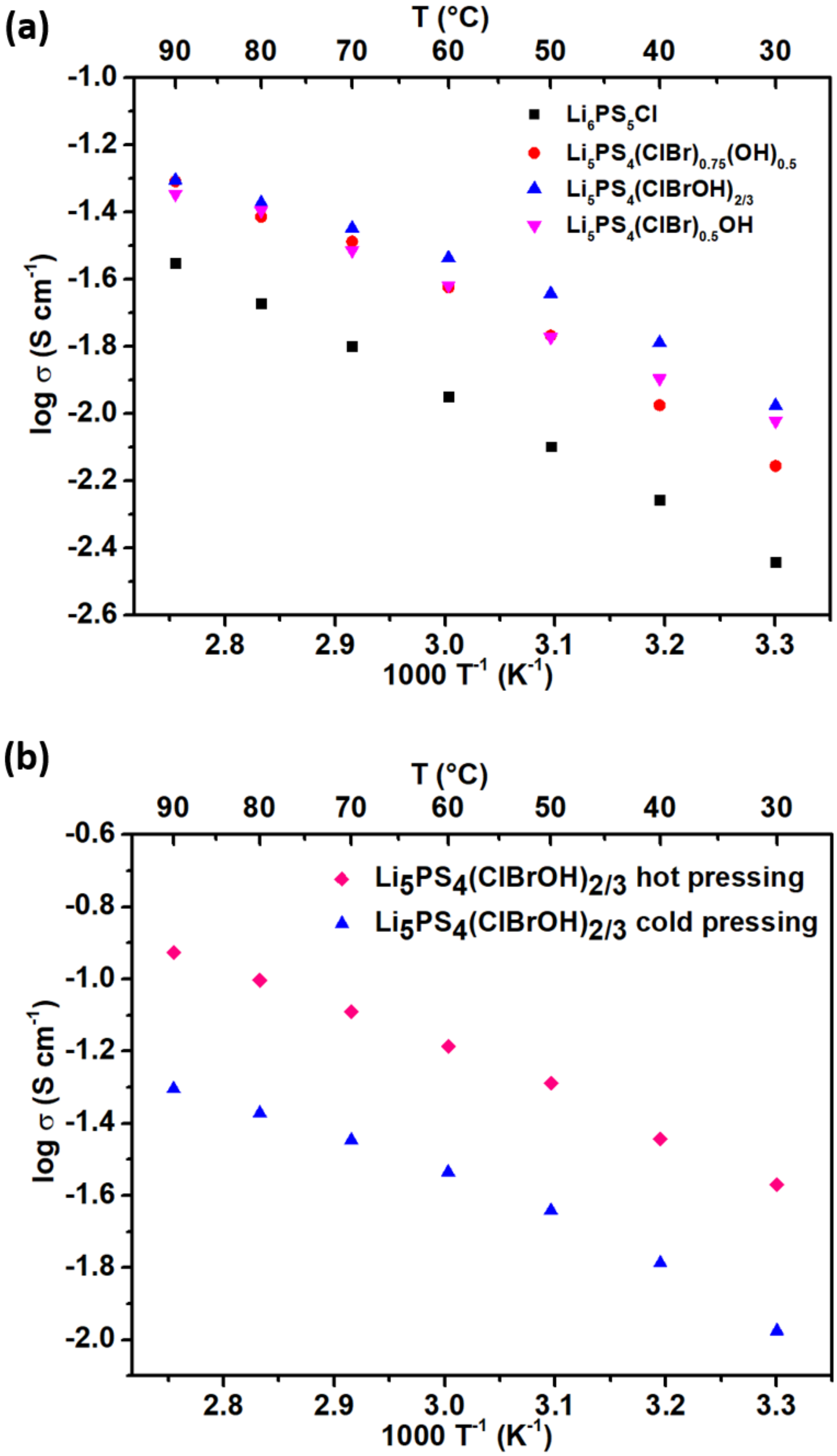

Figure 4.6 Arrhenius plots of (a) $Li_5PS_4(ClBr)_{1-x/2}(OH)_x$ and (b) comparison between ionic conductivity of $Li_5PS_4(ClBrOH)_{2/3}$ pellet obtained by cold- and hot-pressing.

To better understand the Li dynamics within the OH^- doped argyrodite structure, multiple solid-state nuclear magnetic resonance (NMR) spectroscopy techniques were used because of its sensitivity in probing the local chemical environment and Li hopping properties. The ^{31}P magic angle spinning (MAS) NMR spectra (Figure 4.7a) of $Li_5PS_4(ClBr)_{1-x/2}(OH)_x$ show a broad peak around 85 ppm, which demonstrates that P exists in $[PS_4]^{3-}$ tetrahedra form [36]. The broad peak range of ^{31}P implies the wide distribution of chemical shifts, revealing the anion disorder in $Li_5PS_4(ClBr)_{1-x/2}(OH)_x$ [35]. Compared with Li_6PS_5Cl, the resonance of ^{31}P in all the $Li_5PS_4(ClBr)_{1-x/2}(OH)_x$ samples shifts to higher frequency, indicating more paramagnetic component presence around P. On the contrary, the resonance of ^7Li of $Li_5PS_4(ClBr)_{1-x/2}(OH)_x$ (Figure 4.7b) shifts to lower frequency when compared with Li_6PS_5Cl. This is similar to the report of Nazar et al., who tried to create more Li^+ vacancies in Li_6PS_5Cl by substituting more S^{2-} with Cl^- [27]. The replacement of S^{2-} at 4a and 4c sites with Cl^-, Br^- and OH^- decrease the electron density distribution around Li, which potentially promote fast Li diffusion owing to the decreased electrostatic attraction of the mobile Li ions to the rigid framework.

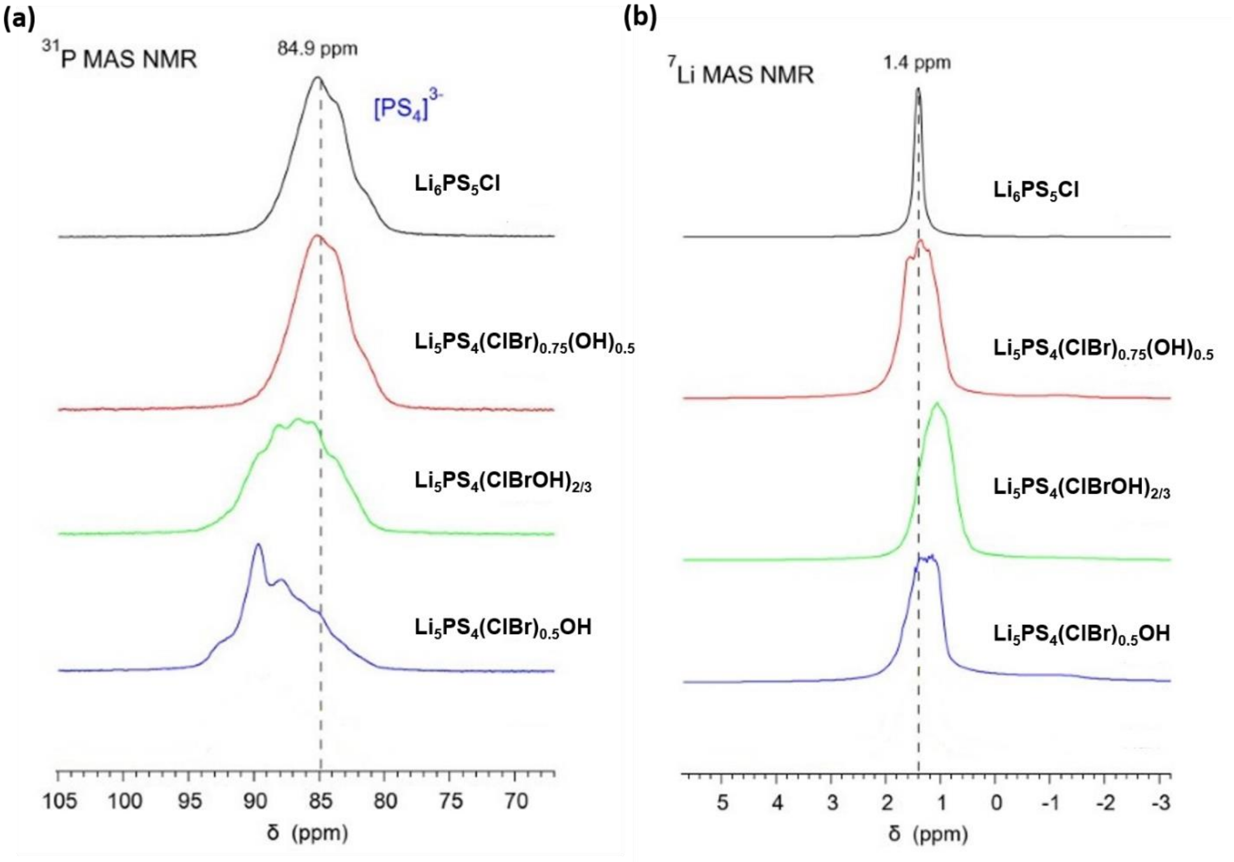

Figure 4.7 MAS NMR spectra of (a) ^{31}P and (b) ^{7}Li of Li_6PS_5Cl, $Li_5PS_4(ClBr)_{0.75}(OH)_{0.5}$, $Li_5PS_4(ClBrOH)_{2/3}$ and $Li_5PS_4(ClBr)_{0.5}OH$

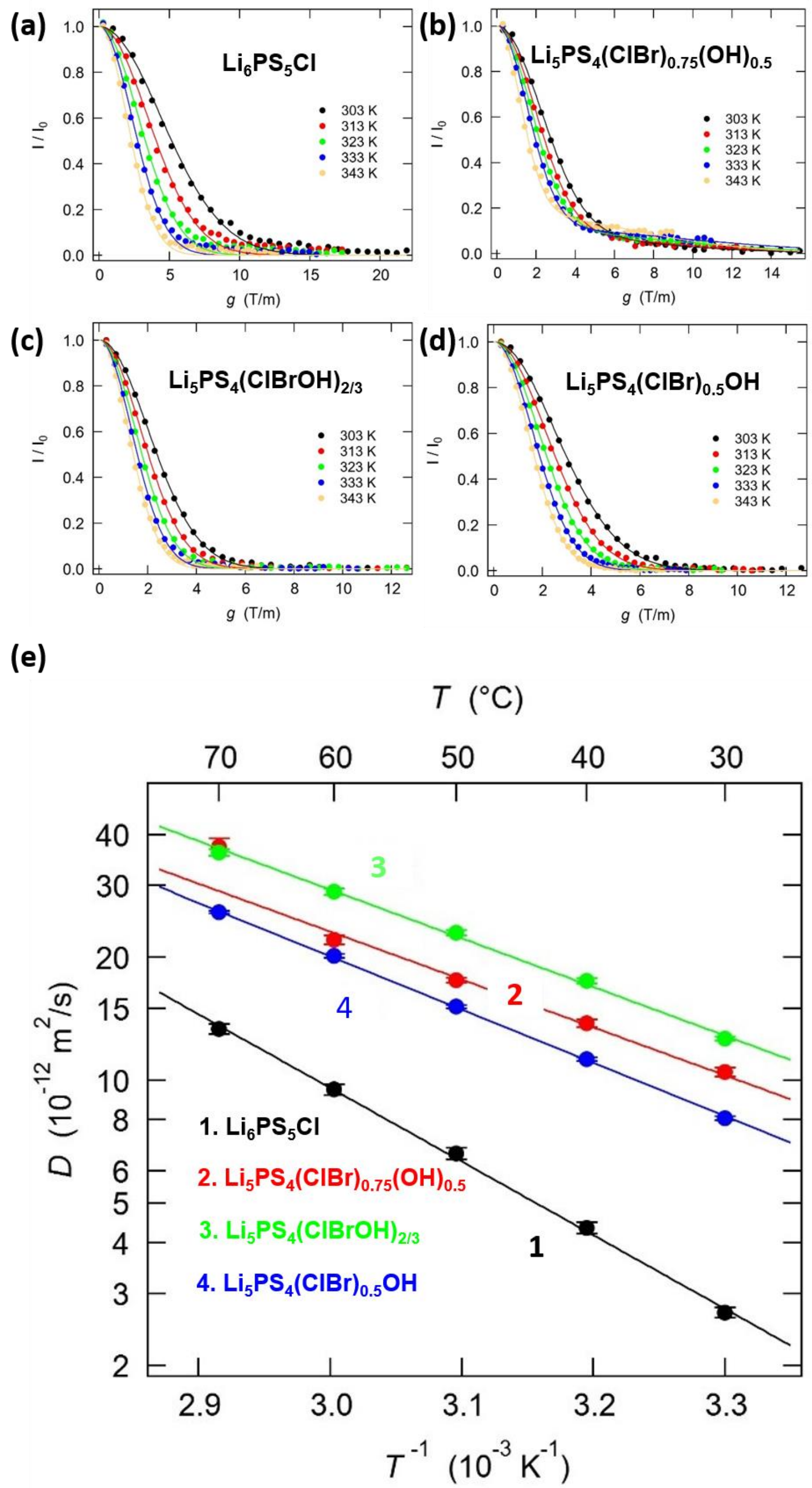

Figure 4.8 PFG NMR of (a) Li_6PS_5Cl; (b) $Li_5PS_4(ClBr)_{0.75}(OH)_{0.5}$; (c) $Li_5PS_4(ClBrOH)_{2/3}$ and (d) $Li_5PS_4(ClBr)_{0.5}OH$. (e) The extracted diffusion coefficients from PFG.

Pulsed field gradient (PFG) NMR experiments were applied to probe Li transport property in long-range. Figure 4.8a-d show echo damping of $Li_5PS_4(ClBr)_{0.75}(OH)_{0.5}$, $Li_5PS_4(ClBrOH)_{2/3}$ and $Li_5PS_4(ClBr)_{0.5}OH$ with Li_6PS_5Cl as reference. The echo damping intensity versus gradient field strength is fitted by the Sejskal-Tanner equation [37] and the extracted tracer diffusion coefficient D^T at different temperature is compared in Figure 4.8 (e). $Li_5PS_4(ClBr)_{0.75}(OH)_{0.5}$, $Li_5PS_4(ClBrOH)_{2/3}$ and $Li_5PS_4(ClBr)_{0.5}OH$ all show much higher D^T than Li_6PS_5Cl at 30 ^oC. $Li_5PS_4(ClBrOH)_{2/3}$ exhibited the highest D^T of 1.3×10^{-11} m^2 s^{-1} at 30 ^oC, which is in consistence with the EIS test results that it shows the highest ionic conductivity. If all the Li ions (2×10^{28} m^{-3}) involved in Li diffusion in totally uncorrelated way, the derived ionic conductivity by Nernst-Einstein equation would be 1.59×10^{-2} S cm^{-1}. This value is a little bit higher than the measured ionic conductivity in cold pressed state (1.06×10^{-2} S cm^{-1}), which also gives hint at the extra resistance from grain boundaries.

The spin lattice relaxation (SLR) NMR experiments were used to probe the Li hoping rate and diffusion activation energy in short range on very short time scales around few nanoseconds. At a magnetic field of 4.7 T, the Larmor frequency ω_0 of ^7Li is 77.8 MHz. As shown in Figure 4.9, T_1^{-1} of $Li_5PS_4(ClBr)_{0.75}(OH)_{0.5}$, $Li_5PS_4(ClBrOH)_{2/3}$ and $Li_5PS_4(ClBr)_{0.5}OH$ all reached the maximum at room temperature, where $\tau\omega_0$ is around 1 [38-39]. Therefore, a hopping rate of 5×10^8 s^{-1} at 298 K is extrapolated. In comparison, the maximum for Li_6PS_5Cl shifts to higher temperature, indicating slower hopping at room temperature. The jump rates obtained from T_1 relaxation experiments can also be used to calculate conductivity. If the speed-limiting process is doublet or intracage hopping, the smaller hopping distance (1.9 Å for doublet and 2.25 Å for intracage hopping) leads to a lower conductivity of 3.5×10^{-3} and 5.0×10^{-3} S cm^{-1} for doublet and intracage hopping, respectively. On the other hand, if intercage jumping is the speed-limiting process, it is reasonable to assume the hopping distance is the length between the cage centers (a = 7.0 Å) [20]. Therefore, D_{298K} is calculated to be 3.9×10^{-11} m^2 s^{-1}, yielding an ionic conductivity around 4.8×10^{-2} S cm^{-1}. This value is in the same order of magnitude as EIS measured results.

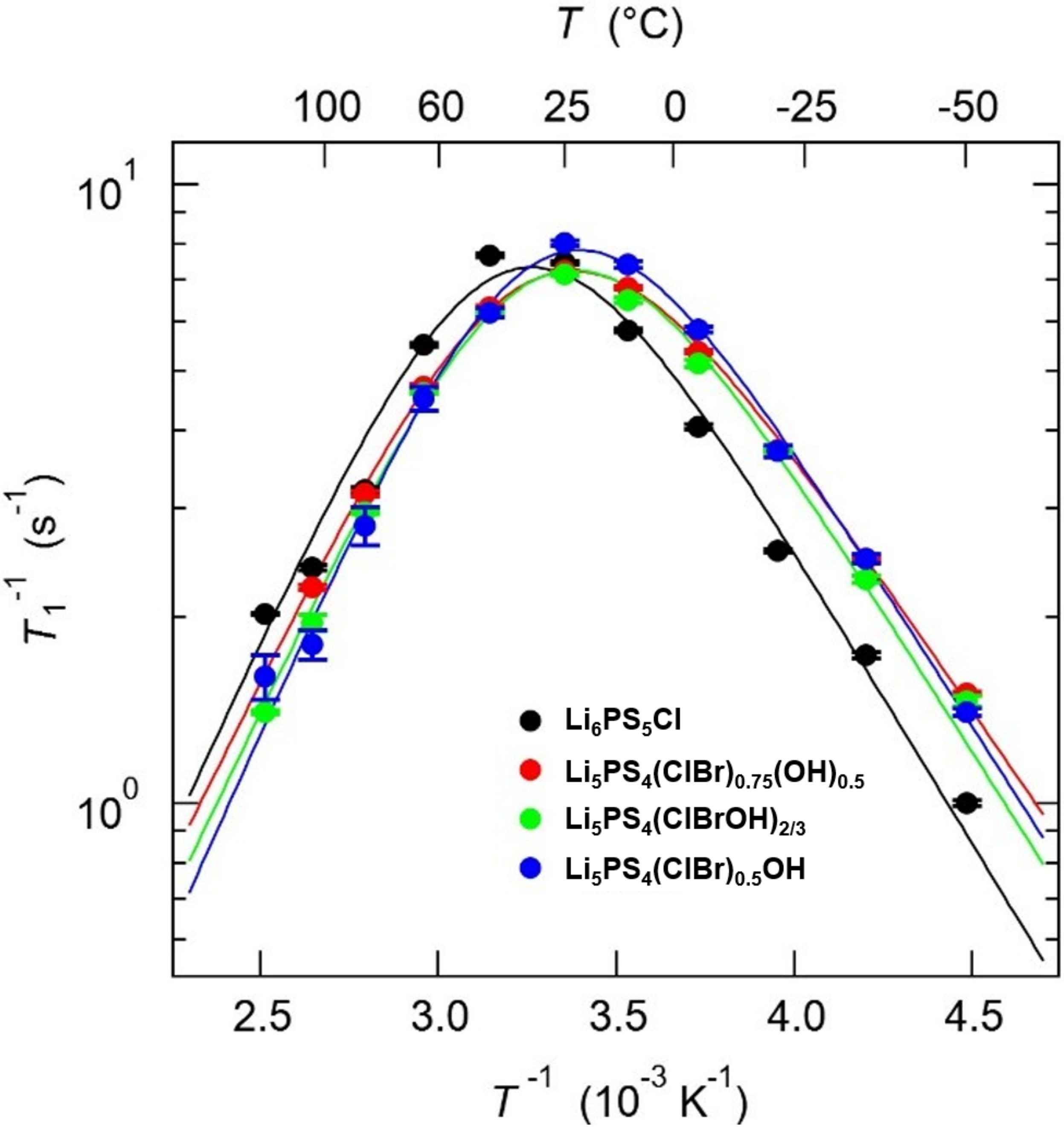

Figure 4.9 ^{7}Li NMR relaxation rates T_1^{-1} of $Li_5PS_4(ClBr)_{0.75}(OH)_{0.5}$, $Li_5PS_4(ClBrOH)_{2/3}$ and $Li_5PS_4(ClBr)_{0.5}OH$.

The activation energies obtained from PFG, SLR NMR experiments and EIS are compared in Table 4.2. The activation energies extracted from PFG NMR experiments are in good consistence with SLR NMR results, while the measured values from EIS tests are a little higher, which may be caused by the grain boundaries. Since $Li_5PS_4(ClBrOH)_{2/3}$ shows the highest ionic conductivity at room temperature with lowest activation energy, it was used for the following experiments.

Table 4.2 Activation energy obtained from different techniques

	E_a (EIS) eV	E_a (PFG) eV	E_a (SLR) eV
$Li_5PS_4(ClBr)_{0.75}(OH)_{0.5}$	0.30	0.23	0.23
$Li_5PS_4(ClBrOH)_{2/3}$	0.26	0.23	0.24
$Li_5PS_4(ClBr)_{0.5}OH$	0.28	0.26	0.26

$Li_5PS_4(ClBrOH)_{2/3}$ was exposed to dry air for one month to evaluate the air stability. Figure 4.10 compares the XRD pattern of fresh-made $Li_5PS_4(ClBrOH)_{2/3}$ and $Li_5PS_4(ClBrOH)_{2/3}$ exposed to dry air for one month. After one-month exposure, the argyrodite structure still remained without obvious impurity phase formation with a drop of ionic conductivity to 5×10^{-3} S/cm. A recent study showed the introduction of oxygen into argyrodite structure may not only improve compatibility with Li metal and oxide cathode, but also enhance the air stability [40]. A similar effect can be expected for be expected for the OH^- doped sample. In $Li_5PS_4(ClBr)_{1-x/2}(OH)_x$, the free S^{2-} are totally replaced, which is beneficial for better stability due to lower sulfur content [27]. Furthermore, since the compositions in $Li_5PS_4(ClBr)_{1-x/2}(OH)_x$ is tunable in a wide range, the decomposed products between SEs and electrode materials can be manipulated by tuning the ratio between Cl, Br and OH$^-$, which provides a new choice for passivation layer design to improve the electrochemical performance of ALSOLIBs.

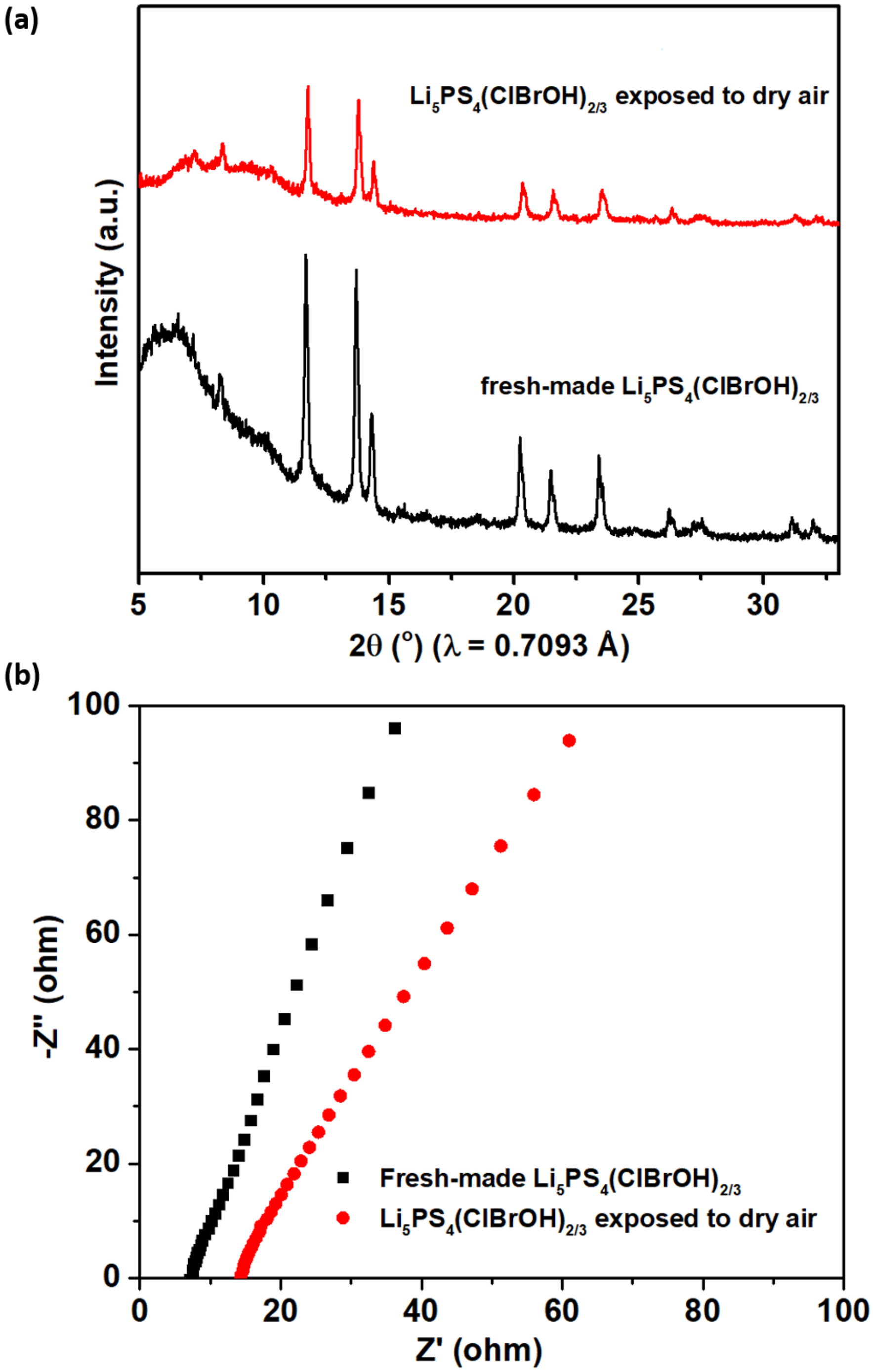

Figure 4.10 (a) XRD patterns and (b) Nyquist plot comparison between fresh-made $Li_5PS_4(ClBrOH)_{2/3}$ and $Li_5PS_4(ClBrOH)_{2/3}$ exposed to dry air for one month.

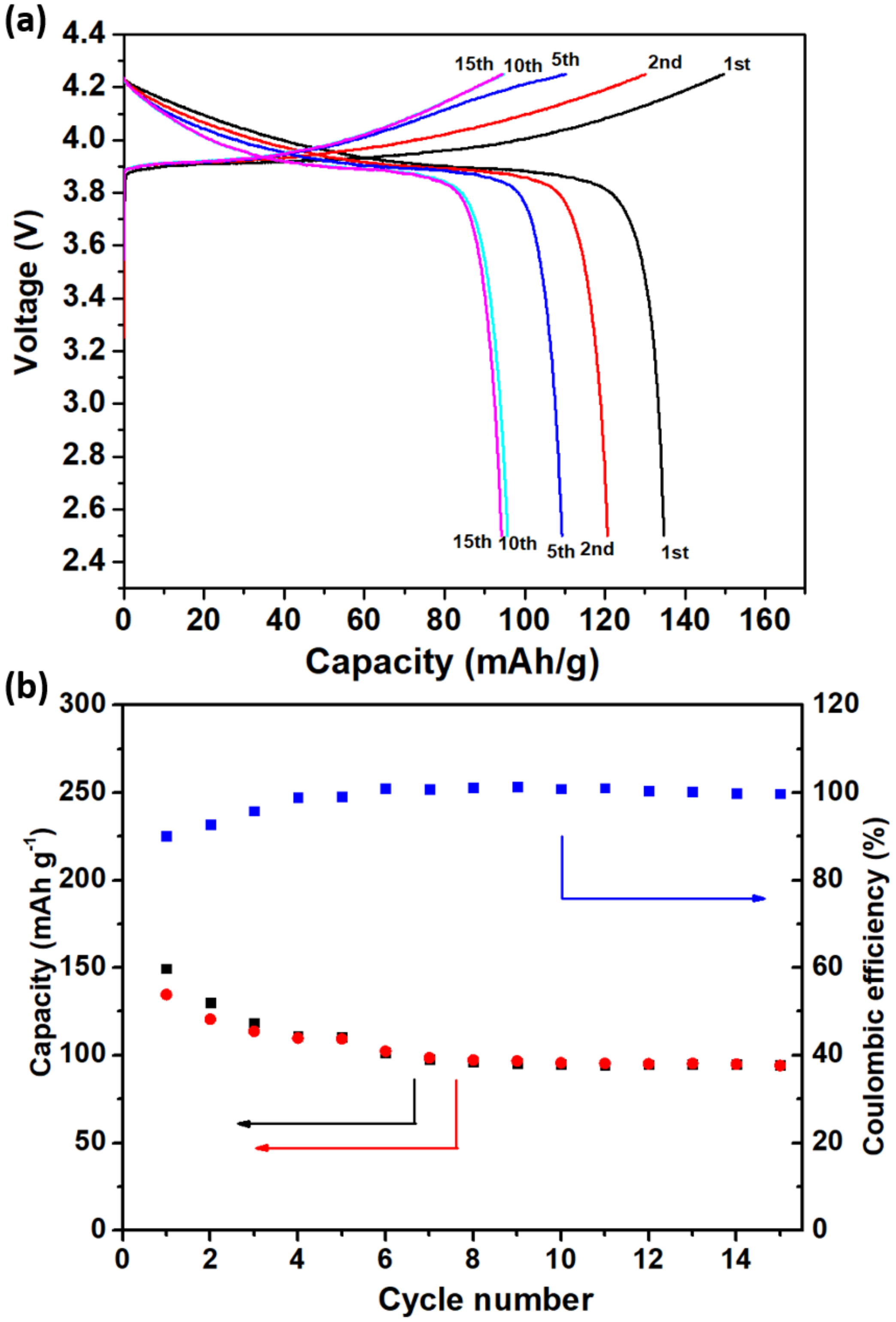

Figure 4.11 (a) Charge-discharge curves of $LiCoO_2/Li_5PS_4(ClBrOH)_{2/3}/Li$ battery for the first, second, 5th, 10th and 15th cycles at 0.1 C. (b) Cycling performance and corresponding Coulombic efficiency.

To evaluate the compatibility of $Li_5PS_4(ClBrOH)_{2/3}$ in full ASOLIBs, $LiCoO_2$/ $Li_5PS_4(ClBrOH)_{2/3}$/Li ALSOLIBs with a cathode mass loading of 10 mg were constructed and cycled at 0.1 C (1 C = 137 mAh g^{-1}). As shown in Figure 4.11, an initial discharge capacity of 134.7 mAh g^{-1} was delivered with an initial coulombic efficiency of 90.03%. The discharged capacity decreased at beginning several cycles and stabilized to 94 mAh/g in the following cycles. The coulombic efficiency also approximated to 100% gradually, which suggests the formation of stable interface between electrode and SEs.

$LiCoO_2$/ $Li_5PS_4(ClBrOH)_{2/3}$/graphite batteries were also assembled and tested at higher current density. Owing to the incorporation of low potential anode graphite, the full batteries still delivered a high voltage around 4 V. With cathode loading of 10 mg, a high initial capacity of 119.4 mAh g^{-1} was delivered with 77% capacity retention after 120 cycles at 1C rate (Fig. 4.12a and 4.12b). In terms of practical applications, batteries with high energy intensity are preferred, which requires increased mass loading of active materials. Here, cells with high cathode mass loading (50 mg) were assembled. With such high mass loading, the cell still delivered an initial capacity of 106.2 mAh g^{-1} at 0.5 C rate at room temperature (Figure 4.12c). Inferior capacity retention was obtained for the high cathode mass loading cell (Figure 4.12d), probably caused by the inhomogeneous distribution of current density due to thicker electrode layer.

The high reversible capacity in $LiCoO_2$/ $Li_5PS_4(ClBrOH)_{2/3}$/graphite batteries operated at relatively high current density proves the fast kinetics of Li ion transportation within the electrolyte and electrolyte-electrode interface. In addition, compared with the $LiCoO_2$/$Li_5PS_4(ClBrOH)_{2/3}$/Li batteries, replacing Li metal with graphite anode lower the initial coulombic efficiency, implying additional side reaction happens at the graphite-electrolyte interface.

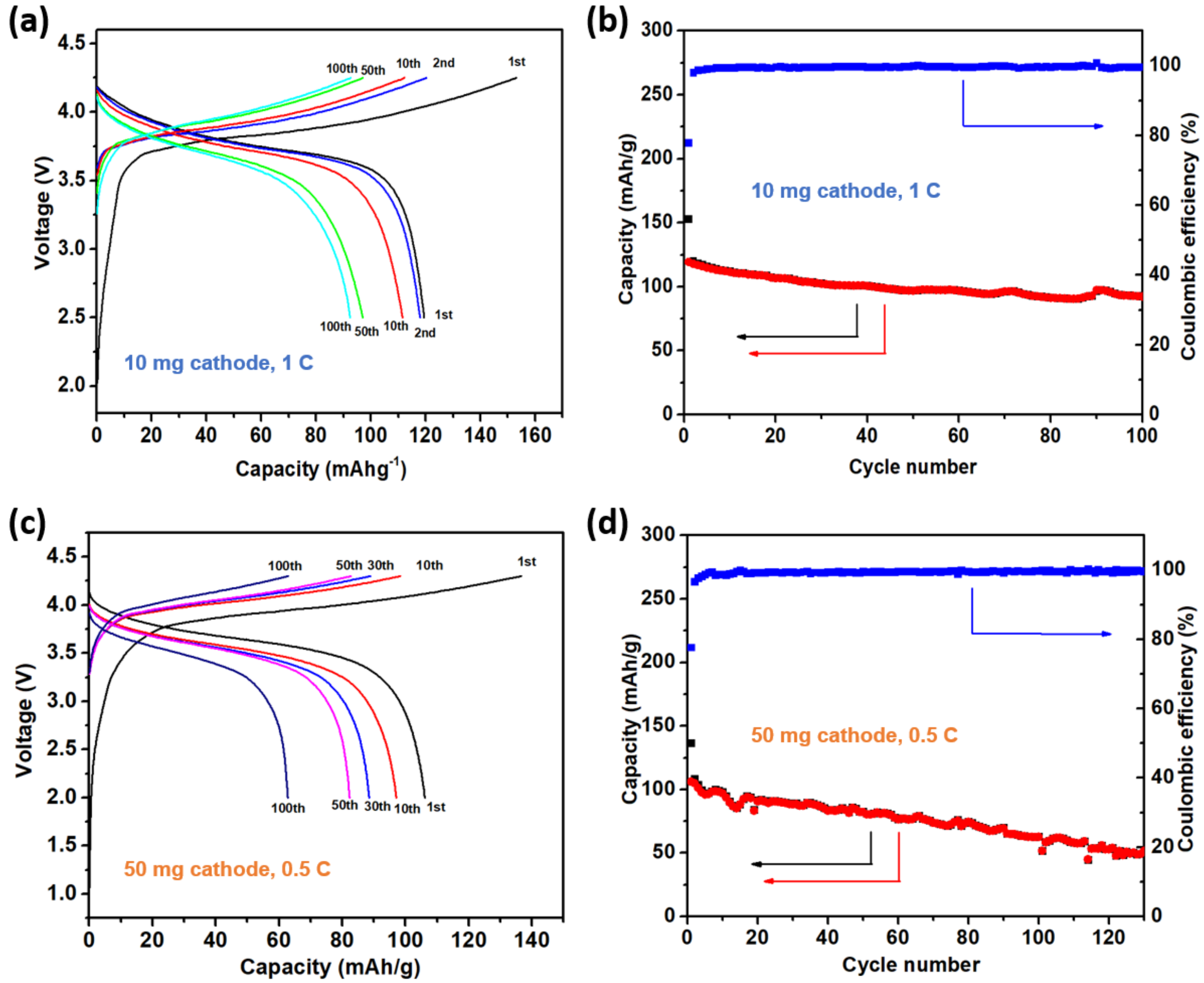

Figure 4.12 Electrochemical performance of $LiCoO_2$/ $Li_5PS_4(ClBrOH)_{2/3}$/graphite cell. (a) Charge-discharge curves of batteries with cathode mass loading of 10 mg and (b) corresponding cycling performance and coulombic efficiency at 1 C rate; (c) Charge-discharge curves of batteries with cathode mass loading of 50 mg and (d) corresponding cycling performance and coulombic efficiency at 0.5 C rate.

The electrochemical performance of $Li_5PS_4(ClBrOH)_{2/3}$ in ALSOLIBs was also evaluated at lower temperature. Because of the low activation energy and high room temperature conductivity of $Li_5PS_4(ClBrOH)_{2/3}$, a moderate ionic conductivity can still be expected at low temperature. Li/$Li_5PS_4(ClBrOH)_{2/3}$/Li symmetric cells were tested at -20 °C at a current density of 0.1 mA cm^{-2} (Figure 4.13). The symmetric cells exhibited good cycling stability over 500 hours with a low potential hysteresis around 0.01 V, corresponding to an internal resistance of ~79 Ω. On the other hand, the EIS test for pure electrolyte pellet with the same thickness (0.640 mm) displayed an ionic conductivity of 1.0×10^{-3} S cm^{-1}, corresponding to an internal resistance of 69 Ω from electrolyte layer. Therefore, the resistance from Li-electrolyte interface is around 10 Ω and kept stable during charge-discharge test.

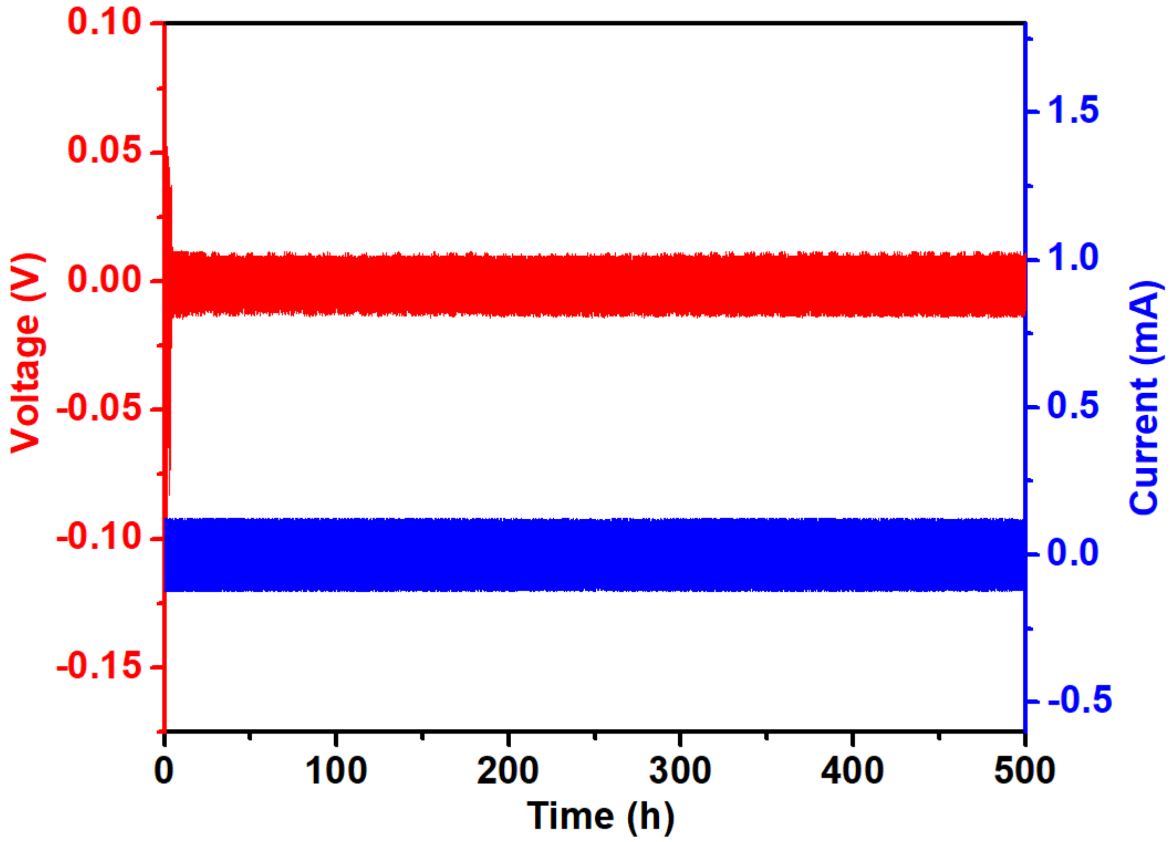

Figure 4.13 Li/$Li_5PS_4(ClBrOH)_{2/3}$/Li symmetric batteries operated at -20 °C.

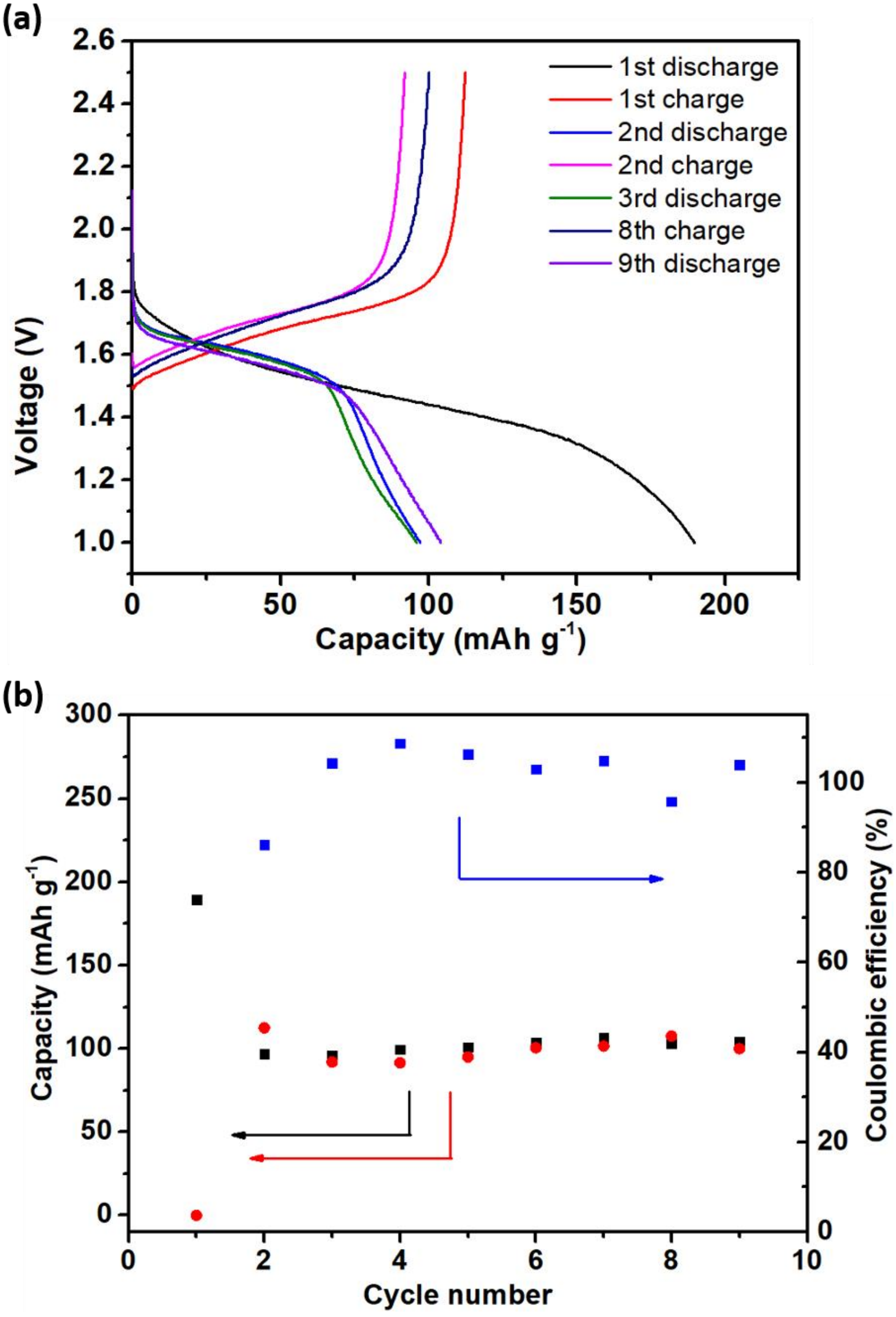

Figure 4.14 Electrochemical performance of TiS_2/ $Li_5PS_4(ClBrOH)_{2/3}$/In-Li batteries. (a) charge-discharge profiles and (b) cycling performance at 15 mA/g at -20 ^oC.

$TiS_2/Li_5PS_4(ClBrOH)_{2/3}/In\text{-}Li$ ALSOLIBs were constructed and operated at -20 ^oC for galvanostatic charge-discharge test at a low current value (15 mA g^{-1}). As shown in Figure 4.14, a high initial discharge capacity of 189.5 mAh g^{-1} was delivered. However, there was a large irreversible capacity during the first cycle and only around half of the inserted Li in TiS_2 can be extracted in the following charge process. In the subsequent cycles, the $TiS_2/Li_5PS_4(ClBrOH)_{2/3}/In\text{-}Li$ cell exhibited a reversible specific capacity around 100 mAh g^{-1}, along with the coulombic efficiency flipping around 100%. In previous studies, ALSOLIBs were seldom tested at temperature below 0 ^oC. Kanno et. al demonstrates an impressive discharge capacity over 120 mAh/g at -30 ^oC with $LiCoO_2$ using LGPS as SEs [15]. However, to the best of our knowledge, there is no report on galvanostatic charge-discharge test for ALSOLIBs at temperature below 0 ^oC. Here, owing to the high ionic conductivity at room temperature and low activation energy, $Li_5PS_4(ClBrOH)_{2/3}$ still shows moderate ionic conductivity at -20 ^oC, which guarantees the all-solid-state batteries operation at low temperature.

4.3 Summary

A series of $Li_5PS_4(ClBr)_{1-x/2}(OH)_x$ compound with high concentration of vacancies in argyrodite structure were successfully stabilized at room temperature with OH^- doping strategy. $Li_5PS_4(ClBr)_{0.75}(OH)_{0.5}$, $Li_5PS_4(ClBrOH)_{2/3}$ and $Li_5PS_4(ClBr)_{0.5}OH$ all show superior ionic conductivity than Li_6PS_5Cl and $Li_5PS_4(ClBrOH)_{2/3}$ exhibits the highest ionic conductivity of 10.6 mS cm^{-1} in cold-pressed state and 26.9 mS cm^{-1} after hot-pressing at 30 ^oC. NMR experiments results indicate the fast Li ion hopping rate and high diffusion coefficient in $Li_5PS_4(ClBr)_{1-x/2}(OH)_x$. The ALSOLIBs utilizing $Li_5PS_4(ClBrOH)_{2/3}$ as SEs exhibit high specific capacity at relatively high current density and ALSOLIBs with high electrode materials mass loading demonstrate high energy density. Even at -20 ^{o}C, the ionic conductivity of $Li_5PS_4(ClBrOH)_{2/3}$ is over 10^{-3} S/cm and $Li/Li_5PS_4(ClBrOH)_{2/3}/Li$ symmetric cell shows low overpotential and extended service life over 500 h. A reversible specific capacity ~100 mAh/g is demonstrated in TiS_2/ $Li_5PS_4(ClBrOH)_{2/3}$/In-Li full cell in the same temperature.

The introduction of OH^- provides a new strategy in boosting the ionic conductivity of SEs in argyrodite structure, which offers wider choice in crystal structure modification for sulfide SEs. The OH^{-1} doped Li argyrodites exhibit high ionic conductivity and feasibility to be operated in wide temperature range, which makes it a promising in applications for energy storage systems.

4.4 Method

The starting materials used for the synthesis of the solid electrolyte $Li_5PS_4(ClBr)_{0.75}(OH)_{0.5}$, $Li_5PS_4(ClBrOH)_{2/3}$, $Li_5PS_4(ClBr)_{0.5}OH$, $Li_5PS_4(ClBr)_{0.25}(OH)_{1.5}$ and $Li_5PS_4(OH)_2$ were Lithium sulfide (Li2S, Sigma-Aldrich, 99.98%), phosphorus pentasulfide (P2S5, Sigma-Aldrich, 99%), lithium chloride (LiCl, Sigma-Aldrich, 99%), lithium bromide (LiBr, 99%) and anhydrous lithium hydroxide (LiOH, Alfa-Aesar, 98%). Li_6PS_5Cl was synthesized by Lithium sulfide (Li2S, Sigma-Aldrich, 99.98%), phosphorus pentasulfide (P_2S_5, Sigma-Aldrich, 99%) and lithium chloride (LiCl, Sigma-Aldrich, 99%). All the reagents were weighed in the appropriate molar ratio and mixed by planetary ball mill (PM 200, Retsch) with a zirconia jar with 10 zirconia balls of 10 mm diameter. The rotation speed was 300 rpm and the milling time was 10h. The ball-milled mixture was then pressed into pellets with a diameter of ½ inch and sealed in a quartz tube. The pellets were heated at 480 ℃ for 10 h and cooled down to room temperature. The cooling rate is 30 ^{o}C/h. The pellets were ground into powder and kept in an Ar-filled glove box for the following characterizations.

All materials were handled under Argon atmosphere during the synthesis, characterization and electrochemical testing processes.

The X-ray diffraction (XRD) data of the powder samples was first collected by using a D8 Advance X-ray Diffractometer (Bruker AXS) with molybdenum radiation ($\lambda_{K\alpha1}$ = 0.7093 Å). *In situ* XRD data of the synthesis process was also collected with using a heat chamber (HTK1200N, Anton Paar) mounted on the diffractometer as follows. The powder of ball-milled mixture of starting materials was filled in quartz capillary in the glove box and sealed. XRD data were collected in each step while the temperature was kept constant during the XRD scan. Synchrotron XRD data were collected at beam line 17-BM-B at the Advanced Photon Source (APS) at Argonne National Laboratory (ANL) with a wavelength of 0.24157 Å and beam line 28-ID-2 at the National Synchrotron Light Source II (NSLS II) at Brookhaven National Laboratory (BNL) with a wavelength of 0.1901 Å. Rietveld refinement against the XRD data was performed with using GSAS II software [41].

Ionic conductivity of the samples was measured with an electrochemical impedance analyzer (VMP3, Bio-Logic) and a custom-built electrochemical cell. Typically, ~130 mg electrolyte powder was pressed into a pellet with a diameter of ½ inch at a pressure of 100 bars. Two stainless steel rods were used as the current collectors. Electrochemical impedance spectra were acquired at different temperature at frequencies between 1MHz and 1Hz and with AC amplitude of 50 mV.

^{6}Li and ^{31}P magic-angle spinning (MAS) NMR spectroscopy was performed with a Bruker Avance 500 MHz spectrometer at a field of 11.7 T, corresponding to resonance frequencies of 73.6 and 202.5 MHz, respectively. Spinning was performed in 2.5 mm zirconia rotors at 20 kHz. The spectra were acquired with a Hahn-echo pulse sequence[42]. The chemical shifts of ^{6}Li and ^{31}P were referenced to an aqueous 1M LiCl solution (0 ppm) and H_3PO_4 (85%, 0 ppm), respectively. Temperature-dependent static ^{7}Li NMR line shapes and spin−lattice relaxation measurements were performed using a Bruker 200 MHz spectrometer at a magnetic field of 4.7 T (77.8 MHz for ^{7}Li), on samples sealed in 10 mm glass vials. The spectra were acquired with a quadrupolar-echo sequence, a $\pi/2$ pulse length of about 3 μs, and a recycle delay of 20 s. ^{7}Li NMR T_1 measurements were performed with a saturation-recovery pulse sequence [39, 43]. ^{7}Li pulsed field-gradient (PFG) NMR measurements were performed on a Bruker Avance 300 MHz spectrometer operated at 116.6 MHz for ^{7}Li, with a Diff50 probe that provides pulsed field gradients up to 30 T/m, and a stimulated-echo pulse sequence with bipolar gradients [44].

For the all-solid-state batteries tested at room temperature, the cathode part consisted of $LiNbO_3$-coated $LiCoO_2$ powder, solid electrolyte and acetylene black powder (AB) (MTI. Corp.). The $LiCoO_2$ (MTI. Corp.) was coated with $LiNbO_3$ by a sol-gel method[45-46].In a typical synthesis, 0.0015 g Li metal was dissolved in 6.85 g anhydrous ethanol (C_2H_5OH, Sigma-Aldrich) and mixed with 0.673 g niobium (V) ethoxide ($Nb(OCH_2CH_3)_5$, Sigma-Aldrich). 3 g $LiCoO_2$ was dispersed in the solution with magnetic stirring. After that, the C_2H_5OH was evaporated at room temperature and the obtained mixture was then calcined at 400 °C for 30 minutes in oxygen atmosphere. The $LiNbO_3$-coated $LiCoO_2$, $Li_5PS_4(ClBrOH)_{2/3}$ and AB were mixed in a weight ratio of 60:35:5 in agate mortar for 10 min as cathode composite. There were two types of anode materials used in all-solid-state batteries tested at room temperature: Li metal and composite graphite anode. The composite graphite anode was prepared by mixing graphite powder (MTI. Corp.) and $Li_5PS_4(ClBrOH)_{2/3}$ in a weight ratio of 40:60. For the fabrication of $LiCoO_2$ cathode/ $Li_5PS_4(ClBrOH)_{2/3}$ electrolyte/graphite anode batteries, 130 mg $Li_5PS_4(ClBrOH)_{2/3}$ was pressed in a PMMA sleeve at 80 bars to form a pellet ½ inch in diameter. Then, 10mg composite cathode and 10mg composite anode were spread on the two sides of pellet respectively and pressed together at 100 bars to form a tri-layer pellet. 50 mg cathode composite and 50 mg anode composite were used in thick electrode cell configuration. To fabricate the all-solid-state cell with Li metal anode, 10 mg $LiCoO_2$ composite cathode and 150 mg $Li_5PS_4(ClBrOH)_{2/3}$ were into a bilayer pellet at 100 bars first and a piece of Li metal was attached on the other side of the bilayer pellet. For the battery tested at -20 ^oC, 10 mg TiS_2- $Li_5PS_4(ClBrOH)_{2/3}$ composite was used as cathode and Li-In alloy was used as anode. The TiS_2- $Li_5PS_4(ClBrOH)_{2/3}$ were weighed in a weight ratio of 1:2 and mixed in in agate mortar for 10 minutes. The In-Li alloy was obtained by pressing a small piece of Li foil to an In foil. The Li/$Li_5PS_4(ClBrOH)_{2/3}$/Li symmetry cell was fabricated by pressing 150 mg $Li_5PS_4(ClBrOH)_{2/3}$ into a pellet at 100 bars and then sandwiched it with two Li foils. The cyclic voltammetry test was operated on a Li/ $Li_5PS_4(ClBrOH)_{2/3}$/stainless steel rods with potential scanning from -0.05 to 5V at a scan rate of 1 mV/s using an electrochemical workstation (VMP3, Bio-Logic), where Li metal was used as counter and reference electrode. In all the cells, stainless steel rods were used as current collectors for both positive and negative electrodes.

The $LiCoO_2$/$Li_5PS_4(ClBrOH)_{2/3}$/Li and $LiCoO_2$/$Li_5PS_4(ClBrOH)_{2/3}$/graphite cell was measured at 0.1C and 1C rate (137 mA/g) between 2.5-4.25 V and 2-4.25 V, respectively, using a battery test system (LAND, C2001A) at room temperature. The thick electrode configuration cell was tested at 0.5 C between 2-4.3 V at room temperature. The TiS_2/$Li_5PS_4(ClBrOH)_{2/3}$/In-Li cell was tested at 50 μA between 1-2.5 V at -20 ^oC. The cell capacity was calculated based on the weight of the active material. Li/ $Li_5PS_4(ClBrOH)_{2/3}$/Li symmetric cell was cycled at a current density of 0.1 mA/cm^2 for 0.5 h in each half cycle at -20 ^oC.

4.5 References

[1] Zhang, Z.; Shao, Y.; Lotsch, B.; Hu, Y.-S.; Li, H.; Janek, J.; Nazar, L. F.; Nan, C.-W.; Maier, J.; Armand, M.; Chen, L., New horizons for inorganic solid state ion conductors. *Energy & Environmental Science* **2018,** *11* (8), 1945-1976.

[2] Zhu, Y.; He, X.; Mo, Y., First principles study on electrochemical and chemical stability of solid electrolyte–electrode interfaces in all-solid-state Li-ion batteries. *Journal of Materials Chemistry A* **2016,** *4* (9), 3253-3266.

[3] Mo, Y.; Ong, S. P.; Ceder, G., First Principles Study of the Li10GeP2S12 Lithium Super Ionic Conductor Material. *Chemistry of Materials* **2012,** *24* (1), 15-17.

[4] Kato, A.; Yamamoto, M.; Sakuda, A.; Hayashi, A.; Tatsumisago, M., Mechanical Properties of Li2S–P2S5 Glasses with Lithium Halides and Application in All-Solid-State Batteries. *ACS Applied Energy Materials* **2018,** *1* (3), 1002-1007.

[5] Sakuda, A.; Hayashi, A.; Tatsumisago, M., Sulfide Solid Electrolyte with Favorable Mechanical Property for All-Solid-State Lithium Battery. *Scientific Reports* **2013,** *3*, 2261.

[6] Kanno, R.; Murayama , M., Lithium Ionic Conductor Thio-LISICON: The Li2 S - GeS2 - P 2 S 5 System. *Journal of The Electrochemical Society* **2001,** *148* (7), A742-A746.

[7] Yu, C.; Ganapathy, S.; van Eck, E. R. H.; van Eijck, L.; Basak, S.; Liu, Y.; Zhang, L.; Zandbergen, H.; Wagemaker, M., Revealing the relation between the structure, Li-ion conductivity and solid-state battery performance of the argyrodite Li6PS5Br solid electrolyte. *Journal of Materials Chemistry A* **2017**.

[8] Deiseroth, H.-J.; Maier, J.; Weichert, K.; Nickel, V.; Kong, S.-T.; Reiner, C., Li7PS6 and Li6PS5X (X: Cl, Br, I): Possible Three-dimensional Diffusion Pathways for Lithium Ions and Temperature Dependence of the Ionic Conductivity by Impedance Measurements. *Zeitschrift für anorganische und allgemeine Chemie* **2011,** *637* (10), 1287-1294.

[9] Rao, R. P.; Adams, S., Studies of lithium argyrodite solid electrolytes for all-solid-state batteries. *physica status solidi (a)* **2011,** *208* (8), 1804-1807.

[10] Yamane, H.; Shibata, M.; Shimane, Y.; Junke, T.; Seino, Y.; Adams, S.; Minami, K.; Hayashi, A.; Tatsumisago, M., Crystal structure of a superionic conductor, Li7P3S11. *Solid State Ionics* **2007,** *178* (15), 1163-1167.

[11] Kamaya, N.; Homma, K.; Yamakawa, Y.; Hirayama, M.; Kanno, R.; Yonemura, M.; Kamiyama, T.; Kato, Y.; Hama, S.; Kawamoto, K.; Mitsui, A., A lithium superionic conductor. *Nat Mater* **2011,** *10* (9), 682-686.

[12] Sun, Y.; Suzuki, K.; Hori, S.; Hirayama, M.; Kanno, R., Superionic Conductors: Li10+δ[SnySi1−y]1+δP2−δS12 with a Li10GeP2S12-type Structure in the Li3PS4–Li4SnS4–Li4SiS4 Quasi-ternary System. *Chemistry of Materials* **2017,** *29* (14), 5858-5864.

[13] Bron, P.; Johansson, S.; Zick, K.; Schmedt auf der Günne, J.; Dehnen, S.; Roling, B., Li10SnP2S12: An Affordable Lithium Superionic Conductor. *Journal of the American Chemical Society* **2013,** *135* (42), 15694-15697.

[14] Hori, S.; Suzuki, K.; Hirayama, M.; Kato, Y.; Saito, T.; Yonemura, M.; Kanno, R., Synthesis, structure, and ionic conductivity of solid solution, Li10+δM1+δP2−δS12 (M = Si, Sn). *Faraday Discussions* **2014,** *176* (0), 83-94.

[15] Kato, Y.; Hori, S.; Saito, T.; Suzuki, K.; Hirayama, M.; Mitsui, A.; Yonemura, M.; Iba, H.; Kanno, R., High-power all-solid-state batteries using sulfide superionic conductors. **2016,** *1*, 16030.

[16] Zhu, Y.; He, X.; Mo, Y., Origin of Outstanding Stability in the Lithium Solid Electrolyte Materials: Insights from Thermodynamic Analyses Based on First-Principles Calculations. *ACS Applied Materials & Interfaces* **2015,** *7* (42), 23685-23693.

[17] Wenzel, S.; Randau, S.; Leichtweiß, T.; Weber, D. A.; Sann, J.; Zeier, W. G.; Janek, J., Direct Observation of the Interfacial Instability of the Fast Ionic Conductor Li10GeP2S12 at the Lithium Metal Anode. *Chemistry of Materials* **2016,** *28* (7), 2400-2407.

[18] Ong, S. P.; Mo, Y.; Richards, W. D.; Miara, L.; Lee, H. S.; Ceder, G., Phase stability, electrochemical stability and ionic conductivity of the Li10±1MP2X12 (M = Ge, Si, Sn, Al or P, and X = O, S or Se) family of superionic conductors. *Energy & Environmental Science* **2013,** *6* (1), 148-156.

[19] Wenzel, S.; Sedlmaier, S. J.; Dietrich, C.; Zeier, W. G.; Janek, J., Interfacial reactivity and interphase growth of argyrodite solid electrolytes at lithium metal electrodes. *Solid State Ionics* **2018,** *318*, 102-112.

[20] de Klerk, N. J. J.; Rosłoń, I.; Wagemaker, M., Diffusion Mechanism of Li Argyrodite Solid Electrolytes for Li-Ion Batteries and Prediction of Optimized Halogen Doping: The Effect of Li Vacancies, Halogens, and Halogen Disorder. *Chemistry of Materials* **2016,** *28* (21), 7955-7963.

[21] Kraft, M. A.; Culver, S. P.; Calderon, M.; Böcher, F.; Krauskopf, T.; Senyshyn, A.; Dietrich, C.; Zevalkink, A.; Janek, J.; Zeier, W. G., Influence of Lattice Polarizability on the Ionic Conductivity in the Lithium Superionic Argyrodites Li6PS5X (X = Cl, Br, I). *Journal of the American Chemical Society* **2017,** *139* (31), 10909-10918.

[22] Deiseroth, H.-J.; Kong, S.-T.; Eckert, H.; Vannahme, J.; Reiner, C.; Zaiß, T.; Schlosser, M., Li6PS5X: A Class of Crystalline Li-Rich Solids With an Unusually High Li+ Mobility. *Angewandte Chemie International Edition* **2008,** *47* (4), 755-758.

[23] On the influence of lattice polarizability on the ionic conductivity in the lithium superionic argyrodites Li6PS5X (X = Cl, Br, I). *Journal of the American Chemical Society* **2017**.

[24] Zhou, L.; Park, K.-H.; Sun, X.; Lalère, F.; Adermann, T.; Hartmann, P.; Nazar, L. F., Solvent-Engineered Design of Argyrodite Li6PS5X (X = Cl, Br, I) Solid Electrolytes with High Ionic Conductivity. *ACS Energy Letters* **2019,** *4* (1), 265-270.

[25] Minafra, N.; Culver, S. P.; Krauskopf, T.; Senyshyn, A.; Zeier, W. G., Effect of Si substitution on the structural and transport properties of superionic Li-argyrodites. *Journal of Materials Chemistry A* **2018,** *6* (2), 645-651.

[26] Kraft, M. A.; Ohno, S.; Zinkevich, T.; Koerver, R.; Culver, S. P.; Fuchs, T.; Senyshyn, A.; Indris, S.; Morgan, B. J.; Zeier, W. G., Inducing High Ionic Conductivity in the Lithium Superionic Argyrodites Li6+xP1–xGexS5I for All-Solid-State Batteries. *Journal of the American Chemical Society* **2018,** *140* (47), 16330-16339.

[27] Adeli, P.; Bazak, J. D.; Park, K. H.; Kochetkov, I.; Huq, A.; Goward, G. R.; Nazar, L. F., Boosting Solid-State Diffusivity and Conductivity in Lithium Superionic Argyrodites by Halide Substitution. *Angewandte Chemie International Edition 0* (0).

[28] Chen, H. M.; Maohua, C.; Adams, S., Stability and ionic mobility in argyrodite-related lithium-ion solid electrolytes. *Physical Chemistry Chemical Physics* **2015,** *17* (25), 16494-16506.

[29] Bérardan, D.; Franger, S.; Meena, A. K.; Dragoe, N., Room temperature lithium superionic conductivity in high entropy oxides. *Journal of Materials Chemistry A* **2016,** *4* (24), 9536-9541.

[30] Rost, C. M.; Sachet, E.; Borman, T.; Moballegh, A.; Dickey, E. C.; Hou, D.; Jones, J. L.; Curtarolo, S.; Maria, J.-P., Entropy-stabilized oxides. *Nature Communications* **2015,** *6* (1), 8485.

[31] Zhang, R.-Z.; Gucci, F.; Zhu, H.; Chen, K.; Reece, M. J., Data-Driven Design of Ecofriendly Thermoelectric High-Entropy Sulfides. *Inorganic Chemistry* **2018,** *57* (20), 13027-13033.

[32] Homma, K.; Yonemura, M.; Kobayashi, T.; Nagao, M.; Hirayama, M.; Kanno, R., Crystal structure and phase transitions of the lithium ionic conductor Li3PS4. *Solid State Ionics* **2011,** *182* (1), 53-58.

[33] Liu, Z.; Zinkevich, T.; Indris, S.; He, X.; Liu, J.; Xu, W.; Bai, J.; Xiong, S.; Mo, Y.; Chen, H., Li15P4S16Cl3, a Lithium Chlorothiophosphate as a Solid-State Ionic Conductor. *Inorganic Chemistry* **2020,** *59* (1), 226-234.

[34] Yu, C.; Hageman, J.; Ganapathy, S.; van Eijck, L.; Zhang, L.; Adair, K. R.; Sun, X.; Wagemaker, M., Tailoring Li6PS5Br ionic conductivity and understanding of its role in cathode mixtures for high performance all-solid-state Li–S batteries. *Journal of Materials Chemistry A* **2019,** *7* (17), 10412-10421.

[35] Hanghofer, I.; Brinek, M.; Eisbacher, S. L.; Bitschnau, B.; Volck, M.; Hennige, V.; Hanzu, I.; Rettenwander, D.; Wilkening, H. M. R., Substitutional disorder: structure and ion dynamics of the argyrodites Li6PS5Cl, Li6PS5Br and Li6PS5I. *Physical Chemistry Chemical Physics* **2019,** *21* (16), 8489-8507.

[36] Synthesis, Structural Characterization, and Lithium Ion Conductivity of the Lithium Thiophosphate Li2P2S6. *Inorganic Chemistry* **2017**.

[37] Stejskal, E. O.; Tanner, J. E., Spin Diffusion Measurements: Spin Echoes in the Presence of a Time-Dependent Field Gradient. *The Journal of Chemical Physics* **1965,** *42* (1), 288-292.

[38] Bloembergen, N.; Purcell, E. M.; Pound, R. V., Relaxation Effects in Nuclear Magnetic Resonance Absorption. *Physical Review* **1948,** *73* (7), 679-712.

[39] Paul Heitjans; Sylvio Indris; Wilkening, M., Solid-State Diffusion and NMR. *Diffusion Fundamentals* **2005,** *2* (45), 1-20.

[40] Zhang, Z.; Zhang, L.; Yan, X.; Wang, H.; Liu, Y.; Yu, C.; Cao, X.; van Eijck, L.; Wen, B., All-in-one improvement toward Li6PS5Br-Based solid electrolytes triggered by compositional tune. *Journal of Power Sources* **2019,** *410-411*, 162-170.

[41] Toby, B. H.; Von Dreele, R. B., GSAS-II: the genesis of a modern open-source all purpose crystallography software package. *Journal of Applied Crystallography* **2013,** *46* (2), 544-549.

[42] Duer, M. J., *Introduction to Solid-State NMR Spectroscopy*. Blackwell Publishing: Oxford: 2004.

[43] Fukushima, E.; Roeder, S. B. W., *Experimental Pulse NMR – A Nuts and Bolts Approach*. Addison-Wesley: Reading: 1981.

[44] Price, W. S., Pulsed-field gradient nuclear magnetic resonance as a tool for studying translational diffusion: Part 1. Basic theory. *Concepts in Magnetic Resonance* **1997,** *9* (5), 299-336.

[45] Ohta, N.; Takada, K.; Sakaguchi, I.; Zhang, L.; Ma, R.; Fukuda, K.; Osada, M.; Sasaki, T., LiNbO3-coated LiCoO2 as cathode material for all solid-state lithium secondary batteries. *Electrochemistry Communications* **2007,** *9* (7), 1486-1490.

[46] Ohta, N.; Takada, K.; Zhang, L.; Ma, R.; Osada, M.; Sasaki, T., Enhancement of the High-Rate Capability of Solid-State Lithium Batteries by Nanoscale Interfacial Modification. *Advanced Materials* **2006,** *18* (17), 2226-2229.

CHAPTER 5. Lithium Sublattice Tuning and Grain Boundary Improving in Mixed Halide Solid Electrolyte $Li_3Y(Br_3Cl_3)$

5.1 Introduction

All-solid-state-batteries (ASSBs) are being actively investigated as the next generation power sources for electric vehicles (EVs), owing to its much better safely properties and potentially much higher energy density than conventional Li-ion batteries (LIBs) [1-2]. Solid electrolyte (SE) is the key enabler and currently the major hurdle for the commercialization of ASSBs. Halides with a general formula of Li_3MX_6 (M= In, Y, Sc, or Er, etc., X=Cl or Br) represent an emerging group of SEs, which owns advantages in cost, air/moisture stability and mass productivity over sulfide SEs and advantages in ionic conductivity over oxide SEs. Yet, their conduction mechanism and detailed structure-property relationship need further explorations. There is still large room to improve their performances. They were studied and explored as solid electrolyte in 1990s-2000s [3-4], though only low to moderate conductivities reported then. In 2018, Asano et al. reported boosted r.t. conductivities achieved in Li_3YCl_6 (LYC) of 0.51 mS/cm and in Li_3YBr_6 (LYB) of 1.7 mS/cm, respectively, via a different synthesis protocol [5], implying synthesis condition and details in the crystal structure may play important roles in ionic conduction. Recently, Zeier et al. also reported that the disordering of Er/Y sites in Li_3ErCl_6 and Li_3YCl_6 samples resulted from aggressive ball-milling may have pronounced positive impacts to the ionic conductivity [6]. Efforts have also been made in designing the chemical composition to improve the ionic conductivity or moisture stability [7]. By aliovalent doping or cation alloying, high r.t. conductivity up to 3 mS/cm were achieved [8-9]. Yet, the current highest r.t. conductivities achieved in halides are still about one order of magnitude lower than those in the state-of-the-art sulfides, such as $Li_{10}GeP_2S_{12}$ family

[10-11] and lithium argyrodite family SEs [12] . Here we report our recent findings in promoting the conductivity of halides by designs of anion mixing and grain boundary (GB) enhancement. Very high r.t. ionic conductivity of 7.2 mS/cm was achieved in novel $Li_3YBr_3Cl_3$ (LYBC) compound benefiting from the fast 3D diffusion pathways promoted by the high population of Li at the tetrahedral sites and a drastically enhanced GB resulted from hot-pressing. These findings also explain the discrepancies in the diffusion activation energies previously reported in theoretical [13] and experimental [5] investigations and provide new insights of these halide SEs.

5.2 Results and Discussion

LYBC and $Li_3ErBr_3Cl_3$ (LEBC) samples were synthesized by using high energy ball-milling and following hot-pressing. Figure 5.1a shows the synchrotron X-ray diffraction (XRD) patterns of LYBC after ball-milling, and LYBC and LEBC after 200 °C hot-pressing. Li_3MX_6 compounds can crystalize in different structures depending on the cation and anions, including monoclinic (Li_3ErBr_6 type, *C2/m*), orthorhombic (Li_3YbCl_6 type, *Pnma*) and trigonal (Li_3ErCl_6 type, $P\bar{3}m1$) phases [3], which affects their ionic conductivities. Asano et al. [5] reported that in their synthesis LYC yielded the trigonal phase, while LYB yielded the monoclinic phase. While in our synthesis of LYBC, after ball-milling, a mixture of LYC-like and LYB-like phases was obtained. The broad Bragg peaks suggests a very fine crystallite size and perhaps some strain resulted from the mechanical synthesis. The ^7Li solid state NMR spectrum also shows a broad feature in the isotropic resonances, which is typical for nanomaterials and amorphous phases (Figure 5.1b). After hot-pressing at 200 °C for 0.5 hour with 44.1 MPa pressure, the mixture transformed into a single LYB-like phase (Figure 5.1a). The ^7Li NMR spectrum also shows a much narrower resonance near 0 ppm, indicating a more uniform local environment than the ball-milled sample.

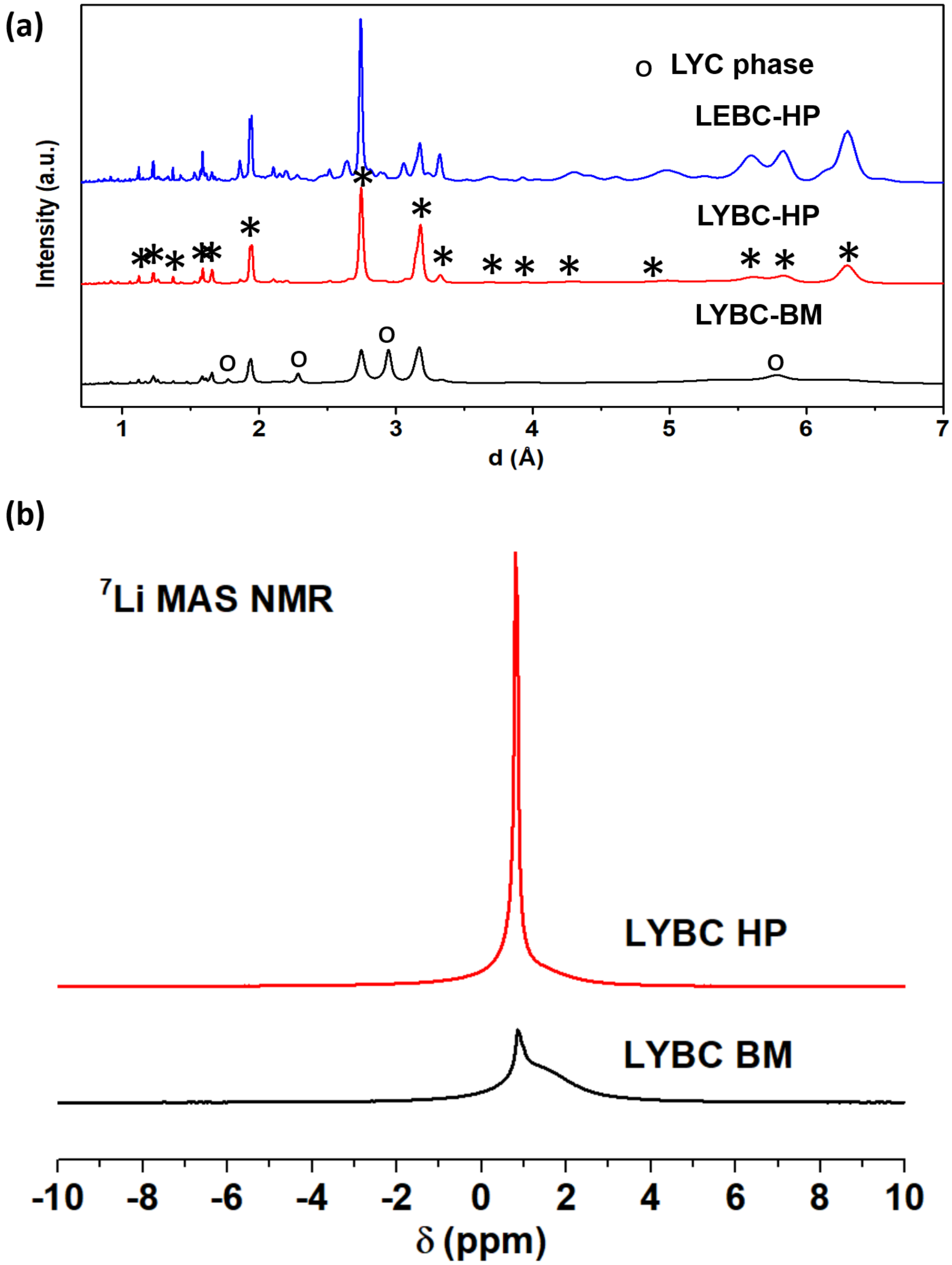

Figure 5.1 (a) XRD diffraction patterns of ball-milled LYBC (LYBC-BM), ball-milled LYBC after 200 ^{o}C hot-press (LYBC-HP), and LEBC after 200 ^{o}C hot-press (LEBC-HP) samples (b) ^{7}Li MAS NMR of LYBC-BM and LYBC-HP

The XRD pattern of this LYB-like phase can be refined using the structural model reported by Asano et al. by replacing half of the Br with Cl (Figure 5.2), where all Li ions solely locate in the octahedral sites (4*g* and 4*h*). However, given the relative insensitivity of X-ray for light atoms such as Li, we also conducted neutron diffraction to elucidate the details of the structure. Our refinement against neutron data revealed unprecedented interesting features in the crystal structure of LYBC.

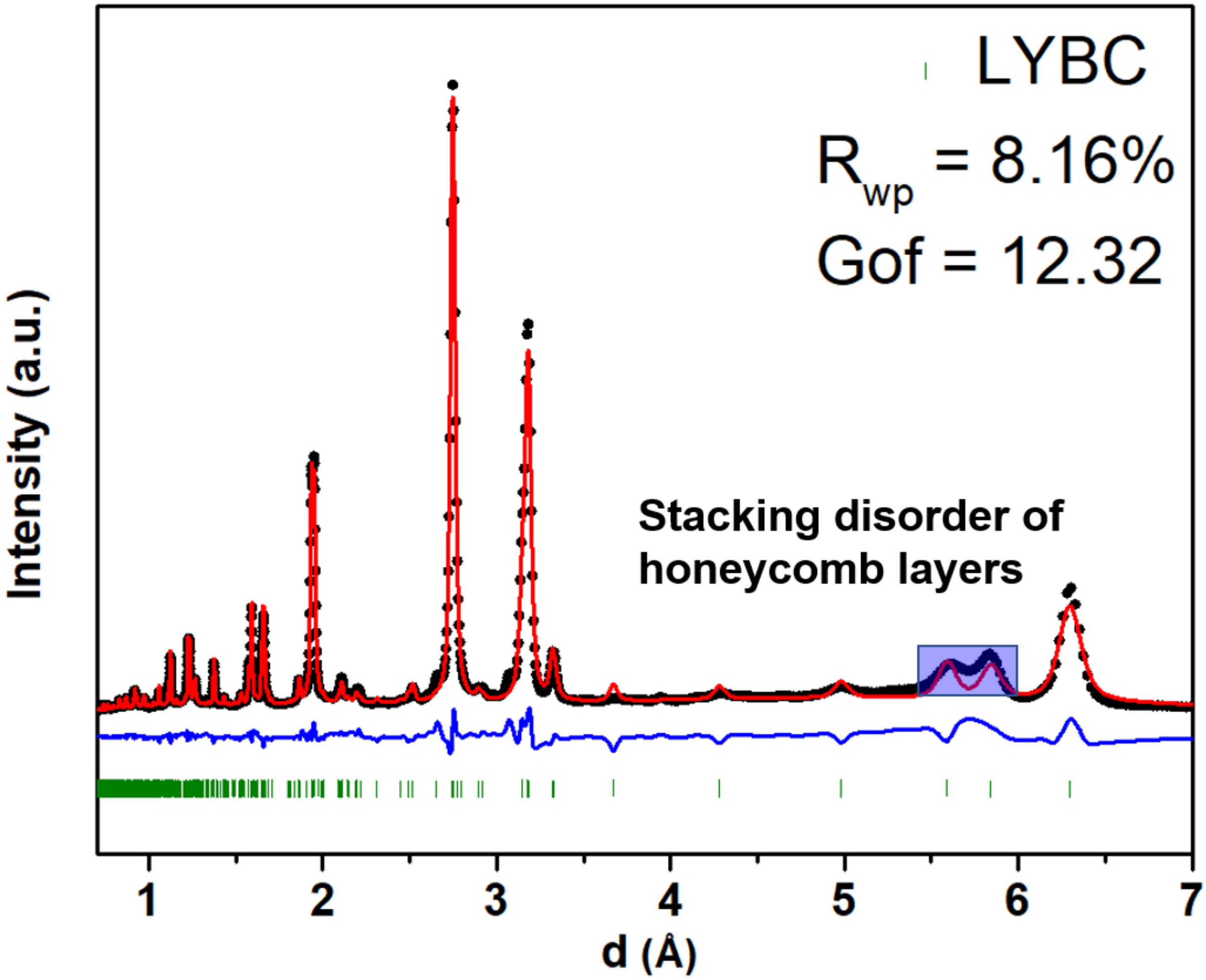

Figure 5.2 Rietveld refinement results of LYBC after hot-pressing (LYBC-HP) against synchrotron X-ray diffraction patterns.

First, the average structure is similar to conventional O3-type $LiCoO_2$ structure [14] with alternating stacking of two types of slabs, but with more vacancies (~1/3) in both slabs. In $LiCoO_2$, the transition metal (TM) slab contains only CoO_6 octahedra and the Li slab only contains LiO_6

octahedra. In this compound of Li_3YX_6, which can be re-written as $Li_{1/3}(Li_{2/3}Y_{1/3})X_2$. The TM slab contains both YX6 and LiX6 octahedra and some vacant octahedral sites, and the Li slab also contains LiX6 octahedra and some vacant octahedral sites (Figure 5.3). The asymmetric peak shapes in 5.5-6 Å range in synchrotron (Figure 5.2) suggests a honeycomb-type local ordering within the TM layer among Y and Li/vacancies, similar to what was observed in Li_2MnO_3 and Li-Mn rich cathode materials [15]. This is not a surprise, owing to the very different valence between Li^+/vacancy and Y^{3+} and the static repulsion among the cations [16]. The local honeycomb ordering within the ab-plane is further confirmed by using X-ray pair distribution function analysis (PDF) with varying fitting range (Figure 5.4). The occupancy of Y at 2a site is close to 1 in short range (r< 20 Å), indicating a well-developed in-plane honeycomb ordering at local scale. While the decreased occupancy in the longer range indicates the effects of the stacking faults along c-axis. Similar locally ordered and long-range disordered (along c-direction via stacking faults) structure is also observed in layered oxides such as $Na_3Ni_2BiO_6$[17] and $Na(Ni_{2/3}Sb_{1/3})O_2$[18].

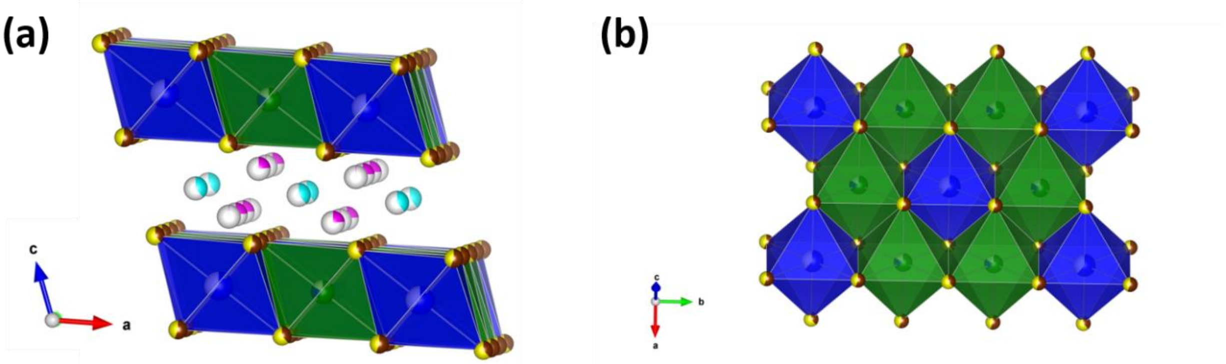

Figure 5.3 Crystal structure of LYBC-HP viewed along different orientations.

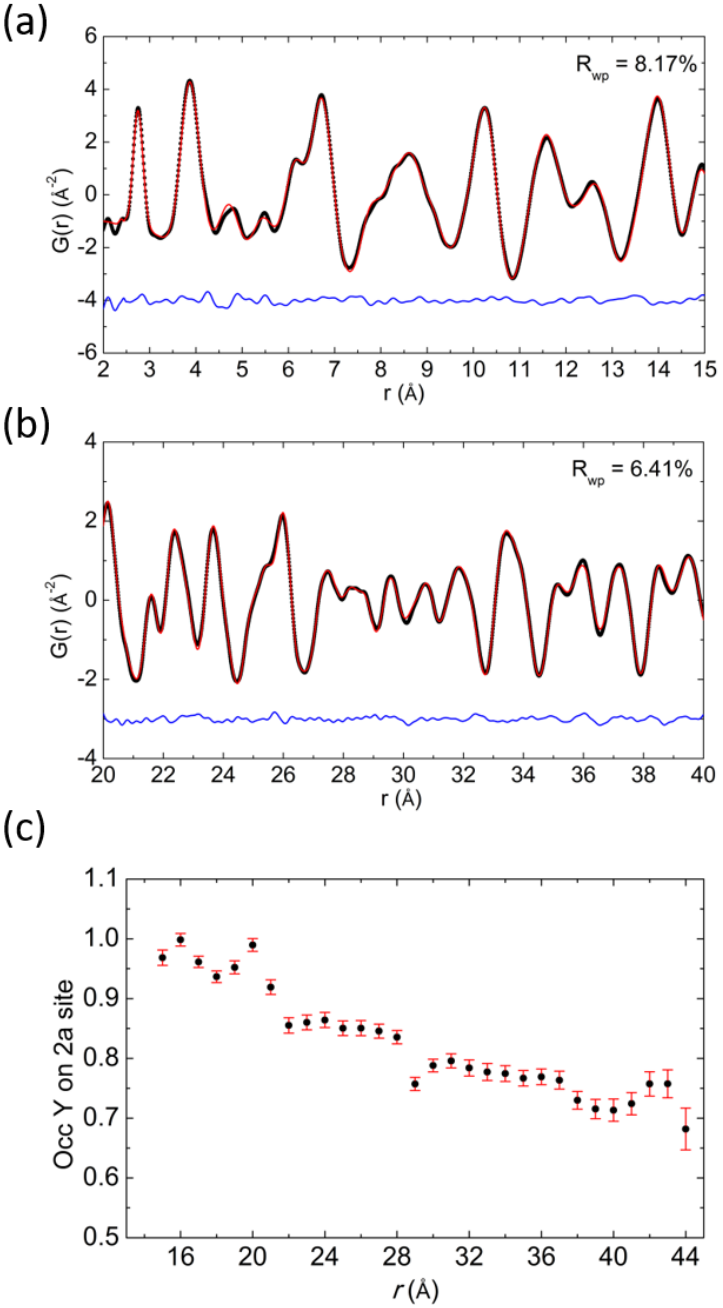

Figure 5.4 Fitting of synchrotron local (a) and intermediate range (b) PDF data using the average structure obtained from Rietveld refinement as the initial structure model. The Y occupancy on the 2a site is refined to be nearly 1 when using the short-range X-ray PDF data, this value is refined to be 0.59(1) when using the intermediate range X-ray PDF data. (c) shows the Y occupancy on the 2a site as a function of pair distances (with a refinement range of 14 Å and an interval of 1 Å). It clearly shows that the site occupancy decreases when increasing the pair-pair distances. These results confirm Li/vacancy and Y are (honeycomb-type) well-ordered within the *ab*-plane, the disordering indeed emerges from the layer disordering along the *c*-axis direction.

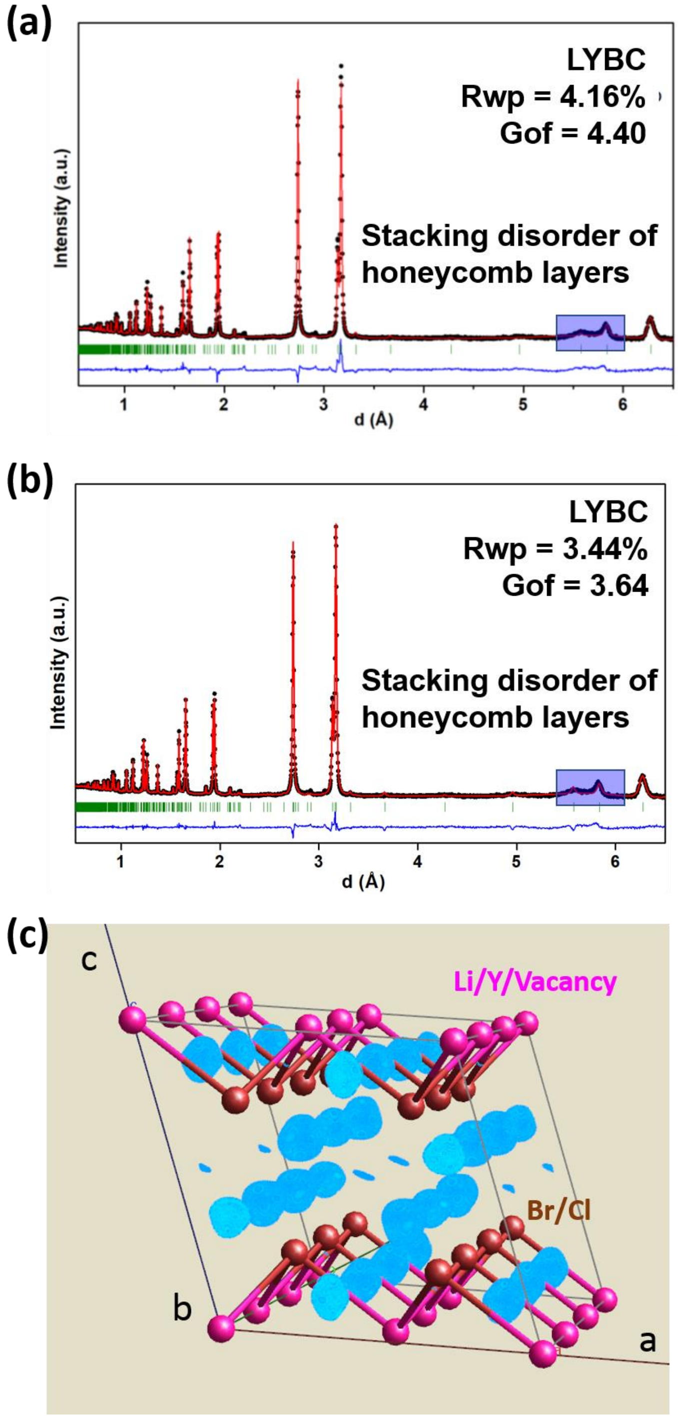

Figure 5.5 Rietveld refinement against neutron diffraction pattern of LYBC-HP (a) without tetrahedral-Li and (b) with tetrahedral-Li. (c) Fourier difference map generated from neutron diffraction of LYBC-HP showing the existence of tetrahedral Li sites.

Second, more interestingly, different from previously model [5], significant amounts of Li ions are found actually occupying multiple tetrahedral sites (8*j*), besides the octahedral sites. The neutron refinement quality is much worse when only incorporating Li on the octahedral sites, as can be seen in Figure 5.5a and 5.5b. More obviously, Fourier difference map (Figure 5.5c) extracted from neutron data clearly shows the residual negative scattering lengths on multiple tetrahedral sites, suggesting Li ions occupy both tetrahedral and octahedral sites.

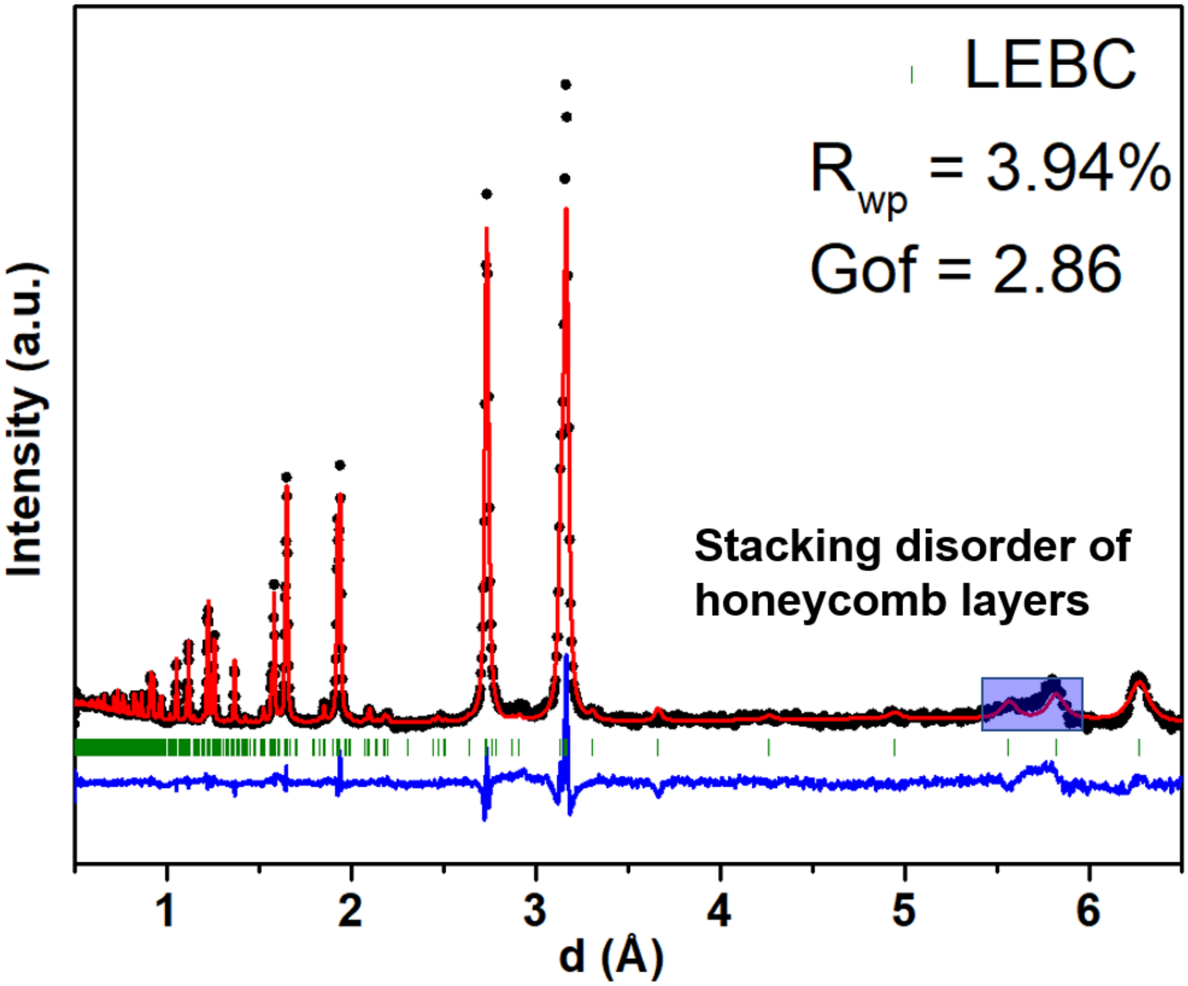

Figure 5.6 Rietveld refinement results of $Li_3ErBr_3Cl_3$ after hot-pressing neutron diffraction patterns

Third, a careful examination using the honeycomb ordered structure (space group *C2/m*) reveals more detailed distribution of Li in the structure. The residual densities (from Fourier difference map) of Li reside on four different tetrahedral sites, with two sets of tetrahedral sites reside within the Li slab while the other two in the TM slab. The tetrahedral sites surrounding YX_6 octahedron are around 2.4 Å apart from the Y site. They are very likely to be empty in the short-range ordered structure due to the repulsion from Y [5, 13]. While the observed residual densities on these sites are likely due to the presence of stacking faults of honeycomb ordered layers along the c-axis, which is rather common in layered structures. This has been further confirmed by our recent neutron PDF study of these type of materials, which will be published elsewhere. After adding Li to the tetrahedral site within the Li slab, the refinement quality improves noticeably with the weighted refinement residual value (R_{wp}) decreasing from 4.16% to 3.44%. Similarly, tetrahedral Li sites are also identified from neutron diffraction patterns of LEBC and the Rietveld refinement results is shown in Figure 5.6.

The final refinement results of LYBC and LEBC are listed in Table 5.1 and Table 5.2. The size of the unit cell (a = 6.7068(4) Å, b = 11.6172(6) Å, c = 6.6329(3) Å, β = 109.675(5)^{o}) is slightly smaller than that of LYB [4-5], agreeing with the mixed occupancy of Br and Cl at the anion sites. In total, about 1/3 of the Li takes the tetrahedral site and 2/3 takes the octahedral sites. The interesting co-existence of tetrahedral Li (T-Li) and octahedral Li (O-Li) in the layered structures was rarely observed previously but is thermodynamically plausible. As discussed in previous theoretical investigations [19], the stable Li site geometry is determined by the type of coordinating anions and lattice volume. Li prefers octahedral sites in small lattice and tetrahedral sites in large lattice. Here by mixing Br and Cl anions and the according change of lattice parameters, a mixed tetrahedral-octahedral distribution of Li is achieved. The existence of T-Li not only creates more vacancies on the octahedral sites, but also possibly change the energy landscape by making it more flat [20-21] and thus may trigger a concerted Li$^+$ diffusion.

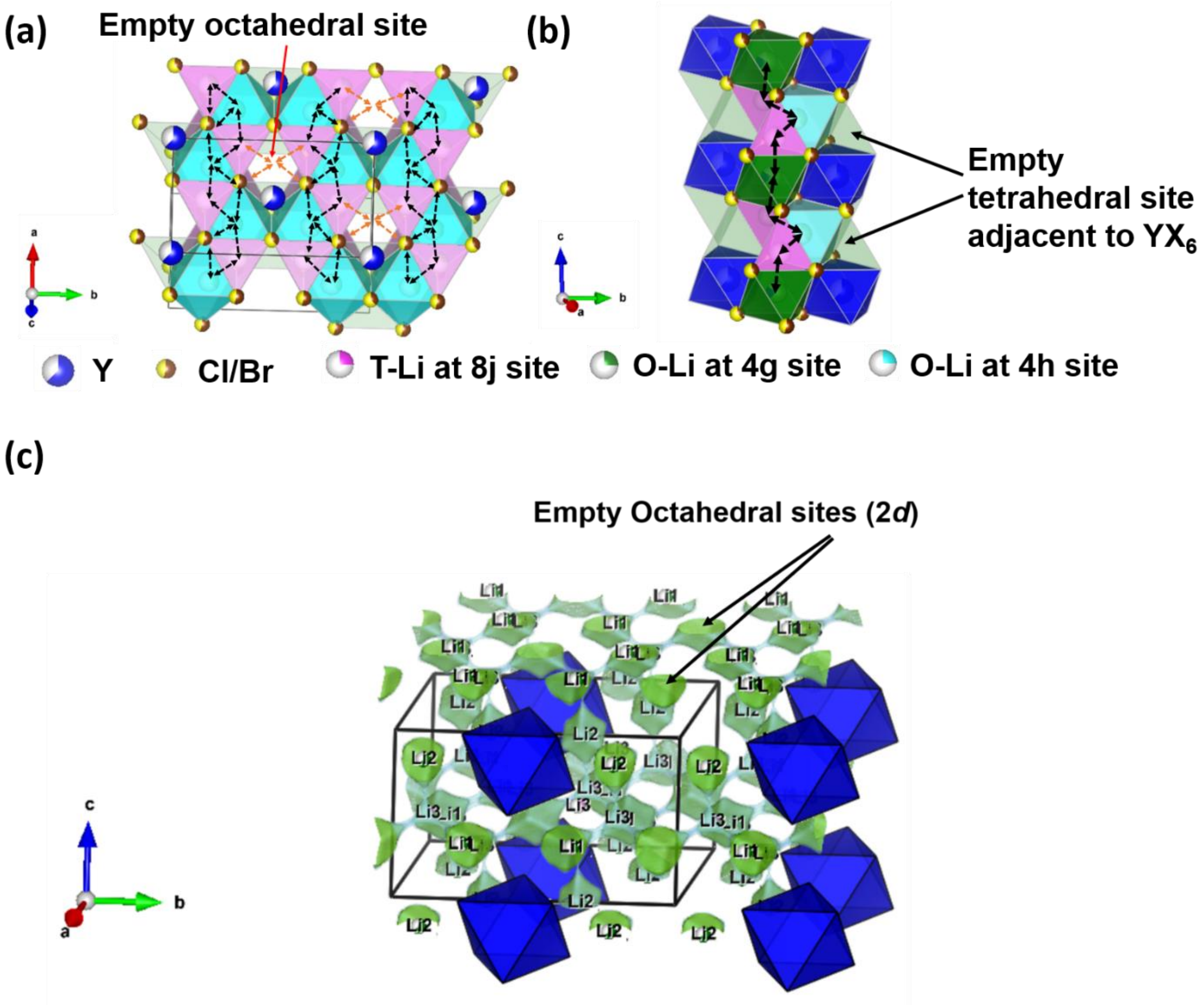

Figure 5.7 (a) and (b) proposed Li$^+$ diffusion pathways along *ab*-plane and *c*-direction, respectively. (c) Diffusion path of LYBCHP suggested by BVSE [22].

Along *ab*-plane, one O-Li is surrounded by other two neighboring T-Li, which enables the O-T-O Li hopping chain along *a*-direction (Figure 5.7a). The empty octahedral sites (2*d*) connect the parallel 1D chains, forming a 2D diffusion network, as suggested by bond valence site energy (BVSE) calculation [22] (Figure 5.7c), which is similar to the 2D pathways that are known in most layered oxide cathode materials. Along *c*-direction, Li ions also hop through the zig-zag "O-T-O-T" route nearby Y sites (Figure 5.7b) [21], making it a 3D diffuser. Such zig-zag pathway along c-axis is previously known in layered oxide cathode [23-24] and in recently developed disordered rock salt cathode [25]. However, in this compound and similar halides reported previously, the high density of vacancies in the TM layer and the relatively lower energy of the T-Li site [13] make the diffusion along c-directly comparable to the fast 2D diffusion within the ab-plane.

Table 5.1 Refined structure of $Li_3YBr_3Cl_3$ using neutron diffraction data

S.G. *C2/m*

a = 6.7068(4) Å b = 11.6172(6) Å c = 6.6329(2) Å β = 109.675(5)°

Site	Wyck.	x	y	Z	Occ.	B_{iso} (Å^2)
Li1	4h	0	0.195(3)	0.5	0.39(5)	1.6(7)
Li2	4g	0	0.33364	0	0.64(2)	1.6(7)
Li3	8j	0.150(6)	0.333(6)	0.371(3)	0.236(15)	1.0(5)
Y1	4g	0	0.33364	0	0.195(6)	1.6(7)
Y2	2a	0	0	0	0.610(12)	1.27(12)
Br1	8j	0.2492(10)	0.1679(4)	0.2410(5)	0.559(11)	2.23(5)
Cl1	8j	0.2492(10)	0.1679(4)	0.2410(5)	0.441(11)	2.23(5)
Br2	4i	0.7504(11)	0	0.2417(8)	0.38(2)	2.03(9)
Cl2	4i	0.7504(11)	0	0.2417(8)	0.62(2)	2.03(9)

Table 5.2 Refined structure of $Li_3YBr_3Cl_3$ using neutron diffraction data

S.G. *C2/m*

a = 6.7200(0) Å b = 11.6446(4) Å c = 6.6535(1) Å β = 109.52(0)°

Site	Wyck.	x	y	z	Occ.	B_{iso} (Å^2)
Li1	4h	0	0.195(3)	0.5	0.393(5)	1.3(8)
Li2	4g	0	0.33364	0	0.732(9)	5.9(1)
Li3	8j	0.150(6)	0.333(6)	0.371(3)	0.186(8)	1.0(5)
Er1	4g	0	0.333(6)	0	0.158(9)	1.6(7)
Er2	2a	0	0	0	0.682(3)	1.27(12)
Br1	8j	0.2492(10)	0.1679(4)	0.2410(5)	0.621(3)	2.23(5)
Cl1	8j	0.2492(10)	0.1679(4)	0.2410(5)	0.378(7)	2.23(5)
Br2	4i	0.7504(11)	0	0.2417(8)	0.257(3)	2.03(9)
Cl2	4i	0.7504(11)	0	0.2417(8)	0.742(7)	2.03(9)

The ionic conductivity of as ball-milled LYBC (LYBC-BM) and ball-milled LEBC (LEBC-BM) samples were measured with variable temperature electrochemical impedance spectroscopy (VT-EIS) and the Arrhenius plots are shown in Figure 5.8. At r.t., the conductivity of pristine LYBC-BM is 1.6 mS/cm, which is already higher than many previously reported halides [5, 7-8]. As the temperature increasing, the slope of the Arrhenius plot becomes obviously more flat above 120 °C (black lines), indicating a lower diffusion activation energy. In cooling, such flat slope was kept, resulting in a much higher r.t conductivity of 4.7 mS/cm. LEBC also exhibits similar phenomenon in VT-EIS test and an ionic conductivity of 4.0 mS/cm is achieved in hot-pressed LEBC pellet.

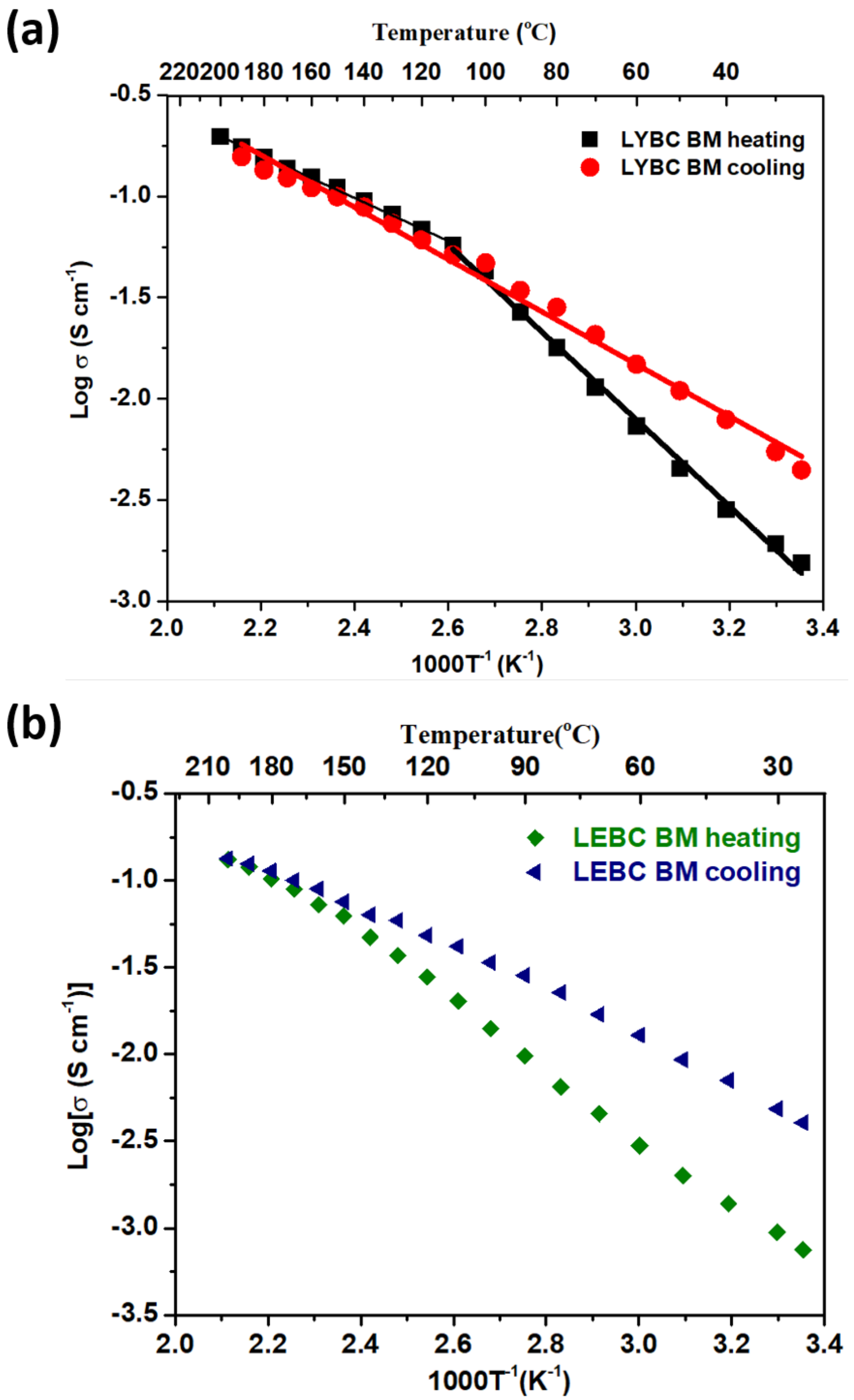

Figure 5. 8 Arrhenius plot of LYBC BM in heating and cooling process

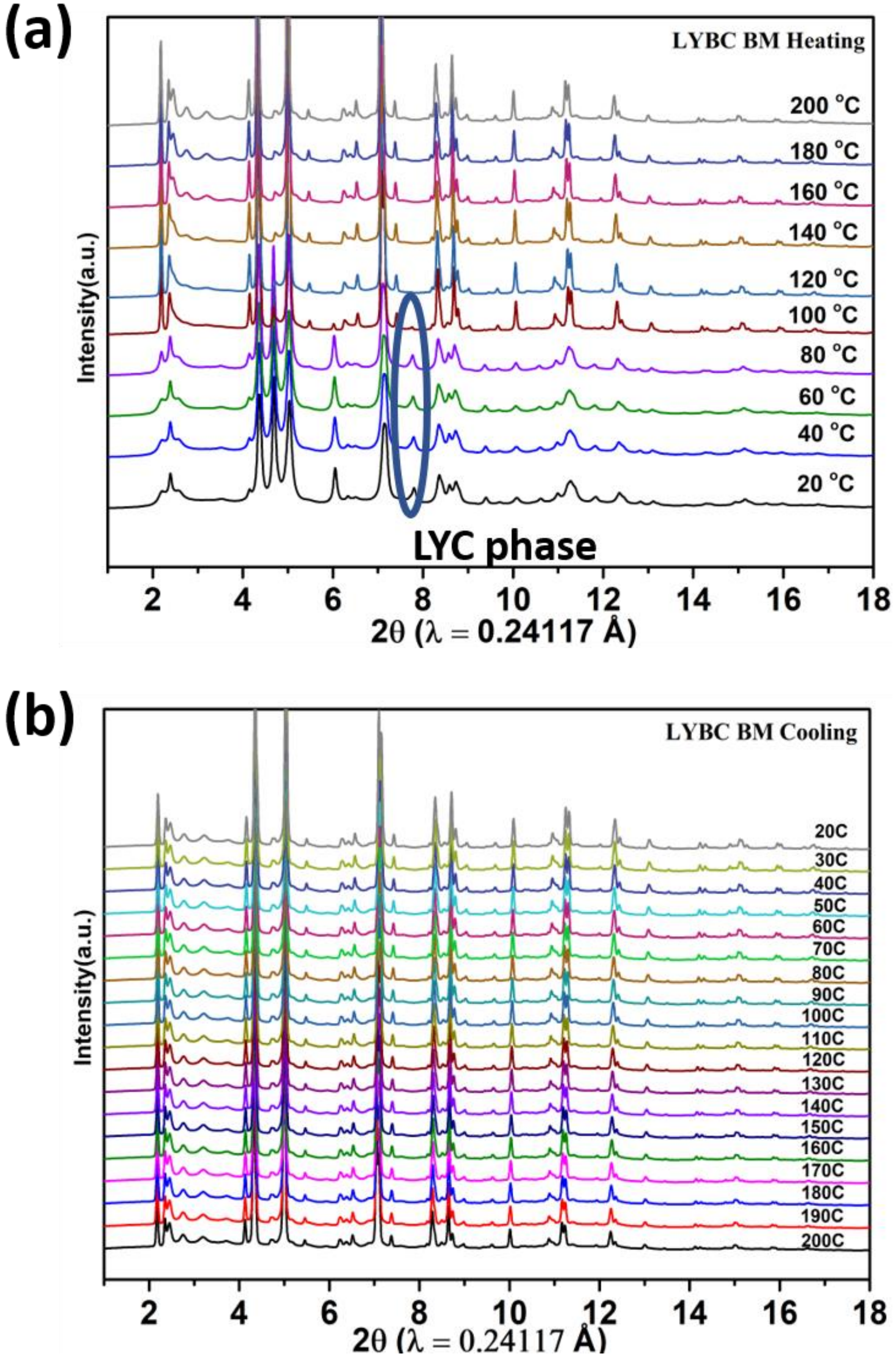

Figure 5.9 In situ (a) heating and (b) cooling XRD patterns of LYBC-BM.

To understand the origin of the slope change and this high conductivity, i*n situ* synchrotron XRD was conducted to monitor the heating process of the LYBC-BM sample. As shown in Figure 5.9a, the mixture of the LYC-like and LYB-like phase in the pristine LYBC-BM sample gradually transforms to a single LYB-like phase in the range of 80-120 ºC. No other phase change is visible in heating as well as in cooling (Figure 5.9a and 5.9b). The in situ XRD results seem to indicate that the LYB-like phase formed at 120 °C is more conductive than the pristine LYBC-BM sample, thus is responsible for the slope change in heating and the higher r.t. conductivity after cooling. However, further investigation made us suspect that this phase change is not the only reason for the improved conductivity. Scanning electron microscopy (SEM) images were taken for LYBC-BM samples after cold- and hot-pressing, respectively (Figure 5.10a and 5.10b). From the image of cold-pressed sample, cubic/spherical particles of ~200-300 nm in aggregation and some micrometer sized voids can be seen. For the hot-pressed sample (LYBC-HP), the particle size becomes bigger (~500-800 nm) as expected. More interestingly, the particles appear to be fused/sintered together to form a denser block. SEM images of the same samples taken on focused ion beam-milled cross-sections can be seen in Figure 5.10c-f, which show similar morphology for each sample, respectively. It is speculated that partial melting at the grain boundaries (GBs) has taken place in the hot-pressing process.

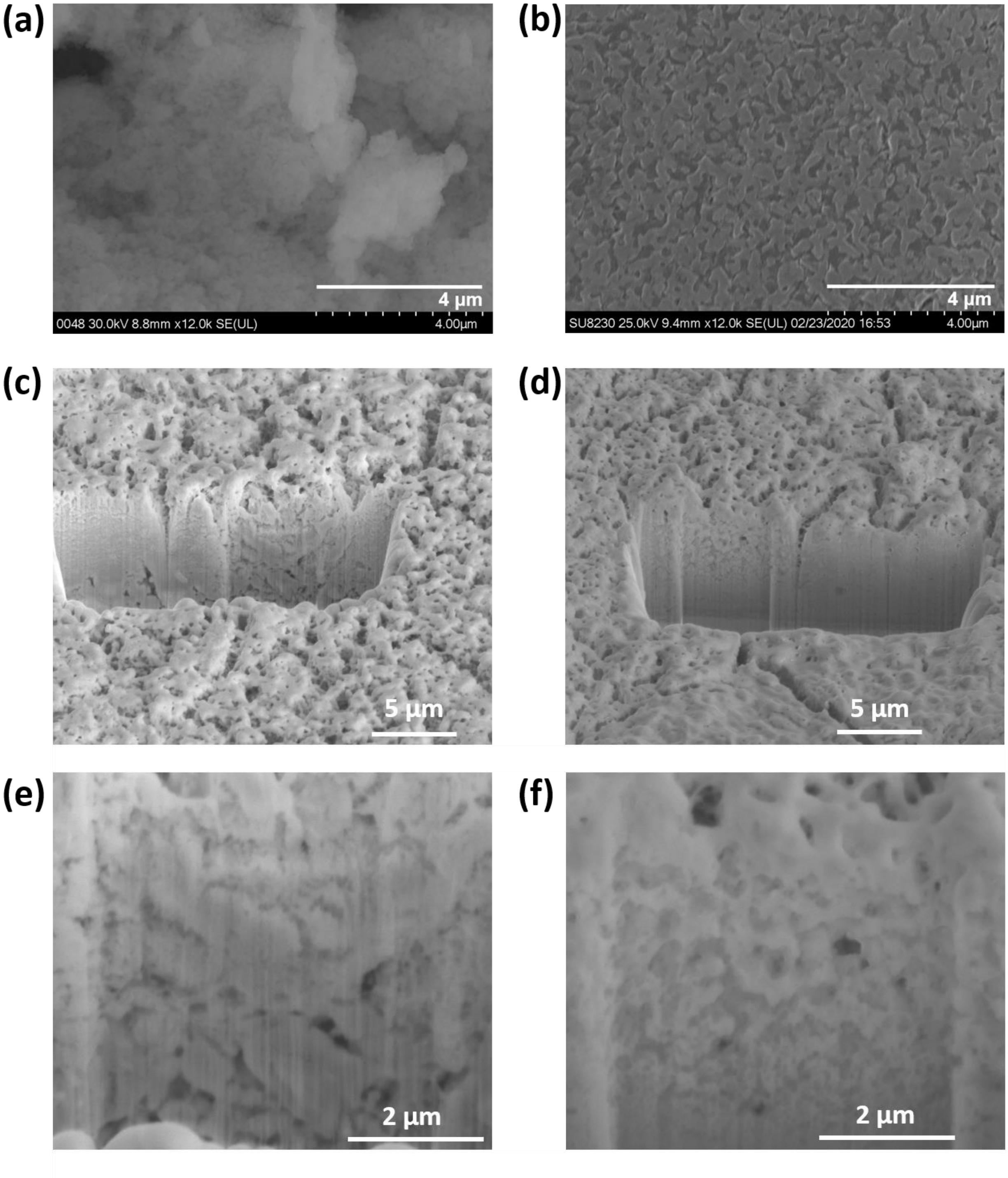

Figure 5.10 SEM image of (a) cold-pressed LYBC-BM and (b) hot-pressed LYBC-HP. FIB-SEM images of (a) (c) cold-pressed LYBC-BM and (d) (f) hot-pressed LYBC-HP.

Differential scanning calorimetry (DSC) tests were conducted for both pristine LYBC-BM and LYBC-HP powders in N_2 gas (Figure 5.11). One endothermic process can be seen centered at 150 °C in both samples, which may be associated with the partial melting of the sample at the GBs. Such fused GB structures commonly benefits the overall conductivity, making us hypothesize that this good GB also contributes to the improved conductivity.

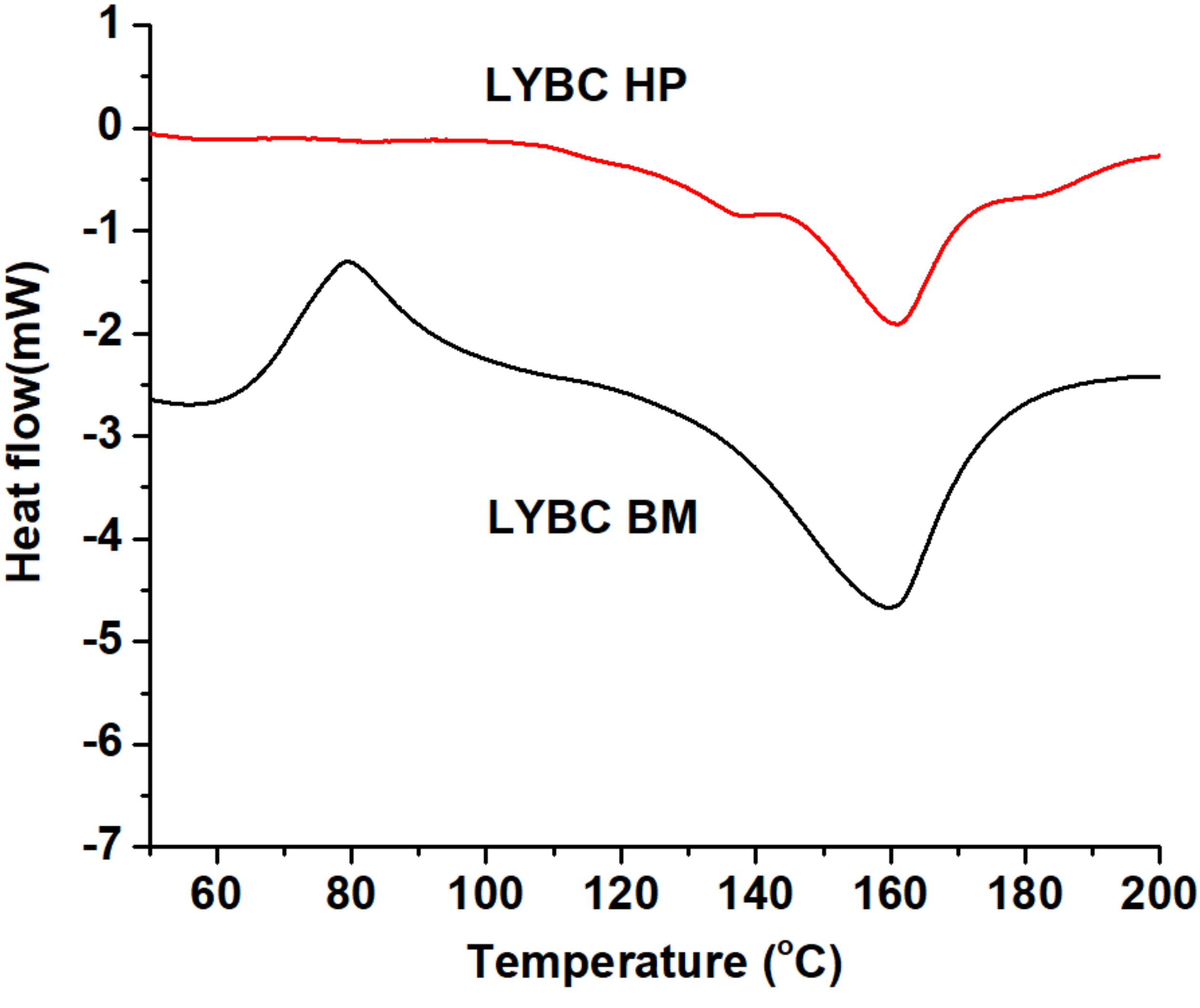

Figure 5.11 DSC curve of LYBC BM and LYBC HP.

To verify this hypothesis, we took the pellet after the VT-EIS test, gently hand-milled it into powder in an Ar-filled glove box, in order to break the GBs formed in the VT-EIS test but not to alter the crystal structure and particle size. Then we cold-pressed the powder into pellet again and did the 2nd VT-EIS test. The resulted Arrhenius curve is also shown in Figure 5.12a. Interestingly, below 120 °C, the curve in the 2nd heating (blue line) shows a slightly more flat slope than that in the 1st heating (black line) but much steeper than that in the 1st cooling (red line). And the slope change above 120 °C was again observed. This observation clearly indicates that the slope change in heating is not solely due to the phase transition, as in the 2nd heating there was not phase change observed in XRD. Rather it is to a greater extend due to the formation of better GB contact than formed in cold-press. When this low resistance GB was destroyed by the gentle hand-grinding, the overall/apparent Arrhenius behavior then was dominated by the resistance from GB, despite that the bulk conductivity of the single LYB-like phase is high. To further confirm this conclusion, we also conducted the 3rd VT-EIS test after the 2nd test without intermediate hand-milling. In this case, the GB structure formed in the 2nd EIS test was preserved. The Arrhenius curve of the 3rd heating (pink line) mostly superposed the 1st cooling curve (red line), as expected , and no slope change was observed. Multiple heating-cooling loops were also conducted to the same sample and the Arrhenius curves in these loops all superpose with the 3rd loop, showing excellent stability.

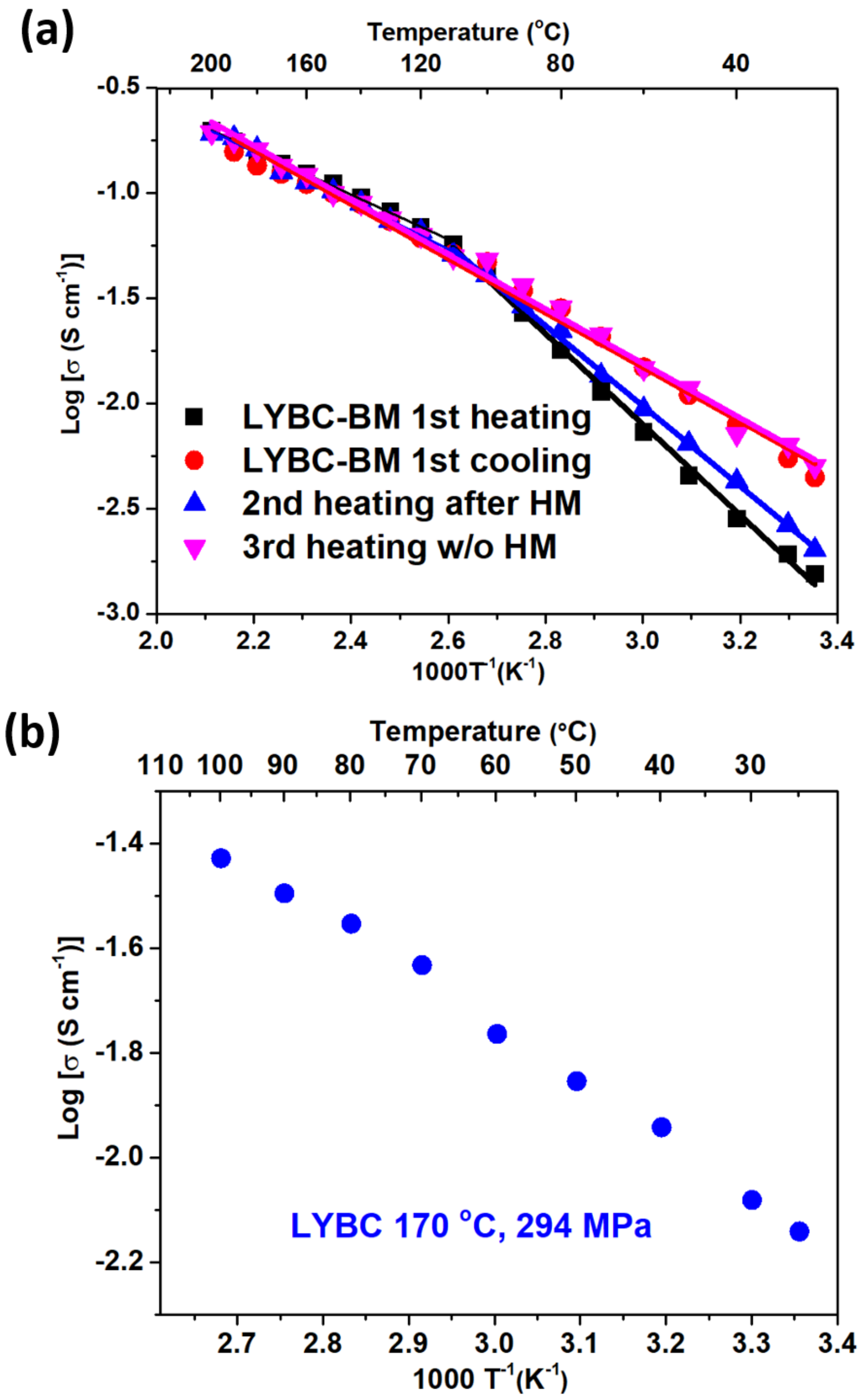

Figure 5.12 (a) Arrhenius plots of conductivities of (a) LYBC-BM samples in the 1st, 2nd (with intermediate hand-milling) and 3rd (without intermediate hand-milling) hot-pressing processes, and (b) LYBC-BM after hot-pressed at 170 °C, 294 MPa.

The results of this series of EIS tests clearly indicate that for LYBC low resistance GB can be formed via hot-pressing. Activation energies of LYBC from different temperature ranges in heating and cooling in Figure 5.12a were calculated separately. The activation energy fitted from the 1st heating (below 120 °C) is 0.45 eV, which is close to those reported for LYB (0.40 eV) by similar EIS measurements[5]. The activation energy fitted from the 1st cooling and 3rd heating are much lower, at 0.32 and 0.31 eV, respectively, which are more close to the theoretically calculated values for LYB (0.28 eV) by Mo et al. with using ab initio molecular dynamics (AIMD) [13]. This finding implies that the discrepancy in former experimental and theoretical investigations may essentially be due to the effect of the GB. To further enhance the GB conduction and inter-particle contact, pushing it to the limit within the capacity of our lab, a LYBC pellet was hot-pressed at higher pressure (294 MPa) at 170 °C and it achieved a further improved r.t. ionic conductivity of **7.2 mS/cm** (Figure 5.12b) with a lower activation energy of 0.25 eV, which is more close to the theoretical estimation on LYB [13]. Such r.t. conductivity is record-high in reported halides and is very close to that of the state-of-the-art sulfides [10].

In order to assess the performance of the LYBC samples in all-solid-state battery cells, a cyclic voltammetry (CV) scan was first performed with using carbon black-LYBC mixture as cathode electrode and Li metal as the counter electrode. Li_6PS_5Cl was inserted between LYBC and Li metal to prevent the LYBC from being reduced by Li metal directly. The result is shown in Figure 5.13. An oxidation peak was observed above 3.5 V, which can be associated with Br^- oxidation and reduction process was observed in 0-1.5 V.

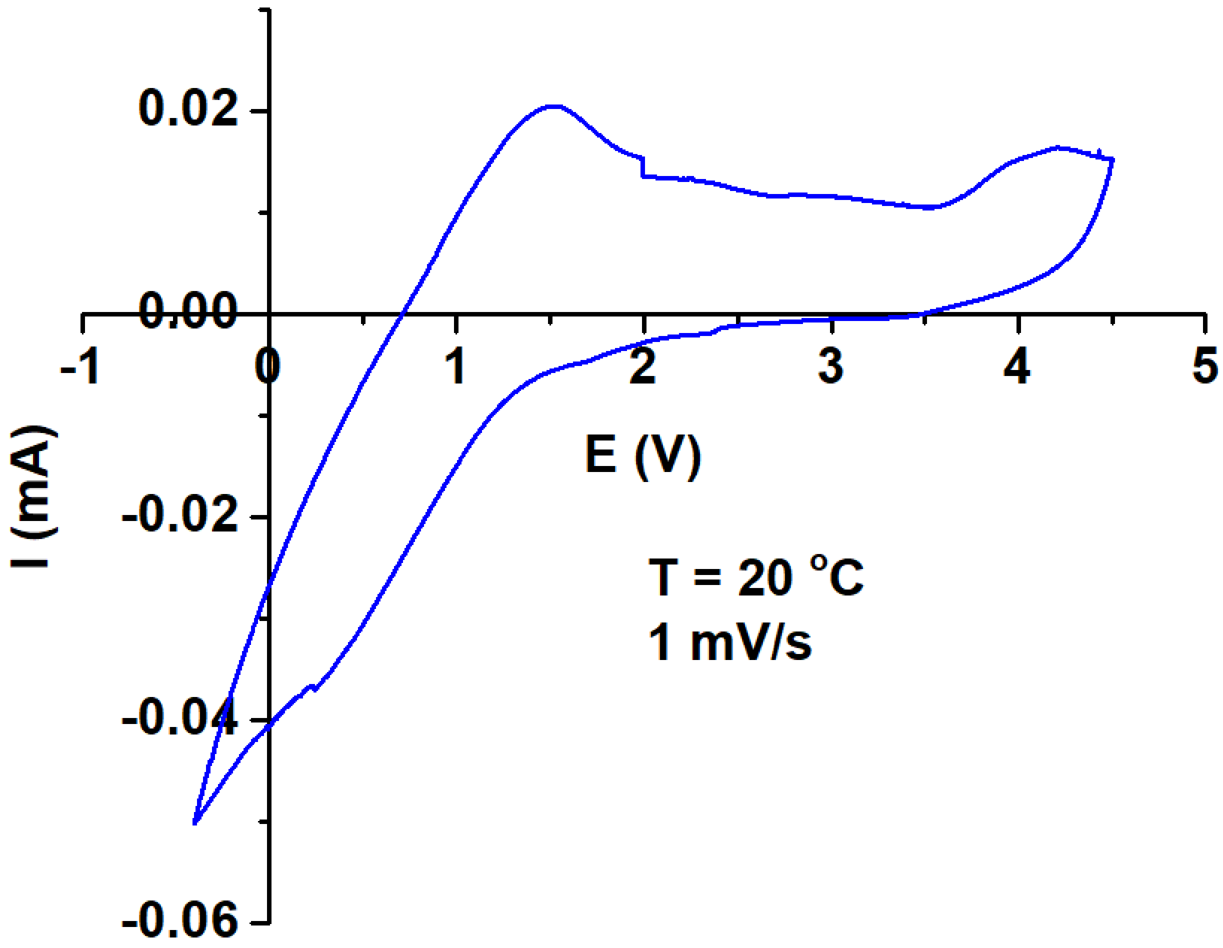

Figure 5.13 Cyclic voltammogram of LYBC. The CV measurements were performed on the Carbon black-LYBC/LYBC/Li_6PS5Cl/Li cell.

Full cells were fabricated with using $LiCoO_2$ as the cathode, LYBC as the separator and Li-In alloy as the anode. High initial discharge capacity of 124 mAh/g and very good average Columbic efficiency of 99.7 % were achieved at r.t. cycled at 0.1 C rate, as shown in Figure 5.14. The rate performance of LYBC was also evaluated with using 0.2 to 1 C rates at r.t. A cell with using LYC as the separator was also tested as comparison. Due to the higher ionic conductivity of LYBC, the cell with LYBC separator showed higher specific capacity than that of the cell with LYC separator. Reasonably high capacities of ~73 mAh/g was achieved at 1 C rate at r.t..

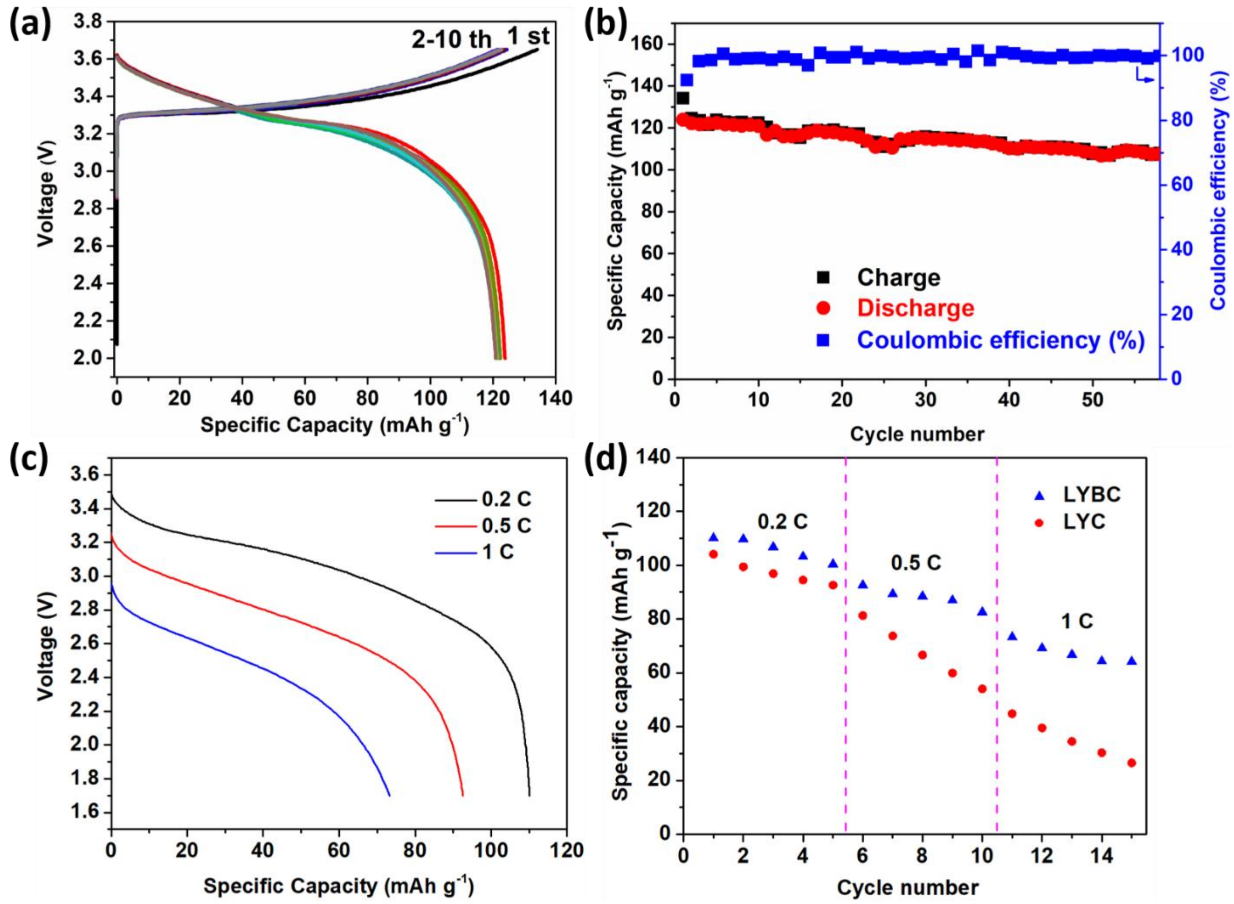

Figure 5.14 Electrochemical performance of LCO//LYBC//In-Li battery. (a) Charge-discharge curves at 0.1 C. (b) cycling performance at 0.1 C rate at r.t. (c) discharge curve at different rates at r.t. (d) r.t. rate performance of ASSB cells with LYBC and LYC separators, respectively.

As demonstrated above, record-high r.t. conductivity of 7.2 mS/cm for lithium halides was obtained from the novel compound LYBC. Such high conductivity comes from the synergetic effect of two factors. First is the high intrinsic/bulk ionic conductivity of the LYBC phase, which is likely due to the existence of the newly identified T-Li and the 3D diffusion pathways. The stable co-existence of O-Li and T-Li in the lattice is very rarely seen in layer structured compounds, such as $LiCoO_2$ and $Li(NiCoMn)_{1/3}O_2$, which solely contains O-Li and the diffusion pathway is purely 2D along the *ab*-plane. The existence of T-Li not only facilitates the diffusion within the *ab*-plane by lowering the activation energy of the O-O hopping, but also helps to promote a zig-zag style O-T-O-T diffusion pathway along the *c*-direction. At this point, it is not clearly yet whether the existence of T-Li is closely related to the mixing of Br^- and Cl^- anions in the LYBC and LEBC samples, or it widely exists in more Li_3MX_6 compounds, which warrants the necessity of further investigations on more compounds of this group. The other benefiting factor for the overall conductivity is the favorable GB formed during the hot-pressing. This effect is rarely seen in oxides and sulfides at such low temperature, because their melting points are commonly much higher. It is not clear at this point what exact chemical composition and crystal structure the GB phase has, which requires further in-depth investigations. Direct transmission electron microscope (TEM) observation is difficult due the sample's sensitivity to beam damage. But it can be reasonably speculated that the formation of this favorable GB is related to the eutectic melting of multiple halide components. Therefore, the design of mixed halogen anions, including Br, Cl and I, may be preferred in that regard. It is also worth noting that the incorporation of Br and I lowers the oxidation stability of the compounds, as suggested by previous theoretical investigation [13]. Accordingly, mitigation strategies such as interface engineering need to be considered. It is well known that oxide solid state ionic conductors, such as $Li_7La_3Zr_2O_{12}$ and β-alumina, must be sintered at high temperature (>1000 °C) [26-28] to reduce the poorly conducting GBs. Sulfide SEs suffer less from low-conducting GBs and can be used with only cold-press. However, most sulfides are sensitive to air and moisture. The halides provide an alternative possibility. Low temperature hot-pressing such as used in this work, can already result in a low GB resistance, which further pave the road towards the commercialization of ASSBs.

5.3 Summary

In summary, the discovery of highly conductive LYBC compound demonstrated that halides are a group of compounds with of high promise for ASSB applications. Our structural investigation on these compounds provides interesting unprecedented insights, indicating that these compounds have higher than expected potentials and abundant space for further compositional and crystal structural designs to promise even higher bulk conductivities. Their easy-forming GBs and air stability also ease their way toward low cost and facile manufacture and commercial applications.

5.4 Methods

LYBC and LYEC were synthesized via solid state reaction. Anhydrous LiBr (>99%, Sigma-Aldrich) and anhydrous YCl_3 (99.99%, Sigma-Aldrich) or $ErCl_3$ (≥99.9%, Beantown Chemical) as starting materials were weighed in a molar ratio of 3:1 and ball-milled with using zirconia jars (50 mL) in a planetary ball mill (PM 200, Retsch) at 500 rpm for 5h. The hot-pressed sample was prepared by pressing the as-ball-milled powder into pellet and heated under 44.1 MPa pressure to 200 ^{o}C for half an hour. All the processes were carried out under Ar atmosphere.

X-ray diffraction patterns and PDF data were collected at synchrotron X-ray source at beam line 17-BM (λ = 0.24117 Å) at the Advanced Photon Source (APS). High-quality powder neutron diffraction (ND) data were collected at r.t. and 100 K at POWGEN at the Spallation Neutron Source (SNS) at Oak Ridge National Laboratory (ORNL) with a center wavelength 1.5 Å. Rietveld refinements against the XRD and ND data were performed with using GSAS II [29] and TOPAS (version 6) [30]. For data analysis using neutron diffraction data, time-of-flight (TOF) data were converted to d-spacing data using the polynomial TOF = ZERO + DIFC*d + DIFA*d^2 + DIFB/d, where ZERO is a constant, DIFC is the diffractometer constant and DIFA and DIFB is empirical terms to correct the sample displacement and absorption caused peak shift. During the refinement, ZERO, DIFC and DIFB were determined from the refinement using a standard NIST Si 640d, while DIFA was allowed to vary to account for the sample displacements. A back to back exponential function convoluted with symmetrical Gaussian function were used to describe the peak profile. PDF data were processed and reduced using GSAS II [29] and fitted by TOPAS version 6 and PDFgui [31]. Box-car type structure refinements were carried out using the X-ray PDF data with an interval of 14 Å. This method was used to extract the Y site (Wyck. 2a) occupancy as a function of pair-pair distances. The crystal structure is visualized by VESTA software [32]. Scanning electron microscopy (SEM) images were taken using a Hitachi SU8230 microscope. ^{7}Li magic-angle-spinning (MAS) NMR was tested using a Bruker Avance 400 MHz spectrometer with the magenetic field of 9.4 T with a rotation speed of 10 kHz.

The BVSE calculation was performed using softBV with updated potential parameters [22, 33].

The electrochemical impedance spectroscopy (EIS) data was collected with using an electrochemical impedance analyzer (VMP3, Bio-logic) and a home-made electrochemical cell. For variable temperature (VT) EIS tests, cold-pressed or hot-pressed LYBC pellet was sandwiched by two piece of Al foils as current collectors and the EIS data was collected at varied temperatures in the frequency range of 1 MHz to 1 Hz with an AC amplitude of 50 mV. A pressure of 44.1 MPa was applied during EIS test. All-solid state cells were fabricated as follows: 150 mg LYBC powder was pressed into SE pellet with 235.2 MPa pressure in a PTFE sleeve of 0.5 inch inner diameter. The composite cathode was made by mixing LCO_2, Li_3YCl_6 and acetylene black in mortar with a weight ratio of 60:37:3. Then 12 mg of composite cathode powder was pressed on the SE pellet with a pressure of 235.2 MPa. In-Li alloy was attached to the other side of the SE pellet as anode. Cycling tests were conducted at room temperature in galvanostatic mode between 2 to 3.65 V.

Cyclic voltammetry (CV) measurements were performed on the carbon black-LYBC/LYBC/Li_6PS_5Cl/Li cell. The carbon black-LYBC mixture was used as cathode and the weight ratio of carbon black is 20%. The data was collected with using an electrochemical impedance analyzer (VMP3, Bio-logic) at a scan rate of 1 mV/s from -0.4 to 4.5 V.

5.5 Notes to Chapter 5

This chapter is based on the paper “High Ionic Conductivity Achieved in $Li_3Y(Br_3Cl_3)$ Mixed Halide Solid Electrolyte via Promoted Diffusion Pathways and Enhanced Grain Boundary” published in ACS Energy Letters [34].

5.6 References

[1] Janek, J.; Zeier, W. G., A solid future for battery development. *Nature Energy* **2016,** *1*, 16141.

[2] Famprikis, T.; Canepa, P.; Dawson, J. A.; Islam, M. S.; Masquelier, C., Fundamentals of inorganic solid-state electrolytes for batteries. *Nature Materials* **2019,** *18* (12), 1278-1291.

[3] Bohnsack, A.; Stenzel, F.; Zajonc, A.; Balzer, G.; Wickleder, M. S.; Meyer, G., Ternäre Halogenide vom Typ A3MX6. VI [1]. Ternäre Chloride der Selten-Erd-Elemente mit Lithium, Li3MCl6 (M □ Tb□Lu, Y, Sc): Synthese, Kristallstrukturen und Ionenbewegung. *Zeitschrift für anorganische und allgemeine Chemie* **1997,** *623* (7), 1067-1073.

[4] Bohnsack, A.; Balzer, G.; Güdel, H.-U.; Wickleder, M. S.; Meyer, G., Ternäre Halogenide vom Typ A3MX6. VII [1]. Die Bromide Li3MBr6 (M=Sm□Lu, Y): Synthese, Kristallstruktur, Ionenbeweglichkeit. *Zeitschrift für anorganische und allgemeine Chemie* **1997,** *623* (9), 1352-1356.

[5] Asano, T.; Sakai, A.; Ouchi, S.; Sakaida, M.; Miyazaki, A.; Hasegawa, S., Solid Halide Electrolytes with High Lithium-Ion Conductivity for Application in 4 V Class Bulk-Type All-Solid-State Batteries. *Advanced Materials* **2018,** *30* (44), 1803075.

[6] Schlem, R.; Muy, S.; Prinz, N.; Banik, A.; Shao-Horn, Y.; Zobel, M.; Zeier, W. G., Mechanochemical Synthesis: A Tool to Tune Cation Site Disorder and Ionic Transport Properties of Li3MCl6 (M = Y, Er) Superionic Conductors. *Advanced Energy Materials n/a* (n/a), 1903719.

[7] Li, X.; Liang, J.; Chen, N.; Luo, J.; Adair, K. R.; Wang, C.; Banis, M. N.; Sham, T.-K.; Zhang, L.; Zhao, S.; Lu, S.; Huang, H.; Li, R.; Sun, X., Water-Mediated Synthesis of a Superionic Halide Solid Electrolyte. *Angewandte Chemie International Edition* **2019,** *58* (46), 16427-16432.

[8] Park, K.-H.; Kaup, K.; Assoud, A.; Zhang, Q.; Wu, X.; Nazar, L. F., High-Voltage Superionic Halide Solid Electrolytes for All-Solid-State Li-Ion Batteries. *ACS Energy Letters* **2020**, 533-539.

[9] Liang, J.; Li, X.; Wang, S.; Adair, K. R.; Li, W.; Zhao, Y.; Wang, C.; Hu, Y.; Zhang, L.; Zhao, S.; Lu, S.; Huang, H.; Li, R.; Mo, Y.; Sun, X., Site-Occupation-Tuned Superionic LixScCl3+xHalide Solid Electrolytes for All-Solid-State Batteries. *Journal of the American Chemical Society* **2020,** *142* (15), 7012-7022.

[10] Kamaya, N.; Homma, K.; Yamakawa, Y.; Hirayama, M.; Kanno, R.; Yonemura, M.; Kamiyama, T.; Kato, Y.; Hama, S.; Kawamoto, K.; Mitsui, A., A lithium superionic conductor. *Nat Mater* **2011,** *10* (9), 682-686.

[11] Kato, Y.; Hori, S.; Saito, T.; Suzuki, K.; Hirayama, M.; Mitsui, A.; Yonemura, M.; Iba, H.; Kanno, R., High-power all-solid-state batteries using sulfide superionic conductors. **2016,** *1*, 16030.

[12] Adeli, P.; Bazak, J. D.; Park, K. H.; Kochetkov, I.; Huq, A.; Goward, G. R.; Nazar, L. F., Boosting Solid-State Diffusivity and Conductivity in Lithium Superionic Argyrodites by Halide Substitution. *Angewandte Chemie International Edition 0* (0).

[13] Wang, S.; Bai, Q.; Nolan, A. M.; Liu, Y.; Gong, S.; Sun, Q.; Mo, Y., Lithium Chlorides and Bromides as Promising Solid-State Chemistries for Fast Ion Conductors with Good Electrochemical Stability. *Angewandte Chemie International Edition* **2019,** *58* (24), 8039-8043.

[14] Paulsen, J. M.; Mueller-Neuhaus, J. R.; Dahn, J. R., Layered LiCoO[sub 2] with a Different Oxygen Stacking (O2 Structure) as a Cathode Material for Rechargeable Lithium Batteries. *Journal of The Electrochemical Society* **2000,** *147* (2), 508.

[15] Jiang, M.; Key, B.; Meng, Y. S.; Grey, C. P., Electrochemical and Structural Study of the Layered, “Li-Excess” Lithium-Ion Battery Electrode Material Li[Li1/9Ni1/3Mn5/9]O2. *Chemistry of Materials* **2009,** *21* (13), 2733-2745.

[16] Meng, Y. S.; Ceder, G.; Grey, C. P.; Yoon, W. S.; Jiang, M.; Bréger, J.; Shao-Horn, Y., Cation Ordering in Layered O3 Li[NixLi1/3-2x/3Mn2/3-x/3]O2 (0 ≤ x ≤ 1/2) Compounds. *Chemistry of Materials* **2005,** *17* (9), 2386-2394.

[17] Liu, J.; Yin, L.; Wu, L.; Bai, J.; Bak, S.-M.; Yu, X.; Zhu, Y.; Yang, X.-Q.; Khalifah, P. G., Quantification of Honeycomb Number-Type Stacking Faults: Application to Na3Ni2BiO6 Cathodes for Na-Ion Batteries. *Inorganic Chemistry* **2016,** *55* (17), 8478-8492.

[18] Ma, J.; Bo, S.-H.; Wu, L.; Zhu, Y.; Grey, C. P.; Khalifah, P. G., Ordered and Disordered Polymorphs of Na(Ni2/3Sb1/3)O2: Honeycomb-Ordered Cathodes for Na-Ion Batteries. *Chemistry of Materials* **2015,** *27* (7), 2387-2399.

[19] Wang, Y.; Richards, W. D.; Ong, S. P.; Miara, L. J.; Kim, J. C.; Mo, Y.; Ceder, G., Design principles for solid-state lithium superionic conductors. *Nature Materials* **2015,** *14* (10), 1026-1031.

[20] Di Stefano, D.; Miglio, A.; Robeyns, K.; Filinchuk, Y.; Lechartier, M.; Senyshyn, A.; Ishida, H.; Spannenberger, S.; Prutsch, D.; Lunghammer, S.; Rettenwander, D.; Wilkening, M.; Roling, B.; Kato, Y.; Hautier, G., Superionic Diffusion through Frustrated Energy Landscape. *Chem* **2019,** *5* (9), 2450-2460.

[21] He, X.; Zhu, Y.; Mo, Y., Origin of fast ion diffusion in super-ionic conductors. *Nature Communications* **2017,** *8* (1), 15893.

[22] Chen, H.; Adams, S., Bond softness sensitive bond-valence parameters for crystal structure plausibility tests. *IUCrJ* **2017,** *4* (Pt 5), 614-625.

[23] Van der Ven, A., Lithium Diffusion in Layered Li[sub x]CoO[sub 2]. *Electrochemical and Solid-State Letters* **1999,** *3* (7), 301.

[24] Bréger, J.; Jiang, M.; Dupré, N.; Meng, Y. S.; Shao-Horn, Y.; Ceder, G.; Grey, C. P., High-resolution X-ray diffraction, DIFFaX, NMR and first principles study of disorder in the Li2MnO3–Li[Ni1/2Mn1/2]O2 solid solution. *Journal of Solid State Chemistry* **2005,** *178* (9), 2575-2585.

[25] Lee, J.; Urban, A.; Li, X.; Su, D.; Hautier, G.; Ceder, G., Unlocking the Potential of Cation-Disordered Oxides for Rechargeable Lithium Batteries. *Science* **2014,** *343* (6170), 519-522.

[26] Song, Y.; Yang, L.; Zhao, W.; Wang, Z.; Zhao, Y.; Wang, Z.; Zhao, Q.; Liu, H.; Pan, F., Revealing the Short-Circuiting Mechanism of Garnet-Based Solid-State Electrolyte. *Advanced Energy Materials* **2019,** *9* (21), 1900671.

[27] Zhao, N.; Khokhar, W.; Bi, Z.; Shi, C.; Guo, X.; Fan, L.-Z.; Nan, C.-W., Solid Garnet Batteries. *Joule* **2019,** *3* (5), 1190-1199.

[28] Murugan, R.; Thangadurai, V.; Weppner, W., Fast Lithium Ion Conduction in Garnet-Type Li7La3Zr2O12. *Angewandte Chemie International Edition* **2007,** *46* (41), 7778-7781.

[29] Toby, B. H.; Von Dreele, R. B., GSAS-II: the genesis of a modern open-source all purpose crystallography software package. *Journal of Applied Crystallography* **2013,** *46* (2), 544-549.

[30] Perl, J.; Shin, J.; Schümann, J.; Faddegon, B.; Paganetti, H., TOPAS: An innovative proton Monte Carlo platform for research and clinical applications. *Medical Physics* **2012,** *39* (11), 6818-6837.

[31] Farrow, C. L.; Juhas, P.; Liu, J. W.; Bryndin, D.; Božin, E. S.; Bloch, J.; Th, P.; Billinge, S. J. L., PDFfit2 and PDFgui: computer programs for studying nanostructure in crystals. *Journal of Physics: Condensed Matter* **2007,** *19* (33), 335219.

[32] Momma, K.; Izumi, F., VESTA: a three-dimensional visualization system for electronic and structural analysis. *J. Appl. Crystallogr.* **2008,** *41*, 653.

[33] Adams, S.; Rao, R. P., High power lithium ion battery materials by computational design. *physica status solidi (a)* **2011,** *208* (8), 1746-1753.

[34] Liu, Z.; Ma, S.; Liu, J.; Xiong, S.; Ma, Y.; Chen, H., High Ionic Conductivity Achieved in Li3Y(Br3Cl3) Mixed Halide Solid Electrolyte via Promoted Diffusion Pathways and Enhanced Grain Boundary. *ACS Energy Letters* **2021,** *6* (1), 298-304.

CHAPTER 6. Conclusions and Future Directions

6.1 Conclusions

In the past decade, with the rapid development of all-solid-state lithium ion batteries (ALSOLIB), the search for solid electrolytes (SEs) with high ionic conductivity gradually became the focus and critical part of in the research of this novel energy storage technology [1-2]. Many SEs with different chemical compositions and crystal structures were explored and they showed different electronic, ionic, electrochemical and mechanical properties. Different from conventional oxide SEs, which are brittle and require high-temperature sintering process [3-4] to achieve intimate contact between electrolyte/electrolyte and electrolyte/electrode particles, high density electrolyte layer and composite cathode with intimate contact can be achieved by simple cold-pressing process for sulfide and halide SEs, which facilitates the batteries assembly and presents a great advantage over oxide SEs [5-6]. More importantly, sulfide and halide based SEs show much higher ionic conductivities than those of oxide SEs. Some sulfide SEs show ionic conductivities that are comparable to liquid electrolytes [7-11]. Yet, none of the existing sulfide or halides meet all requirement in properties for ALSOLIBs. The goals of this work are to 1) develop high performance sulfide and halide SEs and 2) advance our mechanistic understanding of Li ion diffusion behavior in solid state ionic conductors, so to establish better material design principles for SEs and to pave the way towards commercial application of ALSOLIBs. With combining experimental approach, which includes materials synthesis, electrochemical measurement and testing and crystal structure characterization with using cutting-edge ex situ and in situ synchrotron X-ray and neutron techniques, and computational modeling, the impacts of ionic conduction governing structural factors, such as unit cell size, polarizability of anions framework, anions sublattice disordering, Li sublattice and charge carrier concentration etc., are systematically investigated. The major findings are summarized as follows:

(1) A new lithium thio-phosphate compound $Li_{15}P_4S_{16}Cl_3$ was discovered from Li_2S-P_2S_5-LiCl quasi-ternary phase diagram with the help of novel tool of in situ X-ray diffraction for synthesis. Its crystal structure was identified with using synchrotron X-ray and neutron diffraction. Although as-synthesized crystalline $Li_{15}P_4S_{16}Cl_3$ exhibited a poor ionic conductivity as expected, due to the fully occupancy of the two available Li sites, this new crystal structure provides new motif for the design of possible high-performance sulfide SEs.

(2) AIMD computation results suggested that after aliovalent cation doping in $Li_{15}P_4S_{16}Cl_3$ crystal structure, i.e. introducing certain amount of interstitial Li, the ionic conductivity of $Li_{15}P_4S_{16}Cl_3$ can be boosted by orders of magnitude. Ge doped $Li_{15}P_4S_{16}Cl_3$ was successfully designed, synthesized and tested. Neutron diffraction results confirmed the existence of Li at interstitial sites. Because of the strong repulsion between Li ions, the new interstitial Li sites lead to partial occupancy of original Li sites adjacent to them. Thus, the tuned Li sublattice triggers correlated migration of Li ions and results in 3 orders of magnitude higher ionic conductivity and lower activation energy than undoped $Li_{15}P_4S_{16}Cl_3$.

(3) A series of solid solution materials $Li_5PS_4(ClBr)_{1-x/2}(OH)_x$ was designed with using a novel entropy stabilization strategy, which takes the advantage of entropy introduced by multi-principal components and stabilizes the argyrodite structure with extraordinarily high concentration of Li vacancies that are commonly not allowed other sulfide argyrodite compounds. These materials are successfully synthesized, nicely demonstrating the

effectiveness of the entropy stabilization strategy. Results of i*n situ* X-ray diffraction for synthesis confirmed that argyrodite structure with ultra-high Li vacancy concentration can be stabilized at room temperature by increasing the entropy in anion sublattice, which is realized by introducing equiatomic Cl^-, Br^- and OH^- at the anion sites. The changes in both cation and anion sublattices accelerate Li diffusion coefficient drastically, leading to a record-high room temperature conductivity in argyrodite materials of up to xxxx mS/cm.

(4) In the study for halide SEs, anion mixing design strategy was used in order to control and tune the possible Li sublattice transitions. The existence of of Li ions at tetrahedral sites was revealed for the first time with using neutron diffraction characterization, which explains the record-high room temperature conductivity of 7.2 mS/cm in halide SEs achieved in this novel $Li_3YBr_3Cl_3$ material. Our work also revealed unprecedented insights on the formation and influence of grain boundary in halide SEs, which nicely explains previously reported discrepancy between experimentally measured and theoretically predicted conductivity and activation energy values and points new directions for halide SE design and development.

6.2 Future Directions

On top of the successful discovery, design and development of a good number of high-performance sulfide and halide SEs in this work, which show ionic conductivities even exceeding liquid electrolytes, there are still interesting scientific questions and technological challenges remaining to be addressed for ALSOLIBs commercialization. Some possible directions for future research to advance the understanding of ALSOLIBs are proposed as below:

(1) Although ALSOLIBs with utilizing sulfide and halide SEs demonstrate stable cycling life and good rate performance [7, 12-13], most studies utilize batteries configurations with

thick SEs and low cathode mass loading. To realize the advantage of energy density in ALSOLIBs, processing methods that can increase cathode active materials mass loading and reduce the thickness of SEs layer is highly desired.

(2) In current study of crystalline SEs, the structure-property relationships in SEs is extensively studied. The measured ionic conductivities of sulfide and halide SEs are usually regarded as bulk conductivity and the contribution from grain boundary is often neglected. In ALSOLIBs, SEs and cathode are in form of polycrystalline powders and the shuttling of Li ions between cathode and anode is achieved by passing through the solid-solid interfaces between SEs/SEs and SEs/electrode particles. Especially, in ALSOLIBs using sulfide SEs, the rate and cycling performance are highly dependent on the mass and charge transfer rate at SEs/electrode interface. However, the understanding of Li ion transport mechanism through interfaces between SEs/SEs and SEs/electrode particles is still limited. Further studies in both experimental characterization and theoretical simulations on Li ion diffusion across grain boundary and interface are highly desired.

(3) Pushing the limit of ionic conductivity of SEs to a higher level is critical for the development of ALSOLIBs. To date, the highest ionic conductivity reported from SEs has already achieved ~10^{-2} S/cm at room temperature, which is comparable with liquid electrolyte. In order to discover SEs with higher ionic conductivity, combined experimental and theoretical investigations show great promises, which are expected to provide insightful understanding of Li diffusion in SEs and guide the development of SEs with high ionic conductivity.

6.3 References

[1] Pearse, A. J.; Schmitt, T. E.; Fuller, E. J.; El-Gabaly, F.; Lin, C.-F.; Gerasopoulos, K.; Kozen, A. C.; Talin, A. A.; Rubloff, G.; Gregorczyk, K. E., Nanoscale Solid State Batteries Enabled by Thermal Atomic Layer Deposition of a Lithium Polyphosphazene Solid State Electrolyte. *Chemistry of Materials* **2017,** *29* (8), 3740-3753.

[2] Manthiram, A.; Yu, X.; Wang, S., Lithium battery chemistries enabled by solid-state electrolytes. *Nature Reviews Materials* **2017,** *2*, 16103.

[3] Li, Y.; Wang, Z.; Li, C.; Cao, Y.; Guo, X., Densification and ionic-conduction improvement of lithium garnet solid electrolytes by flowing oxygen sintering. *Journal of Power Sources* **2014,** *248*, 642-646.

[4] Ortiz, G. F.; López, M. C.; Lavela, P.; Vidal-Abarca, C.; Tirado, J. L., Improved lithium-ion transport in NASICON-type lithium titanium phosphate by calcium and iron doping. *Solid State Ionics* **2014,** *262*, 573-577.

[5] Sakuda, A., Favorable composite electrodes for all-solid-state batteries. *Journal of the Ceramic Society of Japan* **2018,** *126* (9), 675-683.

[6] Liu, L.; Xu, J.; Wang, S.; Wu, F.; Li, H.; Chen, L., Practical evaluation of energy densities for sulfide solid-state batteries. *eTransportation* **2019,** *1*, 100010.

[7] Kato, Y.; Hori, S.; Saito, T.; Suzuki, K.; Hirayama, M.; Mitsui, A.; Yonemura, M.; Iba, H.; Kanno, R., High-power all-solid-state batteries using sulfide superionic conductors. **2016,** *1*, 16030.

[8] Kamaya, N.; Homma, K.; Yamakawa, Y.; Hirayama, M.; Kanno, R.; Yonemura, M.; Kamiyama, T.; Kato, Y.; Hama, S.; Kawamoto, K.; Mitsui, A., A lithium superionic conductor. *Nature Materials* **2011,** *10*, 682.

[9] Seino, Y.; Ota, T.; Takada, K.; Hayashi, A.; Tatsumisago, M., A sulphide lithium super ion conductor is superior to liquid ion conductors for use in rechargeable batteries. *Energy & Environmental Science* **2014,** *7* (2), 627-631.

[10] Adeli, P.; Bazak, J. D.; Park, K. H.; Kochetkov, I.; Huq, A.; Goward, G. R.; Nazar, L. F., Boosting Solid-State Diffusivity and Conductivity in Lithium Superionic Argyrodites by Halide Substitution. *Angewandte Chemie International Edition 0* (0).

[11] Zhou, L.; Assoud, A.; Zhang, Q.; Wu, X.; Nazar, L. F., New Family of Argyrodite Thioantimonate Lithium Superionic Conductors. *Journal of the American Chemical Society* **2019,** *141* (48), 19002-19013.

[12] Zhou, L.; Kwok, C. Y.; Shyamsunder, A.; Zhang, Q.; Wu, X.; Nazar, L. F., A new halospinel superionic conductor for high-voltage all solid state lithium batteries. *Energy & Environmental Science* **2020,** *13* (7), 2056-2063.

[13] Li, X.; Liang, J.; Luo, J.; Norouzi Banis, M.; Wang, C.; Li, W.; Deng, S.; Yu, C.; Zhao, F.; Hu, Y.; Sham, T.-K.; Zhang, L.; Zhao, S.; Lu, S.; Huang, H.; Li, R.; Adair, K. R.; Sun, X., Air-stable Li3InCl6 electrolyte with high voltage compatibility for all-solid-state batteries. *Energy & Environmental Science* **2019,** *12* (9), 2665-2671.